FUNCTIONAL AND LOCALIZATION STUDIES OF HUMAN KYNURENINE 3-MONOOXYGENASE

Thesis submitted for the degree of
Doctor of Philosophy
at the University of Leicester

by
Aisha Mahmod O. Swaih
Department of Genetics
University of Leicester

March 2016

FUNCTIONAL AND LOCALISATION STUDIES OF HUMAN KYNURENINE 3-MONOOXYGENASE

AISHA MAHMOD O. SWAIH

ABSTRCT

Kynurenine 3-monooxygensae (KMO) is an outer mitochondrial membrane protein which plays a critical regulatory role in the kynurenine pathway (KP), catalysing the production of 3-hydroxykynurenine (3-HK). Increased KMO activity likely contributes to the excitotoxicity seen in neurodegenerative disorders by elevating the levels of the neurotoxic KP metabolites 3-HK and quinolinic acid. Studies employing models of Huntington's disease (HD) have shown that inhibition of KMO is neuroprotective, making KMO a potential therapeutic target for this disorder. This study interrogates the subcellular localisation of human KMO and dissects the interaction between KMO and the huntingtin (HTT) protein, mutations in which cause HD.

Confocal microscopy based co-localisation studies of KMO demonstrated that full length KMO (flKMO) was exclusively localised to the mitochondria when expressed in HEK293T cells. Notably, deleting a C-terminal portion of flKMO which contains a putative transmembrane domain mis-localised the remaining protein (tKMO) to other cellular compartments. Localization of flKMO to the outer mitochondrial membrane was further confirmed via transmission electron microscopy.

To study potential interactions between flKMO and HTT in living cells, bimolecular fluorescence complementation (BiFC) assay was utilised, which is based upon reconstitution of split fluorescence proteins. The BiFC approach allowed visualisation and quantification of flKMO interaction with both WT HTT and soluble mHTT fragments at the mitochondria. The strength of this interaction is inversely correlated to the length of the HTT polyglutamine expansion. Increased mitochondrial sub-cellular localisation of BiFC HTT constructs was confirmed via microscopy. tKMO however did not interact with HTT via the BiFC system, indicating that the C-terminal region of flKMO is important for both mitochondrial localisation and protein interaction. In total, these data suggest that flKMO-HTT interactions at the mitochondria may be biologically significant and could play a role in regulating KMO activity, and that in HD this regulatory process is impaired.

ACKNOWLEDGEMENTS

بِسْمِ اللَّهِ الرَّحْمَٰنِ الرَّحِيمِ

First and foremost, this work would not have been possible without the guidance of Allah the Almighty who facilitated everything, and empowered me to pursue my dreams.

My enduring gratitude goes to my supervisor Professor Flaviano Giorgini for his patience and outstanding support throughout my PhD. It was his generous guidance together with his trust in my abilities that allowed this project to reach its potential. I would also like to acknowledge; Dr Mariaelena Repici for her moral support and valuable input into my project not only for the guidance, discussions and troubleshooting, but also for her friendliness and encouragement. Dr Robert Mason for helping me find my feet with the molecular cloning and for all his appreciated suggestions for the project. Dr Sue Hardy for managing the orders for materials and reagents required for this project and maintaining such a pleasant working environment. My colleagues (past and present) in laboratories 102 and 106 for their help and friendship through all my ups and downs. My thesis committee Dr Eran Tauber and Dr Christopher Talbot, for reviewing my first and third year reports and providing helpful comments and incisive criticism. All the staff and students in the department of Genetics for being very approachable and supportive.

Dr Kees Straatman who was also one of the most helpful people, his patience, suggestions and guidance to all the microscopy related work is much appreciated. In addition, he managed the automated analysis using Scan^R software for my screens. Miss Natalie Allcock for processing, immunogold labelling and imaging my cells for the electron microscopy side of the project. Dr Federico Herrera for generously providing us with the HTT fragment BiFC constructs.

My beloved parents, their care, love and prayers have always surrounded me despite the long distance that kept us apart. My wonderful husband for always being there no matter what, inspiring me and taking care of me; words will not express the amazing support I have received from the three of them. My little daughter Afra to whom I dedicate my thesis to, as she has suffered the most for me not being there for her. Despite this she was very willing to help out with typing extra letters whenever she got a chance. My only sister and brothers whose support kept me going and being there for me in spirit, especially my brother Haidr for helping me settle in Leicester. Thank you to all my friends, especially Shairbanu, for being a second sister and listening to my moaning and bearing with all my frustrations when things were not going too well for me, and more importantly for being a lovely auntie to Afra. A million thanks to Mr Skinner and Professor Whelan for their life long support and encouragement. Finally on a personal note to my dear parents in Arabic script:

إلي والدي العزيزين، لولا فضل الله ثم دعواتكما و دعمكما المتواصلين و تشجيعكما لي لما تمكنت من إنجاز هذه الأطروحة. أطال الله في عمركما و حفظكما و جعلني عند حسن ظنكما بي. كل الحب و الإحترام و التقدير.

CONTENTS

TABLES

FIGURES

ABBREVIATIONS

3-HK	3-Hydroxykynurenine
aa	Amino acid
ADP	Adenosine diphosphate
AHR	Aryl hydrocarbon receptor
AIDS	Acquired immunodeficiency syndrome
Amp	Ampicillin
AMPA	Alpha-amino-3-hydroxy-5-methyl-4-isoxazole propionic acid
ANOVA	Analysis of variance
AP2M1	Adaptor-Related Protein Complex 2, Mu 1 Subunit
APS	Ammonium persulphate
ATP	Adenosine triphosphate
BDNF	Brain derived neurotrophic factor
BiFC	Bimolecular fluorescence complementation
BNA4	Biosynthesis of nicotinic acid 4
BSA	Bovine serum albumin
CC	Carboxyl-terminus of cyan fluorescent protein
CNS	Central nervous system
Co-IP	Co-Immunoprecipitation
CR	Congo red
CREB	cAMP response element-binding protein
CSF	Cerebrospinal fluid
Ctrl	Control
DCTN2	Dynactin 2
DJ-1	Parkinson disease protein 7 (PARK7)
DMEM	Dulbecco’s modified Eagle medium
DMSO	Dimethyl Sulfoxide
DNA	Deoxyribonucleic acid
DTT	Dithiothreitol
EAAT-2	Excitatory amino acid transporter-2
ECL	Enhanced Chemiluminescence
EGDA	Ethylene glycol tetraacetic acid
ETDA	Ethylenediaminetetraacetic acid
FBS	Fetal bovine serum
flKMO	Full length kynurenine 3-monooxygenase
GA	Glutaraldehyde
GAPDH	Glyceraldehyde-3-phosphate dehydrogenasae
GFP	Green fluorescent protein
GLT-1	Glutamate transporter-1
GN	Amino-terminus of enhanced green fluorescent protein
GPR35	G protein-coupled receptor 35
HAP-1	Huntingtin-associated protein-1
HD	Huntington's disease

HEAT	Huntingtin, elongation factor 3, the PR65/A subunit of protein phosphatase 2A and TOR1
HEK293T	Human embryonic kidney cell line
HTT	Huntingtin
HTT-FL	Full length huntingtin
ICC	Immunocytochemistry
ICCB	Intensity correlation coefficient-based
IDO	Indoleamine 2,3-dioxygenase
INF-γ	Interferon gamma
JACoP	Just another co-localisation plugin
Kan	Kanamycin
KAT	kynurenine aminotransferase
kDa	Kilodalton
KIPs	KMO interacting proteins
KMO	Kynurenine 3-monooxygenase
KP	Kynurenine pathway
KYNA	Kynurenic acid
LCL	Lymphoblastoid cell line
L-KYN	L-kynurenine
LTP	Long-term potentiation
mHTT	Mutant huntingtin
MYTH	Membrane yeast two hybrid
NAD	Nicotinamide adenine dinucleotide
NADPH	Nicotinamide adenine dinucleotide phosphate
Neo	Neomycin
NMDA	N-methyl-D-aspartate
NO	Nitric oxide
NOS	Nitric oxide synthase
ORF	Open reading frame
PACSIN1	Protein kinase C and casein kinase 2 substrate in neurons 1
PARP	Poly (ADP-ribose) polymerization
PBS	Phosphate buffered saline
PBS-T	Phosphate buffered Saline -Tween 20
PC	Pearson's coefficient
PCR	Polymerase chain reaction
PET	Positron emission tomography
PFA	Paraformaldehyde
polyP	Polyproline
polyQ	Polyglutamine
PSD-95	Post synaptic density-95
QUIN	Quinolinic acid
RFP	Red fluorescent protein
RNA	Ribonucleic acid
ROS	Reactive oxygen species

SDS	Sodium dodecyl sulphate
SDS-PAGE	Sodium dodecyl sulfate polyacrylamide gel electrophoresis
SEM	Standard error of the mean
shRNA	Short hairpin RNA
SNP	Single nucleotide polymorphism
TBE	Tris-borate-EDTA
TDO	Tryptophan-2,3-dioxygenase
TEM	Transmission electron microscopy
TEMED	Tetramethylethylenediamine
tKMO	Truncated kynurenine 3-monooxygenase
TM	Transmembrane
U2OS	Human osteosarcoma cell line
VC	Carboxyl-terminus of Venus
VN	Amino-terminus of Venus
WT	Wild type
YAC	Yeast artificial chromosome
Zeo	Zeocin
α7nACh	α7 nicotinic acetylcholine

CHAPTER 1 INTRODUCTION

Despite the many advances in modern research, Huntington's disease (HD) has remained incurable, and few treatment options are available. However, over the decades since the causative mutation has been identified, several targets have been approached. With emphasis on kynurenine pathway (KP) dysfunction and its association with hallmarks of this disease, kynurenine 3-monoxygenase (KMO) has been found to be a key modulator of this pathway and thereby likely to have relevance in HD. Nonetheless, the underlying mechanisms linking KMO and the KP to HD are still to be unravelled. In such a context, my thesis research provides a pivotal link via KMO protein interactions which enhances our understanding of KMO biology, and ultimately therapeutic strategies targeting it. Due to the extensiveness and depth of research in this field, a comprehensive review is almost unachievable and beyond the purpose of this thesis. Thus, this chapter briefly reviews the kynurenine pathway: its key enzymes and metabolites; and HD: huntingtin protein, the role that KMO plays in pathogenesis and the potential of KMO in HD therapy.

1.1 Overview of the Kynurenine Pathway (KP)

Tryptophan is an essential amino acid for several biological functions (Bertazzo *et al.*, 2001). Description of tryptophan as a precursor of kynurenine and nicotinic acid was first provided by Beadle *et al.* in (1947). The KP is a major metabolic pathway in mammals through which more than 95% of tryptophan is degraded within the CNS (Stone, 1993) (Figure 1-1). The downstream metabolites of KP are collectively called kynurenines as the name of the pathway suggests. Catabolism through KP is firmly regulated by the immune system (Schwarcz *et al.*, 2012).

The metabolic cascade of the KP is predominantly initiated by two enzymes: tryptophan 2,3-dioxygenase (TDO) and indoleamine 2,3-dioxygenase (IDO) that breakdown tryptophan to form formylkynurenine, which in turn is further metabolised to L-kynurenine (L-KYN) (Thomas and Stocker, 1999). TDO is a substrate limited enzyme which is characterised as tissue specific, and was originally thought to be exclusively expressed in the liver. However, Haber *et al.* (1993) demonstrated that TDO RNA is also present in the rat brain. IDO is widely present in various tissues in mammals

including the CNS (Watanabe *et al.*, 1981), but predominantly expressed in lungs, small intestine and placenta (Yamazaki *et al.*, 1985). Unlike TDO, IDO is a rate-limiting enzyme, its activation is stimulated upon immunological responses that result in cytokine production (Allegri *et al.*, 2003). Interferon gamma (INF-γ) is considered to be the most potent cytokine released from natural killer cells as well as upon activation of T-lymphocytes (Carlin *et al.*, 1989; Chen and Guillemin, 2009; Takikawa *et al.*, 1988), and is indeed capable of up-regulating IDO expression and activity (Carlin *et al.*, 1989; Takikawa *et al.*, 1999). In addition to the predominant IDO (also known as IDO1), the more recently described IDO2 is also involved in tryptophan catabolism (Ball *et al.*, 2007; Metz *et al.*, 2007; Murray, 2007). While IDO and IDO2 are structurally similar, IDO2 is encoded by the *IDO2* gene which is located adjacently downstream of *IDO1* (Ball *et al.*, 2007). Moreover, IDO2 expression is primarily confined to kidney, epididymis, liver, brain and placenta (Ball *et al.*, 2007; Metz *et al.*, 2007). IDO2 differs from IDO in its signalling pathway induction, which is activated independent of tryptophan availability (Ball *et al.*, 2007; Metz *et al.*, 2007). Moreover, it is controversial as to whether expression and activity of IDO2 is up-regulated in response to the stimulant INF-γ (Ball *et al.*, 2007; Fatokun *et al.*, 2013). Therefore, it is postulated that IDO2 might have another role other than its enzymatic activity, which is also supported by its differential expression pattern from IDO1 (Fatokun *et al.*, 2013).

Insufficient synthesis of L-KYN occurs in the brain due to the lower levels of IDO and TDO, thus the KP is mainly driven by L-KYN uptake from the peripheral system via the blood-brain barrier (Fukui *et al.*, 1991; Moroni, 1999). The importance of L-KYN is brought to light by its ability to act as a substrate for two different key enzymatic activities that metabolise L-KYN to generate three different neuroactive metabolites. These key enzymatic steps are catalysed by KMO and the kynurenine aminotransferases (KATs) leading to branching of the pathway into neurotoxic and neuroprotective arms, respectively. Two distinct KATs have been characterised in mammals: KATI (or glutamine transaminase K), KATII (or α-aminoadipate aminotransferase). Although KATI and KATII are both functional in the brain (such as in astrocytes and neurons) with differing kinetics, KATII exhibits more participation in L-KYN catabolism. The two isozymes are segregated by their isoelectric preference: mostly alkaline or neutral pH for KATI and KATII, respectively (Okuno *et al.*, 1991;

Rossi *et al.*, 2008). In addition to KATI and KATII, the mitochondrial aspartate aminotransferase (designated as KATIII) has been recently identified (Yu *et al.*, 2006).

In accordance to the expression of KMO and KATs, the two branches of the pathway are physically segregated in the CNS into different major cellular types (Amori *et al.*, 2009). KMO exhibits activity in microglial cells (Giorgini *et al.*, 2008; Guillemin *et al.*, 2001), where the downstream neurotoxic metabolite 3-hydroxykynurenine (3-HK) is synthesised. 3-HK then acts as a precursor to the intermediate metabolite 3-hydroxyanthranilic acid. The latter is further metabolised to the excitotoxin quinolinic acid (QUIN). QUIN exits the microglia and is subsequently converted to nicotinamide adenine dinucleotide (NAD^+) in astrocytes and neurons (Guillemin *et al.*, 2005). As microglia exhibit very little KATs activity, these cells predominantly utilise KMO to synthesis the neurotoxic KP metabolites. Astrocytes on the other hand, appear to exhibit only KATs activity and thus breakdown L-KYN to the neuroprotective metabolite, kynurenic acid (KYNA) (Guillemin *et al.*, 2001). In addition, kynureninase provides an alternative route for L-KYN catabolism producing anthranilic acid, which can be converted to 3-hydroxyanthranilic acid, the upstream QUIN precursor (Bender and McCreanor, 1982).

1.1.1 The KMO enzyme: function to structure and genetics

KMO (also known as kynurenine 3-hydroxylase) is a flavin monooxygenase functionally dependent on NADPH as electron donor (Nisimoto *et al.*, 1977; Uemura and Hirai, 1998). Back in 1956, KMO was first discovered to be responsible for the conversion of L-KYN to 3-HK in the mitochondria of cat and rat livers (De Castro *et al.*, 1956). Later by using mitochondrial fractionation of rat liver, KMO was described as a mitochondrial outer membrane protein (Horn *et al.*, 1971; Nisimoto *et al.*, 1975; Okamoto *et al.*, 1967). Being a membrane bound enzyme its purification was highly challenging due to the presence of haemoprotein contaminants. For this reason, the enzyme was isolated from pig liver with only 86% purity (Uemura and Hirai, 1998). In the CNS, KMO is predominantly found in microglial cells (Giorgini *et al.*, 2008; Guillemin *et al.*, 2001; Guillemin *et al.*, 2003), whereas in the periphery, KMO is highly expressed in the liver, kidney (Alberati-Giani *et al.*, 1997; Erickson *et al.*, 1992), placenta (Alberati-Giani *et al.*, 1997) and monocytic derivatives (Chiarugi *et al.*, 2001a; Jones *et al.*, 2015).

To date, no structural characterisation of the human native protein has been constructed although the molecular weight of the full length human KMO (486 aa) was estimated to be 55,762 Da, from a cloned human cDNA KMO (Alberati-Giani *et al.*, 1997), while purified pig liver KMO is ~ 49kDa (Uemura and Hirai, 1998). However, Amaral *et al.* (2013) recently published the first crystal structure of *Saccharomyces cerevisiae* KMO, which has similar kinetic properties to the human enzyme despite its C-terminal truncation. The crystal structure of KMO confirmed the analogy of KMO to flavin dependent hydroxylase family, with the classic Rossman fold of five β-sheets and four α-helices (Amaral *et al.*, 2013).

The human *KMO* gene maps to chromosome 1 at the cytogenetic location (1q42-q44) and is composed of 15 exons (GenBank Accession No. NM_003679). It is predicted to have four protein-coding isoforms of 486 aa, 473 aa, 452 aa and 182 aa. The isoforms 486 aa, 473 aa and 182 aa have two putative transmembrane domains, whereas the 452 aa isoform only has a single membrane spanning region (Ensembl database).

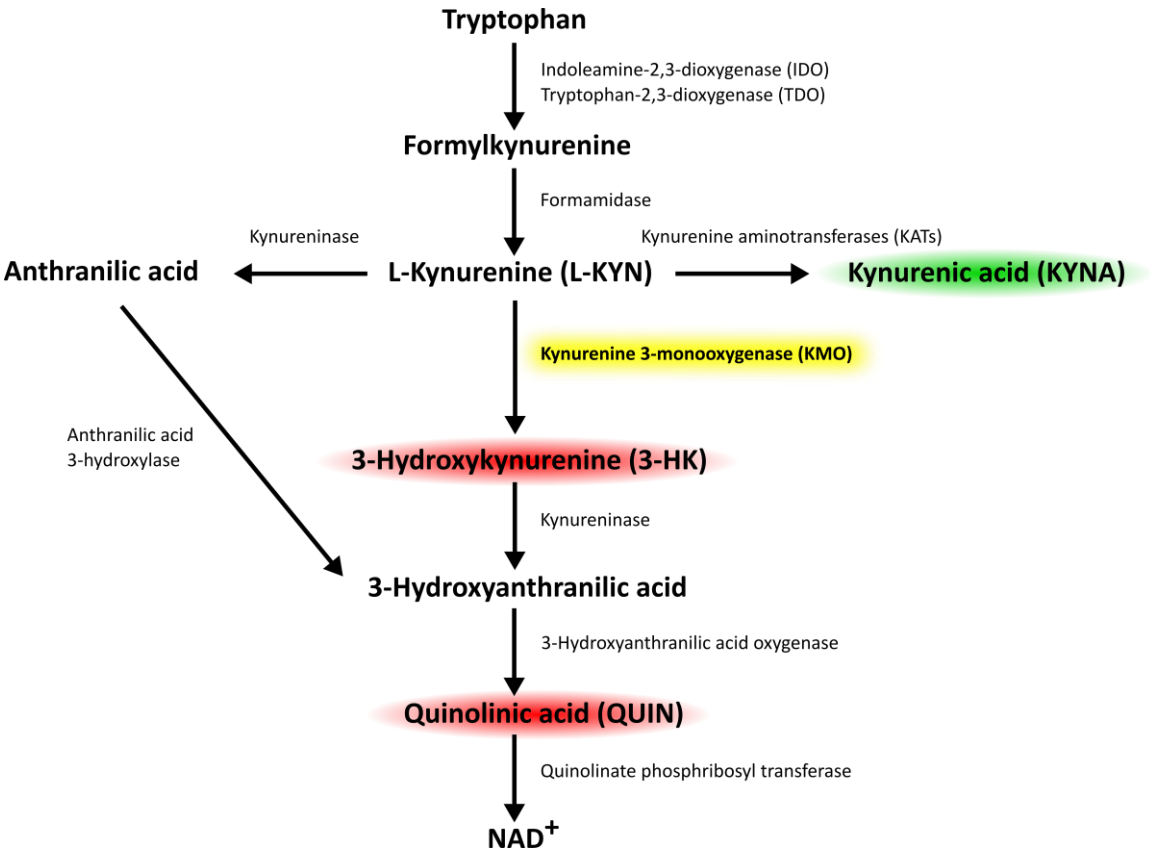

Figure 1-1 Simplified overview of the kynurenine pathway in mammals.
Protective and toxic neuroactive metabolites are highlighted in green and red, respectively. KMO is highlighted in yellow.

1.1.2 Properties of L-KYN neuroactive derivatives

The major kynurenines produced by KATs (KYNA) as well as KMO (3-HK and QUIN) will be discussed in the following sections:

1.1.2.1 Kynurenic acid (KYNA)

KYNA has been known to be produced in mammals since 1853, where it was detected in canine urine (Liebig, 1853). However, its existence in the brain was not identified until (1988) by Moroni *et al.*, and it was later shown that KYNA poorly crosses the blood-brain barrier (Fukui *et al.*, 1991). The neuroprotective significance of this metabolite was highlighted by its antagonistic role at ionotropic glutamate receptors subtypes, which include: N-methyl-D-aspartate (NMDA), kainate and α-amino-3-hydroxy-5-methyl-4-isoxazole propionic acid (AMPA) receptors (Bertolino *et al.*, 1989; Elmslie and Yoshikami, 1985; Foster *et al.*, 1984b; Perkins and Stone, 1982; Prescott *et al.*, 2006). KYNA inhibition of NMDA receptors is allosteric at the glycine binding site (Bertolino *et al.*, 1989; Birch *et al.*, 1988; Johnson and Ascher, 1987), and only requires low levels of KYNA , while higher levels (0.1-1 mM) of KYNA are required for its inhibitory effect on kainate and AMPA receptors (Carpenedo *et al.*, 2001; Stone, 1993). KYNA is also implicated in non-competitive inhibitory effect on α7 nicotinic acetylcholine (α7nACh) receptors (Hilmas *et al.*, 2001) that might also contribute to the inhibition of glutamate release (Carpenedo *et al.*, 2001). In addition, KYNA acts as a ligand for activation of the G protein-coupled receptor GPR35 (Wang *et al.*, 2006), which has been suggested to result in reduction of glutamate concentration in the brain, thereby modulating neuroinflammation (Berlinguer-Palmini *et al.*, 2013; Moroni *et al.*, 2012). KYNA also exhibits antioxidant properties associated with its ability to scavenge free radicals in a manner that is unlikely related to its antagonistic effect on glutamate and nicotinic receptors (Goda *et al.*, 1999; Lugo-Huitrón *et al.*, 2011).

1.1.2.2 3-Hyroxykynurenine (3-HK)

3-HK is a neurotoxic metabolite, as its autooxidation mediates neuronal toxicity through the generation of highly reactive free radicals, that lead to the induction of cell death with apoptotic features (Chiarugi *et al.*, 2001b; Okuda *et al.*, 1996; Okuda *et al.*, 1998). In KP, 3-HK is the bioprecursor of QUIN and increased levels of 3-HK potentiates QUIN excitotoxicity (Guidetti and Schwarcz, 1999). This is particularly

important as 3-HK is capable of crossing the blood-brain barrier and can contribute to the production of QUIN (Fukui *et al.*, 1991).

1.1.2.3 Quinolinic acid (QUIN)

QUIN was first described as a potent excitant agonist of NMDA receptors by Stone and Perkins (1981). QUIN-mediated overstimulation of NMDA receptors is facilitated via impairment of intracellular Ca^{2+} signalling, leading to elevated Ca^{2+} influx through NMDA receptors (Lugo-Huitrón *et al.*, 2013; Tymianski *et al.*, 1993) and depletion of ATP production which eventually cause necrotic cellular death (Chiarugi *et al.*, 2001b). QUIN also induces the formation of reactive oxygen species (ROS), as QUIN administration in human astrocytes and neurons triggers nitric oxide synthase activity (NOS) which induces nitric oxide (NO) production and free radical damage (Braidy *et al.*, 2009). Under normal physiological conditions, QUIN concentration in the human brain is very low (nanomolar range) (Martin *et al.*, 1992). Moreover, the blood-brain barrier seems to prevent peripheral QUIN from penetrating to the CNS QUIN pool (Foster *et al.*, 1984a; Fukui *et al.*, 1991). Thus, QUIN activity in the brain is mainly driven by its synthesis through KP in microglia (Heyes *et al.*, 1996). Such properties make this KP metabolite a pivotal endogenous excitotoxin within the CNS and its implications are vital for disease mechanisms.

1.1.3 Significance of KP in disease mechanisms

The knowledge and insight gained from studying the KP over the decades has shifted the centre from the biological concepts to clinical prospective upon identification of exploitable therapeutic targets. Aside from neurodegenerative disorders such as HD, Alzheimer's disease and Parkinson's disease (Tan *et al.*, 2012), dysfunction of KP or imbalance of its metabolites is involved in several brain and immune disorders. This includes evidence of implications in psychiatric disorders linked to anxiety, depression and schizophrenia. In addition, other disorders such as multiple sclerosis, malaria, acquired immunodeficiency syndrome (AIDS), spinal muscular atrophy, epilepsy and ischaemia have been linked to the KP. These disorders were reviewed in light of kynurenines, specifically QUIN, by Stone (2001). However, the scope of this thesis focuses primarily on HD and thus only kynurenines implications on HD mechanisms and therapeutics in relevance to KMO will be discussed in the rest of this mini review.

1.2 Huntington's disease (HD)

HD is the most common monogenic neurodegenerative disorder with a prevalence of 12.3 per 100,000 in the UK population (Evans *et al.*, 2013). HD is lethal and inherited in an autosomal dominant manner. Although the disease was first described in detail in 1872 by the physician George Huntington (Huntington, 1872), the gene responsible for HD was not successfully cloned until 1993 (The Huntington's Disease Collaborative Research Group, 1993).

1.2.1 HD genetics, pathological features and clinical symptoms

HD is genetically associated with an unstable expansion in a glutamine encoding CAG tract within exon 1 of the huntingtin gene (*HTT*) on chromosome 4 (cytogenetic location: 4p16.3) (The Huntington's Disease Collaborative Research Group, 1993). In non-HD individuals, the normal allele repeat is polymorphic and ranges in length from 6 to 35 CAG repeats. Although the range 35-39 repeat is abnormal, it leads to incomplete penetrance; whereby carriers of this repeat range may or may not develop the disorder. When the defective allele has 40 or more CAG repeats, HD is fully penetrant leading to certain clinical manifestations. Individuals with over 60 repeats develop HD under the age of 20 years, which is known as juvenile HD. The length of the expanded CAG repeat strongly correlates with the age of onset of HD clinical symptoms (Andrew *et al.*, 1993), and this is dominantly determined by the longest expanded inherited HD allele (Lee *et al.*, 2012). Interestingly, anticipation in HD shows inheritance through the paternal line, which is defined by a decrease in the age of onset of the offspring from their affected fathers (Ridley *et al.*, 1988). This decrease was found to range from minor in most cases, to up to 24 years in few cases. On the other hand, such dramatic difference was not seen in the age of onset of the offspring of affected mothers (Ridley *et al.*, 1988). This is mainly due to the instability in the meiotic transmission of the CAG repeat during spermatogenesis, leading to an increased expanded CAG repeat inherited in the offspring (Wheeler *et al.*, 2007). This anticipation phenomenon is likely to be the cause of most juvenile HD cases (Telenius *et al.*, 1993).

HTT encodes for the huntingtin protein (HTT) and the expanded CAG mutation leads to lengthening of a stretch of polyglutamine (polyQ) within the N-terminus of HTT (The Huntington's Disease Collaborative Research Group, 1993), resulting in a toxic gain of

function of mutant HTT (mHTT). However, contribution of the loss of normal HTT allele function (Cattaneo *et al.*, 2001) as well as RNA mediated toxicity (Fiszer and Krzyzosiak, 2013) to the HD pathogenesis cannot be ruled out. Pathologically, HD is generally characterised by fragmentation of mHTT upon proteolytic cleavage of full length mHTT (Martindale *et al.*, 1998). Aberrant splicing of HTT mRNA has also been recently found to result in the formation of short N-terminal exon 1 fragments (Sathasivam *et al.*, 2013). HTT fragments accumulate within the cell and form cytoplasmic and nuclear inclusions (Martindale *et al.*, 1998), which eventually lead to remarkable atrophy of medium spiny striatal neurons in the basal ganglia and cerebral cortex, as demonstrated in the analyses of post-mortem brain tissues (DiFiglia *et al.*, 1997; Vonsattel *et al.*, 1985).

HD strikes in individuals who have expanded CAG repeat (40 or more) in mid-life, typically between the age of 35 and 50 years. The disease is invariably fatal within 10-20 years of the onset of HD symptoms. The hallmark symptom of HD is chorea (involuntary movements) which becomes more severe as the disease progresses leading to dystonia (muscles spasms); and gradually results in muscular rigidity and impaired coordination, featuring bradykinesia. Besides motor dysfunction, HD also causes cognitive decline, behavioural disorders and psychiatric disturbances, reviewed in (Ross *et al.*, 2014).

1.2.2 Structural features of HTT

Full length HTT is a large protein of about 348 kDa, which is encoded by the *HTT* locus spanning over 180kb and consisting of 67 exons (Ambrose *et al.*, 1994). An overview of HTT structure and main domains are highlighted in Figure 1-2. Toward the N-terminus of HTT, the highly conserved first 17 aa (N17: MATLEKLMKAFESLKSF), precede the polyQ (Atwal *et al.*, 2007). The N17 plays a role in membrane association and intracellular trafficking of HTT (Atwal *et al.*, 2007; Burke *et al.*, 2013; Rockabrand *et al.*, 2007), enhance formation of aggregates, and along with polyQ region disrupt Ca^{2+} homeostasis (Rockabrand *et al.*, 2007). N17 also has a nuclear export signal (NES) that interacts with nuclear pore protein and facilitates exporting N-terminal fragments into the cytoplasm: this mechanism is impaired by the presence of increased polyQ expansion leading to mHTT accumulation in the nuclear compartments (Cornett *et al.*,

2005). In addition to the N-terminal NES, another conserved NES is located at the C-terminus of HTT (Xia *et al.*, 2003).

More importantly, the N17 region provides multiple posttranslational modification sites including phosphorylation (Aiken *et al.*, 2009; Thompson *et al.*, 2009), ubiquitination and sumoylation (Steffan *et al.*, 2004), which are crucial for pathogenesis. Phosphorylation regulates HTT clearance, subcellular localisation and toxicity (Atwal *et al.*, 2011); three major phosphorylable residues have been identified within the N17 region: threonine T3 (Aiken *et al.*, 2009), and serine S13 and S16 (Thompson *et al.*, 2009). N17 phosphorylation has been studied by substituting the residues with alanine (A) or (aspartic acid (D)/glutamic acid (E) to generate nonphosphorylable and phosphomimetic mutants, respectively. Aiken *et al.* (2009) showed that T3A slightly decreased HTT aggregates, whereas the phosphorylated mutant (T3D) promoted aggregation (Aiken *et al.*, 2009). On the other hand, S13E and S16E double mutants resulted in reduction in the number of cells with inclusions and prevented significant cell death, whereas the dual mutant of S13A and S16A led to smaller, but more inclusions per cells and was not protective (Atwal *et al.*, 2011). It was also shown that S16D increased nuclear localisation whereas S16A enhanced cytosolic localisation. However, S13D or S13A had no major effect. Double mutation of S13D and S16D or S13A and S16A replicates the effect of S16D or S16A respectively (Atwal *et al.*, 2011). These observations indicate that the targeted-phosphorylation of the two serine (S13 and S16) sites is crucial for modulating HTT aggregation and toxicity as well as subcellular localisation.

Immediately downstream of the N17 is the polymorphic and disease causing polyQ region, followed by the 51 aa proline-rich domain (polyproline or polyP). PolyP mediates HTT protein interactions, such as: WW domain proteins (Faber *et al.*, 1998), lipid membranes (Burke *et al.*, 2013), and protein kinase C and casein kinase 2 substrate in neurons 1 (PACSIN1) (Modregger *et al.*, 2002). Caron *et al.* (2013) showed that flexibility in the polyQ tract permits its flanking regions, N17 and polyP, to interact intramolecularly. This interaction is stabilised by PACSIN1 that binds to both N17 and PolyP regions and is impaired by the increased polyQ expansion that affects HTT flexibly and thus its conformation (Caron *et al.*, 2013). One of the first studies on HTT structure demonstrated that polyQ forms β-sheet structures via strong hydrogen bonding between the polar glutamine amide side chains, via a zipper mechanism (Perutz *et al.*,

1994), which explains the expanded polyQ tract rigidity in Caron's interaction system. Furthermore, Tam *et al.* (2009) illustrated in a mutant HD model that N17 interacts with other N17 domains and thus may facilitate oligomerization or fibers formation; as well as with polyQ tract which might promote aggregation. However, N17 lacked interaction with polyP domain which further supports Caron's findings, (Tam *et al.*, 2009). These studies have shed light on the significance of exon 1 fragment domains in HTT molecular interactions and dynamics.

Full length HTT also contains highly conserved HEAT (huntingtin, elongation factor 3, the PR65/A subunit of protein phosphatase 2A and TOR1) repeat clusters (Andrade and Bork, 1995). HEAT repeat is ~50 aa degenerate helical hairpin motif composed of two anti-parallel α-helices (Li *et al.*, 2006), where repeats arrange in tandem structures that serve as flexible scaffolding facilitating proteins complexes assembly (Neuwald and Hirano, 2000). Proteins containing HEAT repeats similar to those found in HTT were found to be linked with protein-protein interactions associated with cytoplasmic and nuclear transport, microtubule dynamics and chromosomal segregation (Neuwald and Hirano, 2000). HTT therefore might act as a multifunctional scaffold protein as in its association with post synaptic density (PSD-95) modulating formation of multi-protein complexes, including kainate and NMDA receptors (Sun *et al.*, 2001).

In addition, HTT is subjected to other post translational modifications such as phosphorylation, proteolytic cleavage, acetylation and palmitoylation along the length of the protein (Zheng and Diamond, 2012).

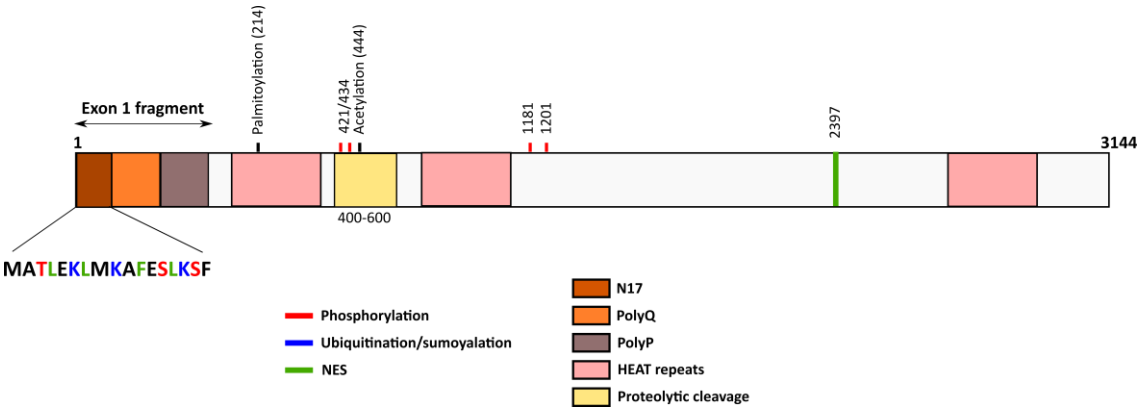

Figure 1-2 Schematic representation of regions present in full length HTT protein.
The exon 1 region is composed of the N17, polyQ and polyP domains at the N-terminus of HTT. The N17 sequence is rich in post translational modification sites and contains a nuclear export signal (NES), indicated by red, blue and green fonts, respectively. Several positions of proteolytic cleavage have been identified within 400-600 aa region. Three HEAT repeats clusters are highlighted as well as further post translational modification sites (red pointed lines are phosphorylation sites) and a C-terminal NES (redrawen from Zheng and Diamond, 2012).

1.2.3 Cellular distribution and function of HTT

HTT is ubiquitously expressed in neuronal and non-neuronal tissues throughout the body, with the highest levels in the CNS in neurons, and in the periphery in testes (Trottier *et al.*, 1995; Zuccato *et al.*, 2010). On the cellular level, HTT is associated with membranous organelles including the Golgi complex, endoplasmic reticulum, nucleus and mitochondria. HTT is also found at the synapses associated with vesicular structures as well as microtubules (Zuccato *et al.*, 2010).

The widespread expression of the large HTT protein makes it difficult to assign specific functions. It has been suggested that HTT plays a role in normal embryonic development, as a knockout of HTT in mice causes embryonic lethality prior to gastrulation stage and the development of nervous system (Duyao *et al.*, 1995; Nasir *et al.*, 1995; Zeitlin *et al.*, 1995). Moreover, embryonic lethality in yeast artificial chromosome (YAC72) mice can be rescued by the compensation effect of human mHTT expressed by the transgene although these mice lack endogenous HTT, suggesting that this role is independent of the length of its CAG tract (Leavitt *et al.*, 2001). Studying HTT interaction networks has facilitated a better understanding of the functions that HTT might be involved in and the possible polyQ disruptions of such functions (Zuccato *et al.*, 2010). Normal HTT is believed to have an anti-apoptotic role

via inactivation of caspase-3 and caspase-9 and disrupting the activity of the apoptosome complex (Rigamonti *et al.*, 2000; Rigamonti *et al.*, 2001). In addition, HTT appears to be involved in axonal and vesicle transport mediated by its interaction with huntingtin-associated protein-1 (HAP-1) (Block-Galarza *et al.*, 1997). Interactions of HTT with cytoskeletal and synaptic vesicle proteins also contribute to the regulation of synaptic activity in the neurons (Smith *et al.*, 2005). HTT is also involved in transcriptional regulation through interactions with various transcription factors (Gil and Rego, 2008), such as the cAMP response element-binding protein (CREB) (Sugars *et al.*, 2004) that regulates alongside other transcription factors the transcription of brain derived neurotrophic factor (BDNF) (Tao *et al.*, 1998). BDNF is a growth factor protein, which is produced by the cerebral cortex and transported in an anterograde manner to neurons where it provides support of neuronal survival, growth and differentiation (Conner *et al.*, 1997). Normal HTT was shown to up-regulate BDNF transcription and this mechanism is impaired with the mutant form of HTT leading to striatal neuronal death due to reduced synthesis of BDNF (Zuccato *et al.*, 2001).

In total, mutation to HTT protein leads to formation of protein aggregates that accumulate in the cells, interfere with cellular pathways and impair functions HTT is involved in. This results in neurodegeneration via several mechanisms: transcriptional dysregulation, proteolysis, mis-folding and aggregation, autophagy, excitotoxicity as well as mitochondrial dysfunction (Zheng and Diamond, 2012).

1.3 KMO as a modulator of the KP: relevance to HD pathogenesis

In 1983, a potential role of QUIN in HD pathogenesis was demonstrated by its capability to produce axon-sparing lesions in rat brain mimicking HD lesions, upon QUIN intracerebral injection (Schwarcz *et al.*, 1983). The neuronal damage of QUIN was further characterised by Beal *et al.* (1986) confirming the close resemblance with HD lesions, unlike lesions affecting all cell types produced by other neuroexcitatory compounds to generate HD-like models (such as kainic acid, ibotenic acid and *N*-methyl-D-aspartate) (Beal *et al.*, 1986).

Under normal physiological conditions, L-KYN intracerebral administration into rat brain showed that the degree of resulting 3-HK and KYNA synthesis is comparable (Guidetti *et al.*, 1995). Alteration in the KP upon immune induction and neuroinflammation results in up-regulation of IDO activity and thus production of the neurotoxic kynurenines increases (Heyes *et al.*, 1992). As consequence, selectively in the neostriatum and the neocortex of early stages in HD patients, 3-HK and QUIN levels were both increased by three to four fold, while the changes in L-KYN and KYNA levels were not as dramatic. Nonetheless, the ratios of 3-HK/KYNA and QUIN/KYNA were significantly higher in early stages HD than the controls, implying the increased flux towards the KMO side of the pathway to produce neurotoxins. This suggests an involvement of 3-HK and QUIN in early disease development, as in HD these regions exhibit the most prominent neuronal loss (Guidetti *et al.*, 2004). Further evidence from earlier studies also supports this as elevated levels of 3-HK were demonstrated in post-mortem brains of HD patients (Pearson and Reynolds, 1992). In another study, increased ratios of L-KYN/KYNA in post-mortem putamen and decreased KYNA concentration in cerebrospinal fluid (CSF) in HD brain were shown (Beal *et al.*, 1992). However, it was reported that the number of astrocytes is increased by 16% in early stages of HD and by 28% in advanced stages in post-mortem HD brains (Vonsattel *et al.*, 1985), which might account for the need to breakdown the excessive QUIN amounts and not necessarily synthesising KYNA. These findings propose that the fluctuation in the levels of kynurenines have discrete effects on the neurodegeneration of HD and the ratio of KYNA versus 3-HK/QUIN is critical for neuroprotection (Schwarcz *et al.*, 2012). The implicated roles that KP and KMO are predicated to play in HD pathogenesis are likely to be related to microglial activation,

excitotoxicity and mitochondrial dysfunction, which will be addressed in the following sections.

1.3.1 Microglia activation in HD

Microglia are a type of non-neuronal macrophage-like glial cells resident in the CNS, where KMO is localised and functional (Giorgini *et al.*, 2008; Guillemin *et al.*, 2001; Guillemin *et al.*, 2003). The role of human microglia in the production of QUIN, which is elevated upon brain immune activation was described by Heyes *et al.* (1996). This solely occurs in microglia, and neither astrocytes nor neurons were capable to yield QUIN in primary cultures of human foetal brain cells stimulated with INF-γ (Guillemin *et al.*, 2005); suggesting the importance of activated microglia in QUIN mediated pathogenesis. Reactive microglia have indeed been detected in neostriatum and cortex of post-mortem HD brains, which accumulated with disease progression (Sapp *et al.*, 2001). This was also supported by *in vivo* studies of patient brains using positron emission tomography (PET) imaging: HD microglia activation was significantly increased in relation to disease severity in cortical regions and striatum (Pavese *et al.*, 2006), and interestingly early microglial activation was also detected in pre-symptomatic HD carriers (Tai *et al.*, 2007). Furthermore, in HD carriers, activated microglia were suggested to be due to a stimulation of the immune system that was featured in elevated interleukin-6 levels as early as 16 years prior to the predicted onset of clinical HD symptoms (Björkqvist *et al.*, 2008). It has also been shown that ferritin accumulate mainly in microglia of early stages of HD of both R6/2 mice model and post-mortem HD patients; suggesting that it might play a role in microgliosis and HD pathogenesis (Simmons *et al.*, 2007). In transgenic mice models, mHTT inclusions were observed in glial cells including microglia (Davies *et al.*, 1999) and mHTT expression detected in activated mouse microglia was accompanied with increased levels of 3-HK (Giorgini *et al.*, 2008). Although the role of mHTT in activating microglia is not understood, Ma *et al.* (2003) showed that HD mice accelerate structural microglial abnormalities associated with aging in comparison to normal mice, and HD microglia eventually became smaller and exhibit condensed nuclei and fragmented cytoplasm (Ma *et al.*, 2003).

1.3.2 Excitotoxicity and the role of NMDA receptors in HD

In mammalian CNS, excitotoxicity is defined by the selective neuronal loss due to overstimulation of glutamate receptor, especially the NMDA receptors subclass, upon the increase in glutamatergic neurotransmission (Zuccato *et al.*, 2010).

NMDA are heteromeric receptors and composed of three subunits: NR1, NR2 and NR3. NR1 contains the co-agonist glycine binding site whereas glutamate binds at NR2 subunit which has four isoforms (NR2A, NR2B, NR2C and NR2D). NR3 has a regulatory function with two isoforms (NR3A and NR3B) (Cull-Candy *et al.*, 2001; Sánchez *et al.*, 2008). The functional subunits combination of NR1/NR2B exhibits increased NMDA-mediated excitotoxicity when compared to NR1/NR2A (Zeron *et al.*, 2001). Medium spiny striatal neurons of caudate and putamen are the predominant cell type affected by the increase in glutamate in the CNS, as a result of the abundant expression of NR2B subunit on their NMDA receptors complex (Zeron *et al.*, 2004). The mechanism of excitotoxic neuronal damage may be also mediated by increased cortical afferents release of glutamate, reduced glial cells uptake of glutamate, elevated Ca^{2+} influx as well as mitochondrial dysfunction and apoptotic pathways (Zuccato *et al.*, 2010).

In HD, corticostriatal glutamate release increases upon disruption of the axonal vesicular transport due to mHTT expression, whereas glial glutamate uptake is impaired (Miller and Bezprozvanny, 2010). Glial cells (microglia, astrocytes and oligodendrocytes) count for 90% of the brain cells (Shin *et al.*, 2005), and one of their important functions is to provide support to neuronal cells: for example they convey protection against glutamate induced excitotoxicity by expressing excitatory amino acid transporter-2 (EAAT-2) in humans or GLT-1, in rodents; that facilitate their capability to remove extracellular glutamate (Maragakis and Rothstein, 2001). However, mHTT interferes with this protective glial role by accumulating in their nuclei leading to reduced expression of glutamate receptors and subsequently their glutamate uptake capacity in cultured astrocytes and HD mouse brains (Shin *et al.*, 2005). In addition, over-activation of NMDA receptors via excitatory amino acids results in increased intracellular Ca^{2+} activity permitting Ca^{2+} entry through NMDA receptor pores (MacDermott *et al.*, 1986), which triggers downstream events that contribute to HD pathogenesis (Zeron *et al.*, 2004).

Selective overstimulation of NMDA receptors is also caused by the endogenous agonist QUIN (Stone and Perkins, 1981), specifically those composed of NR1/NR2A and NR1/NR2B subunits (De Carvalho *et al.*, 1996). QUIN is indeed capable to potentiate excitotoxicity by increasing extracellular glutamate, by which it promotes synaptosomal glutamate release and reduces its astrocytic re-uptake (Tavares *et al.*, 2002). Furthermore, QUIN intrastriatal administration was demonstrated to result in hyperphosphorylation of cytoskeleton proteins in astrocytes and neurons that might be facilitated by Ca^{2+} influx via NMDA channels and oxidative stress in early events of QUIN mediated neurotoxicity (Pierozan *et al.*, 2010).

1.3.3 Mitochondrial dysfunction

Mitochondria play a pivotal role in HD neurodegeneration, as their functions are impaired by several mechanisms including decreased membrane potential, alteration in Ca^{2+} homeostasis, reduced energy metabolism, promotion of oxidative stress and activated caspase-dependent apoptotic events (Zheng and Diamond, 2012).

Defects in mitochondria were postulated to stem from interaction with mHTT lowering mitochondrial Ca^{2+} loading capacity (Choo *et al.*, 2004; Panov *et al.*, 2002), and inducing the opening of the mitochondrial permeability transition pore as well as releasing of cytochrome *c* to the cytosol (Choo *et al.*, 2004). Cytochrome *c* is capable of activating pro-caspase-9 that initiate caspase activation cascade leading to apoptosis (Orrenius, 2004). The mechanism by which cytochrome *c* is released in response to various stimuli is mainly mediated by the BCL-2 family of pro-apoptotic proteins, particularly BAX and BAK (Wei *et al.*, 2001). Moreover, mHTT was found to bind to p53, increasing its expression and transcriptional activity. p53 in turn up-regulates downstream pro-apoptotic proteins such as BAX and PUMA (Bae *et al.*, 2005). On the other hand, the caspase activation cascade might be disturbed by ROS formation and energy depletion redirecting apoptosis to necrosis (Orrenius, 2004). Although mitochondria are a target of ROS, they contribute to oxidative stress by generating ROS via their electron transport chain. Evidence of increased levels of ROS in HD brains has been shown to lead to DNA damage and increased vulnerability to glutamate toxicity (Bogdanov *et al.*, 2001; Browne *et al.*, 1999; Polidori *et al.*, 1999). The complexes II and III of the mitochondrial respiratory chain are majorly impaired in HD brain, and this has been associated with inhibited aconitase activity and increases in NO and

superoxide production, leading to ATP depletion and free radical mediated damage (Tabrizi *et al.*, 1999). ATP depletion is also linked to NMDA mediated Ca^{2+} influx demonstrated by low mitochondrial ADP-uptake and decreased mitochondrial ATP in HD striatum (Seong *et al.*, 2005).

Intrastriatal injection of QUIN, not only results in selective HD-like degeneration, but energy metabolism is also affected. Indeed, oxygen consumption has been found to be reduced at 6 hr post administration of QUIN in rat striatum, whereas ATP and NAD depletion was more pronounced at 12 hr, with a 30–36% reduction. This was accompanied by a drop in aspartate (by 60%) and glutamate (by 38%) in neurons due to ionic imbalance that results in leakage of these neurotransmitters and eventually further enhancement of excitotoxicity and mitochondrial dysfunction (Bordelon *et al.*, 1997).

1.4 KMO based therapeutic advances

The critical position of KMO in the KP diverting it towards the production of neurotoxins gives insight on the importance of this enzyme. Despite the evident studies on KP reactive metabolites potential in HD pathogenesis (Schwarcz, 2004) and the development of KMO inhibitors (Schwarcz and Pellicciari, 2002) it was not until about 11 years ago that a clear KMO causative role in HD was found, when Giorgini *et al.* (2005) provided the first genetic evidence of KMO inhibition as a suppressor of mHTT toxicity. This was the result of a genome-wide loss-of-function suppressor screen performed in a *S. cerevisiae* HD model (HTT103Q). In this study, *BNA4* deletion (the *KMO* homologue in yeast) was found to be a potential suppressor of mHTT toxicity amongst the 28 deletion suppressors that were identified (Giorgini *et al.*, 2005). It was also shown that 3-HK and QUIN levels increased in *S. cerevisiae* cells expressing HTT103Q in comparison to those expressing HTT25Q. Furthermore, the *BNA4* deletion rescued mHTT toxicity which was accompanied by a significant reduction in 3-HK and QUIN levels (Giorgini *et al.*, 2005).

Other recent genetic studies have demonstrated that rescue is seen upon KMO suppression/inhibition in HD model organisms including fruit flies and mice. Genetic and pharmacological inhibition of KMO in a *Drosophila melanogaster* transgenic model of HD resulted in a major decrease in 3-HK/ KYNA ratio, and more importantly this seemed to modulate neurodegeneration and thus HD phenotypes mainly by shifting the KP towards the neuroprotective branch. Moreover, a similar pattern of neurodegeneration was seen when 3-HK or KYNA were ingested by HD flies, whereby 3-HK led to restoring of neurodegeneration whereas KYNA resulted in rescue of disease progression, in a dose-dependent manner (Campesan *et al.*, 2011). This was also demonstrated in mammalian models, where peripheral inhibition of KMO with the compound JM6 in transgenic HD mice extended their life span, prevented synaptic loss and reduced microglial activation (Zwilling *et al.*, 2011). Treatment with JM6 in Alzheimer's disease mice model also prevented some of the disease phenotypes. Furthermore, administration of JM6 in rats showed increased KYNA levels and decreased extracellular glutamate levels in the brain, suggesting the rescue seen upon treatment is due to the inhibition of KMO (Zwilling *et al.*, 2011). Therefore, KMO is considered to be a potential drug target for HD.

Recently, Giorgini *et al.* (2013) generated and characterised the first knockout KMO mice (C57Bl/6J) by targeting the *KMO* gene for deletion, resulting in $KMO^{-/-}$ and $KMO^{+/+}$ genotypes. *KMO* deletion led to significant alterations in KP metabolism, whereby significant reduction in KMO activity and 3-HK production and elevation in KYNA levels were confirmed in brain, liver and plasma. Moreover, $KMO^{-/-}$ mice exhibited substantial decrease in QUIN levels in the periphery, whereas brain QUIN was only marginally reduced, which might attributed to the production of 3-hydroxyanthranilic acid via kynureninase metabolism of L-KYN to anthranilic acid in the KP. Given that deletion of *KMO* did not cause major developmental deficits, these mice provide a powerful tool for studying the possible underlying consequences of KMO inhibition/deletion (Giorgini *et al.*, 2013). Recently, Forrest *et al.* (2015) showed that these $KMO^{-/-}$ mice exhibit impaired long-term potentiation (LTP) in the hippocampus, which might suggest a regulatory role of KP in early neurodevelopment (Forrest *et al.*, 2015).

1.4.1 Future promises

To date KMO drug discovery has provided preliminary proof of concept of KMO inhibition both *in vitro* and *in vivo*, with limitation of crossing the blood-brain barrier. For example two peripherally-acting KMO inhibitors JM6 (a prodrug of Ro 61-8048) and UPF-648 have demonstrated protection in rodent models (Amori *et al.*, 2009; Zwilling *et al.*, 2011). In light of the elucidation of the crystal structure of KMO (Amaral *et al.*, 2013), as well as the advances in the methodology of activity assays and screening for KMO inhibitors, potential drugs might be under way. Sensitive assays have been established to quantify the conversion of L-KYN to 3-HK in cell and tissue extracts using liquid chromatography-tandem mass spectrometry (Winkler *et al.*, 2013). Wilson *et al.* (2015) developed a novel magnetic bead-based binding assay that incorporates 3xFLAG-tagged KMO to overcome the difficulties associated with membrane-bound proteins. The assay also uses mass spectrometry to identify potential compounds that have a specific binding affinity for KMO (Wilson *et al.*, 2015). Moreover, the pharmaceutical company GlaxoSmithKline utilised a high-throughput RapidFire mass spectrometry application to directly screen a total of 78,000 compounds. This robust system allowed activity measurement of membrane-bound GST-fusion KMO in about 7 s per well (Lowe *et al.*, 2013), which led to the identification of the new oxazolidinone GSK180 KMO inhibitor that was tested on a rat

model (Mole *et al.*, 2016). More importantly a preclinical candidate drug CHDI-340246 which holds promises for KMO based therapy of HD has been reported (Mrzljak, 2013).

All things considered, KMO drugs are promised to improve HD symptoms in animal models and eventually HD patients. However, the ultimate goal is to discover a drug that can be given to pre-symptomatic patients to prevent the disease from developing. The question that needs to be fully addressed is then: what are the biological consequences of KMO inhibition and consequent alterations in KP metabolite levels in the CNS and periphery? To facilitate the progression towards translational medicine, extensive studies are needed to elucidate the biological regulatory mechanisms of KMO.

1.5 Project objectives

In light of the need for further KMO characterisation, this project was established in order to interrogate the following objectives:

1. *Characterising the function and cellular localisation of KMO*

Human KMO was used to perform localisation studies using microscopy techniques, as well as to address the confirmation of KMO localization in living cells using the BiFC assay.

2. *Dissecting physical interactions of KMO*

A subset of KMO interactors, previously identified in our laboratory from a yeast screen, shed light on the importance of investigating the possible interaction between KMO and HTT. The KMO-HTT interaction was studied initially using the BiFC system and then using a biochemical approach. The findings were further confirmed by extensive localisation studies.

3. *Investigating the interaction of KMO with endogenous full length HTT*

This was performed to validate this interaction using co-immunoprecipitation of endogenous proteins, which was also supported with localisation studies.

CHAPTER 2 MATERIALS AND METHODS

2.1 Materials

2.1.1 Cell lines

Human embryonic kidney cell line (HEK293T) (from Dr Miguel Martin's laboratory at the MRC Toxicology Unit, University of Leicester) was used for transient transfection, western blotting (WB), immunocytochemistry (ICC), bimolecular fluorescence complementation (BiFC) and co-immunoprecipitation (co-IP). Human osteosarcoma cell line (U2OS) and U2OS mtRFP cell line (provided by Prof. Ruth Luthi-Carter's laboratory, Department of Cell Physiology and Pharmacology, University of Leicester) were used in morphological studies. Lymphoblastoid cell lines (LCL) were used for co-IP studies. The wild type (WT) LCL cells were from Coriell (GM18555); the HD LCL (42Q) cells were established from peripheral blood of HD patients by BioRep (Milan, Italy) for the EHDN.

2.1.2 Antibodies

Table 2-1 List of primary antibodies used in this work.

Catalogue Number	Antigen	Host species/Isotype	Supplier	Application	Dilution
ab6556	GFP	Rabbit polyclonal	Abcam	WB	1:5000
				ICC	1:1000
10698-1-AP	Human KMO	Rabbit polyclonal	Proteintech	WB	1:1000
Lot # 00000888				ICC	1:100
				TEM	1:10
HPA031115	Human KMO	Rabbit polyclonal	Sigma	TEM	1:20
ab130959	Human KMO	Rabbit polyclonal	Abcam	WB	1:1000
				TEM	1:10
ab93195	Human KMO	Rabbit polyclonal	Abcam	WB	1:400
				TEM	1:5
ab83929	Mouse KMO	Rabbit polyclonal	Abcam	WB	1:5000
sc-8035	α-Tubulin	Mouse monoclonal	Santa Cruz Biotechnology	WB	1:1000
sc-32233	Anti-GAPDH	Mouse Monoclonal	Santa Cruz Biotechnology	WB	1:1000
AF1458	HtrA2	Rabbit polyclonal	R&D systems	ICC	1:400
MAB1458	HtrA2	Mouse monoclonal	R&D systems	ICC	1:200
MAB1273	Anti-Mitochondria	Mouse Monoclonal	MAB1273	ICC	1:200
				TEM	1:50
MAB1574	Anti-PolyQ	Mouse Monoclonal	Chemicon	WB	1:1000

Catalogue Number	Antigen	Host species/Isotype	Supplier	Application	Dilution
MAB5374	Anti-HTT (mEM48)	Mouse Monoclonal	Chemicon	WB	1:2000
				ICC	1:1000
				TEM	1:250
MAB2166	Anti-HTT-FL (4C8)	Mouse Monoclonal	Chemicon	WB	1:2000
				ICC	1:1000
				TEM	1:20
				co-IP	7 μg

WB = Western Blot, ICC = Immunocytochemistry, TEM = Transmission electron microscopy, co-IP = co-immunoprecipitation

2.1.3 Plasmids

Table 2-2 Plasmids and cDNA used in this study.

Plasmid	Supplier	Application
pcDNA3.1-mRFP	Dr Robert Mason (UoL)	Mammalian expression vector encoding RFP
pcDNA3.1/Zeo	Invitrogen	Mammalian expression vector
pJET	Thermo Scientific	CloneJET™ PCR Cloning Kit to facilitate cloning
pcDNA3.1-DJ-1-CC	Dr Mariaelena Repici (UoL)	BiFC construct encoding residues 155 to 238 of C-terminus of CFP (CC)
pcDNA3.1-DJ-1-GN	Dr Mariaelena Repici (UoL)	BiFC construct encoding residues 2 to 172 of N-terminus of enhanced GFP (GN)

Plasmid	Supplier	Application
HTTxQ-VN	Dr Federico Herrera (Universidade de Lisboa)	BiFC construct encoding residues 1 to 158 of N-terminus of Venus (VN), x = 19, 46 or 97
HTTxQ-VC	Dr Federico Herrera (Universidade de Lisboa)	BiFC construct encoding residues 1 to 158 of N-terminus of Venus (VC), x = 25, 46 or 97
HTTxQ-FL	Coriell	HTT-FL in pcDNA3.1 vector, x = 23 (CH00022), 73 (CH00023) or 145 (CH00024)
HTT23Q	Coriell	HTT exon 1 fragment in pcDNA3.1 vector (CH00017)
Truncated KMO (tKMO)	Dr Mathuravani Thevandavakkam (UoL)	cDNA screening library
flKMO	Origene	FLAG-tagged mutated full length human KMO (KMO R452C) in pCMV6 vector (RC222594)
HTT25Q-GFP	Prof. Flaviano Giorgini (UoL)	HTT exon 1 fragment in lentiviral vector tagged with full length GFP
shRNA1	Dharmacon	shRNA for human HTT (TRC0000019869)
shRNA2	Dharmacon	shRNA for human HTT (TRC0000019870)
shRNA3	Dharmacon	shRNA for human HTT (TRC0000019871)
shRNA5	Dharmacon	shRNA for human HTT (TRC0000019873)
non-target ctrl	Dharmacon	Non-targeting shRNA control (RH56848)

UoL= University of Leicester

2.1.4 Oligonucleotides

Table 2-3 Sequencing primers.

Primer Name	Sequence	Application
hKMOFseq2	GCTTGGATCTGACAAAGTTCC	hKMO internal forward sequencing primer
hKMORseq2	CATGAGCTGCATCTCCCAG	hKMO internal reverse sequencing primer
hKMOFseq3	CTGGGAGATGCAGCTCATG	hKMO internal forward sequencing primer
T7	TAATACGACTCACTATAGGG	Universal forward sequencing primer for pcDNA3.1
BGH	TAGAAGGCACAGTCGAGG	Universal reverse sequencing primer for pcDNA3.1
VP1.5	GGACTTTCCAAAATGTCG	Forward sequencing primer for pCMV6
XL39	ATTAGGACAAGGCTGGTGGG	Reverse sequencing primer for pCMV6
pJETseqF	CGACTCACTATAGGGAGAGCGGC	Forward sequencing primer for pJET
pJETseqR	AAGAACATCGATTTTCCATGGCAG	Reverse sequencing primer for pJET

Table 2-4 PCR primers.

Primer Name	Sequence	Application
FLKMOF	GATC**GGTACC**GCCACCATGGACTCATCTGTCATTCAAAG	Forward primer for KMO introducing *KpnI* site
FLKMOR	GATC**GGTACC**GCCCTGCTAATGAGATTGGAAATTTG	Reverse primer for KMO introducing *KpnI* site
KMO trunc R	GATC**GGTACC**CTTTTTTGCCAATGCCAACGCTGCAC	Reverse primer for tKMO introducing *KpnI* site
FLKMOTR	GATC**CTGCAG**TCACCTGCTAATGAGATTGGAAATTTGTTC	Reverse primer for KMO introducing *PstI* site
tKMOTR	GATCTCA**CTGCAG**GCTTTTTTGCCAATGCCAACGCTGCAC	Reverse primer for tKMO introducing *PstI* site
hKMOF_BiFC	GATC**GCTAGC**GCCACCATGGACTCATCTGTCATTCAAAG	Forward primer for KMO introducing *NheI* site
hFLKMOR_BiFC	GATC**GTCGAC**GGAGCCTCCCCCGCCGGAGCCTCCCCCGCCC CTGCTAATGAGATTGGAAATTTG	Reverse primer for KMO introducing *SalI* site and $(GGGGS)_2$ linker
htKMOR_BiFC	GATC**GTCGAC**GGAGCCTCCCCCGCCGGAGCCTCCCCCGCCT TTTTGCCAATGCCAACGCTGCAC	Reverse primer for tKMO introducing *SalI* site and $(GGGGS)_2$ linker
GN-linkerF_BiFC	GATC**GCTAGC**GCCACCATGGTGAGCAAGGGCGAGGAGCTG	Forward primer for GN introducing *NheI* site
GN-linkerR_BiFC	GATC**GGTACC**GGAGCCTCCCCCGCCGGAGCCTCCCCCGCCG ATGTTGTGGCGGATCTTGAAGTTC	Reverse primer for GN introducing *KpnI* site and $(GGGGS)_2$ linker
linker-GNF_BiFC	GATC**CTGCAG**GGCGGGGGAGGCTCCGGCGGGGGAGGCTCCG TGAGCAAGGGCGAGGAGCTG	Forward primer for GN introducing *PstI* site and $(GGGGS)_2$ linker
linker-GNR_BiFC	GATC**CTCGAG**TCAGATGTTGTGGCGGATCTTGAAGTTC	Reverse primer for GN introducing *XhoI* site
GNL-flKMO_F	GATC**GGTACC**ATGGACTCATCTGTCATTCAAAG	Forward primer for KMO introducing *KpnI* site
GNL-flKMO_R_2	GATC**GGTACC**TCACCTGCTAATGAGATTGGAAATTTG	Reverse primer for KMO introducing *KpnI* site
CCLF_BiFC	GATC**GGTACC**GCCACCATGGCCGACAAGCAGAAGAACG	Forward primer for CC introducing *KpnI* site

Primer Name	Sequence	Application
CCLR_BiFC	GATC**GGTACC**GGAGCCTCCCCCGCCGGAGCCTCCCCCGCCG GATCCGTCGACCTTGTACAG	Reverse primer for CC introducing *KpnI* site
VN_Fw	GATC**GCGGCCGC**GATGGTGAGCAAGGGCGAGGAGC	Forward primer for VN introducing *NotI* site
VN_Rev	GATC**GCGGCCGC**TCACTGCTTGTCGGCGGTGATATAGAC	Reverse primer for VN introducing *NotI* site

Table 2-5 Site-directed mutagenesis primers

Primer Name	Sequence	Application
SDM5hKMOF	GTCACCACGATCTTTCCTCCGCTTGAGAAGACCATGGAAC	Forward primer for single base pair substitution (T1354C)
SDM5hKMOR	GTTCCATGGTCTTCTCAAGCGGAGGAAAGATCGTGGTGAC	Reverse primer for single base pair substitution (T1354C)

2.1.5 Constructs

Table 2-6 List of all constructs that were generated, for cloning maps refer to the indicated figures from the appendix.

Construct No.	Glycerol Stock No.	Construct Name	Description	Figure
1	14	pcDNA3.1-tKMO-RFP	Truncated KMO tagged with RFP	1
2	17	pcDNA3.1-tKMO	Truncated KMO untagged	2
3	19	pcDNA3.1-flKMO-RFP	Full length KMO tagged with RFP	1
4	20	pJET-flKMO	Full length KMO in pJET plasmid	NA
5	21	pcDNA3.1-flKMO	Full length KMO untagged	2
6	22	pcDNa3.1-GN-Linker	BiFC backbone GN+linker $(GGGGS)_2$	6
7	23	pcDNA3.1-flKMO-CC	Full length flKMO-CC tagged	3
8	24	pcDNA3.1-tKMO-CC	Truncated KMO-CC tagged	3
9	25	pcDNA3.1-GN-GAPDH	GN+linker+GAPDH, BiFC construct	11
10	34	pcDNA3.1-Linker-GN	BiFC backbone linker $(GGGGS)_2$+GN	5
11	35	pcDNA3.1-GAPDH-GN	GAPDH+linker+GN	9
12	36	pcDNA3.1-AP2M1-Linker-GN	AP2M1+linker+GN	9
13	37	pcDNA3.1-VN	BiFC backbone, generated by excision of HTT fragment	NA
14	38	pcDNA3.1-GN-AP2M1	GN+linker+AP2M1	11
15	41	pcDNA3.1-flKMO-GN	Full length KMO+linker+GN	7
16	42	pcDNA3.1-DCTN2-GN	DCTN2+linker+GN	10
17	43	pcDNA3.1-GN-DCTN2	GN+linker+DCTN2	11
18	59	pcDNA3.1-CC-flKMO	Full length KMO tagged with -CC N-terminally	4

Construct No.	Glycerol Stock No.	Construct Name	Description	Figure
19	60	pcDNA3.1-CC-tKMO	Truncated KMO tagged with -CC N-terminally	4
20	61	pcDNA3.1-23QHTT-FL-VN	Full length HTT 23Q tagged with -VN	12
21	62	pcDNA3.1-73QHTT-FL-VN	Full length HTT 73Q tagged with -VN	12
22	63	pcDNA3.1-145QHTT-FL-VN	Full length HTT 145Q tagged with -VN	12
23	64	pcDNA3.1-GN-flKMO	GN+linker+full length KMO	8

2.2 Methods

2.2.1 Molecular cloning using bacteria

2.2.1.1 Bacterial media and growth conditions

Escherichia coli strain DH5α were grown in Luria broth (LB) containing 0.5% (w/v) yeast extract, 1% (w/v) tryptone and 0.5% (w/v) sodium chloride. Solid media was created by supplementation with 0.5% (w/v) agar. To select antibiotic resistant colonies, the media was supplemented with either ampicillin (100 µg/ml) or kanamycin (25 µg/ml). *E.coli* strains were grown at 37°C, with liquid cultures undergoing constant agitation at 250 rpm.

2.2.1.2 Polymerase chain reaction (PCR)

Typical 50 µl PCR reactions were performed using a Labcycler (Geneflow). Reactions contained: 10 µl of 5X HB buffer, 0.2 mM dNTPs (Promega), 0.5 µM of each primer, 1 U of Phusion (Finnzymes) and 50-100 ng of template DNA. PCR cycling conditions were as follows: an initial denaturation at 98°C for 1 min followed by 35 cycles of denaturation at 98°C for 10 s, annealing at the relevant temperature for 30 s and extension at 72°C for 1 min per 1 kb. A final extension at 72°C for 7 min was then performed.

2.2.1.3 Gel agarose electrophoresis

Agarose gels were made using 1% (w/v) Seakem LE agarose (Lonza) dissolved in 1X TBE (0.1 M Tris-HCl (pH 8.0) and 50 mM EDTA). To allow visualisation of DNA, gels were supplemented with ethidium bromide (0.5 $\mu g.ml^{-1}$). DNA samples were mixed with 0.25 volumes of 5X loading dye (10% (w/v) ficoll type 400, 20% (v/v) 0.5 M EDTA, 0.2% (w/v) bromophenol blue, 0.2% (w/v) xylene cyanol and 0.5% (w/v) sodium dodecyl sulphate), and loaded into the agarose gel along with suitable DNA ladders. Agarose gels were then subjected to electrophoresis at 100 V for the appropriate time, and DNA visualised using a UV transilluminator (Kodak). Images were captured, processed and manipulated using Kodak MI software.

2.2.1.4 Restriction digestion

Digestion of 0.5 µg DNA in a 10 µl reaction was set up according to manufacturer's instructions, as follows: 1 µl of 10X buffer (New England Biolabs, NEB), 0.5 µl of restriction enzyme (NEB) and H_2O. 1 µl of 10X BSA (NEB) was added for some

restriction enzymes. Reactions were incubated at 37°C for 3-4 hr. To prevent re-ligation of digested vectors, they were dephosphorylated by adding 1 µl of 10X Antarctic phosphatase reaction buffer (NEB) and 2.5 U of Antarctic phosphatase (NEB). The reaction was incubated at 37°C for 2 hr before the phosphatase was inactivated at 65°C for 20 min.

2.2.1.5 Ligation

Digested inserts and the dephosphorylated plasmids were ligated over night at 16°C in a Labcycler (Geneflow). Ligation reactions contained: 150 ng of vector, insert (3:1 molar ratio of insert:vector), 400 U of T4 DNA ligase (NEB) and 2 µl of ligase T4 buffer (NEB). Following ligation 10 µl of the reaction was transformed into *E.coli*.

2.2.1.6 Transformation of competent E.coli

For each transformation reaction, 100 µl of chemically competent *E.coli* DH5α were incubated with 10-100 ng of DNA on ice for 30 min, heat shocked at 42°C for 2 min, and then chilled on ice for 2 min. 1 ml of LB was added and samples incubated at 37°C with agitation at 300 rpm for 1 hr. Samples were then centrifuged at 15700 *x g* for 1 min, pellets were suspended in 100 µl of LB and plated onto antibiotic supplemented LB media. Plates were incubated statically at 37°C overnight to allow the development of antibiotic resistance colonies.

2.2.1.7 DNA Sequencing

Big Dye® v3.1 sequencing kits (Applied Biosystems) were used for DNA sequencing. A typical 10 µl sequencing reaction contained approximately 500 ng of plasmid DNA, 2 µl of 5X sequencing buffer, 1 µl of Big Dye™ v3.1 and 2 µl (pmol/ µl) of primer. Cycling conditions for sequencing were as follows: 96°C for 1 min, followed by 25 cycles of 96°C for 10 s, 50°C for 5 s, 60°C for 4 min; then 16°C for 5 min. Before purifying the sequencing reaction 2 µl of 2% SDS and 10 µl of H_2O were added and samples heated at 95°C for 10 min to dissolve dye aggregates. After cooling at 22°C for 10 min reactions were purified using Performa® DTR gel filtration cartridges (Edge Bio) to remove the excess dye, low molecular weight DNA and buffer. Samples were applied to the column and centrifuged at 750 *x g* for 3 min. Samples were analyzed using an Applied Biosystems 3730 sequencer at the Protein Nucleic Acid Chemistry Laboratory Facility, University of Leicester.

2.2.1.8 Site-directed mutagenesis

Single base pair substitution was achieved by amplifying human full length KMO R452C using primers that introduced the mutagenesis in the newly synthesized DNA. Primers incorporating the mutation were designed using PrimerX online software (Table 2-5). PCR cycling conditions were as described previously except that 25 µl PCR reactions were performed for each primer for 5 cycles, then the two reactions combined for another 30 cycles with an extension time of 3.5 min. All PCR products were digested overnight with *DpnI* to remove methylated template DNA before being transformed into competent *E.coli*.

2.2.2 Mammalian cell culture, protein applications and microscopy

2.2.2.1 Mammalian cell culture media and growth conditions

Adherent cells (HEK293T, U2OS and U2OS mtRFP cell lines) were routinely cultured in Dulbecco's modified Eagle medium (DMEM) (GlutaMAX™, Life Technologies), while LCL cells were maintained in RPMI 1640 (GlutaMAX™, Life Technologies). Both DMEM and RPMI 1640 were supplemented with 10% fetal bovine serum (FBS, Life Technologies), 1000 units.ml^{-1} penicillin and 100 µg.ml^{-1} streptomycin. Cells were incubated in a humidified incubator at 37°C with 5% CO_2. Adherent cells were routinely passaged when they reached 70-80% confluence. Media was aspirated and cells were washed with 1X phosphate buffered saline (PBS, Life Technologies) to remove dead cells. Cells were then detached by incubating them with Trypsin/EDTA (0.5 mg.ml^{-1} trypsin, 0.22 mg.ml^{-1} EDTA) at 37°C for approximately 2 min. When cells were sufficiently detached, two volumes of media were added and the required volume of cells transferred to a flask containing pre-warmed media. LCL cells were passaged every 2-3 days by re-suspending the cells clumps and adding cells suspension to pre-warmed media at 1:3 ratio.

2.2.2.2 Liquid nitrogen stocks

Low passage numbers of HEK293T and LCL cell lines, at 70-80% confluency, were harvested at 700 *x g* for 5 min; and 2 x 10^6 cells/ml (for HEK293T cells) or 5 x 10^6 cells/ml (for LCL cells) were suspended in pre-chilled FBS with 10% (v/v) Dimethyl sulfoxide (DMSO). Cell suspensions were aliquoted into screw-capped tubes and placed at − 80°C for 24 hr before transferring to liquid nitrogen.

2.2.2.3 Preparation of plasmids for transfection into mammalian cells

E.coli was inoculated into 100 ml LB containing the appropriate antibiotic and grown overnight with continuous agitation. Cells were harvested at 3220 *x g* for 4 min and suspended in 5 ml of solution I containing RNaseA. The re-suspended cells were divided into 10 aliquots and plasmids were extracted from each aliquot using an Endo-free plasmid mini kit II (Omega), according to the manufacturer's instructions. Eluted DNA was pooled and an equal volume of Phenol:Chloroform:Isoamyl alcohol (25:24:1) was added. Samples were mixed by inversion and separated by centrifugation at 13400 *x g* for 1 min. The upper phase was transferred to a new tube, an equal volume of Choroform:Isoamyl alcohol (24:1) was added, and samples were mixed and centrifuged

at 13400 *x g* for 1 min. The upper aqueous phase was transferred to a new tube. DNA was precipitated by adding 2 volumes of 100% ethanol, a tenth the volume of 3 M Sodium Acetate and incubated at − 20°C for 30 min. Precipitated DNA was pelleted at 15700 *x g* for 10 min and pellet were washed with 1 ml 70% ethanol. The DNA was allowed to air-dry and re-suspended in 20 µl of Endo-free Elution buffer (Omega). The DNA concentration and purity were then measured using a Nanophotometer (Implen).

2.2.2.4 Chemical transfection

Adherent cells were grown to 70-80% confluence, detached and seeded at density of 1.5 x 10^5 cells/well into a 6-well plate. Wells were pre-coated with 0.01% Poly-L-lysine (Sigma) for 3 hr and washed three times with 1 ml of PBS prior to seeding of the cells. After 24 hr, media was aspirated; cells were washed once with PBS and 1.6 ml of fresh media was added. Prior to transfection using Effectene reagent (Qiagen), 0.4 µg of plasmid DNA was mixed with 100 µl buffer EC and 3.2 µl of enhancer incubated at room temperature for 5 min. 4 µl of Effectene was added and samples were vortexed for 10 s and incubated at room temperature for 1 hr (when other plates or Petri dishes were used the amount of plasmid DNA, EC buffer, enhancer and Effectene were scaled down/up accordingly). DNA was added in 600 µl of fresh media to the relevant well in a drop-wise manner. 24 hr post transfection, media and transfection reagent were aspirated and cells washed once with PBS before adding 2 ml of fresh media. Cells were used at 24 or 48 hr post transfection, depending on the experiment's requirements. For confocal live cell imaging, cells were seeded into 35 mm ibiTreat dishes (Ibidi) at a density of 1 x 10^5 cells/dish.

2.2.2.5 Preparation of total cell lysates

HEK293T cells were seeded at a density of 1.5 x 10^5 cells/well into 6-well plates. After 48 hr cells were washed twice with ice cold PBS and lysed in 100 µl of lysis buffer for 10 min on ice. Lysis buffer was prepared as follows: 20 mM Trizma Acetate, 0.27 M Sucrose, 1 mM EDTA, 1 mM EGTA, 50 mM NaF, 5 mM Sodium pyrophosphate decahydrate, 1% (v/v) Triton X100, 1X Roche cocktail protease inhibitors, 1 mM Dithiothreitol (DTT), 1 mM Sodium orthovanadate and 10 mM Sodium β-glycerophosphate. Lysates were then centrifuged at 15700 *x g* for 10 min at 4°C. Supernatants were collected and protein concentration was determined using a Nanophotometer (Implen). Protein lysates were stored at − 80°C until used. Lysation

for filter trap assay and co-immunoprecipitation was carried out using different lysis buffer indicated in the relevant section.

2.2.2.6 Immunoblotting (Western blot)

Proteins were separated on 8, 10 or 14% SDS-PAGE. Gels and buffers were prepared as described below. Running gel: 5 ml 4X lower buffer (1.5 M Tris-HCl (pH 8.8) and 0.2% (w/v) SDS), 6.6 ml 30% (w/v) acrylamide/methylene bisacrylamide solution (ProtoGel, EC-890), 8 ml H_2O, 150 µl 10% (w/v) Ammonium persulfate (APS), and 15 µl Tetramethylethylenediamine (TEMED). Stacking gel: 2 ml 4X stacking buffer (0.5 M Tris-HCl (pH 6.8) and 0.4% (w/v) SDS, 1.36 ml 30% (w/v) acrylamide/methylene bisacrylamide solution (ProtoGel), 4.55 ml H_2O, 80 µl 10% (w/v) APS and 8 µl TEMED. 4X loading buffer: 62.5 mM Tris-HCl (pH 6.8), 2% (w/v) SDS, 0.1% (w/v) bromophenol blue, 10% (v/v) glycerol, and 10% (v/v) β-mercaptoethanol. Running buffer: 250 mM Tris, 1.9 M glycine and 0.5% SDS. Transferring buffer: 20 mM Tris, 0.149 M glycine, 0.1% (w/v) SDS and 12% (v/v) methanol. 10X TBS: 200 mM Tris base-HCl (pH 7.6) and 1.5 M NaCl. 1X TBS-T: 1X TBS and 0.1% (v/v) Tween 20.

Protein samples (10-50µg) were denatured in 4X loading buffer at 95°C for 6 min. Dual color Precision plus protein standards (BioRad) were used as molecular markers. After electrophoresis, samples were transferred to PVDF membranes (Bio-Rad) for 2 hr at constant voltage (100 V). Membranes were then washed once with 1X TBS-T and blocked in 5% (w/v) milk in 1X TBS-T for 1 hr. Incubation with the appropriate primary antibodies was overnight at 4°C in blocking solution. Membranes were then washed three times in 1X TBS-T for 10 min, followed by three washes in 1% (w/v) milk in 1X TBS-T for 10 min and incubated for 1 hr at room temperature with the appropriate IgG (anti-mouse or anti-rabbit), peroxidase conjugated secondary antibody; 1:10000 dilution (Vector) in blocking solution. This was followed by three washes in 1X TBS-T for 10 min, and further three washes in 1X TBS. Membranes were then developed using the Enhanced Chemiluminescence (ECL), SuperSignal West Dura (Thermo Scientific) for 5 min. Densitometry was performed using ImageJ (1.50d) where quantification of expression was required.

2.2.2.7 Filter trap assay

HEK293T cells were seeded on a 6-well plate as routinely done. After 48 hr of HTT constructs transfection, cells were washed with PBS and lysed in 300 µl of CellLytic

(MT Cell Lysis Reagent, Sigma Aldrich) with freshly added 1X Roche cocktail protease inhibitors. After this, lysates were left for further 15 min on a rocker at room temperature, then 250 U/ml of Benzonase (Pierce universal nuclease, Thermo Scientific) was added to the lysates and incubated on ice for further 30 min. Protein concentration of the lysates was determined using a Nanophotometer (Implen), then lysates were diluted in PBS containing 2% (w/v) SDS and 50 mM DTT to 1.5 µg/µl; and denatured at 98°C for 3 min. Two sheets of filter paper and cellulose acetate (aggregate binding) membrane were equilibrated in 0.1% (w/v) SDS in PBS. The holes in the blot apparatus were washed with 200 µl 0.1% (w/v) SDS in PBS for four times. 150 µl of fresh diluted lysates were filtered through and followed by four more washes with 200 µl of 0.1% SDS in PBS. The membrane was then blocked in 3% (w/v) milk in 1X TBS-T at 4°C overnight. Incubation with anti-GFP primary antibody (1:10000, Abcam) was for 1 hr at room temperature. After three washes in 1X TBS-T for 10 min, membrane was incubated for 1 hr at room temperature with the anti-rabbit IgG, peroxidase conjugated secondary antibody; 1:20000 dilution (Vector) in 1X TBS-T. This was followed by three washes in 1X TBS-T for 10 min. Membrane was then developed using the Enhanced Chemiluminescence (ECL), SuperSignal West Dura (Thermo Scientific) for 5 min.

2.2.2.8 Immunocytochemistry (ICC)

HEK293T cells were seeded on 20 mm sterile coverslips in a 6-well plate as described before. After 24-48 hr from transfection, cells were fixed in pre-warmed 4% paraformaldehyde (PFA) in PBS for 20 min, washed three times in PBS for 10 min and blocked in 1% bovine serum albumin (BSA) in 0.2% Triton PBS for 30 min. Fixed cells were then incubated with the primary antibody diluted in the blocking solution overnight at 4°C. Cells were washed three times in PBS for 10 min and subjected to nuclear staining with Hoechst 33342 (Invitrogen, H3570); 1:2000 dilution in PBS, for 2 min. Incubation with the appropriate fluorescent conjugated secondary antibody, Alexa Fluor 488, 546, 555 or 647, 1:500 dilution (Invitrogen), was performed in blocking solution in the dark for 1 hr at room temperature. Cells were washed three times in PBS for 10 min. Coverslips were then mounted in Mowiol, placed in the dark for few hours and then kept at 4°C until morphological analysis was performed by Olympus Cell^R imaging system or Olympus confocal FV1000. Confocal images were deconvolved using Essential Huygens software, microscopic parameters were set as follows: for

Hoechst, excitation at 405 nm and emission 422 nm; for Alexa 488, excitation at 488 nm and emission at 508; for RFP, excitation at 559 nm and emission at 608 nm; for Alexa 555, excitation at 555 nm and emission at 568 nm; and for 647, excitation at 647 nm and emission at 670 nm. Mitochondrial co-localisation analyses were performed by JACoP (just another co-localisation plugin) in ImageJ (Version 1.50d), using Pearson's and Mander's coefficients (Bolte and Cordelieres, 2006), when there was no comparison between proteins, the Pearson's coefficient was only presented and multiplied by 100 to obtain percentage of co-localisation.

MitoTracker CMXRox (M-7512, Thermo Fisher Scientific) was used as a mitochondrial marker in HEK293T cells. Cells were stained with 100 nM MitoTracker CMXRox for 30 min and washed once with PBS prior fixation. ICC on stained cells was performed as detailed above, with the following amendments: after fixation cells were permeabilized with 0.2% Triton in PBS for 10 min. Cells were washed three times in 0.1% Tween 20 in PBS (PBS-T), blocking and antibody incubation steps were carried out in 1% BSA in PBS-T, and all washing steps were using PBS-T.

2.2.2.9 Transmission electron microscopy (TEM)

HEK293T cells were seeded on 9 mm coverslips in a 12-well plate at a density of 1 x 10^5 cells/well. Cells were transfected with 0.24 μg of the plasmid expressing gene of interest and 0.06 μg of internal control RFP (75 μl buffer EC, 2.4 μl enhancer and 3 μl Effectene). After 48 hr, cells were fixed in 4% PFA + 0.05% glutaraldehyde (GA) in PBS for 20 min at room temperature. LCL cells were pelleted at 3 x 10^6 cells/ml at 700 *x g* for 5 min, washed twice in 1 ml of PBS prior fixation in 4% PFA + 0.05% GA in PBS.

Fixed cells were washed three times in PBS for 15 min followed by four dehydration steps in ethanol: 30%, 50%, 70% and finally 90%, each step was for 30 min at 4°C. Three further dehydration steps were applied in a solution of 90% ethanol: LR White resin (Agar Scientific); ratios used were 2:1, 1:1 and 1:2; each was for 30 min at 4°C. Finally cells incubated in 100% LR White resin for 30 min at 4°C, then stored in 100% LR White at 4°C. Fresh LR White resin was added three times for 2 hr at 4°C. LR White resin embedded samples were polymerised for 16 hr under UV light at 4°C and in an N_2 atmosphere (MRC Toxicology Unit, Hodgkin Building, University of Leicester). Polymerised samples were then processed into thin sections of 90 nm using an Ultracut

S Ultramicrotome (Leica), and collected onto 200 squares gold mesh grids for immunolabelling. Grid mounted sections were blocked in 30 µl of 1% BSA in 0.1% Tween 20 PBS (PBS-T) for 30 min. Grids were then incubated with primary antibody in 1% BSA in PBS-T for 2 hr, and followed by five 3 min washes with 1% BSA in PBS-T, then 1.5 hr incubation with the appropriate IgG (anti-mouse or anti-rabbit) gold conjugate secondary antibody (BBI Solutions, 1:100) in 1% BSA in PBS-T. Following this, grids were washed once for 3 min with 1% BSA in PBS-T, then four times for 2 min with distilled de-ionised water. Finally, grids were counter-stained in 2% Uranyl acetate (Agar scientific) for 10 min. Cells were visualised on a JEOL JEM-1400 TEM (JEOL, UK) with an accelerating voltage of 80 kV from 5-10 grid squares, and images were captured using Megaview III digital camera with iTEM software. For analysis of the images in Sections (5.2.2.3 and 5.2.2.4), images were taken at 12K or 40K for 30 nm and 10 nm gold particles respectively; to accommodate five immunogold particles per cell from 30 cells of 30 different images which were counted per condition. The electron micrographs were examined and mitochondrial structures were identified. Particles localised or associated directly with mitochondria were counted, and the rest of labelling was considered as not localised to mitochondria. The proportions of mitochondrial immunogold particles were calculated.

2.2.2.10 Bimolecular fluorescence complementation (BiFC)

HEK293T cells were seeded on a 6-well plate as before. Cells were transfected with 0.4 µg of total DNA, 0.16 µg of each GFP-containing construct and 0.08 µg of pcDNA3.1 expressing RFP. Incubation temperature was at 37°C. 48 hr post transfection, media was replaced with phenol red-free DMEM media supplemented with 10% FBS, 2 mM L-glutamine, 1000 units.ml^{-1} penicillin and 100 µg.ml^{-1} streptomycin. Alternatively, cells were transfected only with both GFP-containing constructs (total DNA 0.32 µg), and nuclei were stained with 10 µM of Hoechst for 30 min prior to imaging in phenol red-free DMEM media. Live cells imaging of 100 images per well was performed at 37°C and 5% CO_2 using Olympus Scan^R screening station. Detection of Hoechst signal was at 350/50 nm excitation filter and 440/75 nm emission filter; GFP signal was detected using a 492/18 nm excitation filter and 535/50 nm emission filter, whereas RFP detection was by using excitation filter at 556/30 nm and emission filter between 590-650 nm. 100 images were taken per well and analysed using Scan^R analysis software. Normalisation of BiFC signal was based on RFP expression using edge

detection (refer to Section 4.2.7) or Hoechst stained nuclei plus 30 surrounding pixels as cytoplasm (refer to Section 4.2.8), depending on the experiment. After screening, cells were lysated and protein extracts were kept at − 80°C for western blot analysis.

Congo red (CR) (Sigma) was used in some BiFC experiments as an aggregation inhibitor. The CR stock solution was prepared freshly by dissolving it in 100% DMSO at a concentration of 10 mM; and filter sterilising with a 0.2 µm filter. Cells were treated with 12.5 µM of CR for 48 hr, at the time of transfection. Cells were stained with Hoechst, and then washed with PBS before the addition of imaging media, as described above, without CR. After imaging, cells were prepared for filter trap assays as described in Section (2.2.2.7); same samples were run on 10% SDS-PAGE.

2.2.2.11 Co-Immunoprecipitation (co-IP)

2.2.2.11.1 Using GFP-Trap

HEK293T cells were seeded at a density of 2 x 10^6 cells/dish (10 cm Petri dishes), and transfected with total 2 µg of plasmid DNA (300 µl buffer EC, 16 µl enhancer and 20 µl Effectene). 48 hr post transfection cells were washed twice in ice cold PBS and lysed on ice for 5 min using 400 µl of lysis buffer (20 mM Trizma Acetate (pH 7.4), 150 mM Sodium Chloride, 1 mM EDTA, 1% (v/v) Triton X100 and 1X Roche cocktail protease inhibitors). The immunoprecipitation was then carried out as stated in the GFP-Trap manual (Chromotek).

2.2.2.11.2 Using Protein A/G agarose

To perform co-IP, 20 µl of Protein A/G agarose beads (20421, Thermo Scientific) were used per reaction after three washes in 200 µl of washing buffer (20 mM Trizma Acetate (pH 7.4), 150 mM Sodium Chloride, 1 mM EDTA) with centrifugation at 15700 *x g* for 1 min at 4°C, after each wash. Protein A/G agarose beads were then incubated in 200 µl of PBS containing 7 µg of ascites primary antibody for 4-6 hr at 4°C with end-over-end mixing. Antibody-conjugated beads were washed thrice in 200 µl of washing buffer by centrifugation at 15700 *x g* for 1 min at 4°C.

HEK293T cells were seeded, transfected and lysed in the same manner as when using GFP-Trap, but 500 µl of lysis buffer was added and after 5 min of lysation, lysates were centrifuged at 15700 *x g* for 10 min at 4°C. For LCL cells, 2 x 10^7 cells/ml were pelleted at 700 *x g* for 5 min. Cells were washed twice in 1 ml of ice cold PBS at 700 *x*

g for 5 min at 4°C. Finally cells were re-suspended in 500 µl of lysis buffer for 5 min, and then centrifuged at 15700 *x g* for 10 min at 4°C.

The supernatants of HEK293T cells or LCL cells were transferred to new tubes, and the pellets were discarded. 20 µl of each supernatant was added to 20 µl 4X loading buffer (refer to immunoblotting Section 2.2.2.6), and samples were denatured at 95°C for 6 min; this represents the protein input for co-IP immunoblotting analysis. The rest of the total lysate was pre-cleared by incubating them in pre-washed Protein A/G agarose (as mentioned above) for 1 hr at 4°C with end-over-end mixing. Pre-cleared lysated were then centrifuged at 15700 *x g* for 1 min at 4°C and added to the antibody-conjugated Protein A/G agarose (prepared above) to a total volume of 1 ml in lysis buffer; the mixture was incubated overnight at 4°C, with end-over-end mixing. Non-conjugated Protein A/G agarose beads were used as negative control per condition.

After overnight incubation, Protein A/G agarose beads were collected at 15700 *x g* for 5 min at 4°C, and the 20 µl of each supernatant was denatured with 20 µl 4X loading buffer at 95°C for 6 min, this representing the flow-through in the IP experiments. Four washes were performed on the collected beads at 15700 *x g* for 2 min at 4°C. Finally, beads were re-suspended in 50 µl 2X loading buffer and denatured at 95°C for 10 min, followed by centrifugation at 15700 *x g* for 5 min. The supernatants were saved as the IP fraction for immunoblotting analysis.

Co-IP was also performed under stringent conditions to eliminate the background: the lysis buffer contained a higher salt concentration (300 mM Sodium Chloride), and the lysis buffer was used for all the washing steps instead of the free-detergent washing buffer. Furthermore, Protein A/G agarose beads were blocked in 0.2% BSA in 200 µl of lysis buffer for 2 hr at 4°C.

For affinity-purified primary antibody, 7 µg of antibody were added to the pre-cleared lysate to a total volume of 1 ml in lysis buffer and incubated for 2 hr at 4°C, with end-over-end mixing. The antibody-lysate solution was then added to the pre-washed Protein A/G agarose and the new combination was incubated overnight at 4°C, with end-over-end mixing. The rest of the co-IP was carried out as described above under normal conditions.

2.2.3 Statistical analysis

All statistical analyses were carried out using GraphPad Prism 6 (Version 6.02) and all data were expressed as mean ± SEM. Details of the analysis in each experiment are described below and the number of the analysed samples is illustrated in the Figure legends of each experiment.

Correlations of the co-localisation of the KMO and mitochondrial signals in Section 3.2.4.1 were analysed using unpaired t-test, where the data were considered significant when $P < 0.0001$.

The densitometry data of flKMO-CC and HTT-FL expression (upon co-transfecting HEK293T cells with flKMO-CC and one of the HTT-VN constructs or empty vector in Section 4.2.6) were analysed using one-way ANOVA, followed by Tukey's multiple comparison tests, where $P < 0.05$ the sets of data were considered significant.

BiFC quantification data illustrated in Chapter 3 and Chapter 4 were analysed using one-way ANOVA, followed by Tukey's multiple comparison tests, where the significance is considered when $P < 0.05$. All sets of data were comparing the fluorescence intensity between different wells, where thousands of cells were individually measured (range is indicated in each figure legend), deriving from a single biological replicate (experiment). However, in Section 4.2.7 the data from three biological replicate wells per condition, and were pooled together before carrying out statistics on the mean green intensity.

Finally, the BiFC quantification experiment when cells were treated with CR (Section 4.2.12.2) was analysed using paired t-test and the data were considered significant when $P < 0.05$. The range of number of analysed cells per well is indicated in the figure legend.

CHAPTER 3 CHARACTERISING THE FUNCTION AND CELLULAR LOCALISATION OF KMO

3.1 Introduction

The organelle function within the cells is mainly reflected by the various proteins localised within their compartments. KMO is predicted to localise to the outer mitochondrial membrane (Horn *et al.*, 1971; Nishimoto *et al.*, 1975; Okamoto *et al.*, 1967) and as mitochondria contributes to HD pathogenesis, as discussed in (Section 1.3.3), function and localisation studies of KMO are needed to clarify KMO role in HD.

The human osteosarcoma cell line (U2OS) is widely used when studying mitochondrial dynamics and morphological features (Lihavainen *et al.*, 2015; Plun-Favreau *et al.*, 2007; Westrate *et al.*, 2014) due to its elongated mitochondrial network structures. As the grounds for the localisation studies carried out here did not require mimicking of neurological conditions, this bone derived cell line was first chosen over neuronal based cell lines.

In this chapter microscopy based techniques were employed to explore KMO mitochondrial co-localisation. Confocal studies coupled with intensity correlation coefficient-based (ICCB) analyses were exploited. The ICCB analyses were facilitated by the ImageJ novel public domain tool, called JACoP (just another co-localisation plugin). JACoP groups the main ICCB tools and permits the use of various methods, such as Pearson's coefficient (PC) and Mander's coefficient (M1 and M2) based analyses (Bolte and Cordelieres, 2006). Furthermore, to provide detailed ultrastructure of KMO sub-cellular localisation, transmission electron microscopy (TEM) was also used.

Besides localisation studies, functional studies on KMO were performed and discussed in this chapter. A previous study on DJ-1 dimerization from our laboratory utilised the bimolecular fluorescence complementation (BiFC), a GFP split system (Repici *et al.*, 2013), and therefore the possibility that KMO functions as a dimer was investigated in living cells using this system, BiFC principles were discussed in Section 4.1.2).

3.2 Results

3.2.1 Optimisation of cell lines for mitochondrial co-localisation studies

Obtaining optimal mitochondria morphology in the cell line used for co-localisation studies was of great relevance for the aim of this work, as KMO has been previously shown to be localized to these organelles. Thus, I first analysed the U2OS cell line for mitochondria morphology by immunostaining. Cells were grown on coverslips for 48 hr and then fixed, with ICC performed using HtrA2 antibody. HtrA2 is a mitochondrial intermembrane space protein (Lin and Beal, 2006) often used as a mitochondrial marker. As shown in Figure 3-1A, the staining resulted in a dotted or punctate signal pattern, and mitochondria did not appear as filamentous structures as expected. Similar results were obtained using a different mitochondrial marker to stain the mitochondria (an antibody that recognises the surface of intact mitochondria, specifically a 65 kDa non-glycosylated mitochondrial protein) (Figure 3-1B).

To test whether fixation was affecting mitochondrial morphology in U2OS cells, I employed the U2OS stably expressing mitochondria-targeted RFP (mtRFP) cell line. Cells were grown on ibiTreat dishes and live cells were examined by confocal microscopy. Mitochondria of U2OS mtRFP cells looked more filamentous in live cell imaging; however, their morphology varied greatly from one cell to another. For example, Figure 3-2A shows slightly compromised mitochondria, whereas Figure 3-2B illustrates the ideal mitochondrial structure expected. On the other hand, when U2OS mtRFP cells were fixed, their mitochondrial structure did not differ from U2OS cells (Figure 3-2C). In an attempt to compensate for the effect of fixation, 0.5 μM of Paclitaxel was added to the fixative, which stabilises microtubules and can prevent mitochondrial fragmentation. Despite Paclitaxel fixation, optimal mitochondria morphology was not observed (Figure 3-2D). U2OS cells were also fixed in PFA containing Paclitaxel, but without resulting improvement in morphology (data not shown).

Next, HEK293T cells were tested for mitochondrial labelling. Initially, cells were grown for 48 hr on coverslips and fixed. HtrA2 immunolabelling was used as in U2OS cells, and the mitochondrial labelling appeared punctate (Figure 3-3A). HEK293T cells were also grown on ibiTreat dishes and live cells stained with MitoTracker Red CMXRos, and again mitochondrial staining appeared punctate. As mitochondria

morphology did not differ greatly between HEK293T and U2OS cells, I decided to use HEK293T cell line for the co-localisation studies and for the subsequent work as they are easy to grow, transfect, and very resistant to toxicity from expression of exogenous proteins.

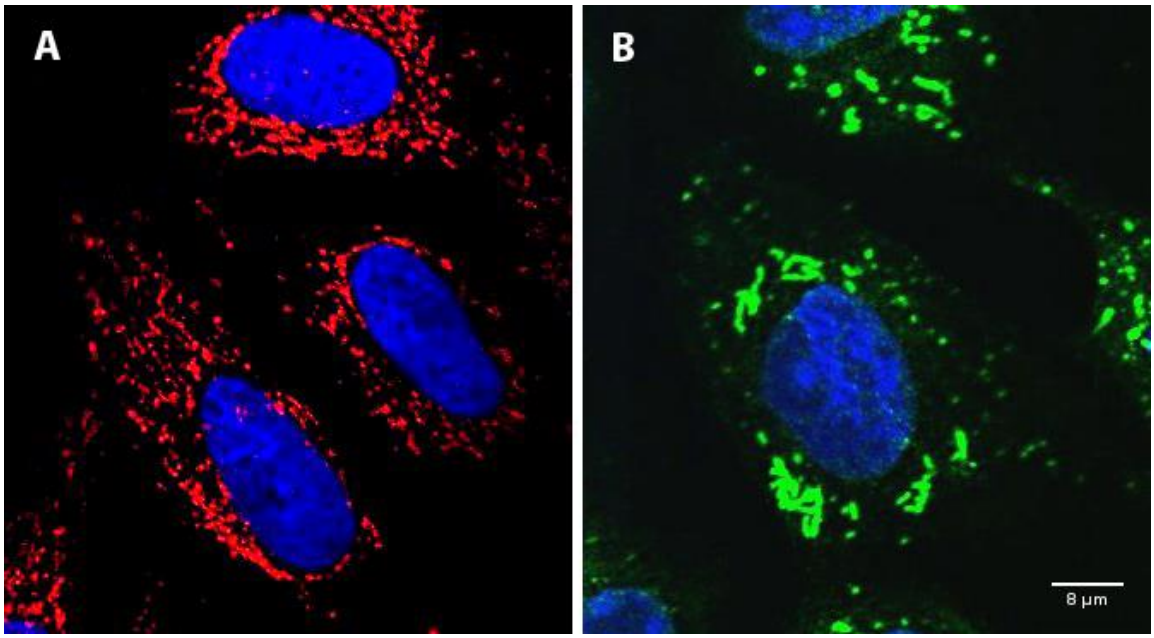

Figure 3-1 Confocal mitochondrial immunolabelling of U2OS cells.
Cells were grown for 48 hr then fixed and immunolabelled either with A) anti-HtrA2/Omi antibody (AF1458) (Alexa Fluor 546); or B) anti-mitochondria antibody (MAB1273) (Alexa Fluor 488). Nuclei were stained with Hoechst 33342. Scale bar = 8 µm.

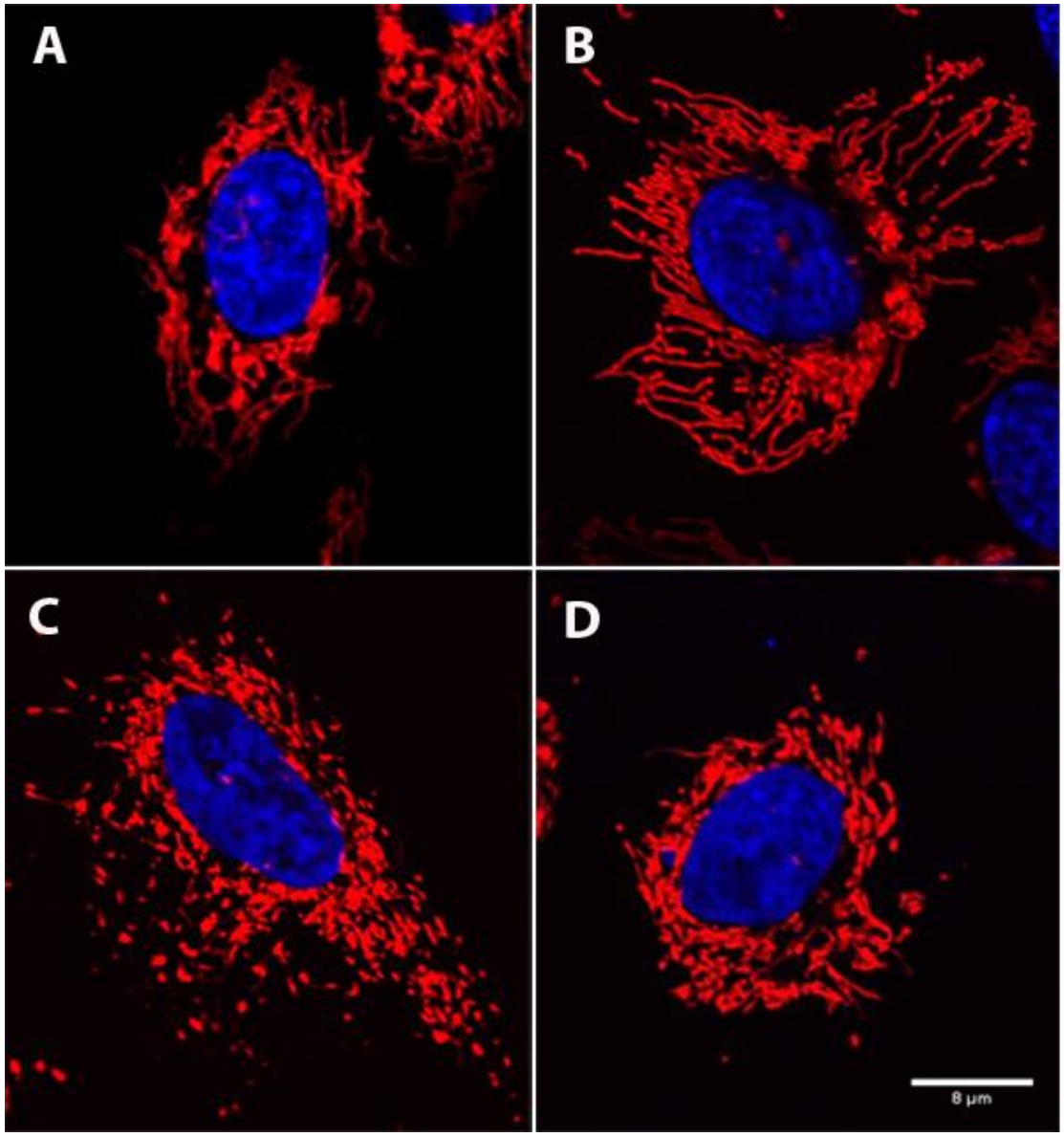

Figure 3-2 Mitochondrial morphology in U2OS mtRFP cells, using confocal microscopy. A) and B) Live cells. C) and D) Fixed cells. C) Cells were fixed in PFA, and D) cells were fixed in PFA with 0.5 µM Paclitaxel. Nuclei were stained with Hoechst 33342. Scale bar = 8 µm.

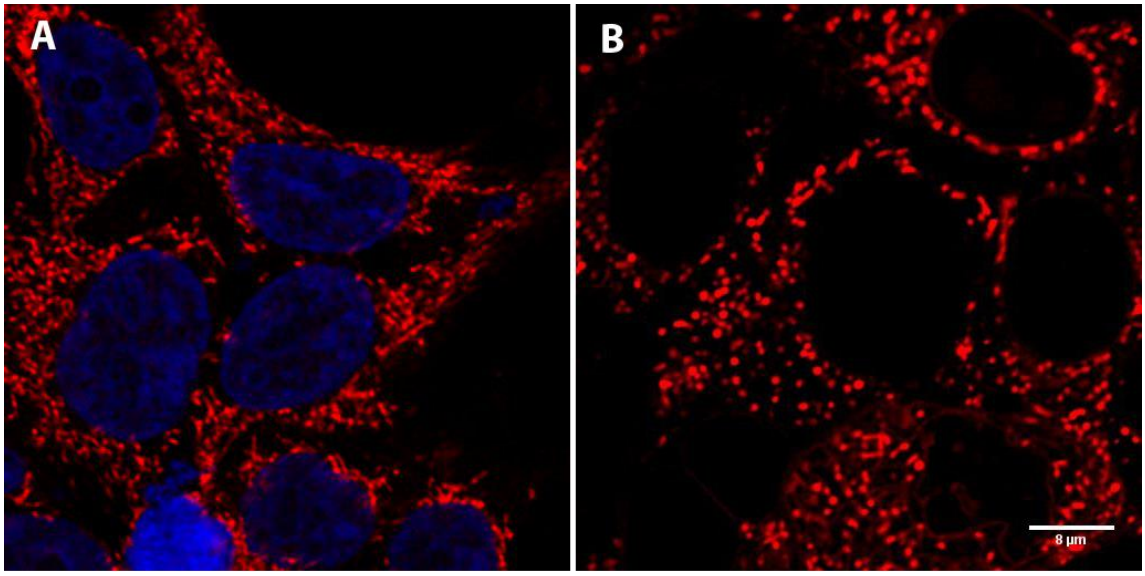

Figure 3-3 Mitochondrial morphology of HEK293T cells using confocal microscopy.
A) Cells were grown for 48 hr then fixed and immunolabelled with anti-HtrA2/Omi antibody (AF1458), followed by Alexa Fluor 546. Nuclei were stained with Hoechst 33342. B) Live cells were stained with MitoTracker Red CMXRos (M-7512). Scale bar = 8 µm.

3.2.2 Domain mapping of full length KMO (flKMO) and truncated KMO (tKMO)

Two versions of human KMO were used for exogenous expression in this study, where were encoded by the following sequences: a 1458 bp KMO cDNA and a 1218 bp truncated cDNA (tKMO) with ORFs of 486 aa and 406 aa, respectively. tKMO is encoded by a widely available cDNA previously used in our laboratory, and thus was employed in parallel with flKMO. The amino acid alignment between flKMO and tKMO shows no differences except at position 367, where in flKMO a methionine 'M' is present, while in tKMO a lysine 'K' is present (Figure 3-4). This is due to the deletion of DNA sequence encoding 13 aa in tKMO which shifts the ORF at that position, and corresponds to a deletion in the 473 aa splice isoform 2 of KMO, as determined by Ensembl. tKMO also has a 67 aa truncation at its C-terminus, leading to deletion of the second putative transmembrane domain. As the C-terminal region of KMO is crucial for mitochondrial targeting (Hirai *et al.*, 2010) and enzymatic activity (Hirai *et al.*, 2010; Wilson *et al.*, 2014), in this study the comparison was made between flKMO and tKMO. To this aim, recombinant flKMO and tKMO were cloned into mammalian expression vectors under regulation of the CMV promoter.

Figure 3-4 Amino acid sequence alignment of human flKMO and tKMO by Clustal.
flKMO is 486 aa and tKMO is 406 aa. tKMO has 80 aa missing towards the C-terminus of the protein: 13 in the middle (368-380) and 67 at the C-terminal end of the sequence (407-486), as indicated by the dashed-lines. The putative TM hydrophobic domains are highlighted in grey (as predicted in Ensembl). tKMO is missing the second TM. Identical amino acids are indicated by the asterisks, non-identical amino acid position 367 indicated by the black up-pointing arrow.

3.2.3 Generation of KMO constructs for co-localisation studies

To investigate the cellular localisation of the KMO constructs, flKMO and tKMO were cloned into pcDNA3.1 vector (untagged) or in pcDNA3.1 containing RFP (RFP-tagged) (Figure 3-5A). 0.4 µg of plasmids expressing flKMO, flKMO-RFP or tKMO-RFP were transfected in HEK293T cells, and 48 hr post-transfection cells were lysed and immunoblotting was performed to confirm expression of all KMO constructs using an anti-KMO antibody. The blot also shows that untransfected HEK293T cells (lane 6) do not express endogenous KMO (Figure 3-5B).

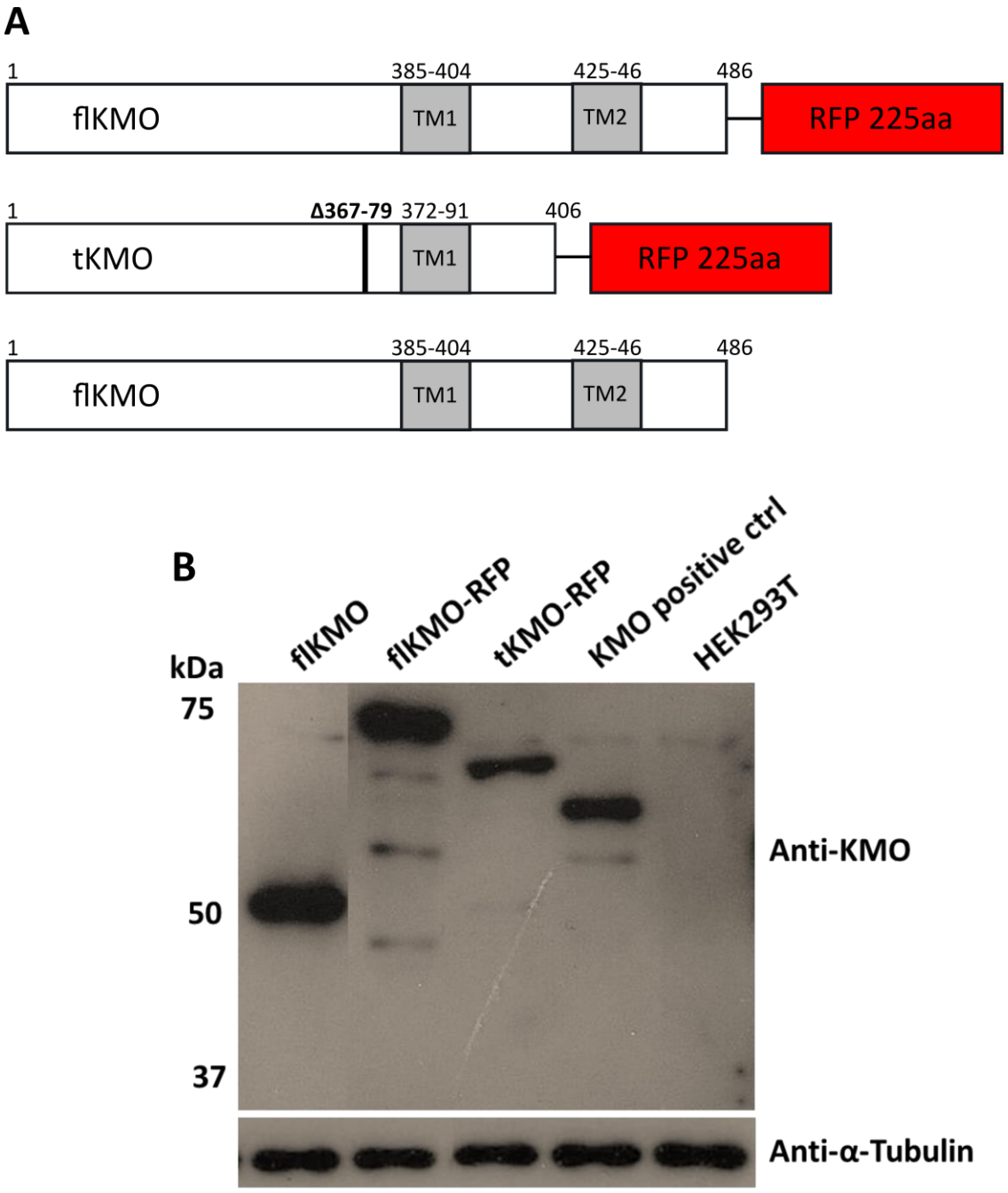

Figure 3-5 Schematic diagram and expression of different KMO constructs.
A) KMO constructs: flKMO-RFP, tKMO-RFP and flKMO. Grey boxes show putative transmembrane domains (TM). tKMO has a deletion from position 368 to 380 that resembles the deletion in KMO isoform 2, but is also truncated at its C-terminus, with 67 aa missing from the protein. B) Immunoblotting of KMO constructs using anti-KMO antibody (10698-1-AP). Anti-α-Tubulin was used as a loading control (sc-8035).

3.2.4 Sub-Cellular localisation of KMO

The localisation of human KMO was examined using immunolabelling and other cellular compartments followed by confocal and electron microscopy studies. Although KMO is described as a mitochondrial outer membrane protein, no electron microscopy has been published to date to confirm the protein localisation in the cellular ultrastructure.

3.2.4.1 Confocal studies of human KMO localisation in HEK293T cells

The purpose of the confocal studies was to examine the effect of the C-terminal truncation as well as the effect of a fluorescent tag (RFP) on human KMO localisation. flKMO-RFP construct was initially transfected into HEK293T cells seeded on ibiTreat dishes. Confocal microscopy was used to evaluate the distribution of the fused RFP signal in living cells which appeared dotted (Figure 3-6).

HEK293T cells were then transfected with either flKMO-RFP or tKMO-RFP and fixed 24 hr post-transfection. Confocal images showed an obvious difference: while flKMO-RFP has a punctate signal suggesting mitochondrial localisation, tKMO-RFP signal is more diffuse throughout the cell (Figure 3-7). Same cells were also immunolabelled with HtrA2 to verify whether flKMO-RFP or tKMO-RFP signal is localised to the mitochondria. Indeed, the flKMO-RFP signal seemed to overlay almost perfectly with the mitochondrial green signal (Figure 3-7A). On the other hand, the tKMO-RFP signal was diffuse in the cytosol with some evidence of mitochondrial and nuclear localisation (signal overlapping with mitochondrial or Hoechst staining respectively) (Figure 3-7C).

To validate these observations, ICCB analyses were used to evaluate the co-localisation. Following deconvolution, eight confocal optical sections from eight different images were chosen for each construct to carry out the analyses using JACoP, where correlation of the red and green pixels in a dual-channel optical section was performed. flKMO-RFP showed a similar distribution of the red (flKMO-RFP) and the green (mitochondrial) pixels with only some noise around the slope of the scatter plot, suggesting complete co-localisation (Figure 3-7B). For tKMO-RFP, the red and green fluorescence intensities differ strongly, leading to deflection of the pixel distribution towards the red axis, with some random noise. This implies a relatively weak correlation between the two channels (Figure 3-7D).

Tools within the JACoP plugin allow for the evaluation of co-localisation by various methods: in this study, PC as well as (M1 and M2) were used. PC analysis revealed a strong co-localisation of flKMO-RFP and the mitochondrial marker with a PC value of 0.8 ± 0.013. However, tKMO-RFP presents poor mitochondrial co-localisation indicated by a PC of 0.44 ± 0.015. The flKMO-RFP PC is significantly different from tKMO-RFP ($P < 0.0001$) (Figure 3-8A). Unlike the PC that measures the presence of the two colours (red and green) in the same pixel, Mander's coefficient represents a proportion of the overlap of each channel with the other over its total intensity (M1: red overlapping green; and M2: green overlapping with red) (Manders *et al.*, 1993). An estimated threshold is set for both M1 and M2 prior analysis to avoid background effects. The M1 for flKMO-RFP is significantly different from the M1 for tKMO-RFP ($P < 0.0001$). There is no significant difference in the M2 for flKMO-RFP and tKMO-RFP; the green is less distributed throughout the cell and its coincidence with the red signal is high so when divided by the total green intensity it leads to almost an integer number (Figure 3-8B). Thus, the Mander's analyses corroborate the PC analyses, suggesting a relatively complete co-localisation for flKMO-RFP, while the poor correlation in tKMO-RFP implies only a partial mitochondrial localisation (Figure 3-8A and B). This strongly suggests that the C-terminus is essential for mitochondrial targeting, and that a deletion of the putative second transmembrane domain leads to mis-localisation of the human KMO, as has been suggested for pig liver KMO (Hirai *et al.*, 2010).

To ensure that the –RFP tag is not enhancing flKMO mitochondrial signal, untagged flKMO was also transfected in HEK293T cells using the same conditions as RFP tagged flKMO. Cells were fixed and double immunolabelling was performed using anti-KMO and anti-mitochondrial antibodies. Interestingly, the tag did not seem to affect flKMO mitochondrial localisation as flKMO localised similarly to flKMO-RFP, with punctate signal overlapping with the mitochondrial signal (Figure 3-9).

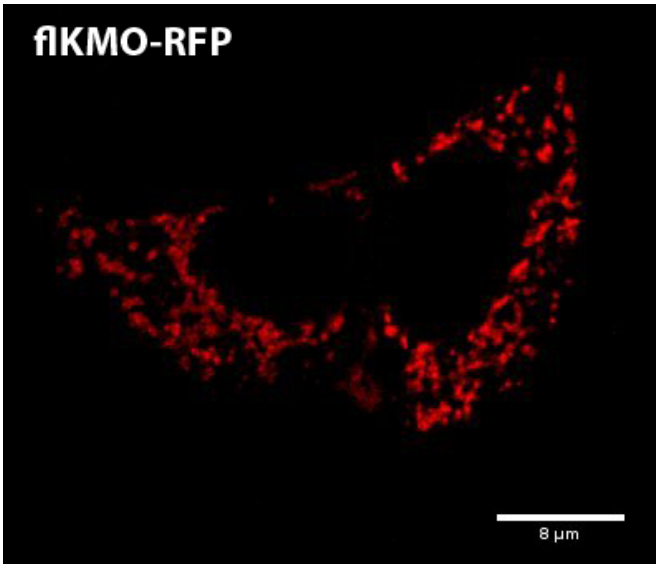

Figure 3-6 Live HEK293T cells expressing the flKMO-RFP construct.
Image was acquired using confocal microscopy and deconvolved. Scale bar = 8 µm.

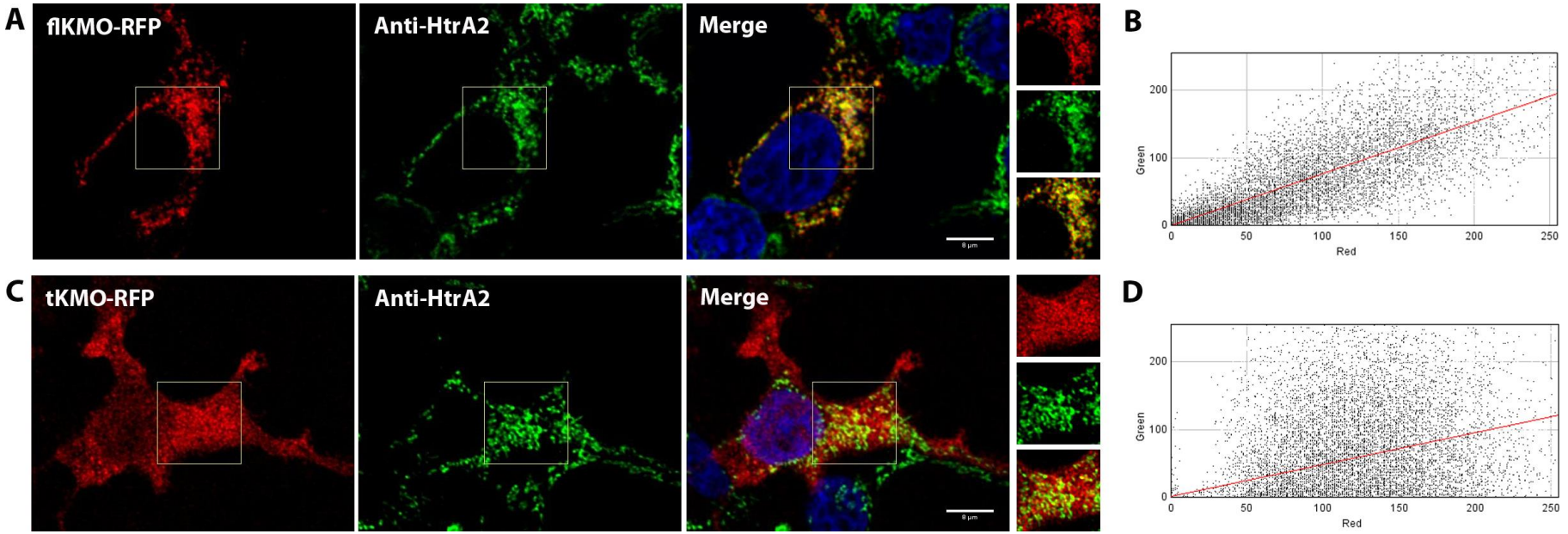

Figure 3-7 Co-localisation analysis of flKMO-RFP and tKMO-RFP deconvolved confocal optical z-sections, using JACoP plugin in ImageJ.
HEK293T cells were transfected with the flKMO-RFP, (A, Left panel) or tKMO-RFP (C, Left panel) construct and fixed 24 hrs after transfection. A) and C) middle panels: immunolabelling for the mitochondrial protein HtrA2 using anti-HtrA2/Omi antibody (AF1458) (Alexa Fluor 488). A) and C) right panels: merge of the RFP and anti HtrA2 signal. Nuclei were stained with Hoechst 33342. Scale bar = 8 µm. flKMO-RFP presents a mitochondrial localisation (punctate structures), while tKMO-RFP signal is diffuse throughout the cell. The squares on the images indicate the selected areas for co-localisation analysis (a zoomed-view of the selected area is shown on the side of each merge panel). B) flKMO-RFP scatter plot showing the correlation between green and red signals. Pixel distribution along the slope shows nearly equivalent fluorescence intensities between the green and the red channels. D) tKMO-RFP scatter plot. The difference in the fluorescent signal localisation results in a completely different distribution of the pixels, showing a very low correlation between the green and the red signals.

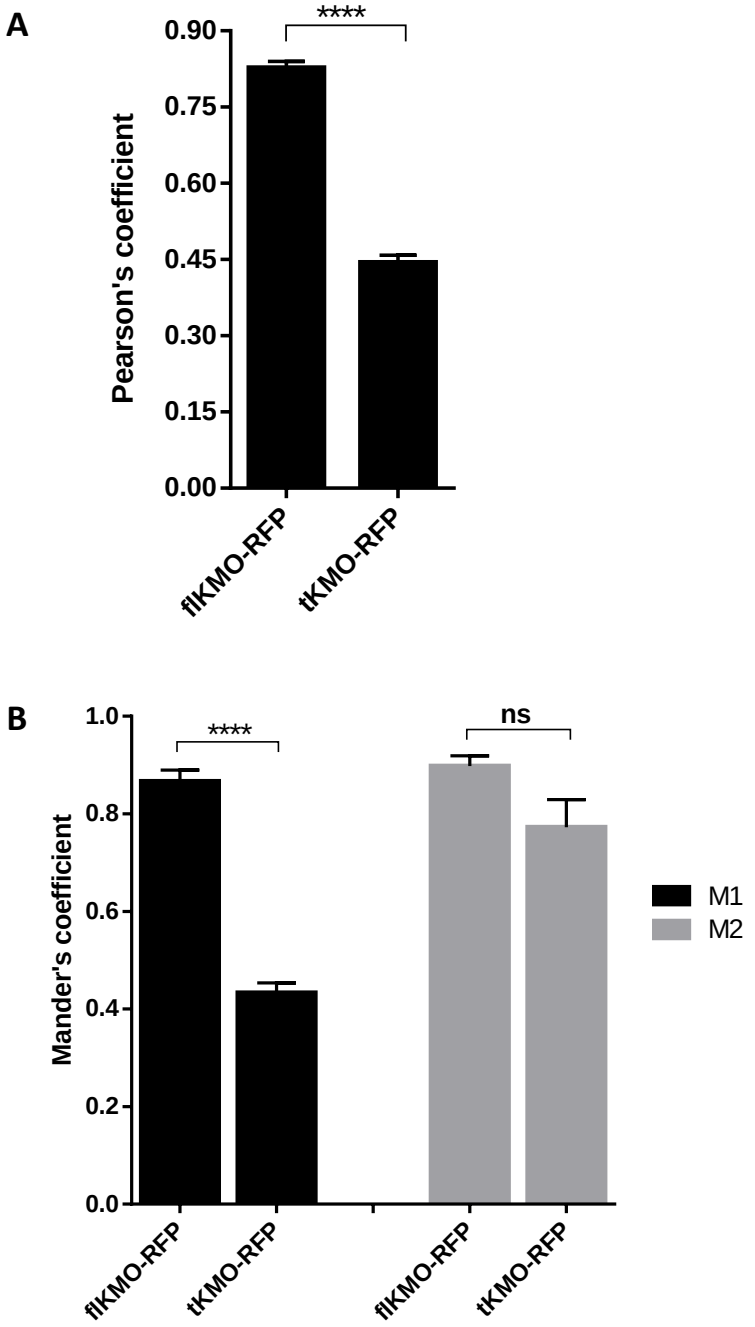

Figure 3-8 Co-localisation analysis of optical z-sections from different deconvolved confocal images, using JACoP in ImgaeJ.
A) Pearson's coefficient shows a very significant difference in the mitochondrial co-localisation of flKMO-RFP and tKMO-RFP. B) Mander's coefficient correlation. M1 represents the red signal overlapping the green signal, while M2 indicates the green signal overlapping the red signal. **** ($P < 0.0001$), for unpaired t-test. ns = not significant. Data are expressed as mean ± SEM, where n = 8.

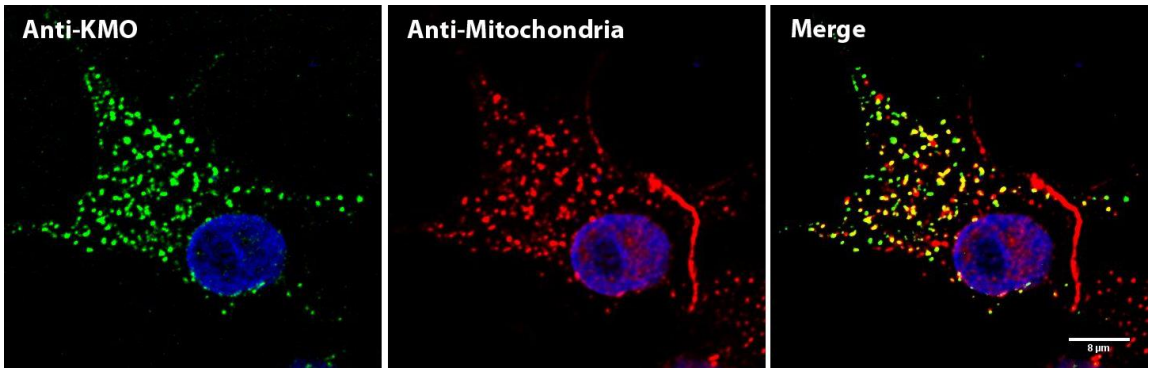

Figure 3-9 Subcellular localisation of the untagged flKMO construct expressed for 48 hr in fixed HEK293T cells, using deconvolved confocal images.
Left panel: flKMO immunolabelling with anti-KMO antibody (10698-1-AP) (Alexa Fluor 555). Middle panel: anti-mitochondria (MAB1273) immunolabelling (Alexa Fluor 647). flKMO and mitochondrial signals are presented with green and red signals for Alexa Fluor 555 and 647, respectively, to ease illustration of green and red overlapping as in the right merge panel. Nuclei were stained with Hoechst 33342. Scale bar = 8 µm.

3.2.4.2 Fine mapping of human flKMO localisation using TEM

Although KMO is defined as a mitochondrial outer membrane protein, to date there has been no fine mapping of its localisation. To this aim, electron microscopy studies were carried out on HEK293T cells that were seeded on 9 mm coverslips and transfected with untagged flKMO construct along with an RFP-expressing plasmid as a transfection reporter; transfection was confirmed by RFP fluorescence visualised prior to fixation of the cells. Mitochondria were immunogold labelled with an antibody that recognises an endogenously expressed mitochondrial non-glycosylated protein of 65 kDa, as a positive control (Figure 3-10A). Other sections were immunogold labelled with anti-KMO antibody to study the localisation of the exogenously expressed flKMO. The electron micrographs clearly show intense labelling indicating that flKMO is localised at the outer surface of the mitochondria. As the outer mitochondrial membrane surrounds the mitochondria it confirms the proposed localisation of KMO. This is the first microscopy-based study showing human KMO as an outer mitochondrial membrane protein (Figure 3-10B), and supports previous studies showing localization of pig liver KMO to the outer mitochondrial membrane (Hirai *et al.*, 2010; Uemura and Hirai, 1998). In addition, untransfected HEK293T cells were immunogold labelled with anti-KMO antibody, and the negative labelling further confirmed KMO absence in this cell model (data not shown).

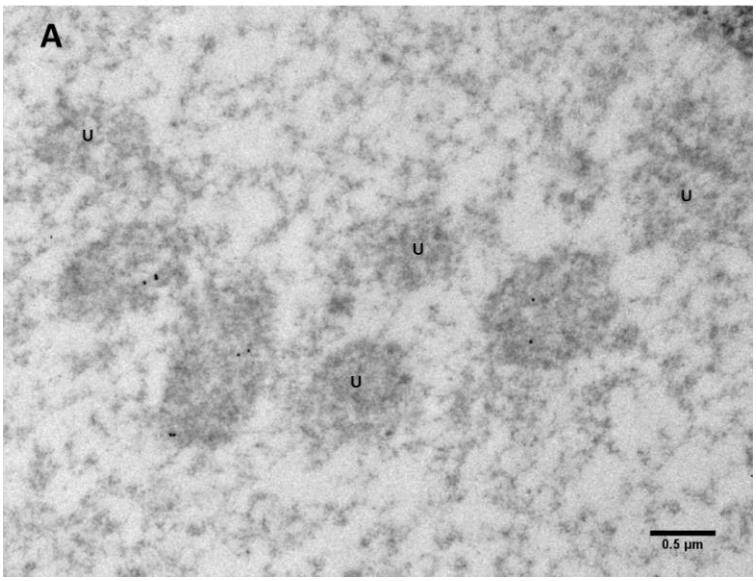
A
U
U
U
U
0.5 µm

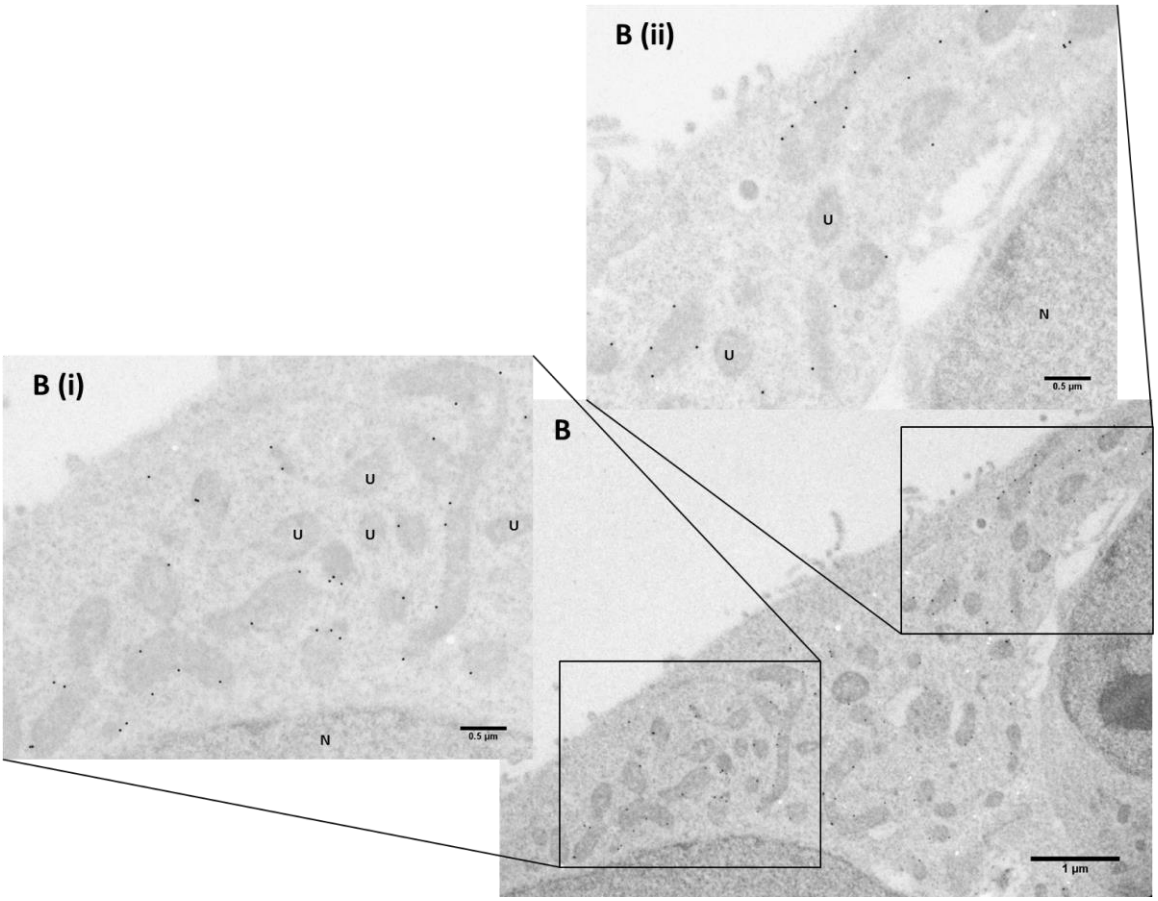
B (ii)
U
U
N
0.5 µm
B (i)
U
U
U
U
N
0.5 µm
B
1 µm

Figure 3-10 Electron micrograph of HEK293T cells showing immunogold labelling of mitochondrial proteins.
Cells were transfected with 0.24 µg of untagged flKMO and 0.06 µg of RFP (transfection reporter) for 48 hr. A) Immunogold labelling of an endogenously expressed non-glycosylated protein that is localised exclusively to the mitochondria; anti-mitochondria antibody (MAB1273). Scale bar = 0.5 µm. B) Sub-cellular localisation of flKMO. The immunogold particles are clearly localised at the outer surface of the mitochondria; anti-KMO antibody (10698-1-AP). Scale bar = 1 µm. B (i) and B (ii) are zoomed in views of the intense flKMO labelling in panel B. Scale bar = 0.5 µm. Mitochondrial structures are identified with the presence of the gold particles. Unlabelled mitochondria are designated with the letter 'U'. Nuclei are denoted with the letter 'N'.

3.2.5 Investigation of KMO dimerization in HEK293T cells

KMO purification studies previously reported that KMO is found in oligomeric form in aqueous solution and as a dimer after detergent solubilisation (Amaral *et al.*, 2013; Nishimoto *et al.*, 1977; Uemura and Hirai, 1998). To reveal the possibility of exogenous human flKMO dimerization in mammalian systems, the BiFC assay was used in living cells to explore potential flKMO interactions. All possible orientations of flKMO BiFC constructs were generated, by fusing flKMO to either the 155-238 aa C-terminal CFP (CC) half or the 1-172 aa N-terminal eGFP (GN) half, as shown in Figure 3-11.

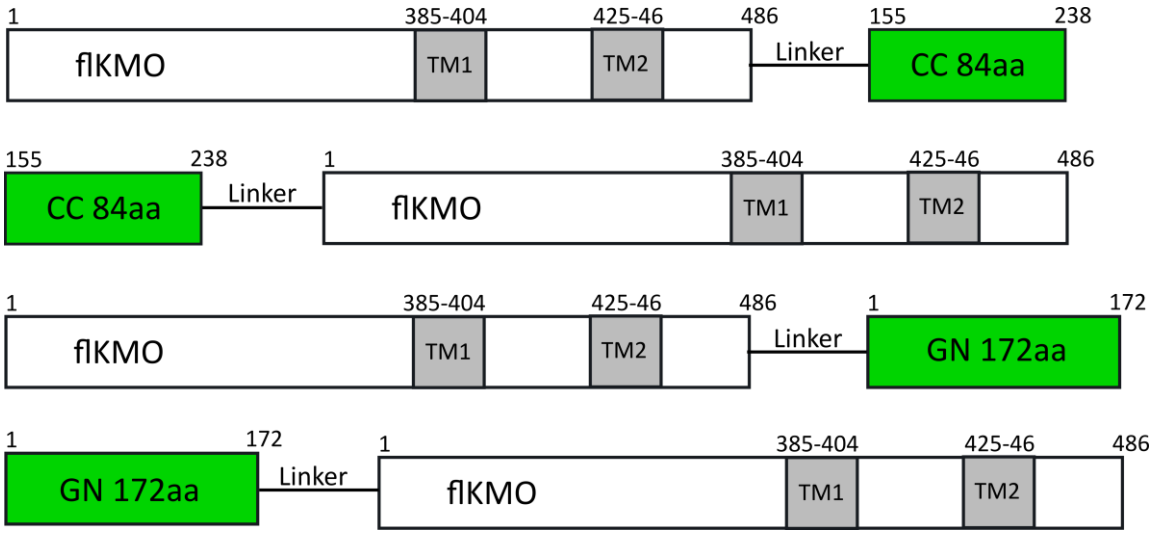

Figure 3-11 Schematic representation of flKMO BiFC constructs.
flKMO BiFC pair contains either the C-terminus of CFP (CC) or the N-terminus of eGFP (GN). Halves of the fluorescent proteins, CC or GN were fused either to the C-terminal or N-terminal end of flKMO, to test all possible orientations, via a $(GGGGS)_2$ linker.

HEK293T cells were co-transfected with the two flKMO constructs (one expressing CC and the other GN) at a concentration of 0.16 µg, along with 0.08 µg of a plasmid expressing RFP, as a control for normalisation, in a 6-well plate. 48 hr post transfection, 100 images in triplet (green, red and bright field channels) were taken per well using the Scan^R screening station for live cell microscopy, at 37ºC and 5% CO_2. Green and red images were analysed using the Scan^R analysis software by measuring the total green intensity and cells area based on RFP expression per cell. The quantification of the BiFC signal was obtained as mean green intensity (total green intensity/ mean cells'

area). Previous BiFC work on DJ-1 dimerization was published from our laboratory where the quantification of BiFC signal was expressed as ratio intensity (Repici *et al.*, 2013). However, due to the fact that the BiFC assay was used with different proteins in this study, some problems were encountered using the ratio intensity as quantification method. I therefore needed to use the mean green intensity as a way of BiFC normalisation throughout this piece of work. Further details of the detailed optimisation can be found in Section (4.2.5).

As presented in Figure 3-12A, quantification of the BiFC signal shows that none of the BiFC flKMO pairs are dimerizing in HEK293T cells. All conditions were significantly different ($P < 0.0001$) from the positive control, the DJ-1 dimer pair previously characterised by Repici *et al.* (2013). DJ-1-GN was co-transfected with flKMO-CC as a negative control, as previous work has shown that flKMO and DJ-1 do not interact with one another (data not shown). Interestingly, the mean green intensity of the combination of flKMO-CC and flKMO-GN was significantly less than the negative control ($P < 0.01$) (Figure 3-12A). After imaging, cells were lysed for immunoblotting to verify protein expression. Both positive and negative control proteins were expressed as expected (Figure 3-12B). However, not all flKMO constructs were immunolabelled when the anti-GFP antibody was used: flKMO-CC and CC-flKMO were easily detected at their predicted molecular weight, the second bands in the CC-flKMO lanes are normally detected even when only CC-flKMO construct was transfected. flKMO-GN and GN-flKMO however were not observed, indicating that a KMO antibody would need to be used in order to confirm the expression of these constructs. Due to the limited availability of the only reliable KMO antibody which detects exogenous KMO, only GFP antibody was used. Moreover, indeed, previous immunoblotting analysis revealed that tKMO-GN was recognised by the anti-KMO antibody, but not by the anti-GFP using the same lysate (data not shown). Thus, the inability of the anti-GFP antibody to recognise flKMO-GN and GN-flKMO might be due to a tag conformational change issue of the flKMO tagged with GN. For this reason, for subsequent BiFC assays only flKMO-CC was used (Chapter 4). In addition, BiFC was also performed with higher DNA concentrations (0.24 µg) for each flKMO BiFC construct, and 0.12 µg of RFP expressing plasmid, but complementation between flKMO constructs did not occur (data not shown). In total, these experiments suggest that flKMO does not dimerize in living cells.

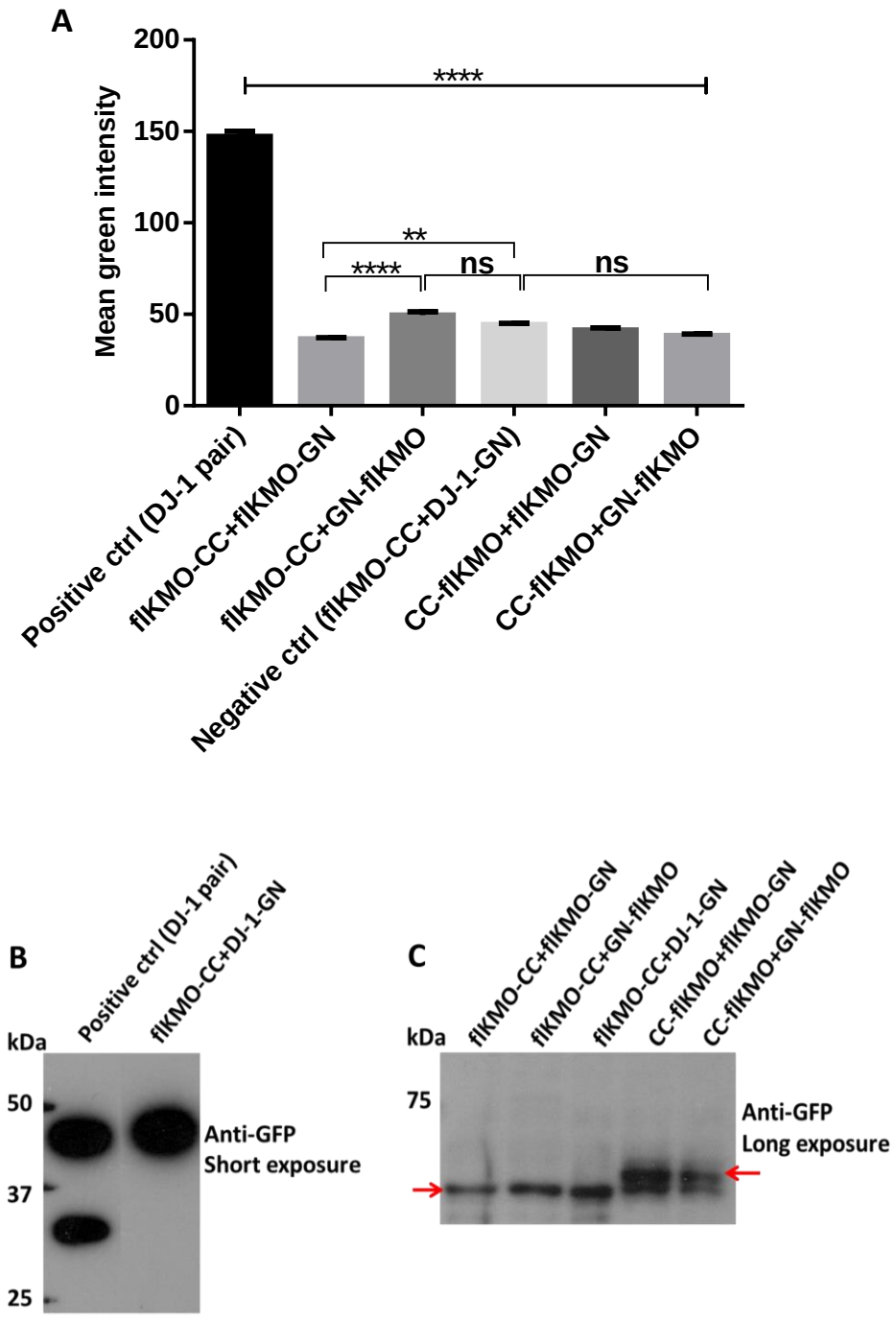

Figure 3-12 flKMO dimerization in living HEK293T cells.
A) BiFC quantification of the mean green intensity of the fluorescence complementation signal. All KMO pairs were significantly different from the positive control **** ($P < 0.0001$), and not significantly different (ns) from the negative control. Only flKMO-CC + flKMO-GN complementation was even less than the background of the negative control, ** ($P < 0.01$), one-way ANOVA, followed by Tukey test. Data are expressed as mean ± SEM per well. The number of analysed cells ranged from 1000 to 3000 cells per well per condition. B) and C) protein expression levels using anti-GFP antibody (ab6556). B) Control constructs, and C) flKMO-CC (first three lanes) and CC-flKMO (last two lanes); correct bands indicated by the arrows.

3.3 Discussion

As this chapter mainly studied KMO mitochondrial localisation, mitochondrial morphology was examined in two cell lines (U2OS and HEK293T) prior to performing localisation studies. HEK293T cells were eventually used, as U2OS cells lacked the desired mitochondrial elongated structure despite the use of Paclitaxel. A reason could be related to the poor stock quality, as the thawed aliquot of cells was ~9 years old and took very long to grow. Moreover, as cells were passed on between several laboratories, cross contamination cannot be excluded. A fresh stock of U2OS cells from a cell line repository would be needed for further validation. However, as the sole purpose of this work was to study KMO mitochondrial co-localisation, the use of HEK293T cells was sufficient.

The results described in this chapter clearly indicate that the KMO C-terminus region is important for co-localisation and might bear the mitochondrial targeting signal. All flKMO constructs, regardless of being fluorescently tagged or not, had punctate mitochondrial signal, whereas tKMO construct showed diffuse signal throughout the cytoplasm. tKMO resembles KMO isoform 2 with regards to deletion of amino acids 368-380, but it also presents a C-terminal truncation and thus is missing the second putative TM domain. This implies that the second putative TM is essential for mitochondrial co-localisation, and that tKMO might be a natural occurring KMO isoform. Despite the deletions in the tKMO protein sequence, it was not completely mis-localised as suggested by the correlation seen between the mitochondrial probing signal and the tKMO RFP signal. My data also suggest some nuclear localisation of tKMO along with the cytosolic one.

KMO needs TM domains to anchor into the mitochondrial outer membrane; Ensembl database suggests that there are two in the flKMO (486 aa): 385-404 and 425-447. These domains are not well characterised, and studies so far have only described the second putative TM domain 425-446 and its role in mitochondrial localisation and enzymatic activity (Hirai *et al.*, 2010; Wilson *et al.*, 2014). However, the first TM domain and other hydrophobic regions upstream and downstream of these TM domains may contribute to the mitochondrial targeting signal of KMO. Domain mapping along with sequence alignment with KMO in other mammalian species are needed for any conservation that might suggest a specific role. The two arginine residues downstream

of the second TM domain R454 and R455 were suggested to add hydrophobicity to the protein and to be important for correct localisation, and appeared to be conserved in all mammals except in rat, where the two residues were substituted by serine (Hirai *et al.*, 2010). Hirai *et al.* (2010) also demonstrated that mutations at these two arginine positions into serine mis-targeted pig liver KMO to the cytosol, with some protein still partially localised to the mitochondria and reduced enzymatic activity. However, when they deleted the C-terminus 20 aa segment downstream of the second TM domain (where the two arginine residues are localised) KMO was localised only to the cytosol, and demonstrated full enzymatic activity (Hirai *et al.*, 2010). Further studies on subcellular localisation using mitochondrial fractionation showed that rat liver KMO is associated with the mitochondrial outer membrane (Nishimoto *et al.*, 1975; Nishimoto *et al.*, 1977; Okamoto *et al.*, 1967). Based on prediction rat KMO may have a dual localisation, the mitochondrial outer membrane, and the cytosol or endoplasmic reticulum, similar to that seen in the family of the outer membrane tail-anchored proteins that KMO was proposed to belong to (Hirai *et al.*, 2010; Hwang *et al.*, 2004).

In addition to my findings on human tKMO localisation, Hirai *et al.* (2010) reported as well that the deletion of the C-terminal 50 aa or 70 aa of pig liver KMO (including the second TM domain) led to cytoplasmic localisation and severely compromised enzymatic activity (Hirai *et al.*, 2010). This was further confirmed by the deletion of the C-terminal 100 aa of 6xHis tagged human KMO expressed in bacterial cells that did not exhibit 3-HK production, and was found mostly soluble and easy to purify suggesting it was not anchored to the mitochondrial membrane. Clearly such a deletion resulted in missing both predicted TMs of human KMO (Wilson *et al.*, 2014). Interestingly, in *S. cerevisiae* our human tKMO construct is mitochondrially targeted (Thevandavakkam, 2011), and a 66 aa C-terminally truncated version of *S. cerevisiae* KMO (with 34% identity and 51% similarity to human KMO) exhibited normal activity (Amaral *et al.*, 2013). This difference implies that the first TM domain in *S. cerevisiae* might compensate for the loss of the second TM domain, whereas the second TM domain is crucial for localisation and activity in mammalian and bacterial systems.

Although fluorescent tags did not affect KMO localisation, a FLAG tag seemed to impair this mitochondrial targeting signal in pig liver KMO, leading to localising the protein to the plasma membrane, mitochondria and cytosol as well as slight reduction in enzymatic activity (Hirai *et al.*, 2010). This was suggested to happen as a result of the

negative charge of the FLAG sequence (DYKDDDDK) that weakened the mitochondrial signal, as well as it may have affected the C-terminal hydrophobicity of the protein (Hirai *et al.*, 2010). Moreover, bacterial expression of human flKMO tagged with 12xHis and 3xFLAG yielded more soluble, but enzymatically active KMO, unlike the counterpart 6xHis tagged flKMO that was mostly insoluble and active, confirming the effect of FLAG tag on the correct mitochondrial localisation.

Our microscopy based co-localisation studies provided the first evidence with comprehensive analyses on human KMO mitochondrial co-localisation. This was preceded by the work on pig liver KMO, were co-localisation was shown by overlaying the immunolabelled KMO green signal with the red MitoTracker staining (Hirai *et al.*, 2010). Although the presence of yellow spots in the merge image indicates co-localisation, this depends on visualisation and can only be reliable if both images exhibit similar grey level dynamics, which cannot be achieved when imaging two fluorochromes with differential signal strength (Bolte and Cordelieres, 2006). Thus, the need to use JACoP for co-localisation arose to validate our observations. The PC method is the most commonly used as most ICCB are based on PC or its derivatives. However, the PC is influenced by the background noise and variation in fluorescence intensities, and therefore scatter plots and PC only provide a first estimate of co-localisation (Bolte and Cordelieres, 2006). To circumvent this limit, the Mander's coefficient (M) that is based on the PC - with average intensities values taken out of the calculations - was also used (Manders *et al.*, 1993). Moreover M1 and M2 can be calculated after setting a threshold to the estimated value of background. Based on this, Bolte and Cordelieres (2006) provided that when multiple images are used for comparison, the use of Pearson's and Mander's coefficients is reliable for co-localisation analyses (Bolte and Cordelieres, 2006). In addition, our studies were enhanced by providing the first electron micrograph of human flKMO localisation with strong immunogold on the outer surface of mitochondria. It is important to note that there were minor immunogold particles outside the mitochondria on some images, which might be due to the use of thin sections, and those particles were labelling the mitochondria on the section above or below.

Indeed, TEM is a powerful tool to provide ultrastructure at high resolution as well as detailed *in situ* localisation facilitated by immunogold labelling. However, the need to use strong fixative to attain enhanced ultrastructure is detrimental to protein antigenicity

(De Paul *et al.*, 2012). In this study, it was challenging to balance between preservation of KMO antigenicity and provide fine ultrastructure of the mitochondria in HEK293T cells. Routinely for confocal immunocytochemistry (ICC) I fix the cells in 4% paraformaldehyde (PFA) in PBS. However, there was no labelling using KMO antibody when cells were fixed in 4% PFA for TEM studies. This is due to the fact that cells undergo extensive processing in preparation for TEM ICC. Glutaraldehyde (GA) has a greater capability to cross-link proteins and stabilise tissue structure than does PFA, but it leads to reduction of antibodies' antigenicity, and thus needs to be carefully used to obtain optimum results (De Paul *et al.*, 2012). In my hands, addition of 0.05% GA to 4% PFA solution solved the antigenicity problem, but not the ultrastructure, and was the best solution to obtain TEM results. A slight increase in GA (to 0.5%) led to almost complete loss of the KMO antibody antigenicity and the ultrastructure did not improve significantly (data not shown). Other fixatives could have also been considered, such as osmium tetroxide which is known to preserve the ultrastructure by strongly cross linking proteins and polypeptide chains, but is extremely detrimental to antigenicity (De Paul *et al.*, 2012). Tannic acid was another available option, but it is also used with PFA and leads to only slight improvement in the structure and thus may not necessarily provide the desired outcome. Therefore, although super detailed ultrastructure of the mitochondria in HEK293T cells was unachievable due to fixative limitations, mitochondria morphology was distinctive from other cellular compartments and as KMO is on the outer membrane its localisation was readily observed.

In total, this work has provided the strongest evidence to date for human KMO mitochondrial co-localisation, which provides a foundation to investigate the localisation of the other KMO splice isoforms.

I next studied KMO dimerization by using the BiFC assay. Although BiFC is a powerful assay to explore dimerization in living cells, the need to use fusion of split fluorescence proteins can be a disadvantage for the correct protein folding necessary for protein-protein interactions. In my KMO dimerization experiment, flKMO-CC and CC-flKMO were nicely detectable with the anti-GFP antibody, moreover flKMO-CC localisation was fully characterised in Sections (4.2.13.1 and 4.2.16.1) and the –CC tag did not interfere with flKMO. However, anti-GFP antibody failed to detect flKMO-GN and GN-flKMO, suggesting that the –GN tag may result in conformational changes which ultimately did not facilitate the re-formation of the fluorophore. Further

characterisations are needed to draw a conclusion on flKMO-GN and GN-flKMO [rs. In addition, it was shown in our laboratory that DJ-1 BiFC complex did not favour mitochondrial localisation (Repici *et al.*, 2013) although the single DJ-1 BiFC constructs exhibit partial mitochondrial co-localisation when transfected individually (Repici, unpublished data). Despite the fact that BiFC assay was previously used to detected protein-protein interactions at the mitochondria (Takahashi *et al.*, 2005), perhaps a different approach would be needed to explore the dimerization possibility of a mitochondrial protein. It has been suggested that blue native gels can be applied to study assembly of mitochondrial protein complexes (Nijtmans *et al.*, 2002). For instance ATP synthase (mitochondrial inner membrane protein) was found to exist as monomeric and dimeric forms using blue native gels following solubilisation of mitochondrial membrane using a low detergent (Arnold *et al.*, 1998). Thus, this method could be applied on flKMO expressed in HEK293T cells in future studies.

CHAPTER 4 DISSECTING PHYSICAL INTERACTIONS OF KMO

4.1 Introduction

Studying physical interactions between proteins is crucial to unravelling functions and mechanisms. HTT is ubiquitously expressed and involved in different cellular mechanisms as suggested by its interacting partners (Harjes and Wanker, 2003). Moreover screening for HTT interactors led to identification of several HD genetic modifiers (Kaltenbach *et al.*, 2007). Although KMO is a key modulator of HD toxicity that is receiving growing interest as a therapeutic target, its physiological roles are not well studied (Campesan *et al.*, 2011; Giorgini *et al.*, 2005; Zwilling *et al.*, 2011). The first screen for KMO interaction partners performed in *S. cerevisiae* found interactors enriched in four functional categories: metabolism, cytoskeleton organisation and biogenesis, intracellular transport and signal transduction (Thevandavakkam, 2011), thus suggesting new possible physiological roles for KMO beyond its known enzymatic activity.

4.1.1 Screening for KMO interacting partners

Thevandavakkam (2011) performed a large scale screen in yeast using the membrane yeast two hybrid (MYTH) system, which is similar in principle to the yeast two hybrid system. However, MYTH was optimised for screening of membrane bound proteins using the split ubiquitin system in which ubiquitin halves re-constitute into a functional ubiquitin upon interaction of the candidate proteins (Thevandavakkam, 2011). The screen in yeast utilised a KMO-containing bait to screen a human foetal cDNA library which led to the identification of 31 KMO interacting proteins (KIPs). These hits were further validated by co-immunoprecipitation (coIP) approach, using FLAG-tagged KMO expressed in yeast extracts. 18 out of the 31 KIPs were detected, confirming their interaction with KMO. Provocatively, 8 of these proteins are known to be HTT interactors, as illustrated in Figure 4-1 (Thevandavakkam, 2011). A subset of the interesting gene candidates (GAPDH, DCTN2 and AP2M1) identified from the KMO physical screen were chosen to be further validated in higher system. In addition, as KMO and HTT share interaction partners (Figure 4-1), the possibility that KMO and HTT interact with one another is also majorly addressed in this chapter. An optimised

assay which is highlighted in the following section was used to dissect KMO interactions in mammalian cells.

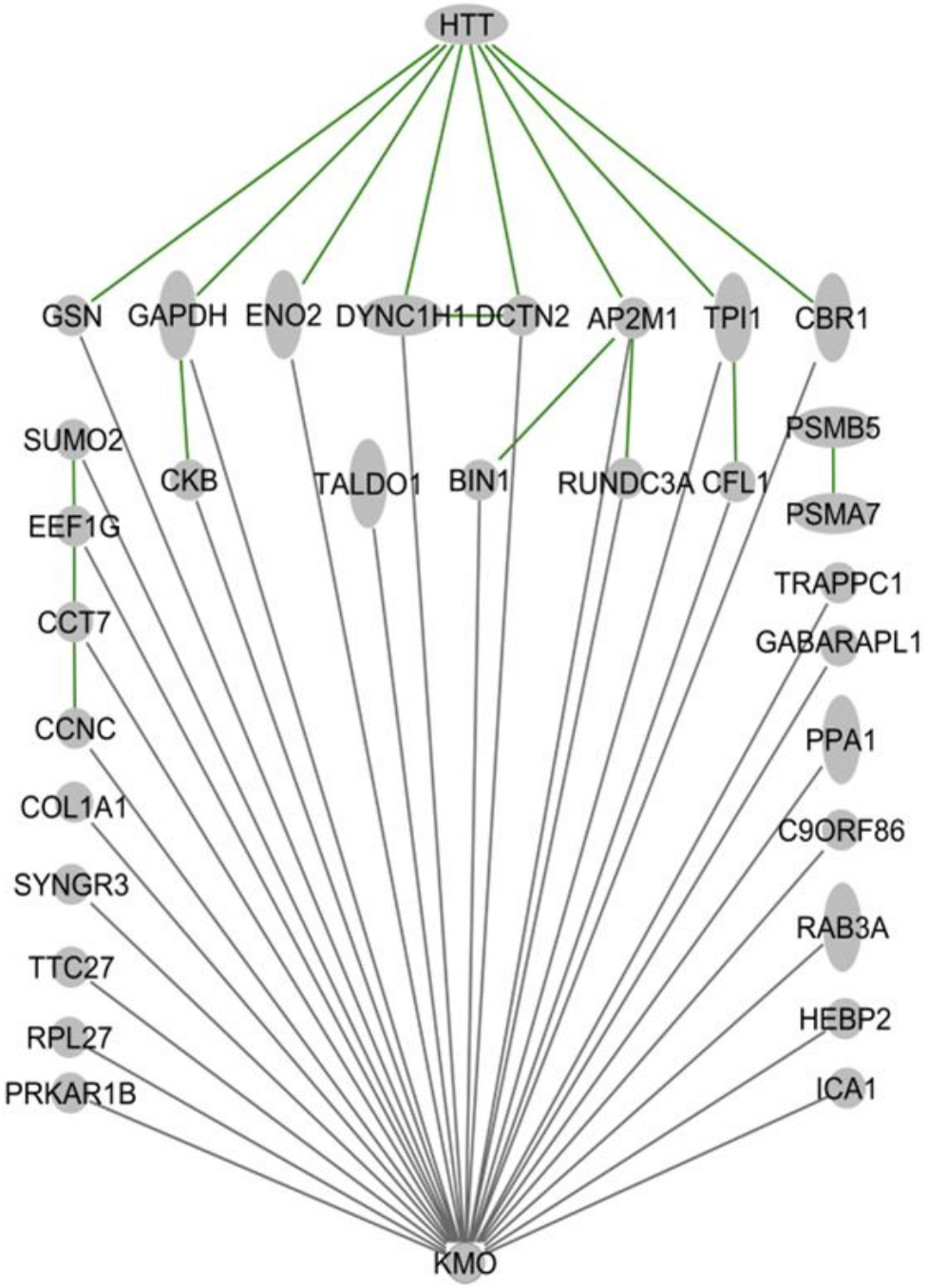

Figure 4-1 KMO and HTT interaction network using IPA analysis tool
(taken from Thevandavakkam, 2011).

4.1.2 Bimolecular fluorescence complementation (BiFC) assay

In order to explore the physical interactions of KMO, I have primarily employed BiFC. This approach utilises a split fluorescent protein (e.g. GFP), where each half of the fluorescent protein is fused to one of two proposed interactors. Only small parts of the fused proteins need to interact for a fluorescent BiFC signal to be detected due to reformation of the fluorophore (Kerppola, 2006a) as shown in Figure 4-2.

However, dynamic flexibility is required for the fluorescent protein fragments to associate in the interaction complex. This can be facilitated by adding a linker sequence between the fused protein and the fluorescent fragment (Kerppola, 2006a). Determination of the appropriate orientation of the fused protein and the fluorescent fragment might require some testing of multiple combinations of N-terminal or C-terminal fusion which makes a total of eight possible BiFC pair combinations (Figure 4-3). Moreover, localisation, expression and function of fused proteins needs to be validated to ensure that the fluorescent fragment is not interfering with its fused protein (Kerppola, 2006a). The BiFC system has been widely employed to study protein-protein interactions both *in vitro* and *in vivo* using various cell lines such as COS-7 cells for studying protein interactions at the mitochondria (Takahashi *et al.*, 2005), and HEK293T cells (Repici *et al.*, 2013); as well as living organisms, some examples include: *Escherichia coli* (Ghosh *et al.*, 2000), *Xenopus* (Saka *et al.*, 2007), *Drosophila melanogaster* (Benton *et al.*, 2006), *Caenorhabditis elegans* (Hiatt *et al.*, 2008) and *Arabidopsis* (Walter *et al.*, 2004).

The significance of the BiFC approach is related to a direct visualisation of protein complexes within their natural environment and provides subcellular localisations of the interacting proteins in living cells (Kerppola, 2006b). In addition, weak and transient interactions might be further stabilised by the fluorescent fragments re-association and likely to be detected using the BiFC assay (Kerppola, 2008). On the other hand, spontaneous association of fluorescent fragments independently of their fused proteins enables background signal of non-specific interaction (Saka *et al.*, 2007; Shyu *et al.*, 2006), which requires optimisation depending on the fluorescent fragments and their fused proteins. Although the BiFC fluorophore takes time to mature to allow observation of interactions indicated by the BiFC signal, it does not permit detection of real-time complex assembly (Kerppola, 2006a; Kerppola, 2008). The BiFC application

is therefore a robust, efficient and reliable system of detecting interaction partners reported in this chapter as well as in Chapter 3.

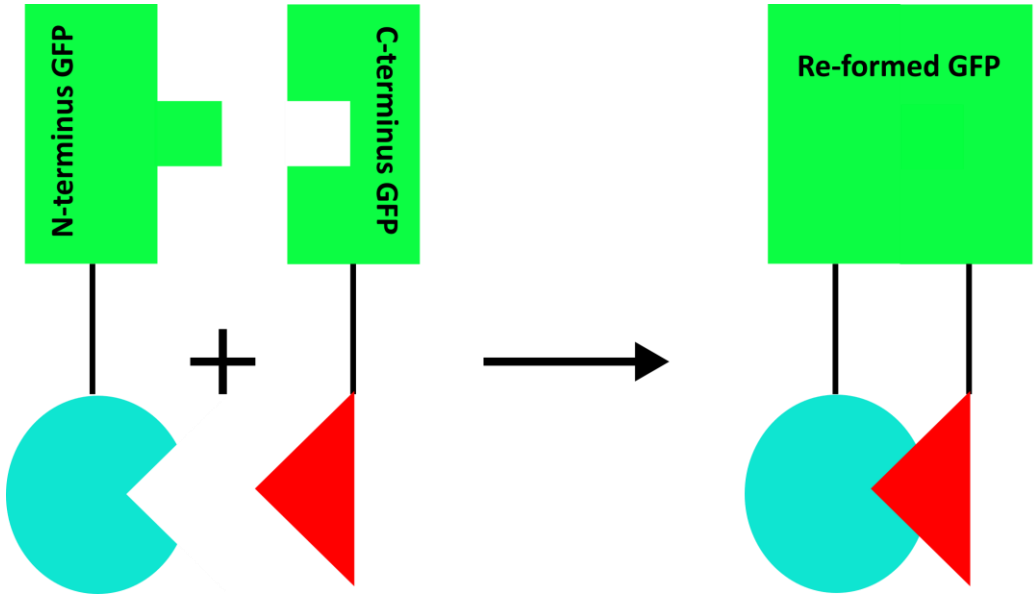

Figure 4-2 Basic principle of the BiFC assay.
If the two proteins interact (represented here with incomplete circle and a triangle), then N-terminal and C-terminal halves of GFP come together re-forming a fluorescent GFP (redrawn from Kerppola, 2006a).

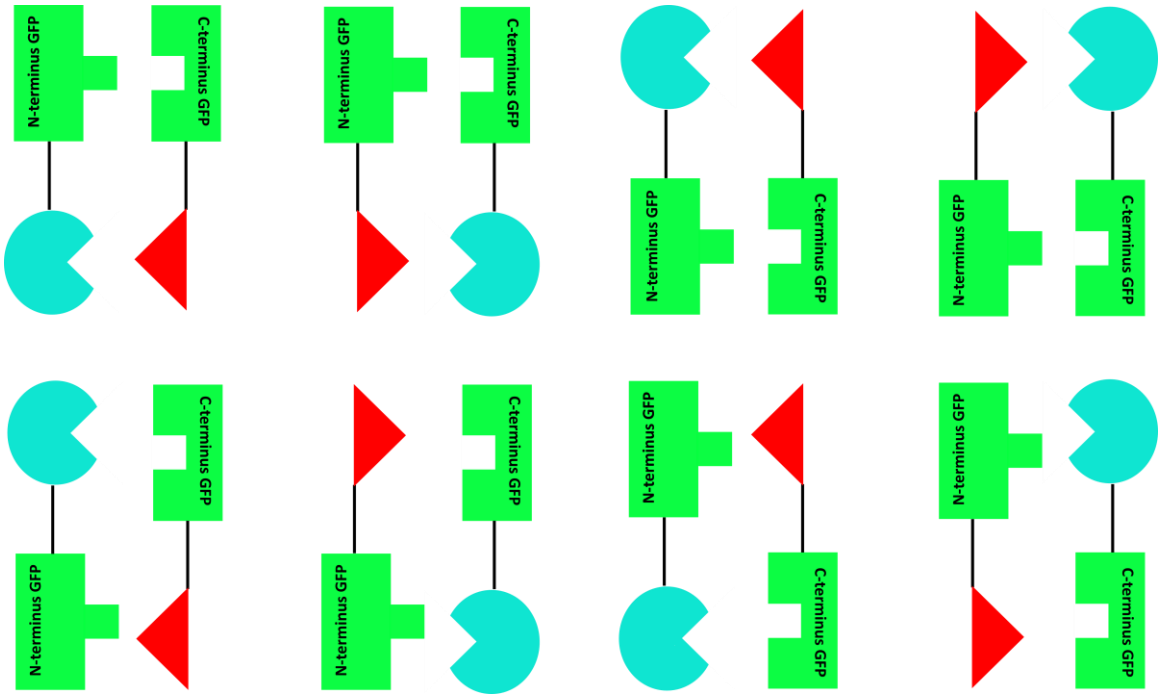

Figure 4-3 Illustration of BiFC combination pairs.
Construction of four different BiFC plasmids allows eight possible combinations to support flexibility required to detect protein-protein interactions (redrawn from Kerppola, 2006a).

As indicated earlier, the BiFC approach permits physical interaction only if the two proteins of interest are localised in close proximity. Therefore the interaction between KMO and HTT does not only provide cellular localisation of the BiFC complex, but it also gives a clue on the localisation of each interactor. Of the two possible interactors analysed in this study, for example, KMO is known to localise solely to the outer mitochondrial membrane (Hirai *et al.*, 2010; Uemura and Hirai, 1998); whereas HTT is predominantly cytoplasmic and membrane-associated (DiFiglia *et al.*, 1995; Sharp *et al.*, 1995), with some evidence of mitochondria localisation (Choo *et al.*, 2004; Gutekunst *et al.*, 1998; Orr *et al.*, 2008; Panov *et al.*, 2002; Rockabrand *et al.*, 2007). Extended confocal co-localisation and electron microscopy studies were used here to reveal the exact subcellular localisation of KMO and HTT by taking advantage of the BiFC system. In addition to investigating the interaction and localisation of the proteins of interest, when studying aggregate-prone proteins, the BiFC technique is a tool for studying aggregation and visualisation of aggregate localisation within the cell, which was exploited here as well.

4.2 Results

4.2.1 Generation of KMO and KIPs BiFC constructs

To validate the interaction of KIPs with KMO in the human HEK293T cell line I used the BiFC assay. In the yeast screen a truncated version of KMO (tKMO) derived from a KMO cDNA was used as the bait, amino acid alignment illustrated in Section (3.2.2). Here, I decided to test the interaction of both full length (flKMO) and tKMO with KIPs. Various possible orientations of BiFC constructs were generated where the C-terminus of CFP (CC) was fused to either the C-terminus or N-terminus of flKMO/tKMO. For the KIPs, the N-terminus of enhanced GFP (GN) was fused to either the C-terminal or N-terminal end of the KIPs, as shown in Figure 4-4.

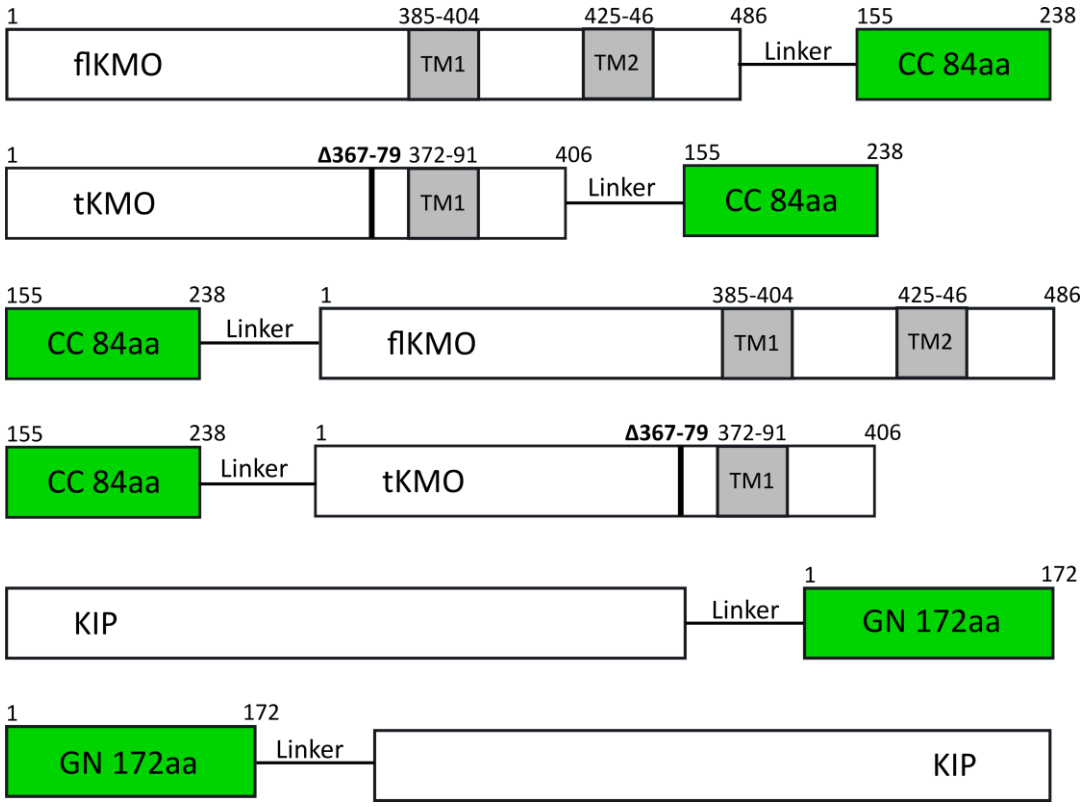

Figure 4-4 Schematic outline of the KMO and KIPs BiFC constructs generated.
flKMO/tKMO were fused C-terminally or N-terminally to the C-terminus of CFP (CC) via $(GGGGS)_2$ linker. KIPs were fused to the N-terminus of enhanced GFP via $(GGGGS)_2$ linker, at either the C-terminal or N-terminal end of the protein. KIP represents GAPDH, DCTN2 or AP2M1.

4.2.2 Exploiting the BiFC system to validate KMO interactions with KIPs in living HEK293T cells

HEK293T cells were transfected with 0.16 μg of each BiFC plasmid as well as 0.08 μg of RFP-encoding plasmid; the BiFC pairs tested for interaction being the following: flKMO-CC/tKMO-CC + KIP-GN or flKMO-CC/tKMO-CC + GN-KIP. As shown in Figure 4-5, none of the tested BiFC combination gave a complementation signal. All flKMO-CC + KIP-GN and tKMO-CC +KIP-GN pairs tested were not significantly different from the negative control (Figure 4-5A and B), as were the pairs flKMO-CC + GN-KIP and tKMO-CC + GN-KIP (Figure 4-5C and D). Surprisingly, when immunoblotting was carried out on 20 μg/sample of the BiFC lysates, none of the KIP-GN nor GN-KIP fusion proteins were detected, while flKMO-CC, tKMO-CC, DJ-1 constructs (used as controls), and RFP (internal control co-transfected in all the wells) were all expressed. All KMO and KIPs proteins were under the control of the same CMV promoter. Therefore, prior further testing with the additional BiFC constructs (CC-flKMO and CC-tKMO with KIP-GN and GN-KIP), expression analysis of the KIPs needed further investigation.

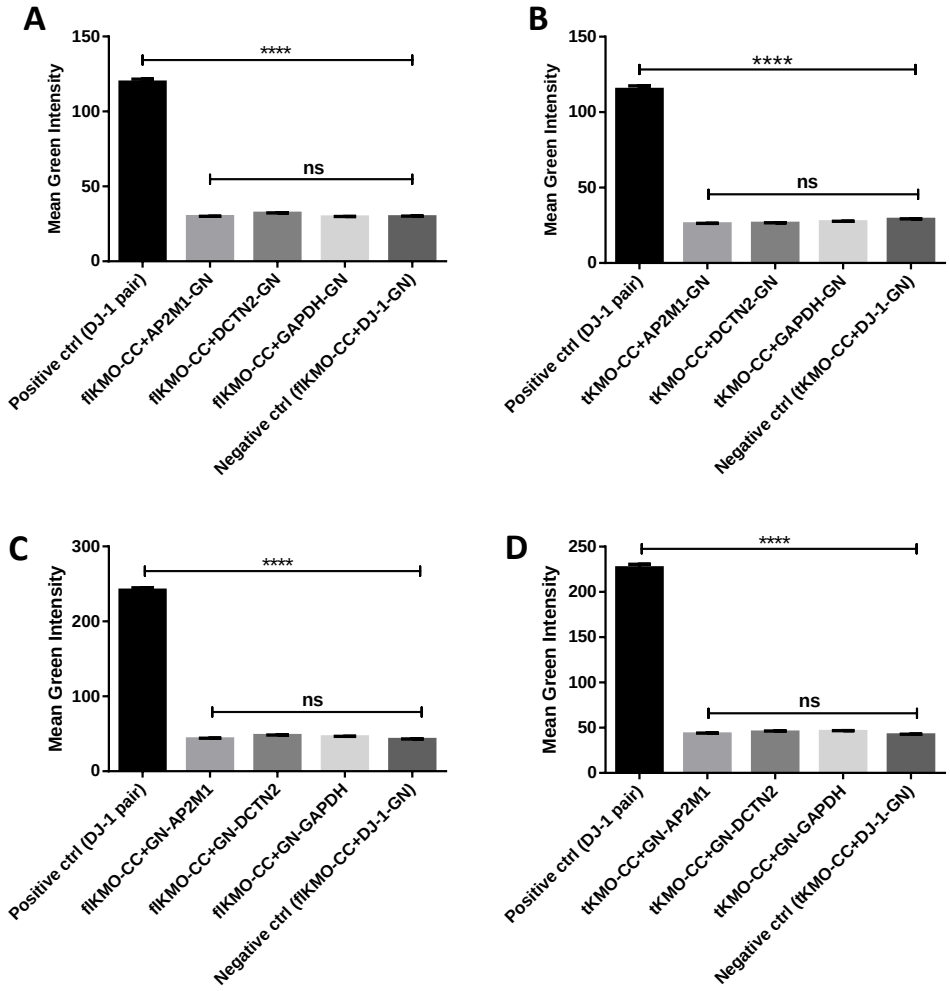

Figure 4-5 Fluorescence complementation of KMO and KIPs in living HEK293T cells. Cells were transfected with 0.16 µg of each BiFC plasmid and 0.08 µg of RFP for 48 hr. A) flKMO-CC and KIP-GN. B) tKMO-CC and KIP-GN. C) flKMO-CC and GN-KIP. D) tKMO-CC and GN-KIP. KIP = AP2M1, DCTN2 or GAPDH. Positive controls were DJ-1 BiFC pair. Negative controls were flKMO-CC/tKMO-CC and DJ-1-GN. ****P < 0.0001 and ns = not significant, using one-way ANOVA, followed by Tukey's multiple comparison test. Data are expressed as mean per well ± SEM. The number of analysed cells ranged from 2000 to 5500 cells per well per condition, in all presented experiments.

4.2.3 Expression of KIPs in HEK293T cells

Routinely, in BiFC experiments 0.16 µg of each plasmid was transfected into HEK293T cells, and which is normally a sufficient amount for abundant protein expression. To check for any effect of KMO co-expression with the KIPs, 0.16 µg of all the KIPs were transfected (without flKMO/tKMO) into HEK293T cells and lysates were obtained 48 hr post transfection. Immunoblotting was performed on the lysates using 20 µg of proteins, and none of the KIPs were detected using an anti-GFP antibody (data not shown). However, when 50 µg of protein extract was loaded bands corresponding to GAPDH-GN (faint signal) and to GN-DCTN2 were visible, as indicated by the red arrows in Figure 4-6A.

As the expression issue seemed to be related to the amount of transfected plasmid, HEK293T cells were transfected again with 0.52 µg of each KIP plasmid, along with 0.08 µg of an RFP encoding plasmid. Transfection efficiency was satisfactory as determined by the fluorescent RFP signal observed in living cells (data not shown). Cells were lysed 48 hr post transfection to perform immunoblot studies. Again, when 20 µg of protein extract was used, nothing was detected with anti-GFP antibody (data not shown). Expression of all KIPs (except AP2M1-GN) was confirmed by using 50 µg of protein (Figure 4-6B), suggesting that expression of the KIPs was very low and requires high amount of plasmids to be transfected. As these blots were probed with an anti-GFP antibody, there might be a GN tag effect on the conformation of the BiFC proteins masking the GN epitope. To rule out this possibility, GAPDH constructs were immunoblotted with GAPDH antibody (the only protein specific antibody available in house): this showed again that GAPDH constructs were expressed at a very low level in comparison to the endogenous GAPDH (Figure 4-6C), thus confirming the low expression level detected was not due to a less efficient recognition by the anti GFP antibody. Thus, BiFC could be repeated with higher plasmid concentration for the KIPs (0.52 µg), which would lead to nearly 0.8 µg of total DNA transfected. This DNA amount would be a strain to the cells, as the highest amount ever used in my experiments on HEK293T cells was 0.6 µg using Effectene transfection reagent. Moreover, the expression of the KIPs may not be enough to detect their interaction with KMO, as normally loading 20 µg of protein extract is sufficient to detect protein expression.

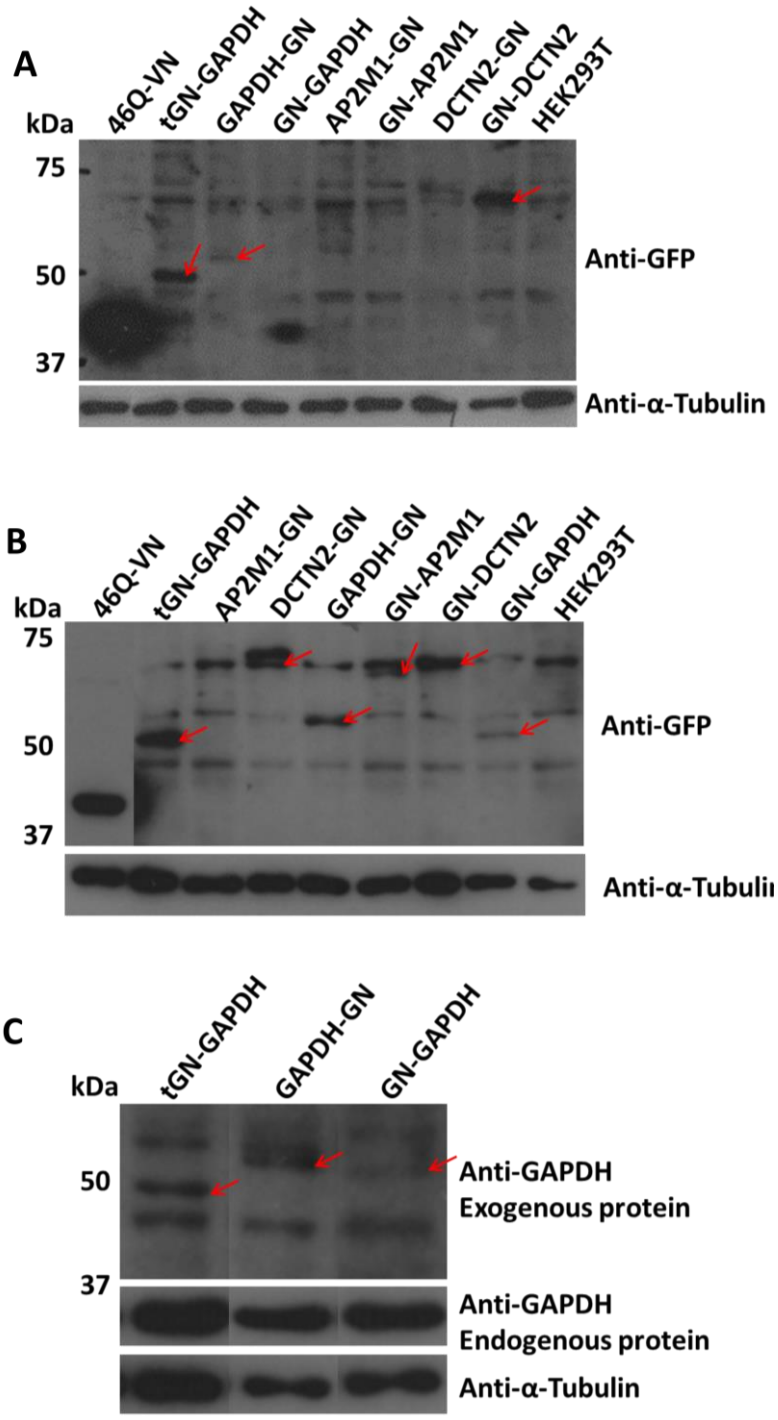

Figure 4-6 Immunodetection of KMO interacting proteins (KIPs) BiFC constructs in HEK293T cells.

A) Cells were transfected with 0.16 µg of plasmids, lysates were blotted and immunolabelled using anti-GFP antibody (ab6556). B) and C) Cells were transfected with 0.52 µg of one of each BiFC plasmid as well as 0.08 of RFP plasmid. In B proteins were immunolabelled with anti-GFP antibody (ab6556), in C with anti-GAPDH (sc-32233). tGN-GAPDH is a control GAPDH BiFC construct that was fused N-terminally to truncated GN. 46Q-VN is a positive control for anti-GFP antibody. Correct sized bands indicated by the red arrows. Anti-α-Tubulin was used as a loading control (sc-8035).

4.2.4 Construction of KMO and HTT BiFC plasmids

To study the interaction between KMO and HTT exon 1 fragments (referred to as HTT, or just XQ, where X = the polyQ length), flKMO or tKMO were fused C-terminally to the C-terminus of CFP, and HTT was fused C-terminally to either halves of Venus (C-terminus or N-terminus) (Figure 4-7A). Expression of flKMO-CC and tKMO-CC was confirmed by transfecting 0.4 µg of each plasmid in HEK293T cells. After 48 hr of transfection, cells were lysed and 20 µg of protein lysates was used for immunoblotting (Figure 4-7B). HTT BiFC constructs were previously validated by (Herrera *et al.*, 2011).

For performing the BiFC assay, HEK293T cells were transfected with the same amount of both BiFC constructs (flKMO and HTT, 0.16 µg), along with a plasmid expressing RFP (0.08 µg) as an internal control for transfection and to allow for normalisation of the BiFC signal.

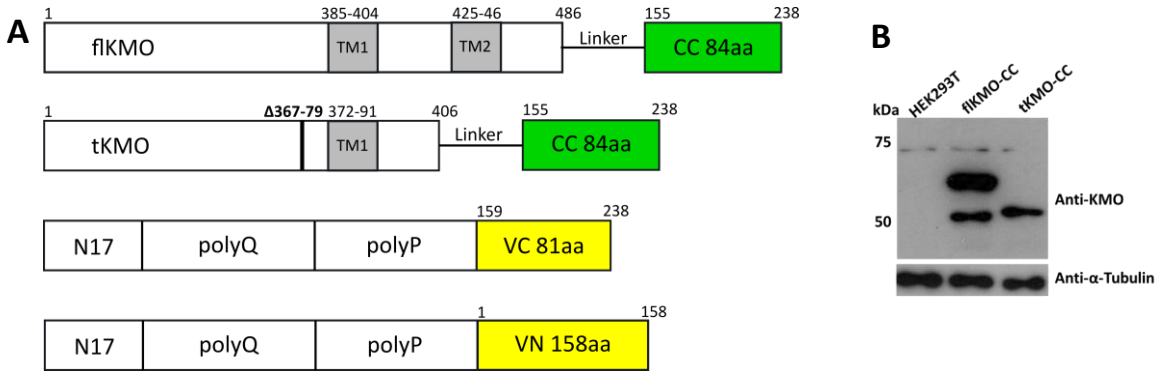

Figure 4-7 KMO and HTT BiFC constructs.
A) Schematic representation of BiFC KMO, tKMO and HTT constructs. flKMO/tKMO were fused to C-terminus of CFP (CC) via a $(GGGGS)_2$ linker. HTT BiFC construct was composed of the N17, polyglutamine (polyQ) and polyproline (polyP) domains fused to either C-terminus or N-terminus halves of Venus (VC or VN). For each of the two BiFC HTT constructs in the illustration three versions were made with different polyQ lengths: 25Q-VC, 19Q-VN; 46Q-VC, 46Q-VN; and 97Q-VC, 97Q-VN. B) Immunoblot of flKMO-CC and tKMO-CC expressed in HEK293T cells using anti-KMO antibody (10698-1-AP), anti-α-Tubulin was used as a loading control (sc-8035).

4.2.5 Optimisation of BiFC experiments

Transfected HEK293T cells should express the two BiFC constructs (KMO and HTT) and present green fluorescence (a combination of CC and VN which emits light at 510 nm, as determined by Olympus confocal microscopy FV1000) if re-formation of a mature fluorophore occurs due to protein-protein interaction. Transfected cells also express RFP, which permits normalization of BiFC fluorescence. In my experiments, the Scan^R screening station was used to take 100 images per well of a 6-well plate, for the green channel, red channel and the bright field image (to have an overview of the cells). Images were analysed using Scan^R analysis software, allowing the study of thousands of transfected cells per well. The selection of transfected cells was based on the RFP signal: the software identifies red cells, quantifies their total RFP intensity and measures the area of each cell by detecting the extent of RFP signal (Figure 4-8). The software also quantifies the total intensity of BiFC (green) signal.

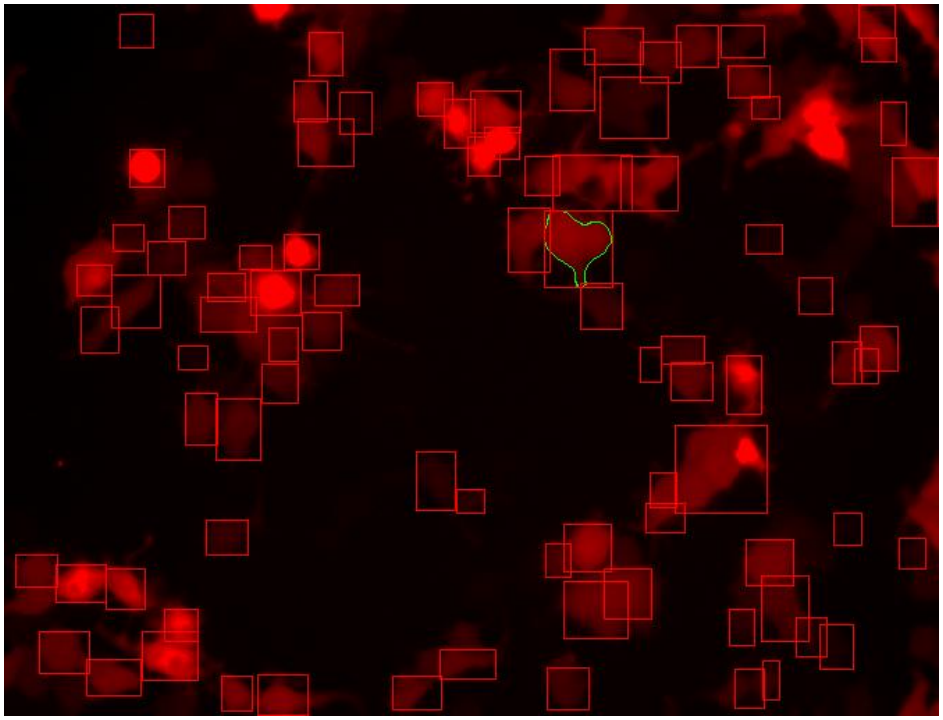

Figure 4-8 RFP filter Scan^R analysis software image.
The software identifies RFP transfected cells (highlighted by the red shapes), and also detects edges of each cell as in the green highlighted cell, allowing measurement of the cell's area.

The BiFC signal was normalised to the RFP signal by dividing the total green intensity by the total RFP intensity, thus obtaining the ratio intensity of the BiFC signal (Figure 4-9), as previously described in our laboratory (Repici *et al.*, 2013). However, as shown in Figure 4-9B, the RFP signal highly fluctuated from one well to another, which therefore prevented correct normalization of the BiFC signal, as the outcome of the ratio intensity greatly differed from the total green intensity per well (Figure 4-9 A and C).

To ensure that the BiFC constructs were not interfering with RFP expression, HEK293T cells were transfected with either RFP only, RFP and flKMO-CC or RFP and HTT-VN (19Q, 46Q or 97Q). When cells were transfected with RFP only, no significant difference in the RFP intensity was observed in different wells (Figure 4-10A). The same results were obtained when cells were transfected with flKMO-CC and RFP (Figure 4-10B). Surprisingly, when cells were transfected with HTT-VN and RFP only, there was a significant difference ($P < 0.0001$) between cells expressing RFP + 46Q-VN and cells expressing RFP + 19Q-VN or RFP + 97Q-VN. No significant difference was observed between cells expressing RFP + 19Q-VN and cells expressing RFP + 97Q-VN (Figure 4-10C). These data suggest that HTT may interfere with RFP expression, as this random fluctuation in the RFP expression was dependent on HTT co-expression. Therefore, it was clear that ratio intensity normalisation could not be employed in the proposed experiments. Instead, I normalised my data on the average cell area per well: total green intensity was divided by the average cell area (calculated based on RFP expression) to give mean green intensity as a quantification of the BiFC signal (Figure 4-11A, B and C). For simplicity, all the BiFC work in this thesis is presented as mean green intensity even if HTT constructs were not used.

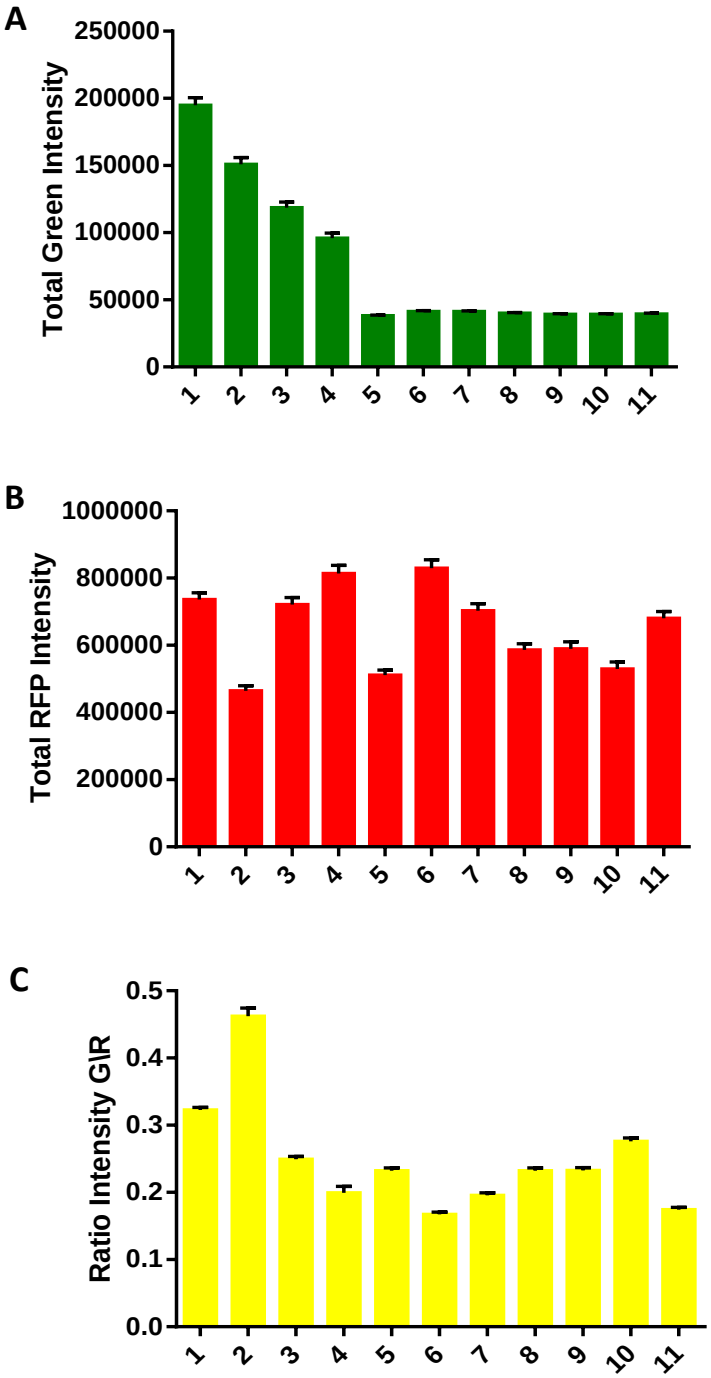

Figure 4-9 Fluorescence quantification using Scan^R in living HEK293T cells 48 hr post transfection.

A) Total BiFC signal intensity in transfected cells (green). B) Total RFP intensity (red). C) Ratio intensity (the total green divided by the total RFP signals). Data are expressed as mean per well ± SEM. The number of analysed cells ranged from 8500 to 11500 cells per well. Numbers on the x-axis correspond to the number of wells.

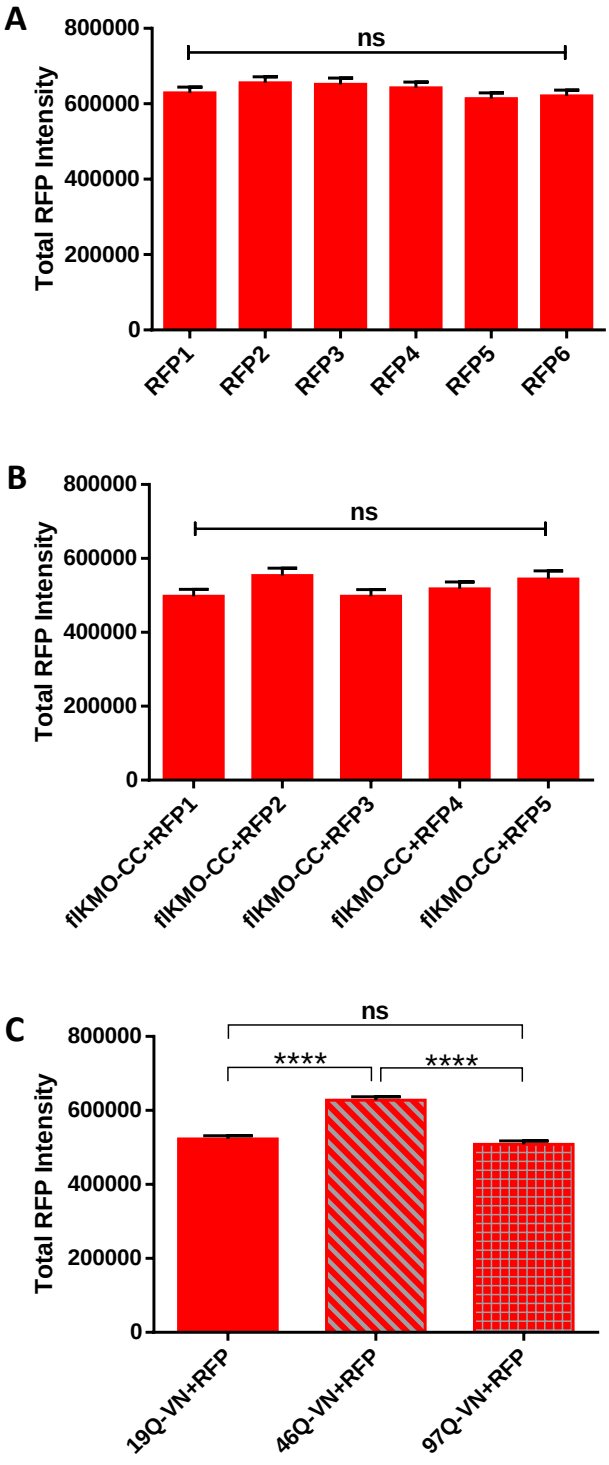

Figure 4-10 Quantification of RFP fluorescence in transfected living HEK293T cells after 48 hr.

Total RFP intensity in cells transfected only with RFP. B) Total RFP intensity in cells transfected with RFP and flKMO-CC. Each bar in A and B represents the signal quantified from a single well. C) Total RFP signal in cells transfected with RFP alongside 19Q-VN, 46Q-VN or 97Q-VN. ****P < 0.0001, for one-way ANOVA, followed by Tukey's multiple comparison tests. ns = not significant. Data are expressed as mean ± SEM. The number of analysed cells ranged from 6500 to 8500 cells per well/bar and from 4000 to 5500 cells per well/bar for A and B respectively. For C, each bar represents an average of the total RFP signal of four independent wells and the cell count ranged from 4500 to 6000 cells per well.

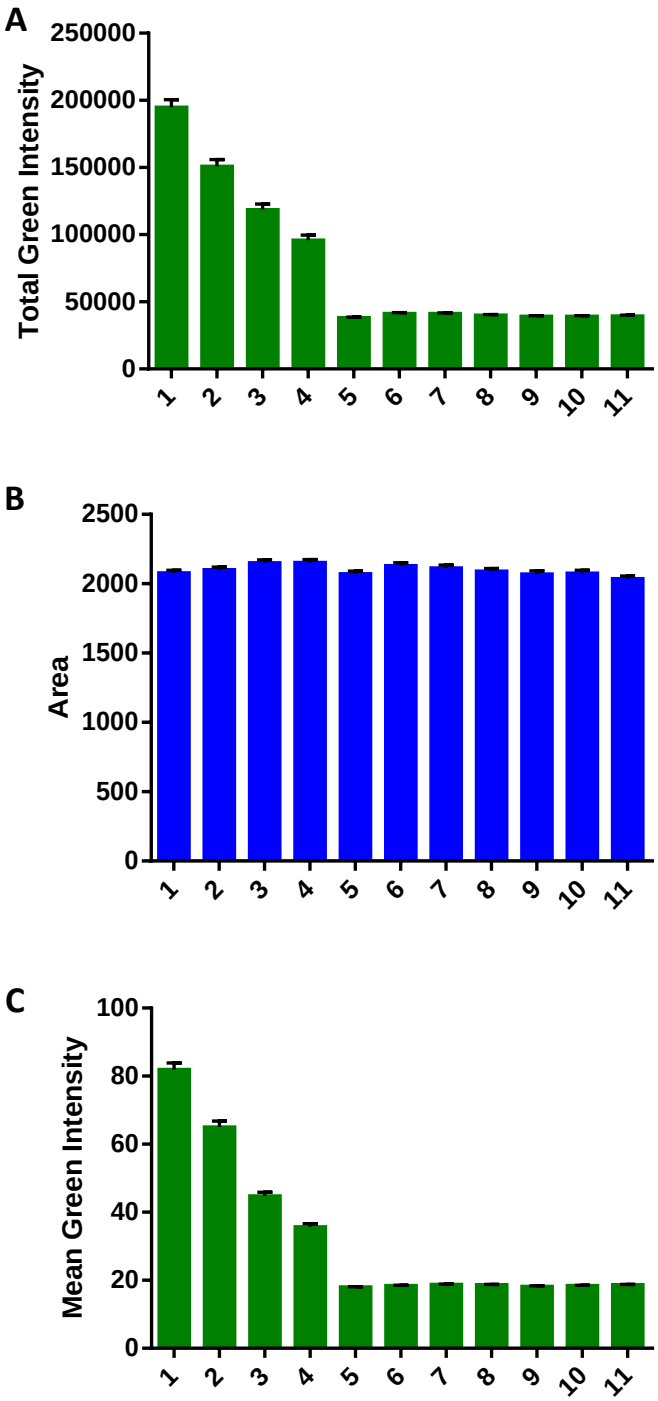

Figure 4-11 Fluorescence complementation of living HEK293T cells 48 hr post transfection.

A) Total BiFC signal intensity. B) Average cell area per well. C) Mean BiFC signal intensity which is obtained by dividing the total green intensity over the cell area. Data are expressed as mean per well ± SEM. The number of analysed cells ranged from 8500 to 11500 cells per well. Numbers on the x-axis correspond to the number of wells.

4.2.6 Influence of HTT-VN BiFC proteins on flKMO-CC and endogenous HTT-FL expression in HEK293T cells

As RFP expression was altered when co-expressed with HTT-VN, it was of interest to investigate flKMO-CC expression in the BiFC context as well, to exclude any HTT effect on KMO. To address this aim, HEK293T cells were transfected with 0.16 µg of each construct (in triplicate for each condition), for 48 hr, as follows: flKMO-CC + empty vector; flKMO-CC + 19Q-VN; flKMO-CC + 46Q-VN; flKMO-CC + 97Q-VN; and untransfected HEK293T cells. 20 µg of proteins were loaded to check for flKMO-CC as well as endogenous full length HTT (full length HTT is referred to as HTT-FL) expression in transfected and untransfected HEK293T cells. Protein expression level was determined by densitometry and normalized versus endogenous α-Tubulin as a loading control; analyses were carried out using ImageJ (Figure 4-12A, B, D and E). As all results presented in Figure 4-12 were obtained using the same lysates, HTT-VN expression was also verified by immunoblotting using anti-GFP antibody, confirming expression of 19Q-VN, 46Q-VN and 97Q-VN as well as flKMO-CC (Figure 4-12C).

The flKMO-CC expression was confirmed from three distinct experiments and several blots for each. Figure 4-12A illustrates flKMO-CC differential expression when co-transfected with empty vector or one of the HTT-VN constructs. The blot was dual labelled with anti-KMO and anti-α-Tubulin antibodies. These data clearly show a reduction in flKMO-CC when co-transfected with the intermediate mHTT (46Q-VN) (Figure 4-12A). Densitometry analysis shows that flKMO-CC expression when co-transfected with either of the mHTT constructs is significantly different from flKMO-CC co-expressed with empty vector ($P < 0.001$). Indeed, the WT HTT (19Q-VN) causes a slight reduction in flKMO-CC in comparison to flKMO-CC expressed along with empty vector ($P < 0.05$), while 46Q-VN led to a significant reduction in flKMO-CC expression, and 97Q-VN resulted in a tremendous increase in flKMO-CC expression which was rather unexpected as they are both forms of mHTT (Figure 4-12B).

Futter *et al.* (2009) previously reported that in HEK293T cells transfected with exon 1 fragments of HTT, endogenous HTT-FL is greatly reduced. For this reason, HTT-FL expression was verified in the BiFC experiment context. Untransfected HEK293T cells were used as a positive control, and our results indicate that both flKMO-CC co-

transfected with empty vector or 97Q-VN did not affect endogenous HTT-FL ($P > 0.05$), whereas 19Q-VN and flKMO-CC co-expression led to a slight increase in endogenous HTT-FL level ($P < 0.05$) (Figure 4-12D and E). Quantification of α-Tubulin showed a small reduction in its expression in transfected cells compared to untransfected. Therefore, GAPDH was also used as a second loading control to confirm if what observed was related to only Tubulin or also other endogenous proteins. GAPDH quantification showed less difference between conditions, but was more variable in between replicates (data not shown). Thus, α-Tubulin was used in normalisation as it was less variant in between replicates (Figure 4-12D). In addition, due to technical limitations flKMO-CC +46Q-VN lysate was not loaded on the blot (Figure 4-12D). However, its effect was tested in a different blot along with 19Q-VN and 97Q-VN in HEK293T cells and the outcome was similar to the effect of 97Q-VN (data not shown). Effect of HTT-VN constructs on HTT-FL in the absence of flKMO-CC expression was not of interest and was not examined here.

In total, flKMO-CC expression is majorly affected when co-expressed with HTT-VN mutant exon-1 fragments. This variation is needed to be taken into account when interpreting flKMO-CC-HTT-VN interactions. Expression of HTT fragments however did not greatly influence the levels of endogenous HTT-FL and rather might have a slight effect on tubulin expression. This ensures that the endogenous HTT-FL expression is comparable in between conditions.

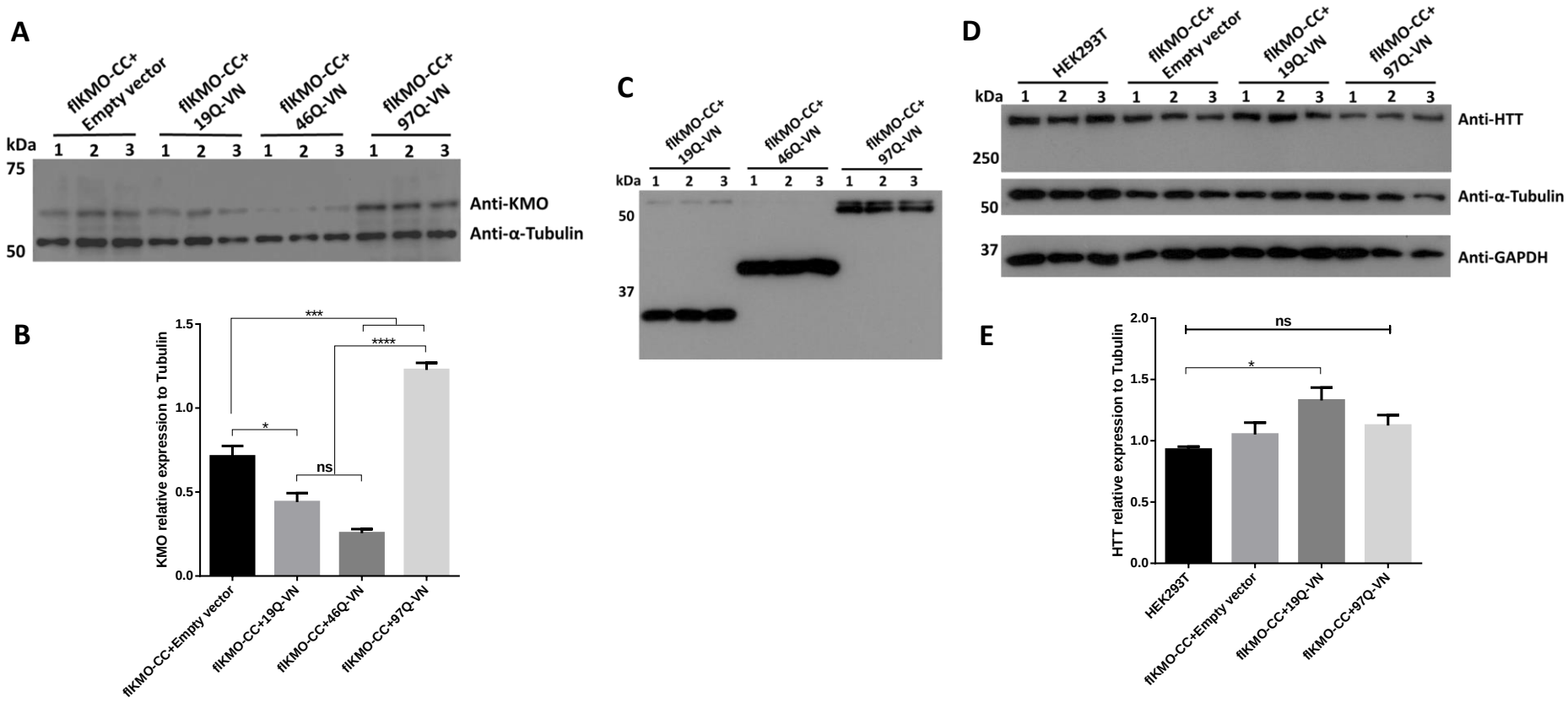

Figure 4-12 Effect of HTT-VN expression on flKMO-CC and endogenous HTT-FL expression in HEK293T cells.
HEK293T cells were either untransfected or co-transfected with 0.16 µg of flKMO-CC as well as 0.16 µg of an empty vector or one of the HTT-VN constructs. A) Dual labelled immunoblot of flKMO-CC using anti-KMO antibody (10698-1-AP) and anti-α-Tubulin antibody (sc-8035) as loading control. B) Quantification of immunoblot shown in A. C) Confirmation of HTT-VN expression within this same experiment using anti-GFP ((ab6556). D) Immunoblot of endogenous HTT-FL in untransfected and transfected HEK293T cells using anti-HTT (4C8) antibody (MAB2166) and anti-α-Tubulin antibody (sc-8035), as loading control, as well as anti-GAPDH (sc-32233) to validate endogenous GAPDH expression. E) Quantification of immunoblot in D. B) and E) ****$P <$ 0.0001, *** $P < 0.001$, * $P < 0.05$ and ns = not significant, for one-way ANOVA, followed by Tukey's multiple comparison test. Data are expressed as mean ± SEM, where n = 3.

4.2.7 KMO interacts with HTT in a polyQ dependent manner in living HEK293T cells

To study HTT-KMO interaction by BiFC, flKMO-CC, HTT-VN and RFP constructs were co-transfected into HEK293T cells seeded in a 6-well plate. 48 hr post transfection, 100 images were taken per well using an Olympus Scan^R screening station, and cells expressing the transfection control (red) were selected for analysis using Scan^R analysis software. The mean intensity of the green signal was calculated after background correction. Figure 4-13A shows the average of mean green intensity of three independent experiments. The average of fluorescence complementation of the KMO-HTT BiFC signal revealed that KMO and HTT specifically interact in living cells and this interaction steadily decreased as the polyQ length increased. There was ~50% reduction in the interaction of flKMO-97Q complex in comparison to flKMO-19Q. Although the interaction decreased significantly with the increase in the polyQ length, flKMO-CC interaction with 97Q-VN is still stronger than the background (flKMO-CC and VN-backbone). The positive control used in this experiment was a well characterised BiFC protein pair unrelated to this work (DJ-1 pair; (Repici *et al.*, 2013)), used just, to ensure the assay is working properly (Figure 4-13A).

The distribution of the mean BiFC green intensity for individual cells per well as well as proteins expression for one of the biological replicates is shown in Figure 4-13B and C. The distribution data demonstrate that the majority of the cell population lies within the group with less mean green intensity as the polyQ length increased, approaching the background level of intensity (Figure 4-13B). After live imaging, cells were lysed and immunoblotting was performed on all lysates to study protein expression of the BiFC constructs. As shown in Figure 4-13C, the positive control BiFC pair were highly expressed. flKMO-CC was expressed in all conditions, and notably its expression was higher when co-transfected with 97Q-VN, confirming the previous observations (Section 4.2.6). Moreover, it illustrates that although more flKMO-CC is available, it interacts the least with 97Q-VN. 19Q-VN and 46Q-VN were similarly expressed, but 97Q-VN band was clearly less intense (Figure 4-13C). This could be due to the majority of 97Q-VN being present in protein aggregates when expressed in cells, and thus being reduced in the soluble protein fractions tested in the immunoblotting experiment. To test this, a filter trap assay was performed, which permits analyses of

insoluble, aggregated proteins. Cells were transfected with 19Q-VN, 46Q-VN or 97Q-VN alone with the same amount of plasmid used in the actual BiFC experiment (0.16 µg). 48 hr post transfection cells were lysed and proteins were blotted on cellulose acetate paper. As illustrated in Figure 4-13D, the blot shows that no aggregates were formed when WT HTT was expressed (19Q-VN). Few aggregates were spotted in the lysate expressing 46Q-VN. However, 97Q-VN dots were fully saturated with aggregates (Figure 4-13D), confirming aggregation of 97Q-VN is likely causing less soluble protein to be detected. Thus, the presence of increased aggregation of 97Q-VN might hinder its interaction with flKMO-CC (Figure 4-13C).

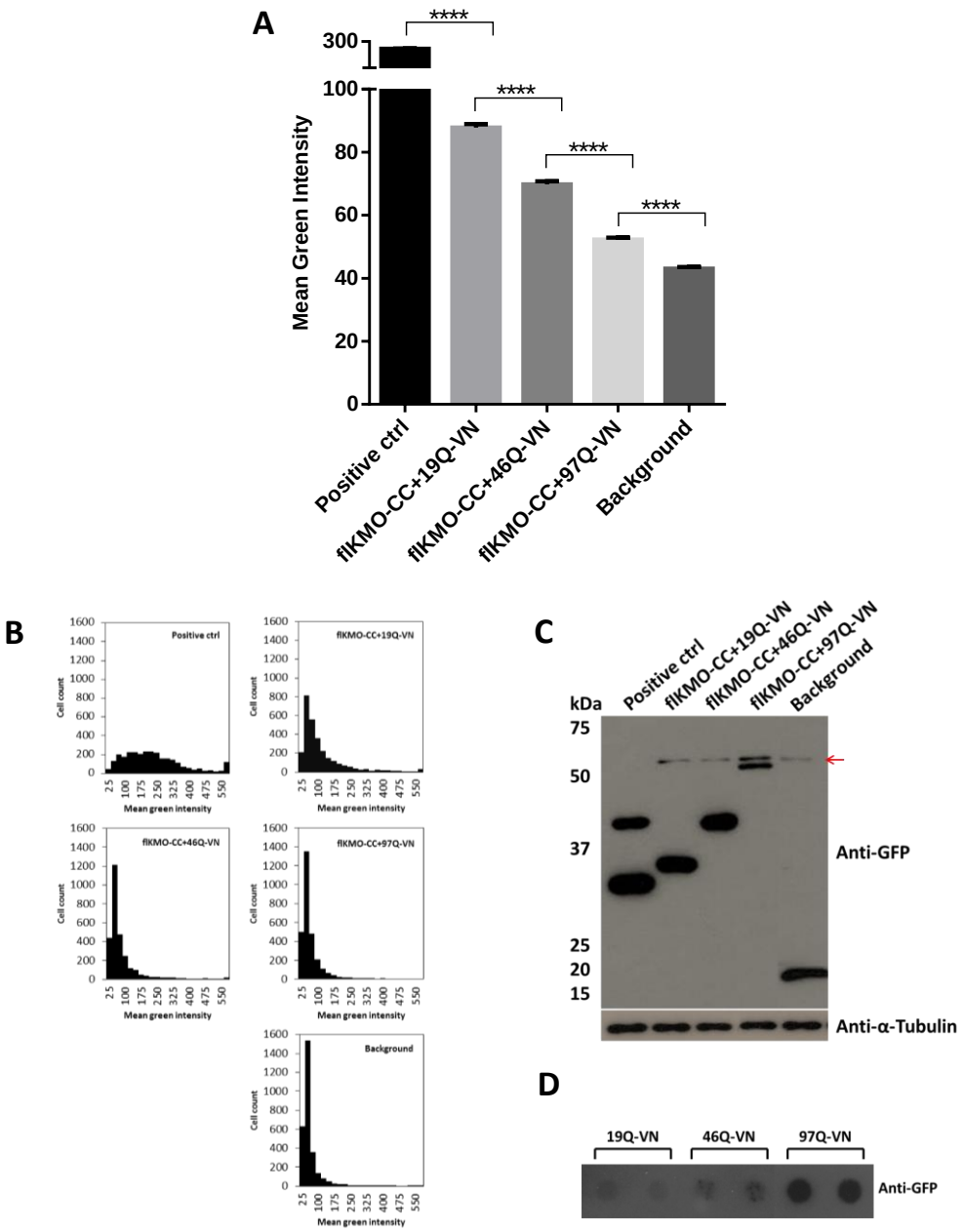

Figure 4-13 Interaction of flKMO-CC and HTT-VN in living HEK293T cells.
Cells were transfected with 0.16 µg of each plasmid and 0.08 µg of RFP, for 48 hr. Fluorescence intensities were analysed using Scan^R analysis software. A) Mean green intensity of the fluorescence complementation signal of three independent experiments shows a clear interaction between flKMO-CC and HTT-VN. The histogram shows a significant reduction in the fluorescence complementation as the polyQ length increased, which is significant different from the background. ****$P < 0.0001$, for one-way ANOVA, followed by Tukey's multiple comparison tests. Data are expressed as mean ± SEM. The number of analysed cells ranged from 15000 to 18500 cells per condition. A representative experiment is illustrated in B and C. B) Distribution of the mean BiFC green fluorescence intensity for each condition. The distribution is shifted to the left as a result of the reduction in the green signals. C) Immunoblot of the lysates from the same BiFC experiments show the expression levels of flKMO-CC (indicated by the red arrow) and the soluble fraction of HTT-VN proteins, using anti-GFP antibody (ab6556). Anti-α-Tubulin antibody (sc-8035) was used as loading control. D) Filter trap of cells lysates expressing only HTT-VN to reveal the polyQ dependent protein aggregation, using anti-GFP antibody (ab6556; 1:10,000); each lysate was blotted in duplicate.

4.2.8 Validation of the KMO-HTT interaction using Hoechst stained nuclei for normalisation

To validate the identified KMO-HTT interaction, RFP expressing plasmid was excluded to eliminate the possibility that RFP expression fluctuation between wells may affect the BiFC outcome, and also to prove that the BiFC signal intensity (and hence the interaction) is polyQ dependent regardless of the method used for normalisation. Cells were co-transfected with flKMO-CC and HTT-VN plasmids in a 6-well plate. 48 hr post transfection, nuclei were stained with Hoechst prior to live cell imaging. 100 images were taken per well using an Olympus Scan^R screening station. In this case, analysis was based on the software identification of stained nuclei and 30 surrounding pixels as cytoplasm of transfected and untransfected cells. Furthermore, the total green intensity (of green cells) was calculated after background correction (Figure 4-14) and normalised to the estimated cells' area, to give the average mean green intensity per well, as shown in Figure 4-15A. In general, the difference in the mean green intensity amongst the different polyQ lengths was not as profound as shown previously in (Section 4.2.7), perhaps because the signal was normalised on a larger population of cells compared to the area of transfected cells only used in the previous experiments. Nonetheless, 19Q-VN was significantly different from 46Q-VN ($P < 0.01$) and 97Q-VN as well as the background ($P < 0.0001$). There is a slight reduction in the fluorescence complementation seen in 97Q-VN in comparison to 46Q-VN ($P < 0.05$). Nevertheless, both 46Q-VN and 97Q-VN were significantly increased from the background signal, where $P < 0.001$ (Figure 4-15A). Lysates from the same BiFC experiment were immunoblotted to confirm protein expression levels (Figure 4-15B). In total, these data confirmed my observations in Section (4.2.7).

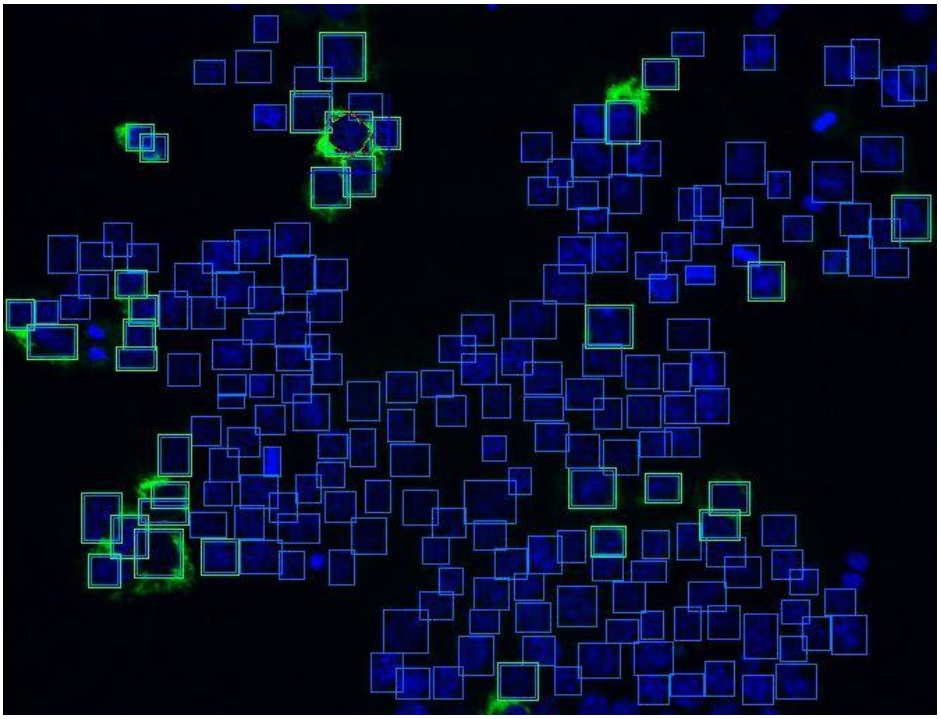

Figure 4-14 Scan^R analysis software overlay image.
Hoechst stained nuclei (highlighted by the blue shapes) were used for estimating area of cells. Cells expressing BiFC constructs (highlighted by the green shapes) were used for total green intensity calculations.

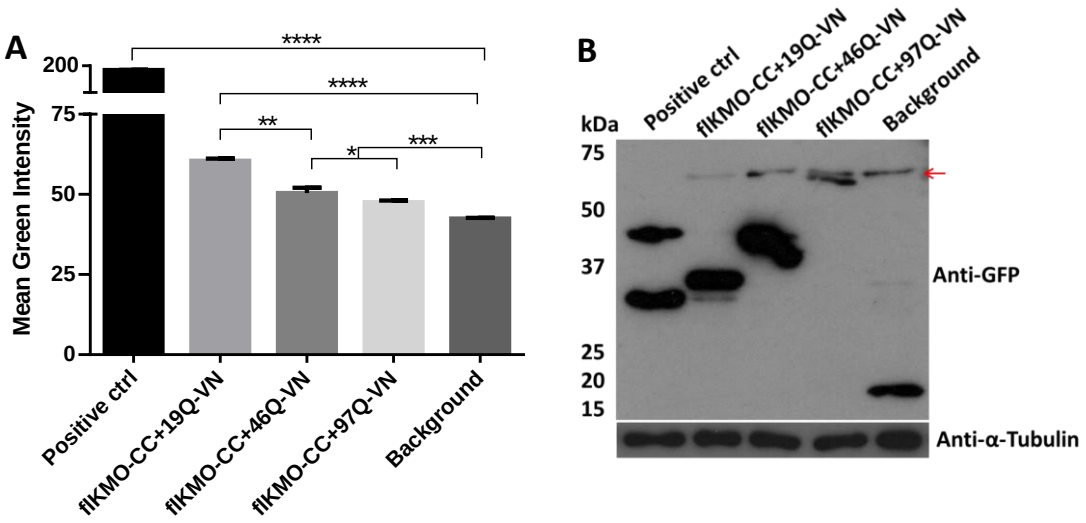

Figure 4-15 Interaction of flKMO-CC and HTT-VN in living HEK293T cells using Hoechst stained nuclei for normalisation.

Cells were transfected with 0.16 µg of each plasmid for 48 hr and live cells were stained with 10 µM of Hoechst 33342 prior imaging. Fluorescence intensities were analysed using Scan^R analysis software. A) Fluorescence complementation of mean green intensity of different polyQ lengths shows a decrease in the interaction as the polyQ length increased. ****$P < 0.0001$, ***$P < 0.001$, **$P < 0.01$ and *$P < 0.05$ for one-way ANOVA, followed by Tukey's multiple comparison tests. Data are expressed as mean per well ± SEM. The number of analysed cells ranged from 8500 to 12000 cells per well per condition. B) Immunoblot of the same BiFC experiment showing the expression levels of KMO-CC and the soluble fraction of HTT proteins, using anti-GFP antibody (ab6556). Anti-α-Tubulin antibody (sc-8035) was used as a loading control.

4.2.9 Biochemical validation of KMO-HTT interactions by immunoprecipitation (IP)

In order to make a robust conclusion on KMO-HTT interaction, I next used a biochemical approach (the GFP-Trap system) to further validate my findings from the BiFC experiments in living cells. This assay employs agarose beads coupled to alpaca anti-GFP antibody to pull down GFP-fused proteins from cellular extracts. GFP-Trap beads bind only to the full length GFP and they are minimally efficient at binding to only one half of the fluorescent protein. This allows the validation of the BiFC flKMO-HTT interaction results, as proteins will only be detected if the reconstitution of CC and VN halves has occurred.

HEK293T cells were grown in 10 cm Petri dishes and transfected with pairs of BiFC constructs (flKMO-CC and HTT-VN or VN). 48 hr after transfection, cells were lysed and IP was performed using GFP-Trap beads. The IP fraction was then immunoblotted using anti-GFP antibody (Figure 4-16A). In comparison to 19Q-VN, less 46Q-VN was pulled down and the 46Q-VN signal was more intense than the non-specific pulldown of the negative control VN-backbone, though it was not possible to draw a conclusion on 97Q-VN as the protein size is very close to flKMO-CC and the two bands overlapped on this blot (Figure 4-16A). In addition to the anti-GFP antibody, I employed protein specific antibodies. The IP fraction was first probed with anti-HTT (mEM48) antibody to confirm the pull-down of HTT. There is a clear polyQ length dependent decrease in HTT-VN levels, with 19Q-VN being the greatest and 97Q-VN the lowest signal (Figure 4-16B). This strongly indicates that the flKMO-CC interacts with HTT-VN in a polyQ dependent manner and these results strongly confirm my findings using the BiFC assay in living cells. The blot was finally immunolabelled with anti-KMO to reveal flKMO-CC pull-down per condition, and flKMO-CC protein levels were satisfactory, with obvious decrease in flKMO-CC expression when co-transfected with 46Q-VN, which support the findings in Section 4.2.6) (Figure 4-16C). Input (IN) and flow-through (FT) or unbound proteins were also immunoblotted, to confirm protein expression, using anti-GFP antibody (Figure 4-16D).

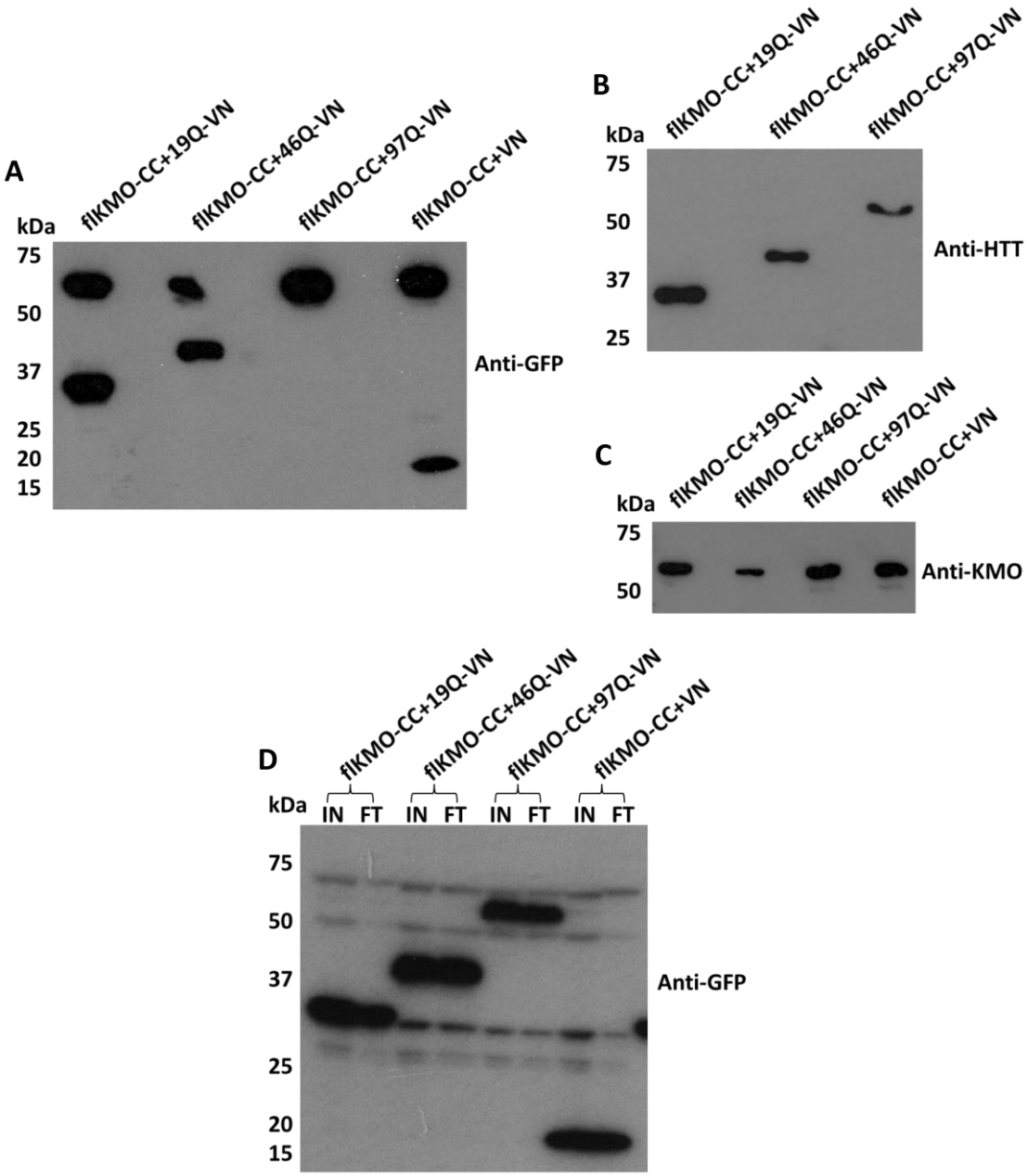

Figure 4-16 Immunoblots of BiFC constructs after GFP-Trap IP. Cells were transfected with 1 µg of each BiFC construct and lysed 48 hr transfection.
Immunoprecipitated BiFC pairs were detected using: A) anti-GFP antibody (ab6556). B) anti-HTT (mEM48) antibody (MAB5374). C) anti-KMO antibody (10698-1-AP). D) Input (IN) and flow-through proteins were probed with anti-GFP antibody (ab6556).

4.2.10 Effect of the KMO C-terminus on KMO-HTT interactions

It was demonstrated in Section (3.2.4.1) that the C-terminal deletion in the tKMO construct (tKMO resembles KMO splice isoform 2 with C-terminal truncation that results in deletion of the second TM) affects KMO mitochondrial localisation. In addition, there are two other studies that confirm these findings (Hirai *et al.*, 2010; Wilson *et al.*, 2014) with some evidence of compromised KMO activity when the KMO C-terminus is deleted (Hirai *et al.*, 2010). Thus, it is important to consider the effect of KMO C-terminus – and thereby KMO localization – on the interaction with HTT using the BiFC assay. HEK293T cells were transfected with 0.16 µg of each BiFC construct along with 0.08 µg of RFP, and after 48 hr of transfection cells were imaged and analysis was carried out as described in Section (4.2.7). As shown in Figure 4-17A, none of the HTT-VN proteins interacted with tKMO-CC and were not significantly different ($P > 0.05$) from the background (tKMO-CC + VN-backbone) (Figure 4-17A). This suggests that the KMO C-terminus is not only crucial for enzymatic activity and mitochondrial localisation, but also mediates interactions with HTT. Immunoblotting was performed on the BiFC experiment lysates using anti-GFP which probed positive control, 19Q-VN, 46Q-VN, 97Q-VN and negative control, whereas tKMO-CC was hardly visible when using anti-GFP (Figure 4-17B). However when anti-KMO was used, tKMO-CC bands were seen (Figure 4-17C).

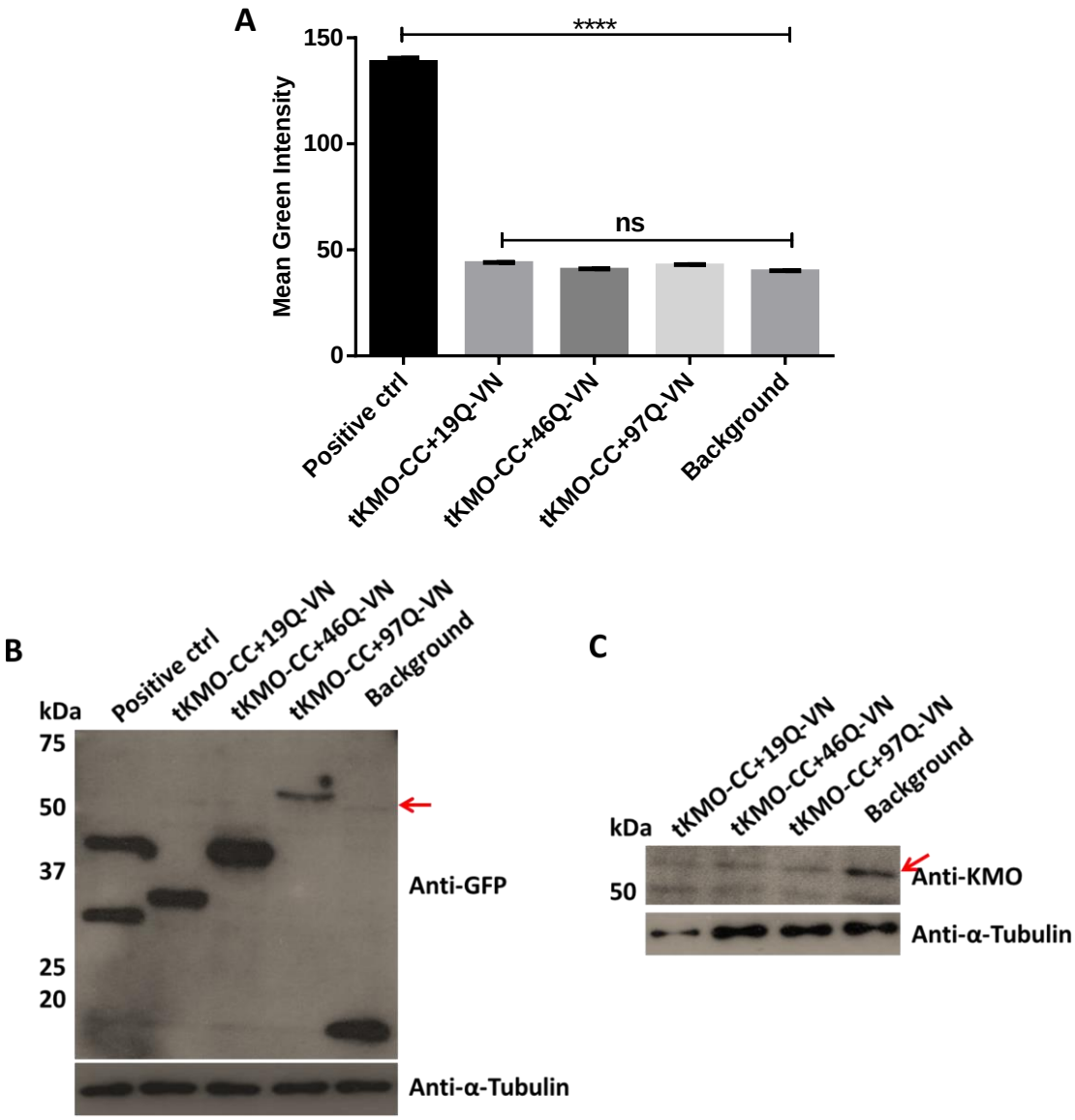

Figure 4-17 tKMO-CC and HTT interaction in living HEK293T cells 48 hr post transfection.

Cells were transfected with 0.16 µg of each plasmid as well as 0.08 µg of RFP. A) Mean green intensity of different polyQ lengths HTT-VN co-transfected with tKMO-CC: no interaction was seen in any of the conditions. ****$P < 0.0001$ and ns = not significant, for one-way ANOVA, followed by Tukey's multiple comparison tests. Data are expressed as mean per well ± SEM. The number of analysed cells ranged from 2500 to 4000 cells per well per condition. B) Immunoblot of the same BiFC experiment: while expression of the soluble HTT-VN is clearly visible tKMO-CC bands were very faint using anti-GFP (ab6556). C) tKMO-CC immunoblot using anti-KMO antibody (10698-1-AP). The bands of tKMO-CC are indicated by the red arrows. Anti-α-Tubulin was used as loading control (sc-8035).

4.2.11 Conformational state of HTT that interacts with KMO

HTT is known to aggregate when it has an expanded polyQ tract, therefore it is important to address whether KMO interacts with HTT aggregates or with soluble HTT. To this aim I first examined HTT independently of KMO using 19Q-VN and 25Q-VC constructs to study WT HTT, and the 97Q pair to study mHTT aggregates by BiFC. These constructs were transfected in HEK293T cells along with a RFP expressing plasmid, and live and fixed cells were examined by confocal microscopy (Figure 4-18A and B). A clear BiFC signal, mainly cytoplasmic, was observed when cells were transfected with WT HTT due to the ability of HTT monomer to interact with one another (Figure 4-18A), the WT HTT BiFC signal localisation is further characterised in Section (4.2.15). mHTT, on the other hand, was capable of forming cytoplasmic signal as well as clear bright inclusions (Figure 4-18B). There was no major difference in the fluorescence signal in living and fixed cells, apart from the fact that it was easier to visualize HTT inclusions in fixed cells (Figure 4-18A and B).

In order to answer the question in what form (soluble or insoluble) HTT interacts with KMO, cells were transfected with the HTT construct with the longest polyQ (97Q-VN), highly prone to aggregate in mammalian cells, as well as flKMO-CC and RFP plasmid. Live and fixed cells were observed by confocal microscopy to examine BiFC signal as well as HTT aggregates. Interestingly, interaction between flKMO-CC and 97Q-VN led to a mitochondrial like signal and no inclusions were seen, unlike with 97Q BiFC alone (Figure 4-18C), indicating that flKMO-CC interacts with the soluble HTT-VN, and is not sequestered into HTT aggregates. These data suggest that a soluble population of 97Q-VN is present which is available to interact with KMO localised to the mitochondria, and highlights an important relationship between localisation of HTT and its interaction with KMO.

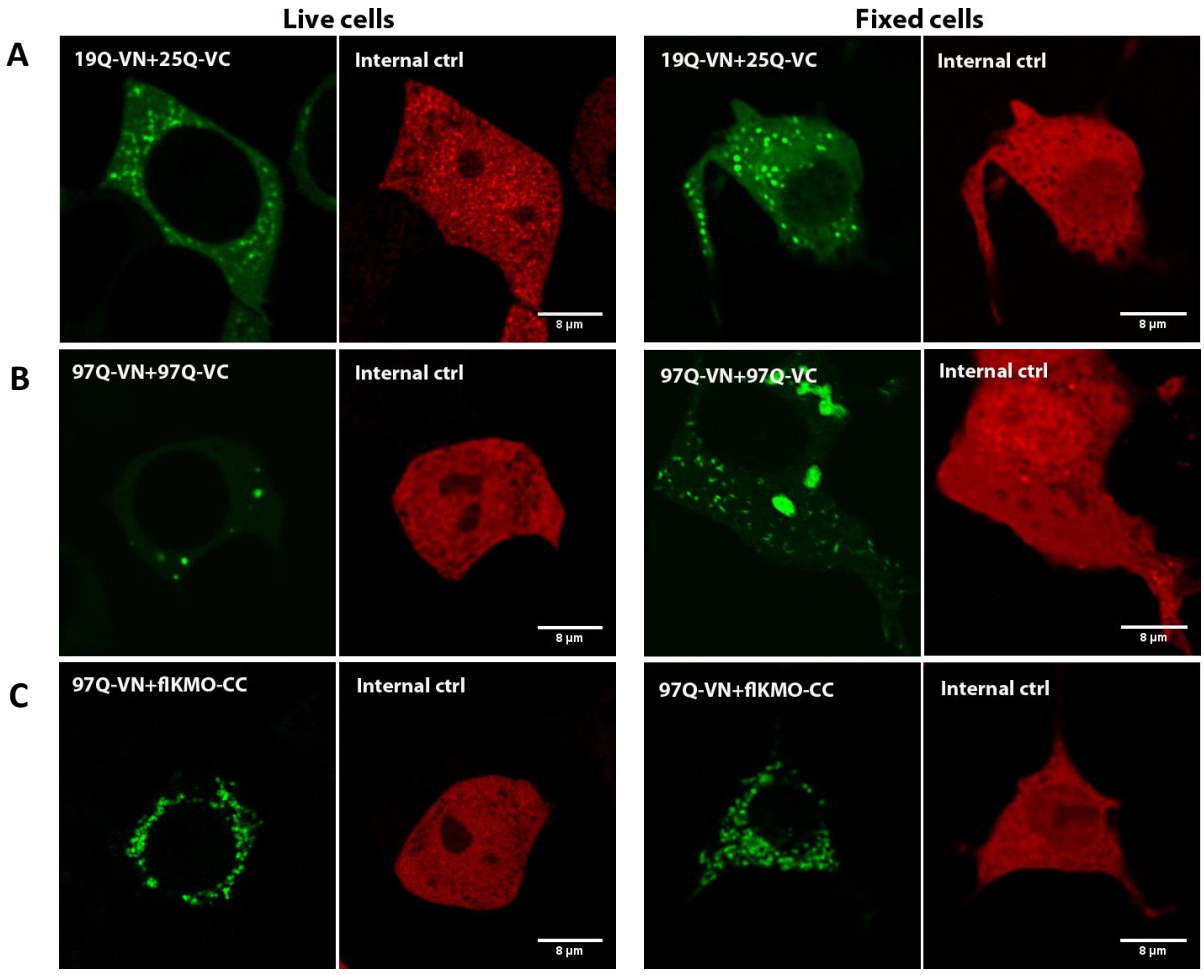

Figure 4-18 Visualising HTT aggregates using the BiFC system.
Confocal images of live (left panels) and fixed (right panels) HEK293T cells expressing BiFC constructs and RFP containing plasmid as internal control 48 hr after transfection (BiFC signal = left image, and internal control RFP signal = right image) in each panel. A) Cells were transfected with 19Q-VN, 25Q-VC and RFP, the BiFC signal is cytosolic. B) Cells were transfected with 97Q pair and RFP, the BiFC signal seen is generally cytosolic with presence of HTT inclusions. C) Cells were transfected with flKMO-CC, 97Q-VN and RFP; the BiFC signal is mainly mitochondrial as suggested by the dotted appearance of the signal. Scale bar = 8 µm.

4.2.12 Implication of mHTT aggregation on its interaction with KMO

It was demonstrated in Section (4.2.7), that the lowest levels of HTT-VN interaction with flKMO-CC were seen when cells were co-transfected with 97Q-VN, likely because the amount of soluble 97Q-VN is far less than 46Q-VN and most of it is present in aggregated form. Therefore, I was interested in addressing whether the HTT-KMO interaction is modulated/ inhibited by the expansion of the polyQ region. To address this, a protein aggregation inhibitor that was available in house was tested (Congo Red, CR), which was previously used to inhibit HTT aggregation in transiently transfected cells (Heiser *et al.*, 2000). I first tested this chemical on the 97Q BiFC pair to determine the optimal concentration, and then CR treatment was applied to KMO-97Q transfected cells.

4.2.12.1 Effect of CR treatment on HTT BiFC

The 97Q pair were studied first to determine the effect of CR treatment on aggregate formation (oligomerization of BiFC pairs) as well as the amount of soluble proteins. HEK293T cells were transfected with 0.1 µg of each 97Q BiFC construct (97Q-VN and 97Q-VC), for a total of 0.2 µg of 97Q. CR treatment was introduced at the time of transfection, and a range of concentrations was used: 50, 25, 12.5, 6.25, 1.6 and 0 µM, the latter serving as control (untreated cells). BiFC signal was observed 24 hr and 48 hr post transfection on treated and untreated HEK293T cells transfected with the BiFC 97Q pair. After 48 hr, microscopic observations of the 97Q pair BiFC signal showed diminishing of BiFC signal on treated cells that correlates with the increase in CR concentration. Cells expressing the 97Q pair and treated with higher doses of CR (50 or 25 µM) completely abolished BiFC signal. However, 12.5 µM of CR treatment resulted in only a few 97Q pair green cells; and more widely presence of BiFC signal when lower CR concentrations were used (data not shown).

Post observations, cells were lysed and filter trap and SDS-PAGE experiments were performed on 1.5 µg/ µl of proteins, followed by probing with anti-GFP. As shown in the filter trap blot Figure 4-19A, CR treatment successfully inhibited aggregation in a dose-dependent manner. No aggregates were detected when high concentrations (25 or 50 µM) of CR were employed, and only low levels of aggregation was seen on cells treated with 12.5 µM. In agreement with these data, cells treated with 1.6 or 6.25 µM and untreated cells showed high levels of aggregation (Figure 4-19A). By SDS-PAGE,

both soluble and insoluble (representing aggregates) 97Q were able to be detected using anti-GFP antibody (Figure 4-19B). Soluble 97Q-VN bands of similar intensity were visible in all the lanes at ~ 60 kDa, and although 97Q-VC was not probed on this blot the presence of BiFC signal confirms its expression (many data from our laboratory suggest that –VC tagged proteins are not well recognised by anti-GFP antibody). In addition, the insoluble fraction of 97Q-VN was present at the top of the stacking gel, and predominantly detected in untreated cells, and with the lower concentrations of CR used (1.6 and 6.25 µM), validating the filter blot results (Figure 4-19B).

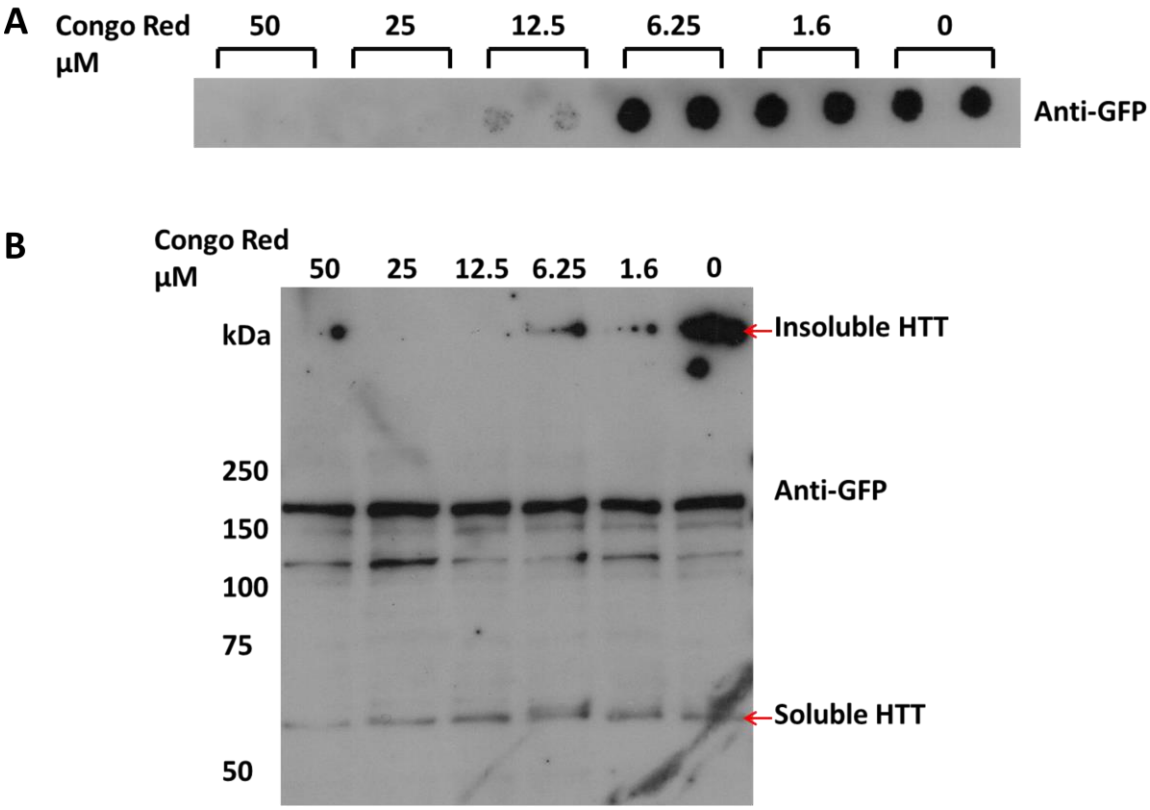

Figure 4-19 Congo Red (CR) treatment of HEK293T cells transfected with 97Q BiFC pair. Cells were transfected with 0.1 µg of each 97Q construct, and treated with serial dilutions of CR (50, 25, 12.5, 6.25, 1.6 and 0 µM) for 48 hr at the time of transfection. A) Filter trap blot shows levels of aggregates present in each transfected cells depending on CR concentration, using anti-GFP antibody (ab6556; 1:10,000). B) SDS-PAGE blot illustrates soluble level of HTT, using anti-GFP antibody (ab6556).

4.2.12.2 CR inhibition of mHTT aggregation and KMO-97Q interaction

It was clear from Figure 4-19B that CR treatment had no major effect on the level of soluble HTT, although it interfered with the 97Q BiFC pair interaction resulting in a strong decrease of the BiFC signal. Thus, it may not necessarily improve KMO-97Q interaction intensity evaluated by BiFC. However, the experiment was performed to confirm the impact that CR might have on mHTT interaction with flKMO-CC. HEK293T cells were co-transfected with 0.2 µg of flKMO-CC along with 0.2 µg of 97Q-VN or VN-backbone (as negative control). Cells were either untreated or treated with 12.5 µM of CR for 48 hr. Live cells were imaged using Scan^R screening station; analysed using Scan^R analysis software; and normalised based on Hoechst stained nuclei, as previously described in Section (4.2.8). As illustrated in Figure 4-20A, CR treatment dramatically decreased the flKMO-CC + 97Q-VN BiFC signal intensity, ($P < 0.0001$). This drop in the mean green intensity of flKMO-CC + 97Q-VN treated cells reflects a reduction of the BiFC signal of the 97Q pair, probably indicating that CR binds to 97Q and prevents its BiFC interactions. In contrast, CR treatment enhanced the background intensity, where treated and untreated cells transfected with flKMO-CC and VN-backbone were significantly different ($P < 0.0001$). Treated flKMO-CC + 97Q-VN cells were however still slightly stronger than the background of treated cells ($P < 0.05$). The boost in the background mean green intensity (Figure 4-20A) could be due to CR spectra properties as further addressed in the Discussion Section (4.3.4). Filter trap blot clearly shows that CR treatment incredibly decreased aggregates on flKMO-CC + 97Q-VN cells, and nothing was detected on the background slots as expected (Figure 4-20B). Considering these findings, CR was not the ideal aggregation inhibitor to test this experimental hypothesis.

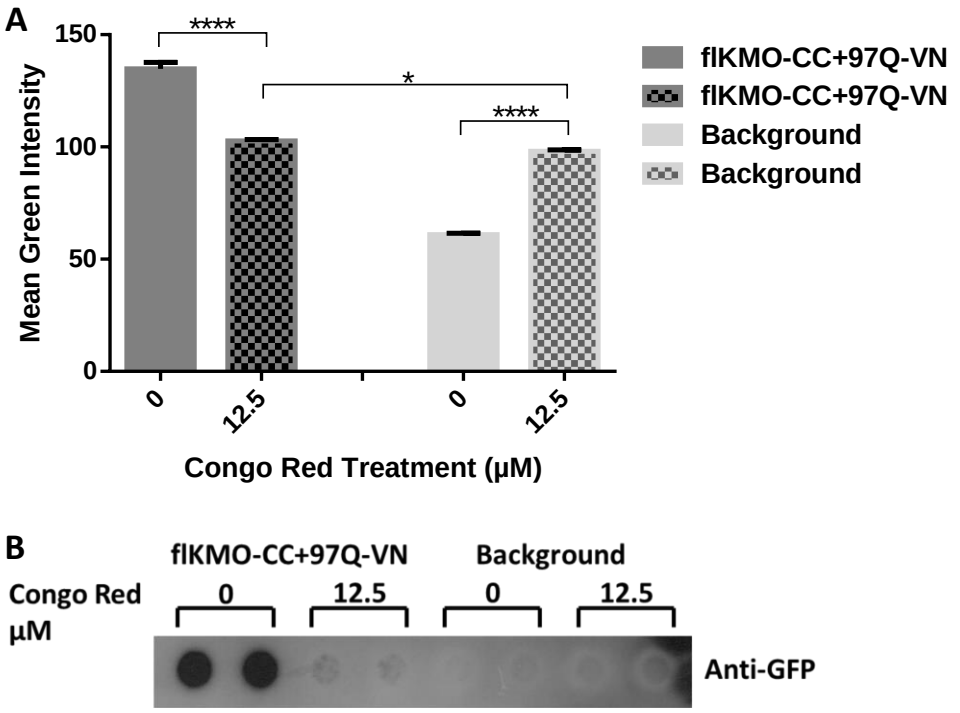

Figure 4-20 Effect of Congo Red (CR) treatment on HEK293T cells transfected with BiFC constructs.

Cells were transfected with 0.2 µg of flKMO-CC as well as 0.2 µg of 97Q-VN or VN-backbone (background). Cells were left untreated or treated with12.5 µM of CR at the time of transfection (48h treatment). A) Mean green intensity of the fluorescence complementation signal per well. CR treatment significantly reduced flKMO-CC+97Q-VN BiFC signal, but dramatically increased background signal. **** ($P < 0.0001$) and * ($P < 0.05$) for paired t-test. Data are expressed as mean per well ± SEM. The number of analysed ranged from 6000 to 8000 cells per well per condition, for untreated cells, whereas from 13000 to 14000 for treated cells. B) Filter trap blot shows levels of aggregates present in untreated cells in comparison to CR treated transfected cells, using anti-GFP antibody (ab6556; 1:10,000).

4.2.13 Mitochondrial co-localisation of flKMO-CC and HTT-VN proteins in HEK293T cells

The co-localisation of interaction partners within the cell is crucial for protein-protein interactions to occur. Thus, I decided to study flKMO-CC and HTT-VN localisation in order to unravel the cellular location of the BiFC complexes as well as to study HTT mitochondrial localisation. Constructs were transfected individually in HEK293T cells for 48 hr and immunolabelling was carried out on fixed cells to enable confocal analysis.

4.2.13.1 Localisation of flKMO-CC/tKMO-CC

HEK293T cells transfected with either flKMO-CC or tKMO-CC were immunolabelled with an anti-GFP antibody. My results indicated that the flKMO-CC signal was punctate (Figure 4-21A), whereas tKMO-CC was more diffuse over the entire cell (Figure 4-21B). To confirm that the punctate appearance of flKMO-CC is mitochondrial, flKMO-CC localisation was probed using an anti-KMO antibody along with an anti-mitochondria antibody. Indeed, the flKMO-CC and mitochondrial signals co-localised as indicated in the merge confocal image (Figure 4-22). These data regarding KMO localisation further confirm my previous findings in Section (3.2.4.1).

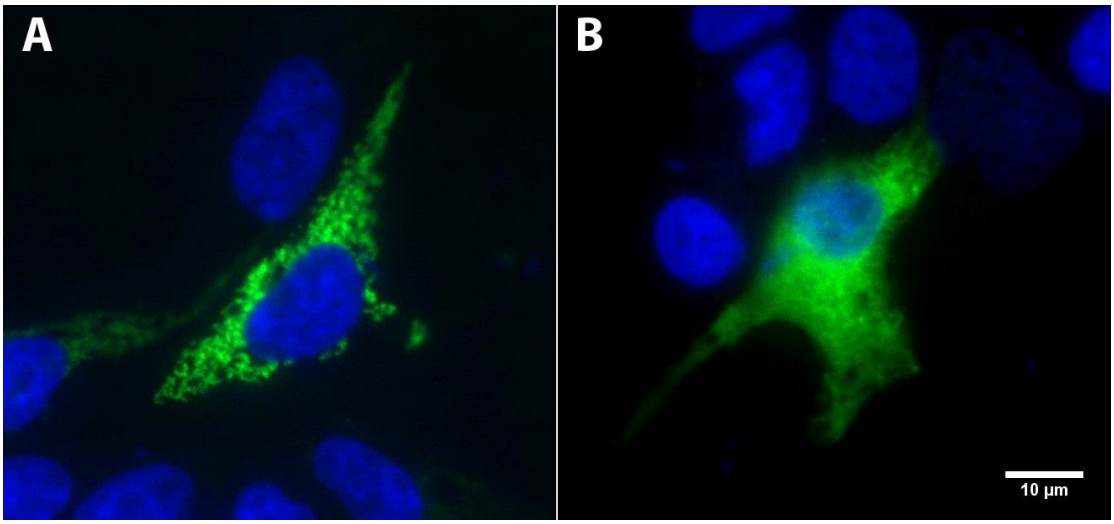

Figure 4-21 Fluorescence microscopy images of HEK293T cells transfected with KMO BiFC constructs.
A) flKMO-CC and B) tKMO-CC. Cells were immunolabelled with anti-GFP (ab6556) (Alexa Fluor 488). Nuclei were stained with Hoechst 33342. flKMO-CC has a dotted signal, confirming mitochondrial localisation, whereas tKMO-CC shows a diffused signal. Scale bar = 10 µm.

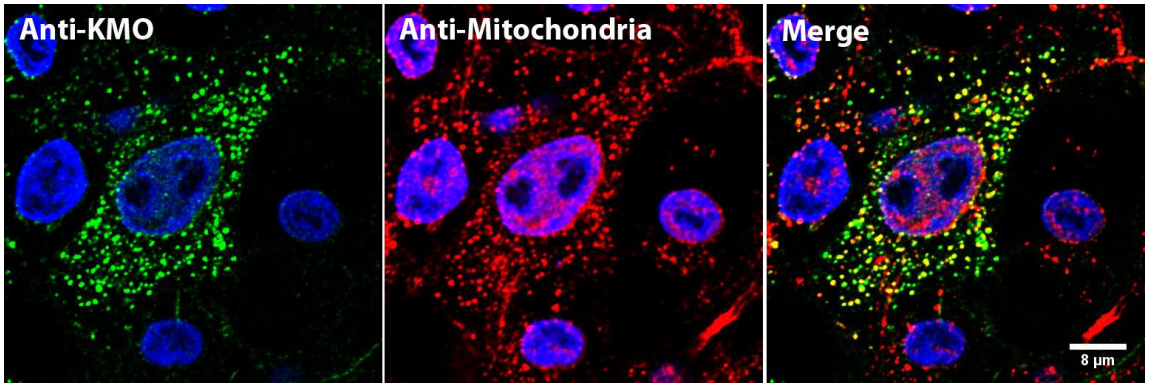

Figure 4-22 Subcellular localisation of flKMO-CC in fixed HEK293T cells.
Images were acquired using confocal microscopy and deconvolved. Anti-KMO antibody (10698-1-AP) immunolabelling of flKMO-CC (Alexa Fluor 555) (left panel). Anti-mitochondria (MAB1273) immunolabelling (Alexa Fluor 647). Green and red were used to represent Alexa Fluor 555 and 647 respectively to illustrate the overlapping (in yellow) as in the right merge panel. Nuclei were stained with Hoechst 33342. Scale bar = 8 µm.

4.2.13.2 19Q-VN protein localization in HEK293T cells

To gain insight into 19Q-VN HTT construct localization I used two parallel immunolabelling approaches: HEK293T cells expressing 19Q-VN were probed with either anti-HTT (mEM48) + anti-HtrA2 (Figure 4-23A) or with anti-GFP + anti-mitochondria (Figure 4-23B). 19Q-VN mitochondrial localization was indeed detected as clearly shown in the merged illustration (Figure 4-23A and B). Co-localisation analysis using JACoP plugin was performed on the regions indicated on the presented deconvolved optical sections. In Figure 4-23A, correlation between the red (19Q-VN) and the green (mitochondria) signals was very high, showing 82.7% co-localisation with mitochondria (Figure 4-23A). As the anti-HTT and anti-HtrA2 labelling was neater, 10 further optical z-sections (of different images) were analysed and the average co-localisation was of 79.7% ± 1.6 (data not shown). Figure 4-23B also shows strong correlation of 72.9% between 19Q-VN and mitochondrial signals (Figure 4-23B). This suggests that 19Q-VN localisation in HEK293T cells is in large part mitochondrial, which is not a usual observation and was not expected.

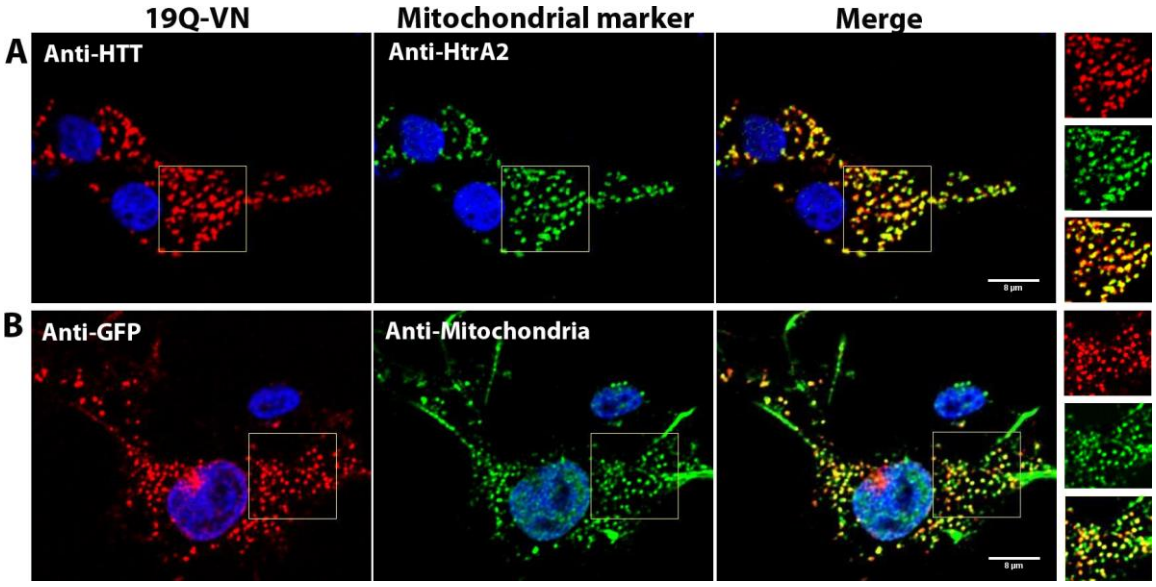

Figure 4-23 Co-localisation analysis of 19Q-VN and mitochondrial fluorescent signals on deconvolved confocal optical z-sections, using JACoP plugin in ImageJ.
HEK293T cells were transfected with 19Q-VN, and after 48 hr cells were fixed and immunolabelled. Left panel, 19Q-VN immunolabelling using: A) Anti-HTT (mEM48) antibody (MAB5374), (Alexa Fluor 647). B) Anti-GFP antibody (ab6556) (Alexa Fluor 555). Middle panel, mitochondrial immunolabelling: A) Anti-HtrA2/Omi antibody (AF1458) (Alexa Fluor 555). B) Anti-mitochondria antibody (MAB1273) (Alexa Flour 647). Right panels: merge image of the HTT and mitochondrial signals. Nuclei were stained with Hoechst 33342. Scale bar = 8 µm. Co-localisation analysis were carried out on the regions of interest indicated on the images; and a zoomed-in is presented on the right of panel A and B. 19Q-VN signal appears punctate and co-localises majorly with mitochondrial, 82.7% and 72.9% for panel A and B respectively. Analysis was done on the presented images.

4.2.13.3 Localisation of mHTT BiFC proteins in HEK293T cells

Cells expressing BiFC mHTT constructs 46Q-VN or 97Q-VN were probed as for 19Q-VN, using anti-HTT (mEM48) and HtrA2 antibodies. Although mEM48 antibody mostly detected soluble HTT, bright inclusions were clearly visible especially in the case of 97Q-VN (Figure 4-24B). Indeed, 46Q-VN labelling appeared dotted and co-localised with mitochondrial labelling as shown in the merged image. No co-localisation analysis was carried out as there were not enough images without obvious inclusions, which interfere with this analysis (Figure 4-24A). 97Q-VN labelling showed more aggregation that was very bright and made the dotted signal very weak. When a non-overexposed representation was successfully captured, the increase in the image brightness allowed the punctate background signal to be enhanced and visible enough to check for its co-localisation with the mitochondria, as supported with the merge image (Figure 4-24B). This provided sufficient evidence for a subset of mHTT being localized to the mitochondria.

Cells expressing 46Q-VN and 97Q-VN were also immunolabelled with the anti-GFP antibody for confirmation. 46Q-VN appeared either dotted (Figure 4-25A) or dotted with some inclusions (Figure 4-25B) while as expected, 97Q-VN images show strong presence of inclusions (Figure 4-25C and D).

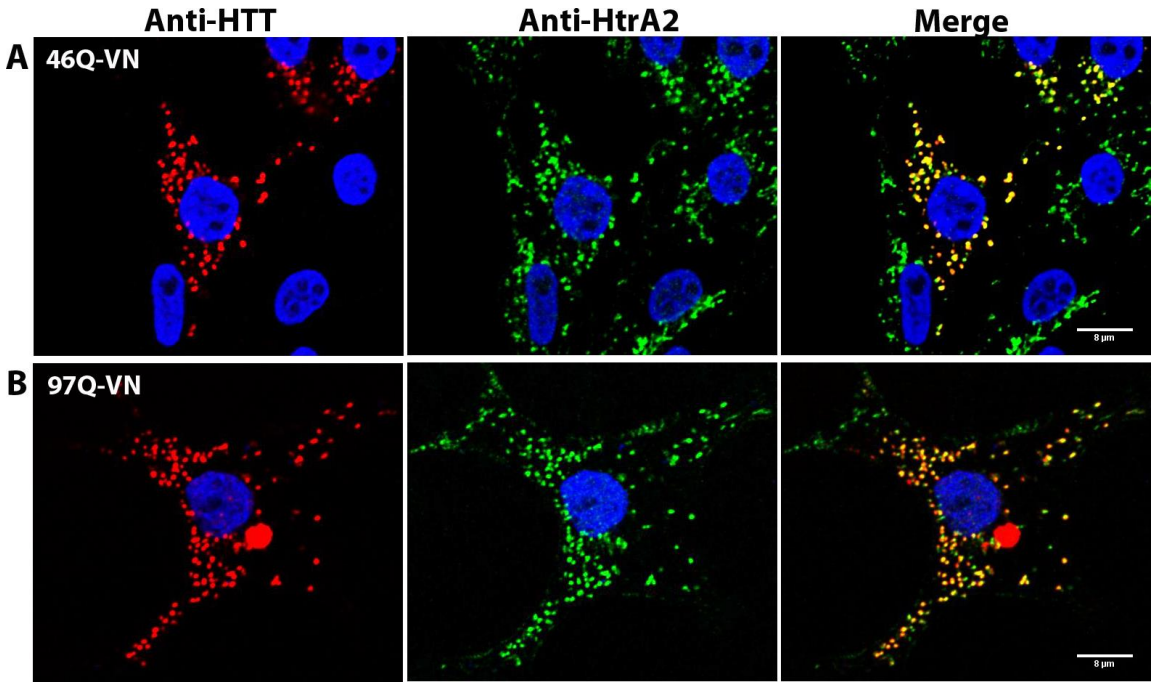

Figure 4-24 Deconvolved confocal co-localisation studies of mHTT with mitochondria. HEK293T cells were transfected with either 46Q-VN or 97Q-VN for 48 hr, then fixed and immunolabelled. Left panel: anti-HTT (mEM48) antibody (MAB5374) (Alexa Fluor 647); where A) 46Q-VN and B) 97Q-VN. Middle panel: anti-HtrA2/Omi antibody (AF1458) (Alexa Fluor 555). Right panel: merge of HTT and mitochondrial signals. Nuclei were stained with Hoechst 33342. Scale bar = 8 µm. Anti-HTT signal co-localises with mitochondrial signal, but presence of aggregates (bright inclusions) makes images unquantifiable.

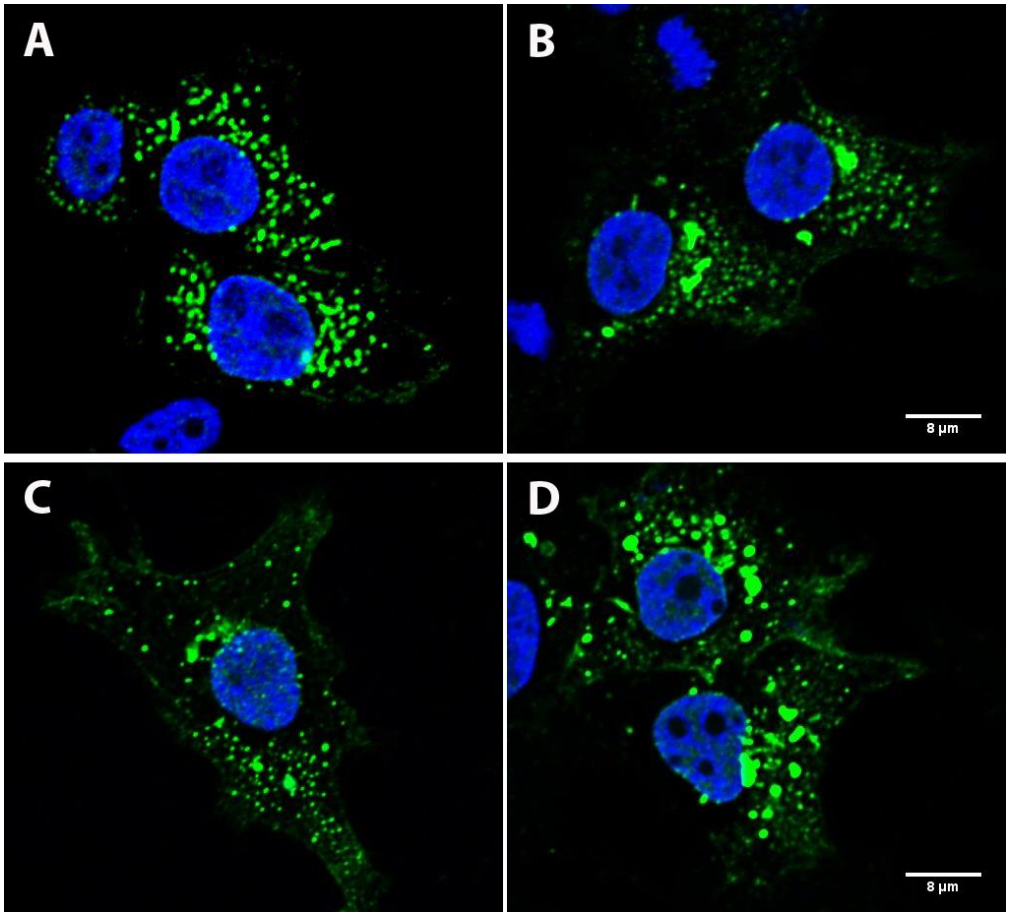

Figure 4-25 Deconvolved confocal images of mHTT in HEK293T cells.
Cells were transfected with either 46Q-VN (A and B) or 97Q-VN (C and D) for 48 hr. Cells were then fixed and immunolabelled with anti-GFP anti-body (ab6556) (Alexa Fluor 647). Nuclei were stained with Hoechst 33342. Scale bar = 8 µm. Clearly cells in B and D (46Q-VN and 97Q-VN respectively) showed more inclusios than A (46Q-VN) and C (97Q-VN).

4.2.14 Sub-cellular localisation of the BiFC KMO-HTT interaction complexes in HEK293T cells

As flKMO-CC and HTT-VN were shown to be localized to mitochondria, confirmation of the KMO-HTT BiFC complexes was needed to prove they interact at the mitochondria. Towards this aim, cells were seeded in ibiTreat dishes, transfected with the BiFC pair as in the BiFC experiment (Section 4.2.6): flKMO-CC along with 19Q-VN, 46Q-VN or 97Q-VN. Live cells were then stained with MitoTracker Red CMXRos and examined by confocal microscopy. The BiFC signal resulting from the interaction between flKMO-CC and HTT-VN showed a punctate pattern, similar to what was observed for the MitoTracker staining; the merge picture indeed showed the two signals co-localised (Figure 4-26A, B and C). When cells were fixed before confocal examination, again the BiFC signal of flKMO-CC and HTT-VN was dotted as was the MitoTracker staining. The merge picture of the fixed cells confirms the co-localisation of BiFC and MitoTracker signals for all HTT-VN interacting with flKMO-CC (Figure 4-27A, B and C). These findings clearly showed the mitochondrial localization of the flKMO-HTT BiFC interaction complexes.

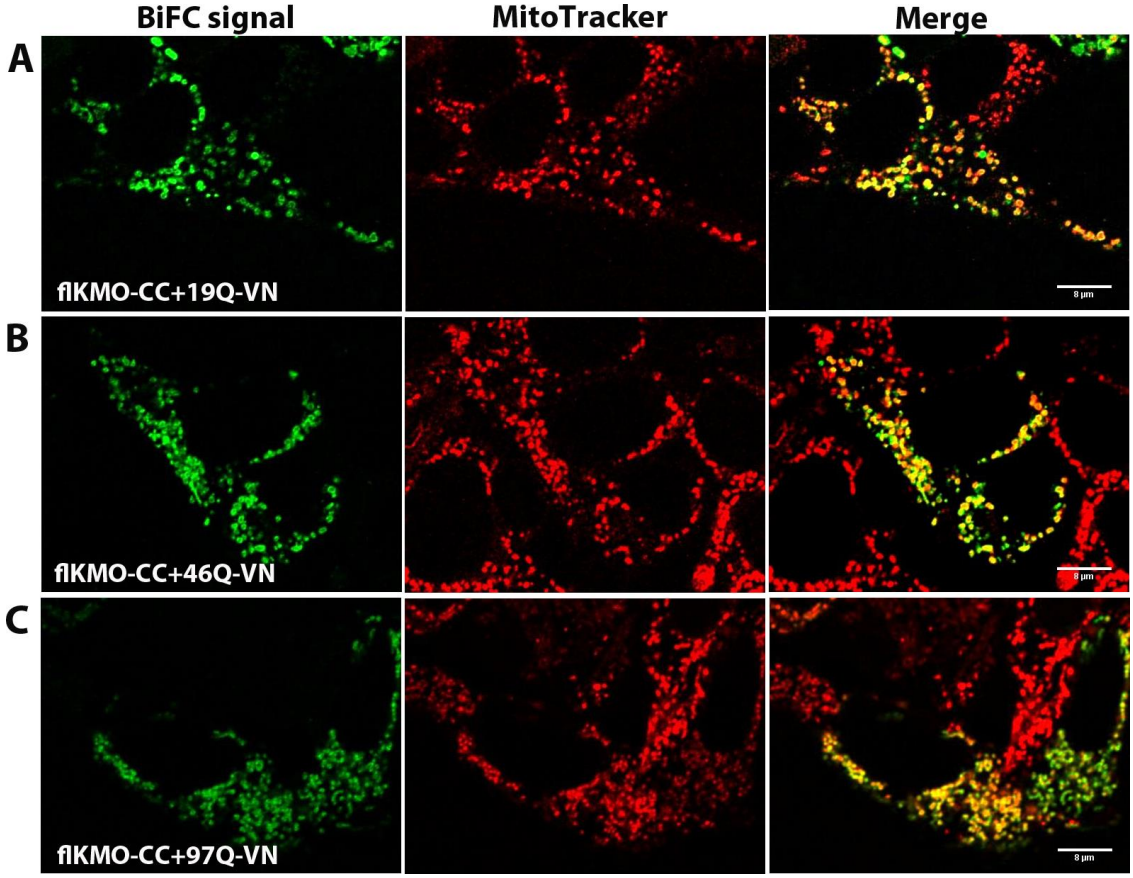

Figure 4-26 Cellular localisation of KMO-HTT BiFC complexes in live HEK293T cells, using confocal microscopy.
Cells were seeded on ibiTreat dishes and co-transfected with BiFC constructs for48 hr. Left panels BiFC signal of: A) flKMO-CC and HTT19Q-VN, B) flKMO-CC and HTT46Q-VN, and C) flKMO-CC and HTT97Q-VN. Second column of panels (A, B and C): mitochondria stained with MitoTracker Red CMXRox (M-7512). Third column of panels (A, B and C): merge of the BiFC signal and the MitoTracker signal. Scale bar = 8 µm. BiFC signal in panels A, B and C presents dotted structures that co-localise with the MitoTracker signal, as seen in the merge images in the right panels of A,B and C. This confirms the mitochondrial localisation of all the BiFC complexes of flKMO-CC with different polyQ length of HTT-VN.

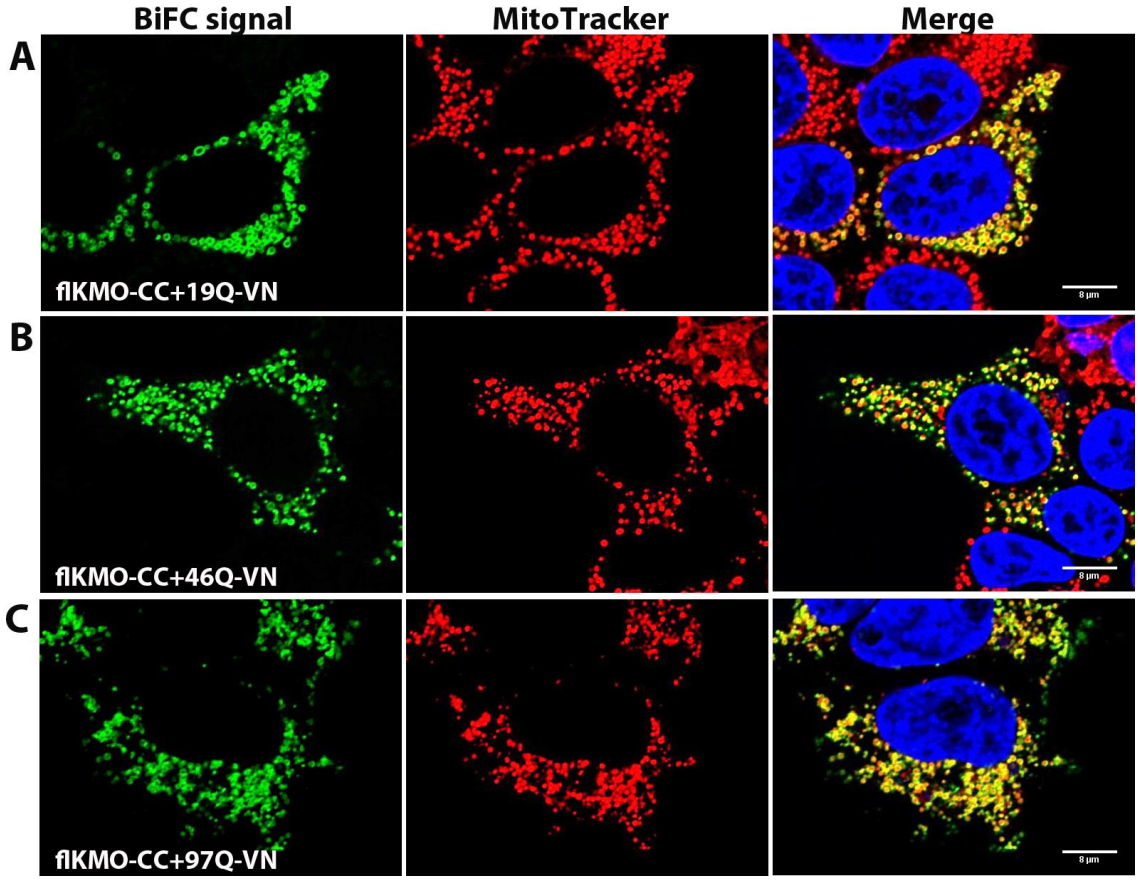

Figure 4-27 Mitochondrial co-localisation of KMO-HTT BiFC complexes in fixed HEK293T cells, using confocal microscopy.
Cells were co-transfected with BiFC constructs and fixed 48 hr after transfection. Left panels BiFC signal of: A) flKMO-CC and HTT19Q-VN, B) flKMO-CC and HTT46Q-VN, and C) flKMO-CC and HTT97Q-VN. Middle panels: mitochondria stained with MitoTracker Red CMXRox (M-7512). Right panels: merge of the BiFC signal and the MitoTracker signal. Nuclei were stained with Hoechst 33342. Scale bar = 8 µm.

4.2.15 Characterisation of the "tag effect" on WT HTT mitochondrial localisation in HEK293T cells

To better understand mitochondrial localization of BiFC HTT (19Q-VN) and its strong interaction with flKMO-CC I next studied the effect of its fluorescent tag on protein location within cells. Unfortunately, it was not possible to use untagged WT HTT for reasons detailed later on (Section 4.2.16.2), and thus tagged versions as well as the construct tag VN were used. To perform confocal analyses, HEK293T cells were transfected with these constructs for 48 hr.

4.2.15.1 Half Venus (VN) distribution in fixed HEK293T cells

As HTT-VN immunolabelling confocal studies suggested major mitochondrial localisation of both WT and mHTT, it was important to check whether this was driven by the –VN tag on the constructs. To test this, cells were transfected with the control BiFC backbone expressing VN, fixed and probed with anti-GFP antibody. My results indicated that VN is mostly localized in the nucleus (possibly in the nucleoli structures), with some faint dotted cytoplasmic signal hardly overlapping with the mitochondrial signal. JACoP analysis provided poor correlation between anti-GFP and anti-mitochondrial signals, found to be 52%, suggesting minor VN presence in the mitochondria (Figure 4-28).

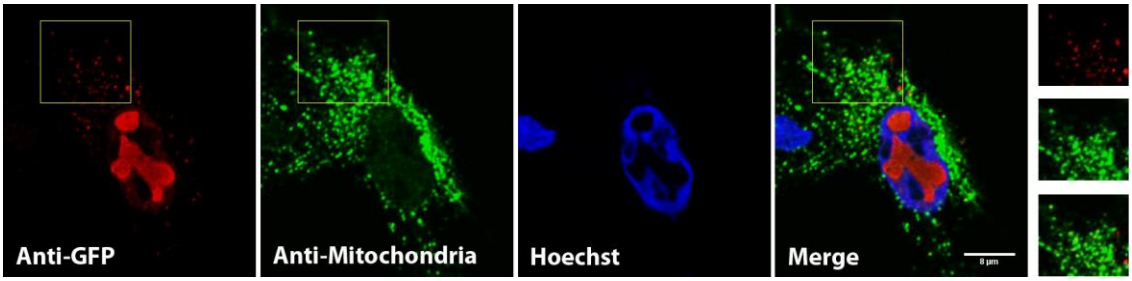

Figure 4-28 Co-localisation analysis of N-terminal half of Venus (VN) expressed in HEK293T cells.
A deconvolved confocal optical section was analysed using JACoP plugin in ImageJ. Cells were transfected with VN-backbone for 48 hr, fixed and dual immunolabelling was performed. Left panel: anti-GFP (ab6556) (Alexa Fluor 555). Middle left panel: anti-mitochondria antibody (MAB1273) (Alexa Flour 647). Middle right panel: stained nuclei with Hoechst 33342. Right panel: merge of the first three panels. Scale bar = 8 µm. Selected regions for co-localisation analysis are shown on the images and also presented on the right of the merge panel. Co-localisation analysis showed 52% correlation indicating slight mitochondrial co-localisation.

4.2.15.2 Localisation of 25Q-VC in fixed HEK293T cells

HEK293T cells that express 25Q-VC (WT HTT fused to the C-terminus of Venus) were fixed and double immunolabelled with anti-HTT (mEM48) and anti-HtrA2. This construct also clearly co-localised with the mitochondria as shown by its punctate appearance (Figure 4-29).

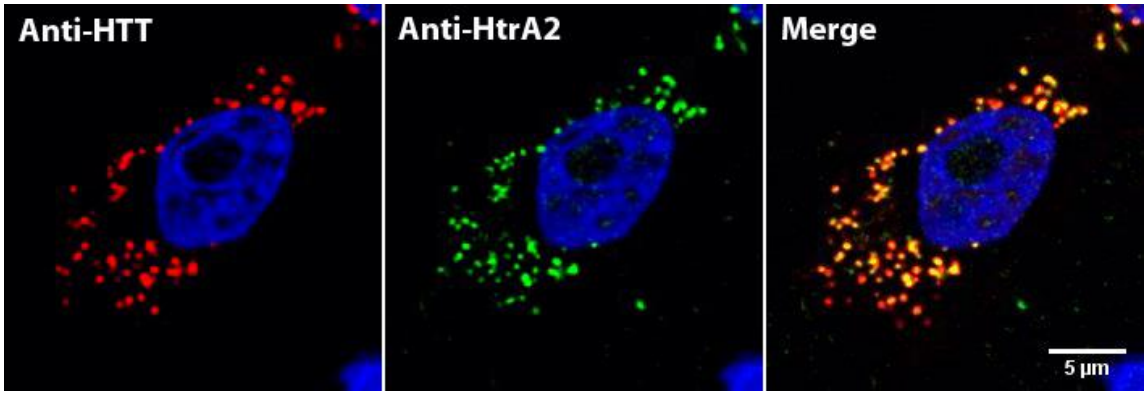

Figure 4-29 Cellular localisation of 25Q-VC in HEK293T cells.
Deconvolved confocal illustration of cells transfected with 25Q-VC for 48 hr, fixed and double immunolabelled with: Left panel: anti-HTT (mEM48) antibody (MAB5374) (Alexa Fluor 647). Middle panel: anti-HtrA2/Omi antibody (AF1458) (Alexa Fluor 555). Right panel: merge of HTT and HtrA2 signals and nuclei were stained with Hoechst 33342. Scale bar = 5 µm. 25Q-VC co-localises with mitochondria.

4.2.15.3 WT BiFC pair (19Q-VN and 25Q-VC) localisation in living HEK293T cells

Next, the two WT HTT BiFC constructs were transfected in HEK293T cells. Cells were stained with MitoTracker and then examined by confocal microscopy. BiFC signal (WT HTT and the combination of Venus halves) was dotted and spread throughout the cytosol, as suggested by the green background. Indeed merging the BiFC signal with the mitochondrial signal revealed that the dotted BiFC signal co-localises nicely with the MitoTracker staining (Figure 4-30).

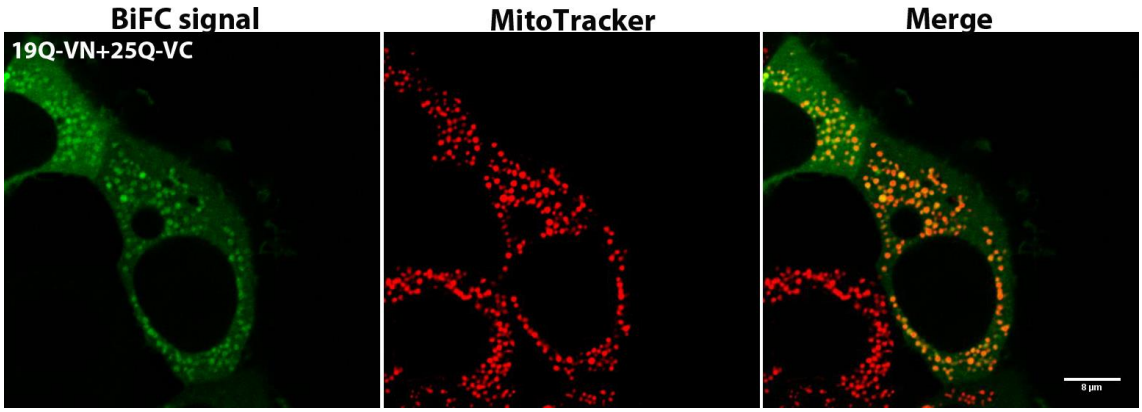

Figure 4-30 Localisation of WT HTT pair in live HEK293T cells.
Cells were seeded in ibiTreat dishes and co-transfected with 19Q-VN and 25Q-VC for 48 hr. Live cells were stained with MitoTracker Red CMXRox (M-7512) prior to confocal examination. Acquired images were deconvolved. Left panel: BiFC signal of 19Q-VN and 25Q-VC. Middle panel: MitoTracker signal. Right panel: merge of BiFC and MitoTracker signals. Scale bar = 8 µm. BiFC signal of WT HTT is mitochondrial (indicated by the co-localisation with MitoTracker) as well as cytosolic.

4.2.15.4 Localisation of 25Q-GFP in living HEK293T cells

As last control for tag influence on protein localization, WT HTT was fused to full length GFP, transfected and examined after MitoTracker staining. Interestingly the GFP signal was majorly cytosolic and did not co-localise at all with the mitochondrial signal. Merging of the images shows green only or red only regions, and no overlay between the two (Figure 4-31).

These studies suggest that half Venus tags fused to WT HTT enhance mitochondrial localisation, whereas full length GFP fusion to WT HTT eliminates any mitochondrial localisation. However untagged HTT would be needed to confirm where this construct would localise without the influence of tags, as HTT is not normally an exclusively mitochondrial protein.

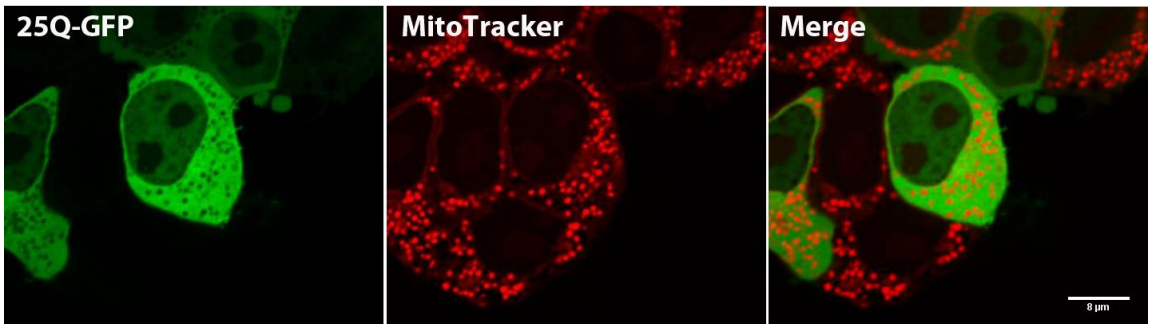

Figure 4-31 Deconvolved confocal illustration of 25Q-GFP localisation in HEK293T cells. Cells were seeded in ibiTreat and transfected with 25Q-GFP for 48 hr, and then stained with MitoTracker Red CMXRox (M-7512). Left panel: GFP signal showing the fused 25Q localisation. Middle panel: MitoTracker signal. Right panel: merge of the 25Q-GFP and MitoTracker signals. Scale bar = 8 µm. 25Q-GFP expressed in the cytosol, with complete exclusion of mitochondrial localisation.

4.2.16 Ultra-structure of flKMO-CC and HTT-VN proteins localisation in HEK293T cell

As a result of the limited resolution of confocal microscopy, TEM was needed to unravel a specific *in situ* localisation and distribution of flKMO-CC and 19Q-VN. Thus, HEK293T cells were seeded on coverslips, transfected with the appropriate construct for 48 hr, then fixed and immunogold labelling was performed.

4.2.16.1 Association of flKMO-CC and 19Q-VN labelling with mitochondria

Sections of cells expressing flKMO-CC were immunogold labelled with anti-KMO antibody. The electron micrograph clearly shows that flKMO-CC is localised to the outer surface of the mitochondria, which confirms my previous TEM data of untagged flKMO localisation (Section 3.2.4.2), and thus both tagged and untagged flKMO are localised similarly to the mitochondria (Figure 4-32A). On the other hand, anti-HTT (mEM48) labelling of 19Q-VN transfected cell sections displayed a different mitochondrial signal where the gold particles where mostly localized inside the mitochondria with a few close to the mitochondrial surface. Interestingly, TEM also revealed a minor cytosolic and nuclear labelling of 19Q-VN, which was never detected for flKMO-CC, and thus was more exclusively mitochondrial. This confirms that a subset of 19Q-VN is present outside the mitochondria, which was undetectable when confocal microscopy was used (Figure 4-32B).

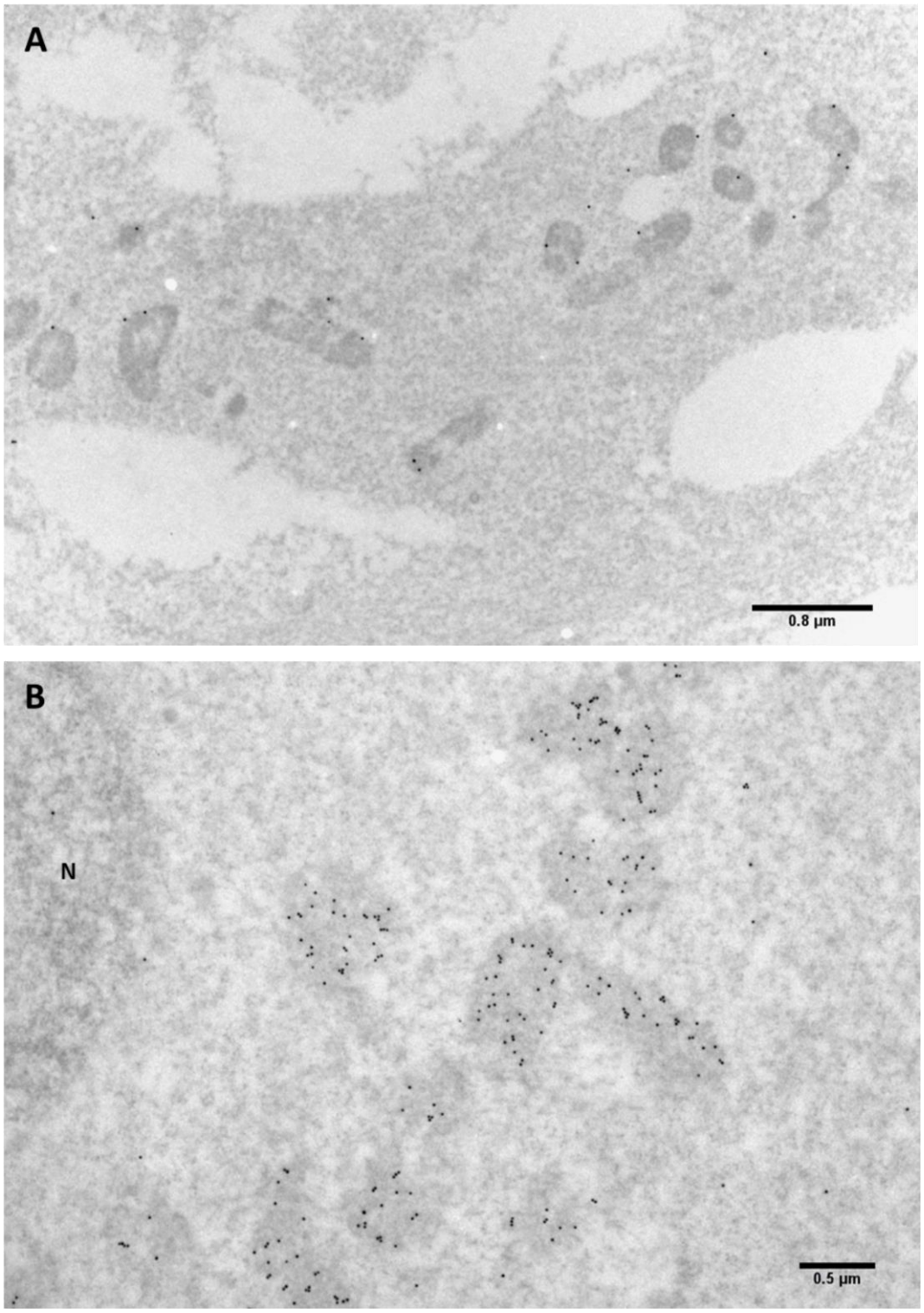

Figure 4-32 Electron micrographs of transfected HEK293T cells.
Cells were transfected for 48 hr with either flKMO-CC or 19Q-VN. Immunogold labelling shows sub-cellular localisation of the transfected proteins. The darkened structures are the mitochondria. A) flKMO-CC immunogold labelling is clearly on the outer surface of mitochondria; anti-KMO antibody (10698-1-AP). Scale bar = 0.8 µm. B) Gold particles labelling 19Q-VN were heavily mitochondrial, with few others around the cell; anti-HTT, mEM48 antibody (MAB5374). Nucleus is denoted with the letter 'N'. Scale bar = 0.5 µm.

4.2.16.2 Unravelling untagged WT HTT localisation in HEK293T cells

An untagged HTT23Q construct (the only in house available untagged HTT WT construct) was transfected in HEK293T cells and immunogold labelled via anti-HTT (mEM48) antibody. The TEM showed a rather unusual heavy labelling with particles spread throughout the cell. Labelling seemed specific to a number of cells, suggesting it was not random and was specific to cells expressing 23Q (Figure 4-33A). As these data were not particularly clear, validation of proper 23Q expression was needed. Lysates of cells expressing 23Q were immunoblotted along with 103Q (used as a control for untagged HTT) using anti-HTT (mEM48) antibody and the HTT BiFC constructs were used as positive controls. While the BiFC constructs were well expressed, the 23Q and 103Q samples were expressed at low levels with several faint bands detected, with one band of approximately 18 kDa seen, which likely corresponds to the 23Q protein. No obvious band that might represent 103Q was seen, which could be explained by 103Q being more prone to aggregation and thus less soluble. In conclusion, immunoblot results indicate that 23Q and 103Q expression levels were not satisfactory to be used as untagged HTT controls (Figure 4-33B), and that this way be the reason for the poor TEM results using the 23Q construct.

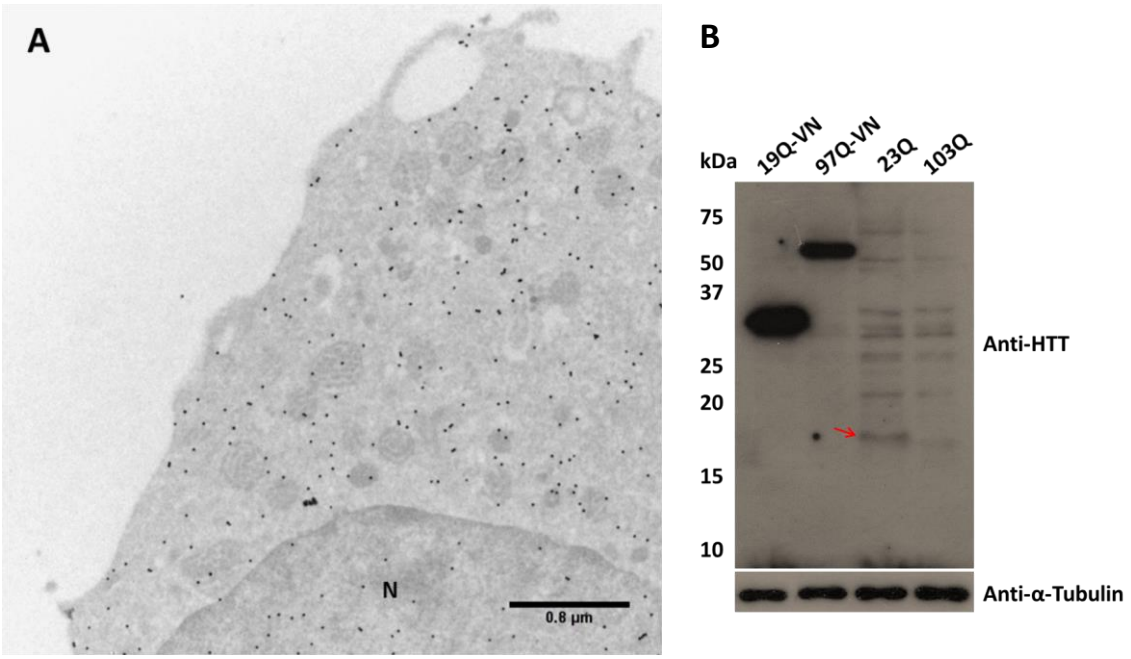

Figure 4-33 Localisation and expression of untagged HTT in HEK293T cells.
A) Electron micrograph of HEK293T cells expressing 23Q for 48 hr. Immunogold labelling seemed to be scattered all over the cell; anti-HTT (mEM48) antibody (MAB5374). Nucleus is denoted with the letter 'N'. Scale bar = 0.8µm. B) Cells were transfected with 0.32 µg of HTT constructs for 48 hr. Lysates were immunoblotted with anti-HTT (mEM48) antibody (MAB5374): 19Q-VN and 97Q-VN BiFC lysates (positive controls) as well as 23Q and 103Q (untagged HTT). Several faint bands were detected in 23Q and 103Q lanes, with one possible correct band of about 18 kDa in 23Q lane (pointed by the red arrow). Anti-α-Tubulin antibody was used as a loading control (anti-α-Tubulin: sc-8035).

4.2.16.3 Dual TEM immunoglod labelling to validate the mitochondrial localisation of KMO-HTT BiFC complexes

After obtaining the TEM data on flKMO-CC and 19Q-VN sub-cellular localisation, we investigated the impact they might have on the localisation of one another when co-transfected. The rationale behind this experiment was: (i) to demonstrated that their localisation is unaffected with co-transfection; (ii) to further confirm their interaction.

HEK293T cells were seeded on coverslips and co-transfected with either flKMO-CC and 19Q-VN or untagged flKMO and 19Q-VN for 48 hr. Anti-KMO and anti-HTT (mEM48) antibodies were used to immunolabel cells (Figure 4-34). TEM results showed a similar labelling of cells co-expressing flKMO-CC and 19Q-VN to cells transfected with individual constructs. Indeed, 19Q-VN labelling was heavier than flKMO-CC as indicated with 15 nm particles, and majorly mitochondrial. On the other hand, flKMO-CC labelling with the 30 nm particles appeared on the outer membrane of some mitochondria. Interestingly, our TEM results not only confirmed the presence of both flKMO-CC and 19Q-VN in the same mitochondrion, but also pointed out that particles were very close to one another, supporting more facile interactions (Figure 4-34A). To ensure that localization data of flKMO-CC and 19Q-VN labelling was not influenced by the BiFC system, cells co-expressing flKMO and 19Q-VN were also labelled. Similarly, the same mitochondrion was co-labelled with the 30 nm particles (flKMO) and the 15 nm particles (19Q-VN) very closely, suggesting that flKMO could readily interact with 19Q-VN although it does not have the half tag to complement its partner (Figure 4-34B).

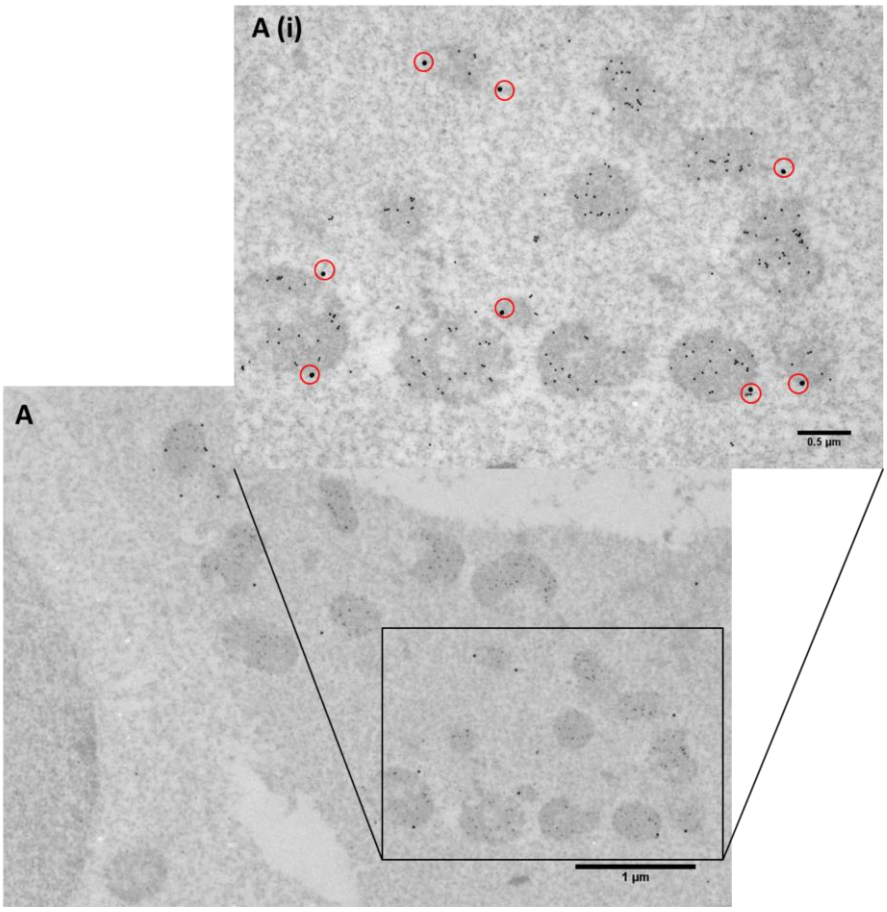
A (i)
A
0.5 µm
1 µm

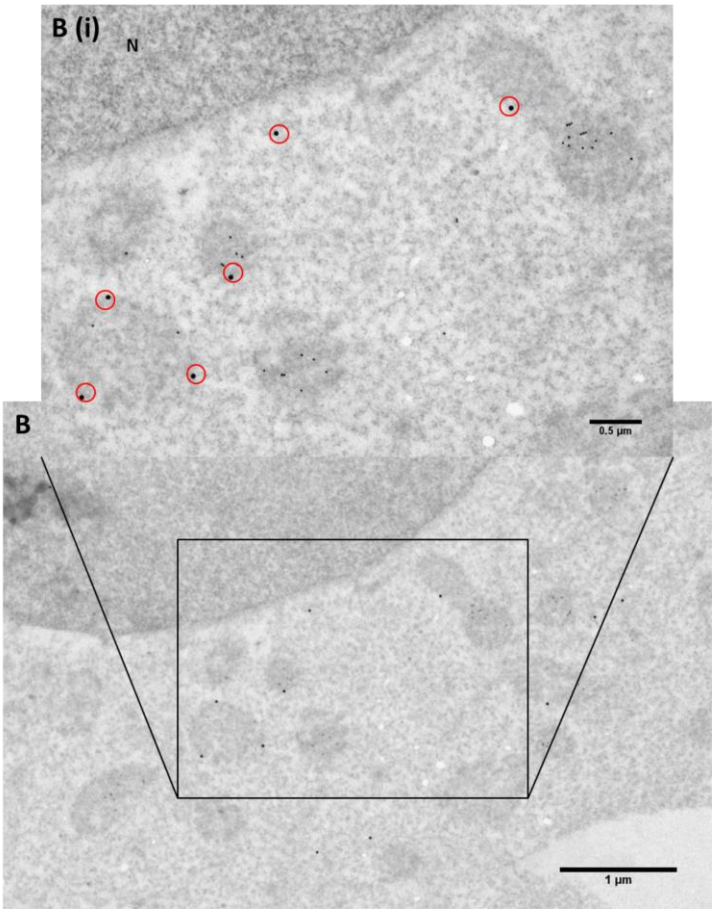
B (i)
N
B
0.5 µm
1 µm

Figure 4-34 Electron micrographs of dual immunoglod labelling in transfected HEK293T cells for 48 hr.

Cells were co-transfected and co-probed with anti-KMO antibody (10698-1-AP) and anti-HTT (mEM48) antibody (MAB5374), followed by 30 and 15 nm gold conjugate secondary antibodies, respectively. A) Overview of dual labelling of flKMO-CC and 19Q-VN. Scale bar = 1 µm. A (i) A zoomed view of the region indicated with the black box. Mitochondria were all intensely labelled with HTT (15 nm particles); also some particles were in the cytoplasm. flKMO-CC was labelled on the outer of some of HTT-labelled mitochondria (30 nm particles) as denoted with red circles. Scale bar = 0.5 µm. B) flKMO and 19Q-VN overview labelling. Scale bar = 1 µm. B (i) A zoomed in image of some mitochondria showing HTT labelling mostly in the mitochondria with some outside (15 nm particles), whereas labelling of flKMO (30 nm particles) is on the surface of the mitochondria as indicated with the red circles. Scale bar = 0.5 µm.

4.2.17 Exploring interactions of full length HTT (HTT-FL) with KMO

The strongest KMO-HTT interaction was with the WT HTT exon 1 fragment, which is not known to be widely present *in vivo*. Furthermore, it has been previously shown that maximal HTT-phospholipid association requires 171-287 aa region (Kegel *et al.*, 2009). This might suggest an increased association of HTT-FL with mitochondrial membranes and consequently an increased interaction with KMO. To address this aim, HTT-FL BiFC (23Q, 73Q and 145Q) constructs were generated by fusing them C-terminally to the N-terminus of Venus (VN), to be paired with flKMO-CC in the complementation assay (Figure 4-35A).

HEK293T cells were transfected with 0.32 µg of HTT-FL-VN constructs for 48 hr to validate their expression. Two available anti-HTT antibodies were used to detect HTT-FL expression. One is anti-(HTT) 4C8, which recognises all HTT-FL regardless of the tag or polyQ length. However 23Q-FL-VN is similar in size to the untagged 23Q-FL and to endogenous HTT-FL present in the HEK293T cells. Thus, it was not possible to discriminate the detectable bands as exogenous or endogenous HTT-FL. 73Q-FL-VN and 145Q-FL-VN were both clearly detectable using 4C8 antibody (Figure 4-35B). The second available antibody was anti-polyQ (1C2) that recognises only expanded polyQ (>37). 1C2 antibody further confirmed 73Q-FL-VN and 145Q-FL-FV expression, and also 97Q-VN (exon 1 fragment) which was included as a positive control (Figure 4-35C).

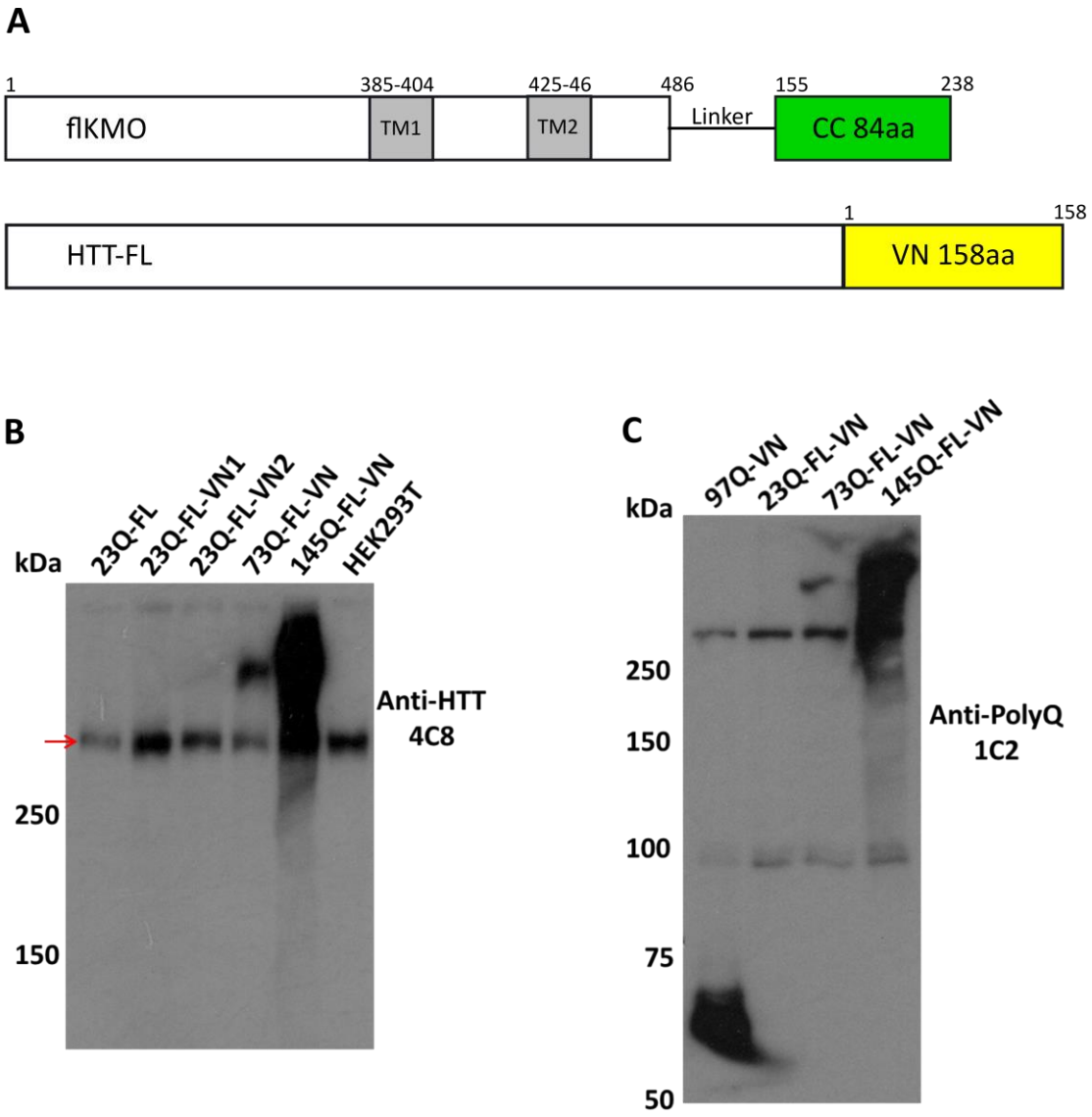

Figure 4-35 flKMO and HTT-FL BiFC constructs.
A) Schematic representation of BiFC flKMO and HTT-FL constructs. flKMO fused to C-terminus of CFP (CC) via a the $(GGGS)_2$ linker. HTT-FL fused to N-terminus of Venus (VN); giving three constructs: 23Q-FL-VN, 73Q-FL-VN and 145Q-FL-VN. B) and C) 8% SDS-PAGE of HTT-FL-VN constructs expressed in HEK293T cells. B) Anti-HTT, 4C8 antibody (MAB2166), 23Q-FL (untagged) and untransfected HEK293T cells were used as controls. 23Q-FL-VN1 and 23Q-FL-VN2 were different lysates. The size similarity of 23Q-FL (tagged and untagged) with endogenous HTT-FL in HEK293T cells, makes it difficult to confirm their expression (indicated with the red arrow). C) Anti-polyQ, 1C2 antibody (MAB1574), it recognised only expanded polyQ 73Q-FL-VN and 145Q-FL-VN; while 97Q-VN fragment was used as positive control.

4.2.17.1 Exploiting the BiFC system to study flKMO-CC and HTT-FL-VN in living HEK293T cells

HEK293T cells were transfected as routinely done with 0.16 µg of each BiFC construct along with 0.08 µg of RFP plasmid, for 48 hr, as described in Section (4.2.6). Images were analysed with Scan^R analysis software and they clearly showed no complementation of HTT-FL-VN with flKMO-CC. In fact, mean green intensities of HTT-FL-VN were significantly less than the background ($P < 0.0001$) (Figure 4-36A). BiFC experiment lysates were immunoblotted to validate the expression of the constructs. All flKMO-CC as well as positive and negative (background of complementing with VN-backbone) controls were satisfactorily expressed, where they were immunolabelled with anti-KMO and anti-GFP respectively (Figure 4-36B). Expression of HTT-FL-VN was also verified with the 4C8 antibody: both 23Q-FL-VN and 145Q-FLVN were detectable. Endogenous HTT-FL was present as faint bands in 73Q-FL-VN and 145Q-FL-VN lanes, confirming the identity of the strong 23Q-FL-VN signal in its lane. Finally 73Q-FL-VN was not detectable in this blot; however as none of the other HTT-FL-VN constructs interacted with flKMO-CC, this is likely not the reason for the lack of interaction (Figure 4-36C). Thus, these data suggest that KMO may not interact with HTT-FL using the BiFC system.

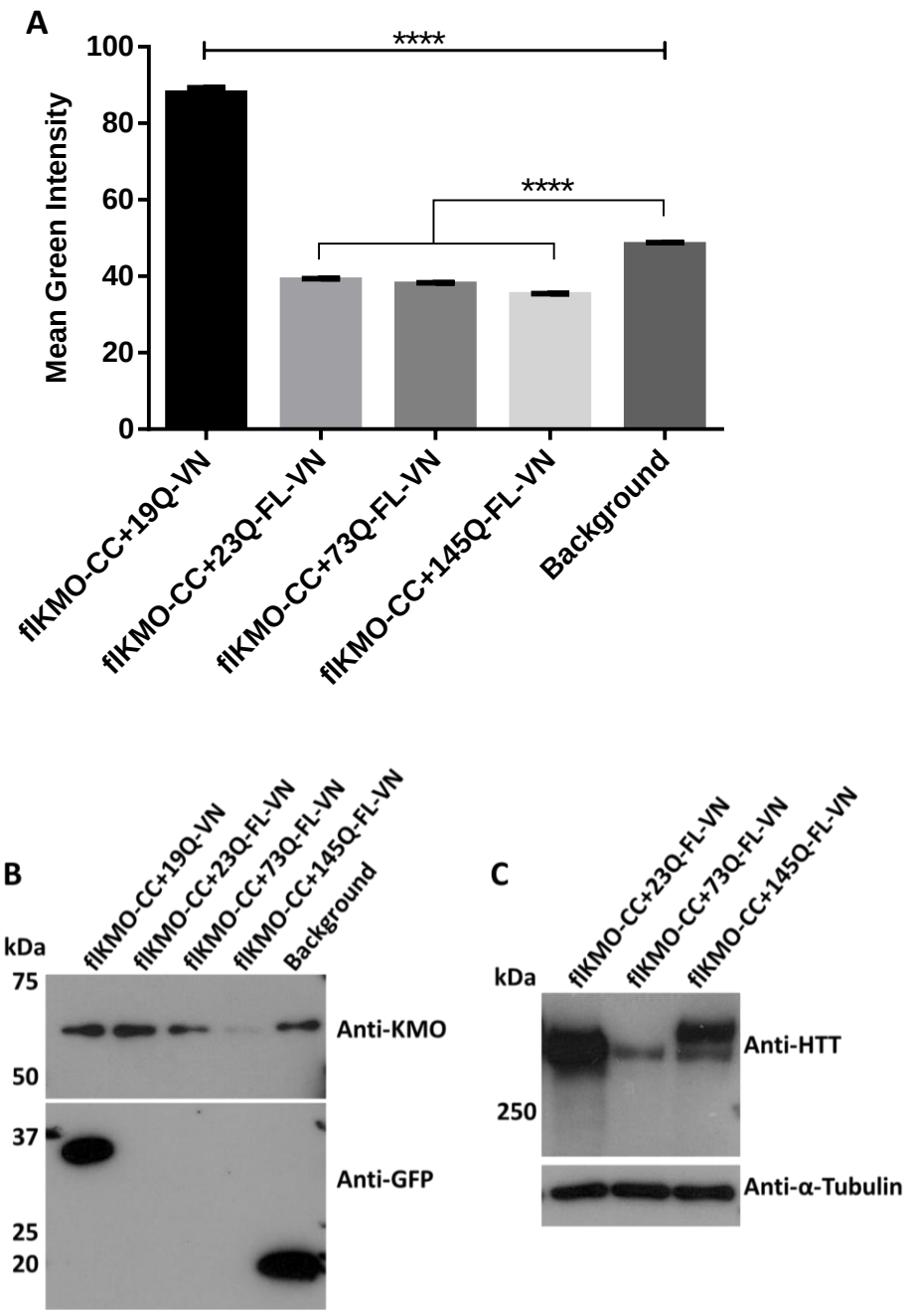

Figure 4-36 BiFC assay of flKMO-CC and HTT-FL-VN in live HEK293T cells.
Cells were transfected with 0.16 µg of each BiFC construct along with 0.08 µg of RFP plasmid for 48 hr. A) Mean green intensity of BiFC signal, where all flKMO-CC and HTT-FL-VN pairs failed to complement one another ****$P < 0.0001$ for one-way ANOVA, followed by Tukey's multiple comparison tests. Data are expressed as mean per well ± SEM. The number of analysed cells ranged from 2500 to 2800 cells per well per condition. B) and C) 10% SDS-PAGE of BiFC lysates. B) Anti-KMO antibody (10698-1-AP) to probe flKMO-CC (top blot); and anti-GFP antibody (ab6556) to label 19Q-VN and VN-backbone (bottom blot). C) Anti-HTT, 4C8 antibody (MAB2166) to label HTT-FL-VN, only 73Q-FL-VN did not seem to be expressed. Anti-α-Tubulin antibody was used as a loading control (anti-α-Tubulin: sc-8035).

4.2.18 RNAi for endogenous HTT-FL in HEK293T cells

To investigate the significance of KMO-HTT interactions in HEK293T cells in relation to HD mechanisms, it would be of interest to examine KMO enzymatic activity when interacting with various polyQ lengths of HTT. As an initial experiment towards this goal, I wished to examine any possible effect of endogenous HTT-FL on KMO activity. I thus attempted to optimize RNAi knockdown of endogenous HTT-FL in HEK293T cells so that any possible effect upon KMO activity could be monitored. In this study four targeting short hairpin RNAs from Dharmacon (shRNA1, shRNA2, shRNA3 and shRNA5) and a non-targeting control shRNA (ctrl shRNA) were exploited to achieve HTT-FL knockdown in HEK293T cells.

4.2.18.1 Optimisation of endogenous HTT-FL knockdown in HEK293T cells

First HEK293T cells were transfected with 0.4 µg of shRNAs for 48 hr. Immunoblotting using anti-HTT (4C8) antibody was used and densitometry analysis of HTT-FL expression relative to endogenous α-Tubulin was performed using ImageJ. shRNA1 and shRNA2 resulted in a strong knockdown of HTT-FL levels, with ~50% and ~35% reduction in expression respectively, in comparison to ctrl shRNA and untransfected cells (Figure 4-37A and B). In the context of the planned KMO activity experiments, KMO needs to be exogenously expressed in HEK293T cells, and thus the flKMO construct was co-transfected with shRNAs. In order to achieve a higher knockdown of HTT-FL, cells were transfected for 72 hr with a lower DNA amount for optimisation purposes. Equal amounts of untagged flKMO and each shRNA (0.175 µg) were co-transfected in HEK293T cells. Lysates were immunoblotted using 4C8 antibody (Figure 4-37C), and relative quantification of HTT-FL was carried out. Robust knockdown was again observed, with ~55% for shRNA1 and ~62% for shRNA2 in comparison to the controls HTT-FL expression (Figure 4-37D). Clearly, shRNA1 and shRNA2 provided the best knockdown in both experimental conditions. Therefore they were transfected alongside the ctrl shRNA and untransfected HEK293T cells, all in triplicate to allow statistical analysis to be carried out. Moreover, the DNA concentration of shRNA constructs was doubled (0.35 µg) and co-transfected with 0.175 µg of untagged flKMO for 72 hr. Interestingly, immunoblots of shRNA lysates showed a dramatic decrease in HTT-FL levels, but also in α-Tubulin levels, which made blot quantification not possible (Figure 4-38). α-Tubulin forms a heterodimer with β-Tubulin, and the latter is a known interactor of HTT-FL (Hoffner *et al.*, 2002),

and thus interruption of this interaction may somehow affect α-Tubulin expression. In total, high levels of shRNA seemed to be detrimental to the cells, as cells were not very healthy on microscopic observations prior lysis, and the decrease in α-Tubulin levels may reflect general toxicity to the cells.

Thus, to perform the enzymatic activity experiment it may be best to employ more moderate knockdown of HTT-FL expression with nearly 60% knockdown of HTT-FL (achieved upon transfection of 0.175 µg of shRNA for 72 hr) or 0.35 µg of shRNA for 48 hr could also be tested. Indeed, further experiments would be needed to ensure optimisation of the best level of HTT-FL knockdown, though this initial work is an encouraging first step for these future studies.

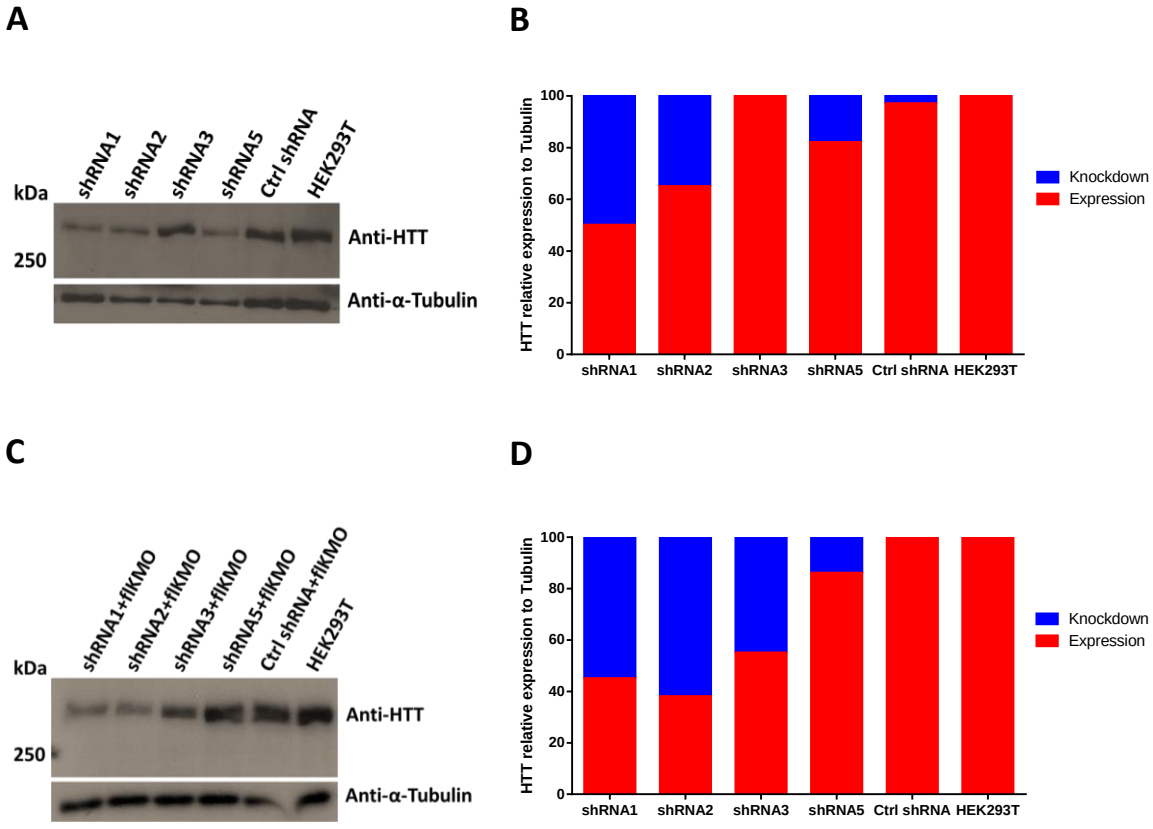

Figure 4-37 Optimisation of endogenous HTT-FL knockdown in HEK293T cells.
A) and C) Immunoblots of untransfected and shRNA transfected HEK293T cells using anti-HTT, 4C8 antibody (MAB2166). Anti-α-Tubulin antibody (sc-8035) was used as a loading control. A) Cells were transfected with 0.4 µg of shRNA for 48 hr. C) Cells were co-transfected with 0.175 µg of flKMO and shRNA, for 72 hr. B) and D) Blots densitometry analysis. Both graphs show that shRNA1 and shRN2 resulted in the most potent HTT-FL knockdown. B) Quantification of blot A. D) Quantification of blot C.

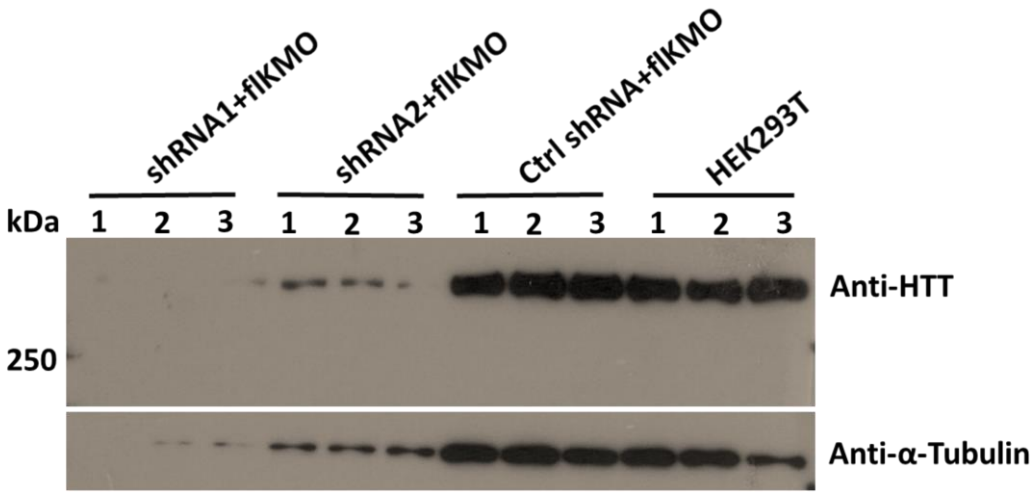

Figure 4-38 Effect of optimal shRNA knockdown of HTT-FL in HEK293T cells.
Cells were co-transfected with 0.175 µg of flKMO and 0.35 µg of shRNA1, shRNA2 or control shRNA, each in triplicate, for 72 hr. Lysates were blotted and probed with anti-HTT, 4C8 antibody (MAB2166); and anti-α-Tubulin antibody (sc-8035) was used as a loading control (sc-8035). shRNA1 and shRNA2 knockdown of HTT-FL had detrimental effect on α-tubulin expression and quantification was not possible.

4.3 Discussion

In this chapter, I mainly investigated KMO interactions initially with the KIPs, then with HTT. Extensive optimisation of the BiFC assay as well as detailed localisation studies were carried out to support the findings, as discussed in the following sections.

4.3.1 Expression of KIPs and their interaction with KMO

KIPs were identified from a yeast screen and in order to validate their interactions in mammalian systems, the BiFC approach was used. As discussed earlier (4.1.2), the success of generating BiFC construct pairs depends on the orientation of fusion protein to the fluorescent fragments as well as the flexibility of resulting constructs. Repici *et al.* (2013) previously used the flexible linker $(GGGGS)_2$ in our laboratory to covalently join DJ-1 protein to either GN or CC (Repici *et al.*, 2013), therefore the same linkers were used to construct KMO and KIPs BiFC constructs. However, interactions of KMO with KIPs were inconclusive due to the low expression of KIPs in HEK293T cells. Inefficient expression of KIPs might be attributed to the $(GGGGS)_2$ linker, as it can result in poor expression, compromised bioactivity and degradation of the fused protein (Chen *et al.*, 2013; Kerppola, 2006a). This might be due to the flexibility of the linker which makes it incapable to separate protein domains and reduce their interference effectively (Chen *et al.*, 2013). Several studies have reported expression issues with the GGGGS linker, for example: fusion of granulocyte colony stimulating factor (G-CSF) and transferrin (Tf) via $(GGGGS)_3$ prevented G-CSF-Tf expression, whereas with the insertion of a rigid helical linker $LEA(EAAAK)_4ALEA(EAAAK)_4ALE$ between the two proteins, high expression and activity were achieved (Amet *et al.*, 2009). In another study, the protein G domain that has immunoglobulin binding capability was fused to *Vargula* luciferase via a GGGGS linker which led to unrecoverable binding activity of the protein G which was restored by the use of three α-helices of protein A instead (Maeda *et al.*, 1997). In addition, Chen *et al.* (2013) examined different lengths of $(GGGGS)_n$ (n = 1,2 and 4) linker used to fuse penicillin amidase to a chaperon and found that the longest linker resulted in enzymatic activity comparable to the free enzyme, implying that length of flexible linkers can be optimised to achieve the desired length that would keep the fused proteins apart and retain activity (Chen *et al.*, 2013). Thus, although rigid linkers seem to support expression and stability of their fused proteins, long flexible linkers can also do. In the BiFC context, a rigid linker may not

facilitate the interaction and therefore the most appropriate investigation would be re-constructing KIPs fusion to GN without a linker (similar to the HTT-VN constructs used to study KMO-HTT interactions) as well as untagged KIPs. This would also confirm if the reason behind the low expression was the flexible linker introduced between the proteins.

4.3.2 Complementation of CC and VN fluorescent fragments and effects of over expression of mHTT-VN

Interaction of KMO and HTT in mammalian cells was extensively characterised in this chapter. This interaction was first studied using the BiFC technique in living HEK293T cells. BiFC fluorescent protein fragments CC and VN were fused to flKMO and HTT, respectively. Typically, when constructing BiFC plasmids, a split fluorescent protein is used such as GFP. However, BiFC complementation efficiency is enhanced when using other combinations of fluorescent protein fragments derived from Venus and Cerulean as identified by Shyu *et al.* (2006). Their work demonstrated that the new combination between CC155 of ECFP and VN173 of Venus and Cerulean were the best combination, leading to higher complementation efficiency and lower signal bleed-through. Moreover, only a small amount of BiFC plasmids is needed for transfection by this approach, which also eliminates the requirement of incubation of the cells at 30ºC prior live imaging (Shyu *et al.*, 2006). Therefore CC155 was used, instead of VC of Venus, to complement VN158 when studying the flKMO and HTT interaction. The CC155 and VN158 combination emission spectrum was determined at 510 nm by Olympus confocal microscopy, FV1000. This is very comparable to the previously published observation where combination of C155 of ECFP and N173 of Venus resulted in a spectra that emits light at 513 nm (Shyu *et al.*, 2006).

The BiFC fluorescence complementation assay is based on co-transfecting the cells with BiFC plasmids together with a plasmid expressing an intact fluorescent protein (e.g. RFP) to enable the selection for RFP expressing (transfected) cells. The ratio intensity between the BiFC green signal and RFP is often used as quantitative analysis of the BiFC complementation efficiency per condition (Kerppola, 2006a; Repici *et al.*, 2013), with the obvious condition that the RFP signal variation among different wells is very low. However, when using flKMO-CC and HTT-VN as a BiFC pair, the RFP expression fluctuated between wells thus leading to alteration of the ratio intensity not

due to a variation of the total green intensity. I was able to demonstrate that signal intensity of RFP is affected by the presence of HTT-VN. Thus in this study, quantification was solely based on the BiFC total green intensity which was divided by cell area to give mean green intensities to quantify fluorescence complementation. In addition, flKMO-CC expression was investigated when co-transfected with HTT-VN constructs: my results indicated that flKMO-CC expression increased in the presence of 97Q-VN and decreased in the case of 46Q-VN. Although it is well-known that transcriptional dysregulation of several genes is observed upon expression of mHTT (Sugars and Rubinsztein, 2003), it is not clear how it effects expression of RFP and flKMO-CC when they are expressed under the CMV promoter. Moreover, there is some evidence that over expression of exon 1 fragments reduce endogenous HTT-FL expression (Futter *et al.*, 2009), my data demonstrated that over expression of HTT-VN constructs along with flKMO-CC did not majorly change endogenous HTT-FL expression. This makes it unlikely for transcriptional dysregulation to be behind the differential expression of exogenous proteins. One could argue that induction of autophagy by 46Q-VN may clear up some of flKMO-CC that is interacting with HTT, while defects in clearance machinery were attributed to 97Q-VN aggregation thus explaining why flKMO-CC was not affected. However, this hypothesis is not supported by a reduction in 46Q-VN levels, and flKMO-CC levels were increased when co-expressed with 97Q-VN, unlike flKMO-CC co-expressed with the 19Q-VN. Thus, the mechanism of how HTT-VN affects these proteins' expression remained obscure. However, it did not seem to affect the interaction trend exhibited between flKMO-CC and HTT-VN.

4.3.3 KMO-HTT interaction through the BiFC system and beyond

The KMO-HTT interaction demonstrated here was mainly BiFC based, including the biochemical validation where BiFC constructs were used. Hence further validations are needed such as the use of untagged exon 1 fragments and flKMO as well as endogenous proteins. This is particularly important as fusing HTT to VN affected its sub-cellular localisation, as it will be discussed in Section (4.3.5). In addition, the BiFC signal of the background was detectable due to the re-association of CC and VN. However, it was significantly lower than KMO-HTT interaction signal. Furthermore, it is possible to minimise the background level by fusing the BiFC backbone to a peptide/protein that does not interact with the protein of interest (Kerppola, 2006b). Indeed, the use of VN-

Tau ΔK280 instead of the VN-backbone provided less background signal (data not shown). Some studies demonstrated that Venus fragments (VN 1-210 aa and VC 210-238 aa) are the most efficient in rescuing the background level (Gookin and Assmann, 2014; Ohashi *et al.*, 2012). Finally, the BiFC approach was unfortunately not successful at elucidating interactions of flKMO-CC with HTT-FL. As HTT-FL is a huge protein of ~350 kDa, the dynamic and structure of HTT-FL-VN may not favour such an interaction, but does not necessarily mean absence of this interaction.

To overcome BiFC limitations, one could consider using the micro-tagging split-GFP system that has been characterised in bacterial and mammalian cells. This new system is based upon two short GFP fragments: GFP10 (194-212 aa) and GFP11 (213-233 aa) to be fused to the proposed interacting partners, and a third long detecting fragment GFP1-9 (1-193 aa). The latter fragment was stably expressed in HEK293 cells, and the GFP10 and GFP11 fused to the interacting proteins were expressed transiently. Only when proteins interact GFP10 and GFP11 reconstitute with GFP1-9 to give a fluorescent GFP (Cabantous *et al.*, 2013). The sensitivity of detecting the interaction via this tripartite system and employability of small GFP fusions will make studying protein interactions more feasible and efficient.

4.3.4 CR interference with BiFC signal

Although some evidence demonstrated the presence of mitochondrial N-terminal mHTT aggregates (Panov *et al.*, 2002; Yu *et al.*, 2003), the absence of fluorescently visible HTT aggregates when flKMO-CC and HTT97Q-VN were co-transfected indicates that only soluble mHTT interacts with flKMO, and thus sequestering of flKMO into HTT aggregates is excluded. In order to further characterise the interaction of flKMO-CC with 97Q-VN and address whether the interaction was hindered by the increase in the aggregated form of 97Q-VN, CR was used to inhibit aggregation while performing BiFC. Initially, CR was used on cells expressing the 97Q BiFC pair, where it successfully inhibited aggregation and blocked the BiFC pair association. This suggests that CR associates with 97Q and prevents its oligomerization. However, the levels of soluble 97Q did not seem to increase upon CR treatment (requiring further validation with densitometry), which was also previously shown by Heiser *et al.* (2000). Interestingly, monomeric mHTT lacking the polyP region treated with CR was targeted to complete proteolytic degradation when treated with proteinase K, unlike its

aggregated counterpart that was not treated with CR (Heiser *et al.*, 2000). This might explain the decrease in the aggregated form and lack of major change in the soluble HTT. This proposed explanation is not in line with my findings, as flKMO-CC interaction with 97Q-VN is reduced upon CR treatment. However, our microscopy studies indicated that flKMO-CC interacts with soluble 97Q-VN, and thus their interaction should not be decreased significantly when treated with CR. The mechanism of CR inhibition is widely believed to be by binding to the protein β-sheet structures through a combination of hydrophobic interactions and thus preventing protein aggregation (Frid *et al.*, 2007). Nevertheless, Khurana *et al.* (2001) demonstrated that CR binds to native proteins of all classes including α-helical, β-sheet and α-helical/ β-sheet configurations (Khurana *et al.*, 2001). Therefore, one cannot exclude CR binding to flKMO [which is composed of five β-sheets and four α-helices (Amaral *et al.*, 2013)] and preventing it from interacting with 97Q-VN which is also bound to CR. Based on the BiFC outcome, CR treated cells expressing flKMO-CC and 97Q-VN hardly exhibited any BiFC signal (data not shown), although their BiFC signal was significantly different from the background level, which was increased upon CR treatment. This could be explained by CR spectra properties, whose absorption is maximal at 490 nm in aqueous solution. However, upon binding to β-sheet structures the maximal absorption shifts to 540 nm (Wu *et al.*, 2012). Moreover, when CR binds to native proteins the maximal absorption peak is around 525 nm, which was shown to be 10-fold less than the favourable configuration binding peaks of CR (Khurana *et al.*, 2001). In light of my findings, this explains the decrease in the BiFC signal in the case of flKMO-CC + 97Q-VN, where CR bound to 97Q-VN and almost completely prevented its interaction with flKMO-CC, but also bound less favourably to flKMO-CC and resulted in a shift to around 525 nm of the CR absorption. This 525 nm signal must have overlapped with 510 nm (the BiFC emission signal) and contributed to signal detection. For the flKMO-CC + VN backbone combination, CR bound to flKMO-CC, but also unbound CR of 490 nm absorption, may have contributed to the BiFC signal to some degree, which accounts for the increase in the background signal. This could be further confirmed with untransfected HEK293T cells stained with CR, where they should exhibit some signal, due to either free CR or endogenous native proteins bound to CR. Although our findings did not serve the purpose of the experiment due to the dye interference with the readout of the BiFC system, it showed a possibility of CR binding

to KMO. This further confirms the non-specificity of CR inhibitor binding under normal conditions.

4.3.5 Enhanced mitochondrial localisation of HTT

In this study, BiFC HTT proteins co-localised with mitochondria using confocal microscopy, which was further validated using TEM for 19Q-VN localisation. It was clear that when HTT was tagged with a fluorescent fragment it enhanced localisation to the mitochondria, whereas the WT HTT BiFC pair exhibited both cytosolic and mitochondrial localisation. Interestingly, 25Q tagged with full length GFP did not show mitochondrial localisation and mainly demonstrated a cytosolic signal. Rockabrand *et al.* (2007) however, showed that 44% of 25Q-GFP transfected in St12.7 fixed cells co-localised with mitochondria, while GFP alone did not localise to mitochondria (Rockabrand *et al.*, 2007). Indeed, localisation of fused proteins might be dependent upon the cell type and the fused fluorescent proteins. For example, Venus may favour localisation of HTT to mitochondria, as the VN backbone was partially localised to mitochondria, and may thereby have increased 19Q-VN mitochondrial localisation (>70%). The Venus tagging system thus enriches mitochondrial HTT localisation and fortuitously helped address its interaction with KMO.

It is vital to note that although HTT mitochondrial localisation is still debatable, it has been reported in the literature. Several electron microscopy studies showed N-terminal mHTT association with mitochondria: neuronal mitochondrial membrane of YAC72 transgenic mice brain (Panov *et al.*, 2002), cerebral cortex mitochondria of *Hdh* (150Q) knockin mice model. (Orr *et al.*, 2008), neuronal mitochondria of transgenic rat (tgHD) (Petrasch-Parwez *et al.*, 2007), and also on the surface and inside of degenerated mitochondria of R6/2 mice brain cortex (Yu *et al.*, 2003). Gutekunst *et al.* (1998) however showed, using quantitative analysis of electron microscopy studies, that about 10% of HTT normally associates with the mitochondria of rat brains. In addition, sub-fractionation studies of mitochondria from clonal striatal cell line revealed that both WT and mutant HTT-FL were associated with the outer mitochondrial membrane (Choo *et al.*, 2004). Furthermore, Kegel *et al.* (2005; 2009a; 2009b) investigated HTT association with membranes phospholipids and was able to show that both WT and mutant HTT-FL associate specifically to cardiolipin (a phospholipid specific to the inner mitochondrial membrane) (Kegel *et al.*, 2009a). Moreover, the region 171-287 aa

was required for maximal HTT association with cellular membranes (Kegel *et al.*, 2005; Kegel *et al.*, 2009a). These findings shed the light on the importance of testing flKMO interaction with HTT-FL, as full length HTT might be better associated with mitochondrial membranes, which will be investigated in the following chapter.

CHAPTER 5 INVESTIGATING THE INTERACTION OF KMO WITH ENDOGENOUS HTT-FL

5.1 Introduction

I demonstrated in the previous chapter that flKMO-CC and HTT-VN transfected in HEK293T cells interact in a polyQ dependent manner via the BiFC system. However, HTT-FL-VN failed to complement flKMO-CC using the same assay. For this reason, I decided to study endogenous HTT-FL instead of the transgenic version to ensure consistency in protein expression and avoid protein tagging. Thus, I needed a cell model that expresses both endogenous KMO and HTT-FL abundantly. Due to the low expression of KMO in the brain (Repici, unpublished data), one could employ cells derived from peripheral tissues – such as liver or kidney – where both endogenous KMO (Alberati-Giani *et al.*, 1997; Erickson *et al.*, 1992) and HTT-FL (Trottier *et al.*, 1995) are abundantly expressed. However, as a transient step, the use of immortalised cell lines enables easier manipulation and validation of the interaction. Lymphoblastoid cell lines (LCL) derived from a normal individual as well as an HD patient (with 42 CAG repeat) were available in house to validate expression, localisation and interaction of these proteins. As HEK293T cells also express endogenous HTT-FL, but lack the expression of endogenous KMO, transfected cells with flKMO enabled testing of the interaction between HTT-FL and flKMO in HEK293T cells. To identify stable interacting complexes from protein lysates, co-IP was used as an approach where antibody-conjugated beads co-immunoprecipitated one protein (HTT-FL when anti-HTT is used), as well as its interacting partner (KMO, which can be revealed using anti-KMO). One disadvantage of the co-IP method is that it requires cell lysates and thus it might facilitate interaction of protein partners that were not in close proximity in the intact cells. Although cell fractionation is a way to avoid such a problem, I here chose to first confirm a possible co-localisation of endogenous KMO and HTT-FL using microscopy techniques prior to performing co-IP.

5.2 Results

5.2.1 Validation of endogenous protein expression in cell lines

Protein extracts of LCL cell lines (WT and HD) were used to confirm endogenous KMO and HTT-FL expression by immunolabelling with anti-KMO or anti-(HTT) 4C8 antibody, respectively. As shown in Figure 5-1 (A and B), endogenous KMO bands of ~ 49 kDa were detected in WT LCL and HD LCL using two different KMO antibodies. Both antibodies are capable of detecting KMO expressed in WT and HD LCL (one cell line was used as a representative for each antibody) (Figure 5-1A and B). Expression of endogenous HTT-FL was detected in both WT and HD LCL cells as shown in Figure 5-1C.

HEK293T cells lack endogenous KMO but express endogenous HTT-FL, as demonstrated earlier (Section 3.2.3) and (Section 4.2.17), respectively.

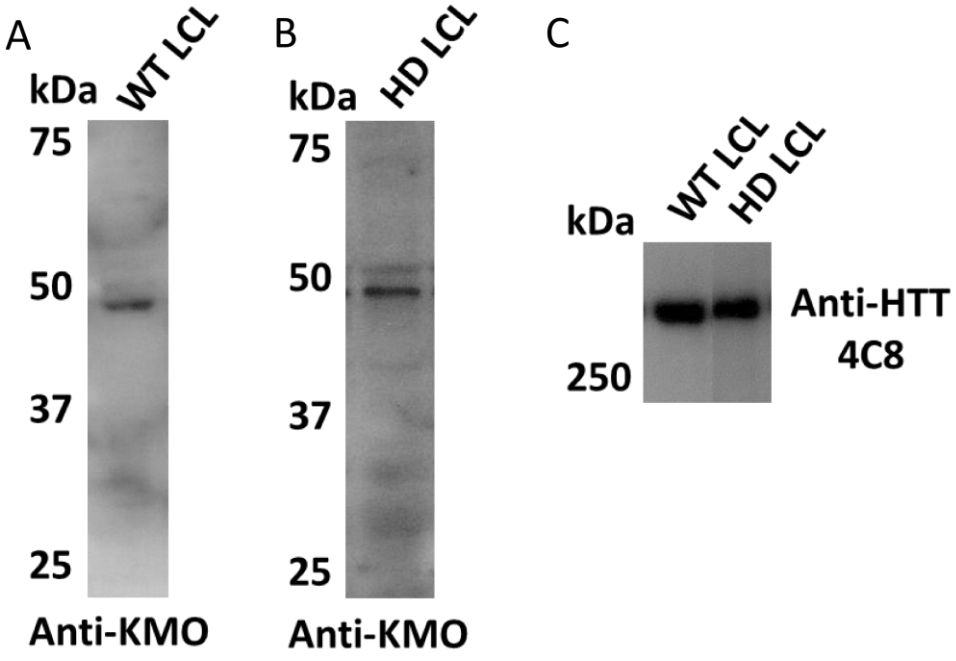

Figure 5-1 Expression of endogenous KMO and HTT-FL in LCL cell lines.
WT/HD LCL protein extracts were loaded at 50 µg and the blots were probed with: A) anti-KMO antibody (ab93195), B) anti-KMO antibody (ab130959), and C) anti-HTT, 4C8 antibody (MAB2166). Endogenous KMO expression was detected at ~ 49 kDa (A and B), whereas endogenous HTT-FL was ~ 350 kDa (C).

5.2.2 Characterisation of the sub-cellular localisation of endogenous KMO and HTT-FL

Insight into the localisation of the endogenous proteins is important to address the possibility of their interactions. Therefore, the distribution of endogenous KMO and HTT-FL in LCL (WT and HD) as well as endogenous HTT-FL in HEK293T cells was examined using both confocal microscopy and TEM, with the main purpose of elucidating the possible mitochondrial localisation of these proteins.

5.2.2.1 Mitochondrial morphology in LCL cells

Prior to performing ICC on LCL cells in suspension, live cells were stained with MitoTracker Red CMXRos and visualised under confocal microscopy. As shown in Figure 5-2A and B, LCL appeared as small rounded cells and were not feasible to use confocal immunolabelling to characterise protein localisation. For this reason TEM was used to provide enhanced ultrastructure as well as a clear sub-cellular localisation.

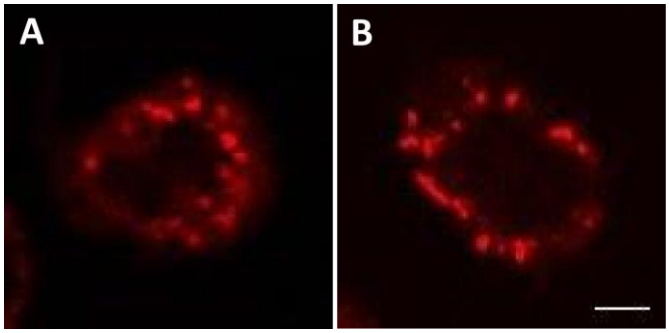

Figure 5-2 Mitochondrial morphology of LCL cells using confocal microscopy.
Live cells were stained with MitoTracker Red CMXRos (M-7512). A) WT LCL and B) HD LCL. Scale bar = 4 µm.

5.2.2.2 Cellular distribution of endogenous HTT-FL in HEK293T cells

HEK293T cells were stained with MitoTracker, fixed and immunolabelled with anti-HTT (4C8) to probe for endogenous HTT-FL. HTT-FL signal looked punctate and partially co-localised with the mitochondrial signal as illustrated in the merge image in Figure 5-3. Correlation between the HTT-FL (green) and mitochondrial (red) signals was estimated as 52% of mitochondrial co-localisation (Figure 5-3); whereas the average correlation of 10 optical z-sections was 49% ± 2.9, confirming a partial localisation of endogenous HTT-FL at the mitochondria (data not shown). Thus, a subset of endogenous HTT-FL co-localises with mitochondria in HEK293T cells.

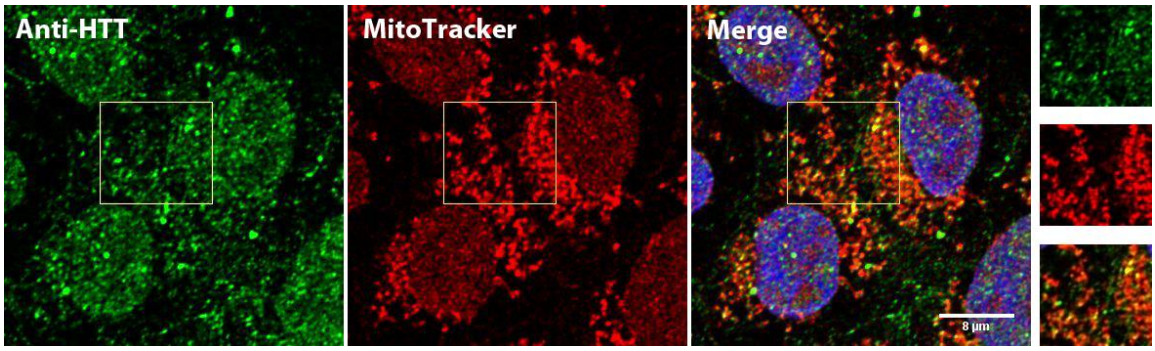

Figure 5-3 Co-localisation analysis of endogenous HTT-FL with mitochondria on deconvolved confocal optical z-sections of HEK293T cells.
Left panel: HTT-FL immunolabelling using anti-HTT (4C8) antibody (MAB2166) (Alexa Fluor 488). Middle panel: MitoTracker Red CMXRos (M-7512) staining. Right panel: merge image of the HTT-FL and mitochondrial signals. Nuclei were stained with Hoechst 33342. Scale bar = 8 µm. The selected regions of interest on the images were used for co-localisation analysis, using JACoP plugin ImageJ. Zoomed-in views are presented to the right of the panels. HTT-FL signal is punctate and co-localises partially with the mitochondrial signal, 52%.

5.2.2.3 TEM quantitative labelling of HTT-FL in cell lines

For TEM studies of endogenous HTT-FL in LCL and HEK293T cells, anti-HTT (4C8) antibody was used to label the cells with 30 nm immunogold particles. Images were taken at 12K as 4C8 labelling was not intense and the criteria of at least five immunogold particles per cell was set to allow the analysis of 30 cells from 30 different images.

Representative images of 4C8 labelled WT and HD LCL cells are shown in Figure 5-4; images were taken at 25K. Figure 5-4A shows HTT-FL localisation in WT LCL cells: immunogold particles were localised to mitochondria and in the cytoplasm (Figure 5-4A). HD LCL cells also exhibited mitochondrial and cytosolic localisation of HTT-FL (Figure 5-4B). The counting of the immunogold particles labelling HTT-FL associated with mitochondria of WT and HD LCL cells found the proportion of HTT-FL at the mitochondria to be ~7.2% and 10.5% for WT and HD LCL cells, respectively. In addition, WT and HD LCL cells showed HTT-FL minor nuclear immunogold labelling (data not shown).

Similarly, HTT-FL localised to mitochondria and cytoplasm in HEK293T cells (Figure 5-5). However, quantification of the mitochondria-associated HTT-FL immunogold particles suggested that ~21.9% of the labelled HTT-FL was mitochondrial. These data confirm the presence of endogenous HTT-FL at mitochondria.

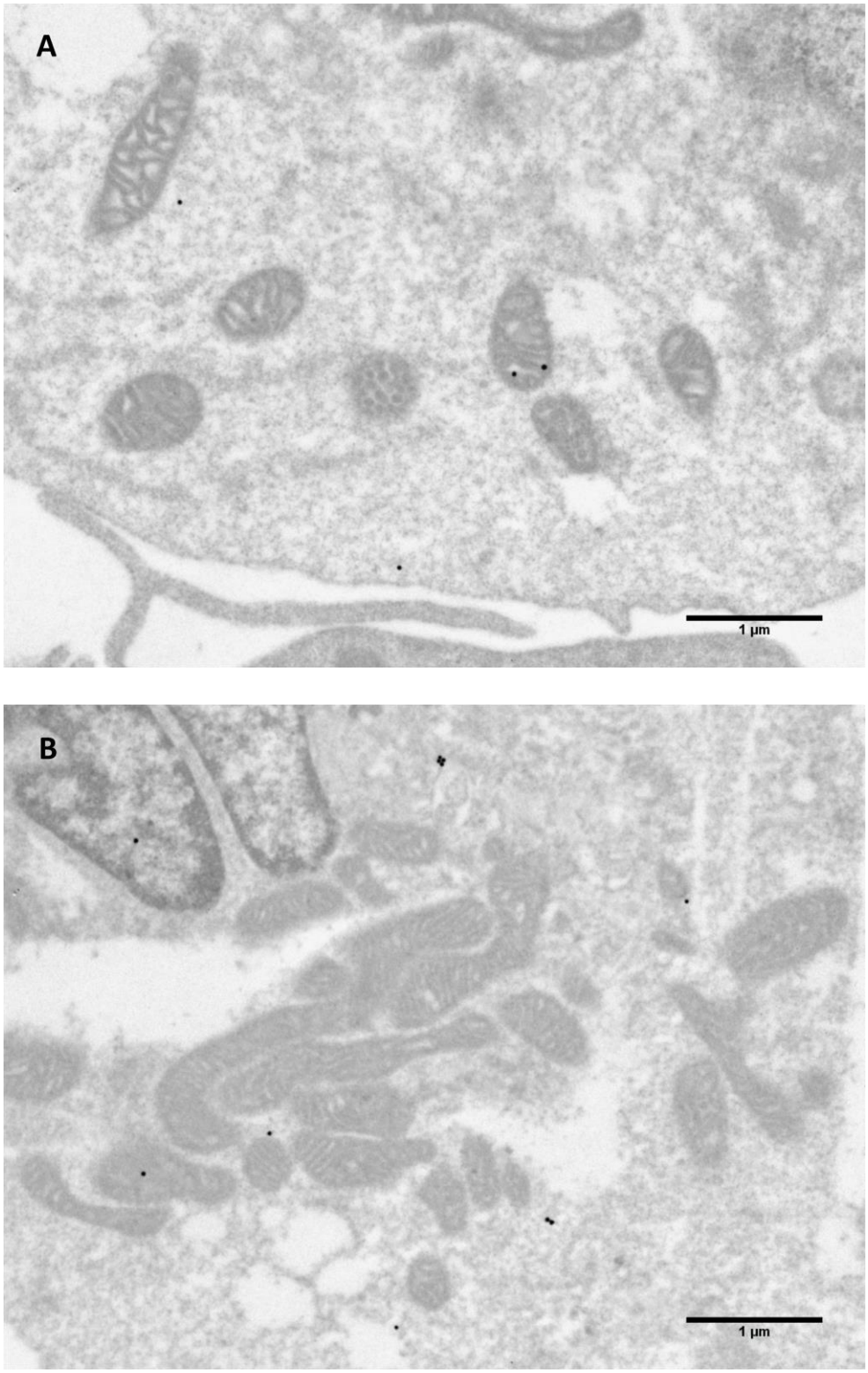

Figure 5-4 Electron micrograph of endogenous HTT-FL in LCL cells.
Immunogold labelling of cells using anti-HTT, 4C8 antibody (MAB2166). A) WT LCL cells, and B) HD LCL cells. Scale bar = 1 µm.

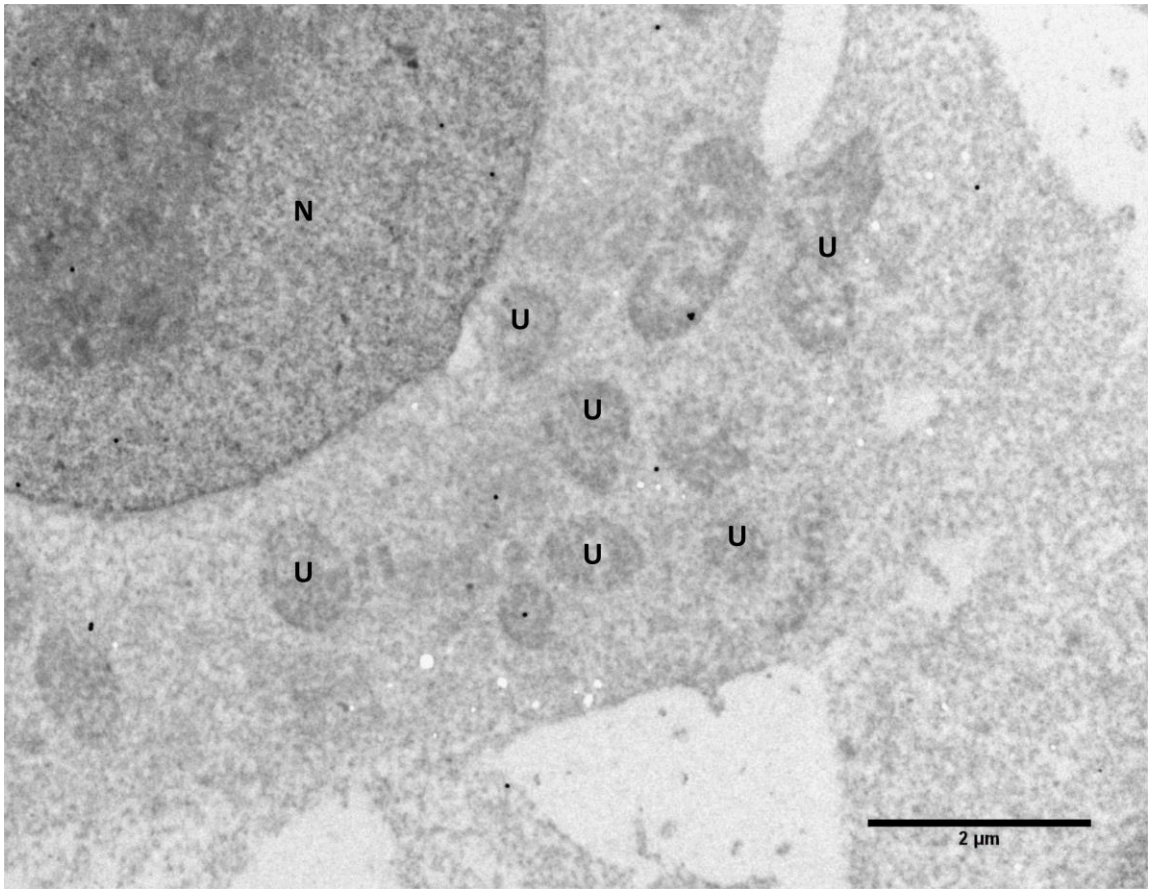

Figure 5-5 Electron micrograph of endogenous in HEK293T cells.
HTT-FL immunogold labelling was using anti-HTT, 4C8 antibody (MAB2166). Scale bar = 2 µm. Mitochondrial structures are identified by gold particles. Unlabelled mitochondria are designated with the letter 'U'. Nuclei are denoted with the letter 'N'.

5.2.2.4 Quantification of mitochondrial association of endogenous KMO in LCL cells

For localisation studies on endogenous KMO, both WT and HD LCL cells were labelled with 10 nm immunogold particles using four different KMO antibodies. Images were taken at 40K for analysis to allow visualisation of the small particles.

The first two KMO antibodies (10698-1-AP and HPA031115) showed low level scattered immunogold labelling which appeared to be non-specific background signal, and exhibited very little mitochondrial labelling. Moreover many particles were localized to the nucleus in case of the HPA031115 antibody (data not shown). The third KMO antibody (ab130959) exhibited reasonable labelling which seemed more concentrated around and at the mitochondria, but immunogold particles were noticed also in the cytoplasm and nucleus (Figure 5-6A and Figure 5-7A for WT and HD LCL labelling respectively). The fourth KMO antibody (ab93195) also showed mitochondrial localisation as well as some cytosolic and nuclear signal for WT LCL cells (Figure 5-6B) and HD LCL cells (Figure 5-7B). Thus, none of the antibodies showed an exclusive mitochondrial localisation, and surprisingly even the partial mitochondrial labelling was not only present at the outer surface, but throughout these organelles.

The latter antibody (ab93195) seemed to be the most reliable and was thus used for analysis. Quantification studies of mitochondrial localisation of endogenous KMO in WT and HD LCL cells showed that mitochondrial association of KMO is ~37.5% in WT LCL, while ~26.5% in HD LCL. Although these data implies that KMO might be localised elsewhere in addition to mitochondria, it gives insight into the importance of studying endogenous protein localisation using TEM microscopy technique.

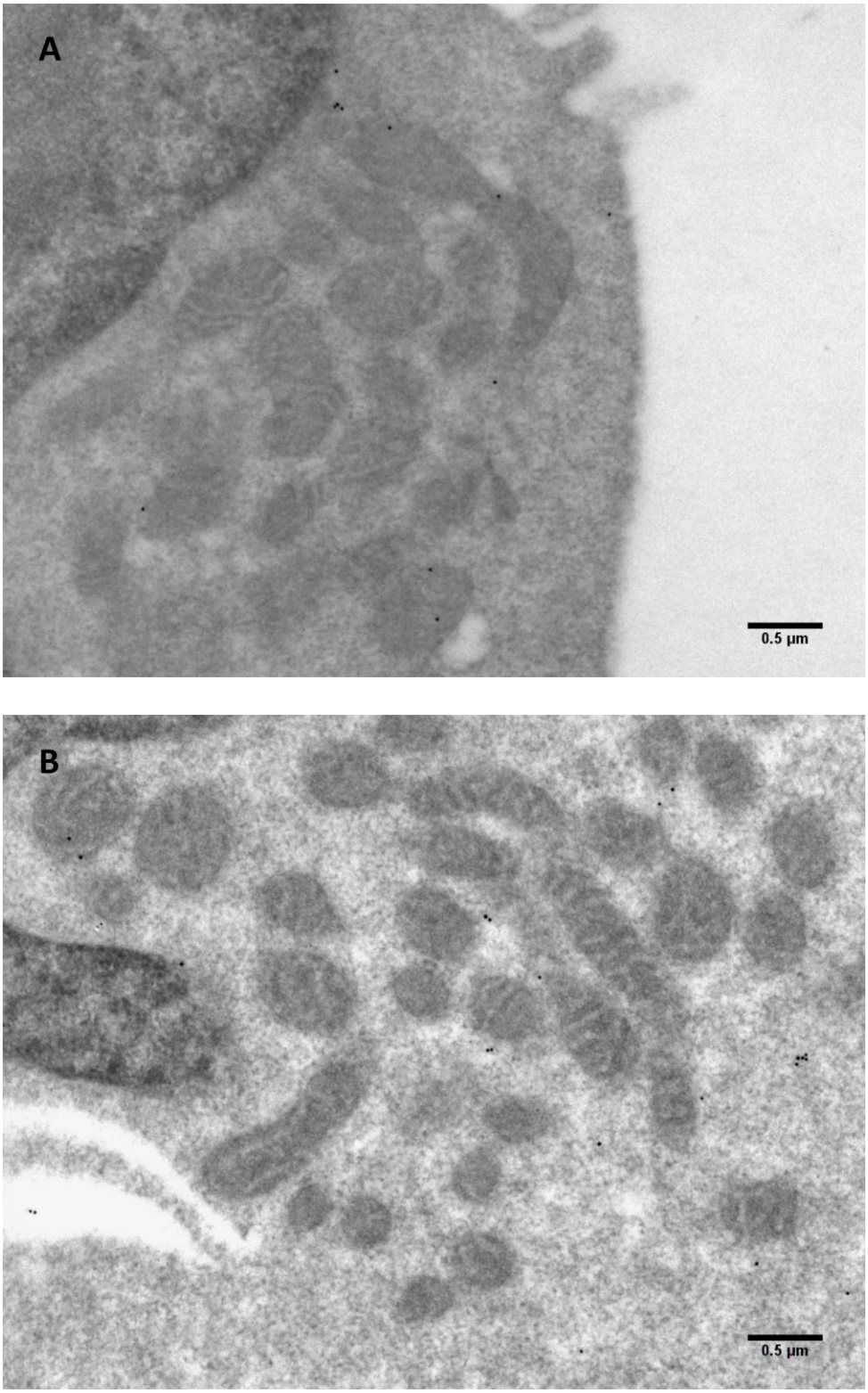

Figure 5-6 Electron micrograph of endogenous KMO in WT LCL.
Immunogold labelling of cells, using A) anti-KMO antibody (ab130959). B) anti-KMO antibody (ab93195). Scale bar = 0.5 µm.

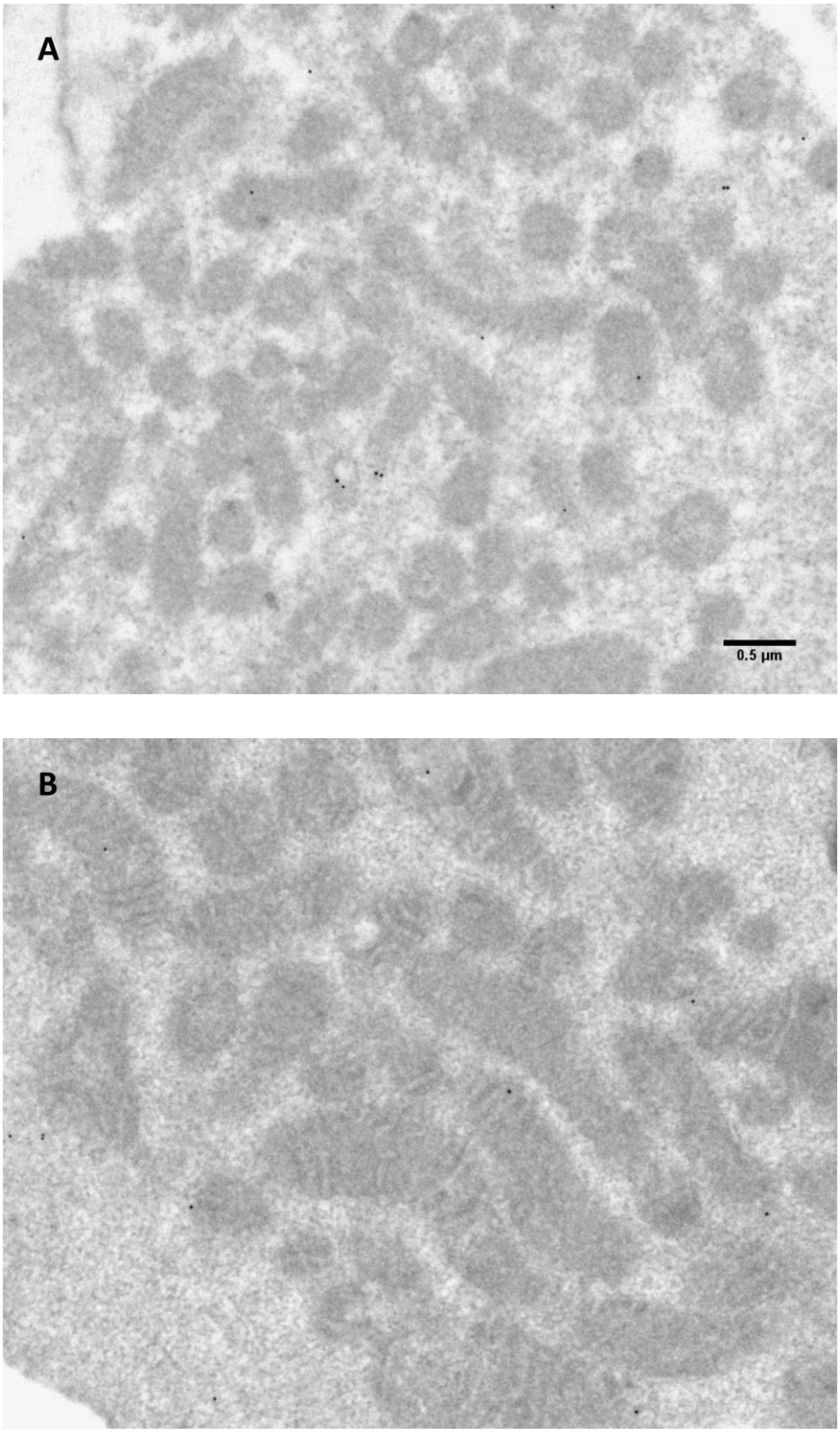

Figure 5-7 Electron micrograph of endogenous KMO in HD LCL.
Immunogold labelling of cells, using A) anti-KMO antibody (ab130959). B) anti-KMO antibody (ab93195). Scale bar = 0.5 µm.

5.2.3 Investigating endogenous HTT-FL protein interactions

Our TEM data indicate that both endogenous KMO and HTT-FL are found at the mitochondria, and belong to the same sub-cellular compartment, which is an essential condition for protein-protein interaction. To further validate this hypothesis, co-IP was used to explore endogenous HTT-FL interaction in LCL cells (WT and HD) with endogenous KMO, as well as HTT-FL in HEK293T cells exogenously expressing flKMO.

5.2.3.1 Co-IP on LCL cells

To study HTT-FL and KMO interaction in WT and HD LCL, HTT-FL was first co-immunoprecipitated using anti-HTT (4C8) antibody under normal conditions (refer to methods in Section 2.2.2.11.2). As shown in Figure 5-8A HTT-FL was detected in the protein input (IN) and flow-through (FT) or unbound fraction. It was also well precipitated in the IP fraction of both WT and HD lanes when the antibody-conjugated beads were used. The unconjugated beads lane for the WT sample shows that some HTT-FL bound to the beads even though lysates were pre-cleared using the same beads. Only one reliable anti-HTT antibody was available in house to detect HTT-FL, and thus was used for both HTT-FL co-immunoprecipitation and revealing HTT-FL (Figure 5-8A). When membranes were probed with the KMO antibody, a relatively low level of KMO was detected in the IN and FT, and no KMO was co-immunoprecipitated with HTT-FL. The KMO blot showed ambiguous detection in the IP fraction with a strong band >50 kDa that does not correspond to IgG as it is present in both conjugated and unconjugated beads. (Figure 5-8B). I next decided to use a GAPDH antibody to test for its interaction with HTT-FL. As presented in Figure 5-8C, expression of GAPDH in the IN and FT was robustly detected, but GAPDH was not found in the IP fraction as shown in Figure 5-8C. In this case the IgG 25 kDa and 50 kDa bands were visible for the anti-body-conjugated beads, suggesting that the background previously observed was indeed due to the KMO antibody. HTT-FL precipitation was also performed under more stringent conditions; as detailed in the methods (Section 2.2.2.11.2) in order to eliminate the unspecific bands detected when revealed with KMO antibody, however no improvement was achieved (data not shown).

Next, I tried to co-immunoprecipitate KMO under normal conditions using different KMO antibodies and detect it with the same antibody used above. Although KMO

expression was detected in all IN and FT lanes, the IP fraction exhibited the same indistinct bands and only with the antibody-conjugated beads which results in even more uncertainty. Moreover, the, absence of KMO bands in the IP fraction suggests that the antibody is not working for co-IP purposes (Figure 5-9A), which was further confirmed by the blank IP blot obtained using 4C8 antibody (Figure 5-9B).

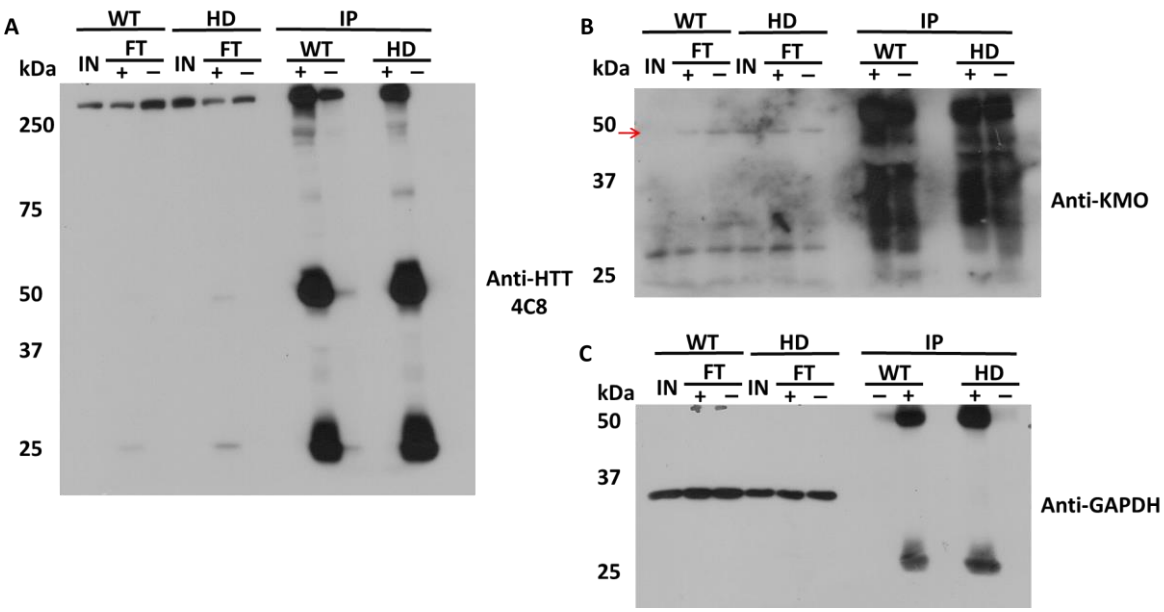

Figure 5-8 Co-IP of HTT-FL on WT and HD LCL cells.
Cells lysates were co-immunoprecipitated with anti-HTT, 4C8 antibody (MAB2166). A) Expression and confirmation of precipitation of HTT-FL using 4C8 antibody. Possible protein co-immunoprecipitation was revealed using B) anti-KMO (ab93195) and C) anti-GAPDH (sc-32233). Co-IPs were performed under normal conditions. Lanes assigned with + or – indicate the use of antibody-conjugated beads or unconjugated beads, respectively. IN = input and FT = flow-through.

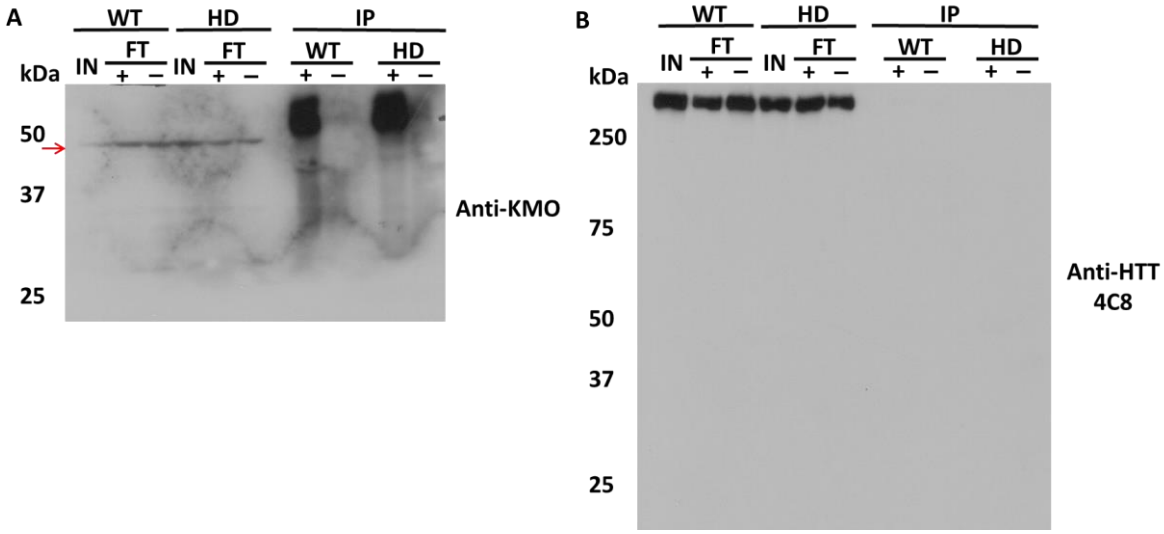

Figure 5-9 Co-IP of KMO on WT and HD LCL cells.
Co-IP of KMO on cells lysates was performed using anti-KMO (ab130959). A) Absence of KMO precipitation was confirmed using anti-KMO (ab93195). B) Lack of co-immunoprecipitation of HTT-FL using anti-HTT, 4C8 antibody (MAB2166). Co-IPs were performed under normal conditions. Lanes assigned with + or – indicate the use of antibody-conjugated beads or unconjugated beads, respectively. IN = input and FT = flow-through.

5.2.3.2 Co-IP of HTT-FL in HEK293T cells

I next analysed HTT-FL-KMO interaction by co-IP in HEK293T expressing exogenous flKMO for 48 hr after transfection. Again, both normal and stringent conditions were used. The results displayed in Figure 5-10 were purposefully the stringent one to provide a wide representation of the work done. Endogenous HTT-FL precipitation was detected in the lanes where antibody-conjugated beads were used. The additional band ~ 100 kDa could be the BSA used to block the beads prior to conjugation. However, it is higher than the expected molecular weight for BSA of ~ 66.5 kDa (Figure 5-10A). Figure 5-10B shows the KMO detection blot obtained by using a KMO antibody (different from the two used with LCL cells). Again, flKMO expression is detectable in IN and FT lanes, whereas the IP fraction again shows the >50 kDa band, which was below the size of flKMO, just between flKMO and the sub-band beneath it (Figure 5-10B).

Moreover, on the same samples used to study HTT-FL interaction with flKMO under normal conditions, GAPDH co-immunoprecipitation with HTT-FL was also examined. Figure 5-11A shows HTT-FL precipitation confirmation, where a faint band of HTT-FL was also detected with unconjugated beads despite pre-clearing the lysates (Figure 5-11A). This was also observed in the WT LCL as well (Figure 5-8A), which might suggest that WT HTT-FL is more prone to associate to agarose beads. GAPDH expression was detected only in the IN and FT lanes and not in the IP fraction, which corroborates the finding in the LCL cells.

In conclusion, although HTT-FL co-IP was successful, these experiments do not allow us to conclude on the HTT-KMO interaction in LCL and HEK293T cells. This does not necessarily mean a lack of KMO interaction with HTT-FL, as will be discussed in the following Section (5.3). GAPDH however clearly does not interact with HTT-FL in both LCL and HEK293T cells.

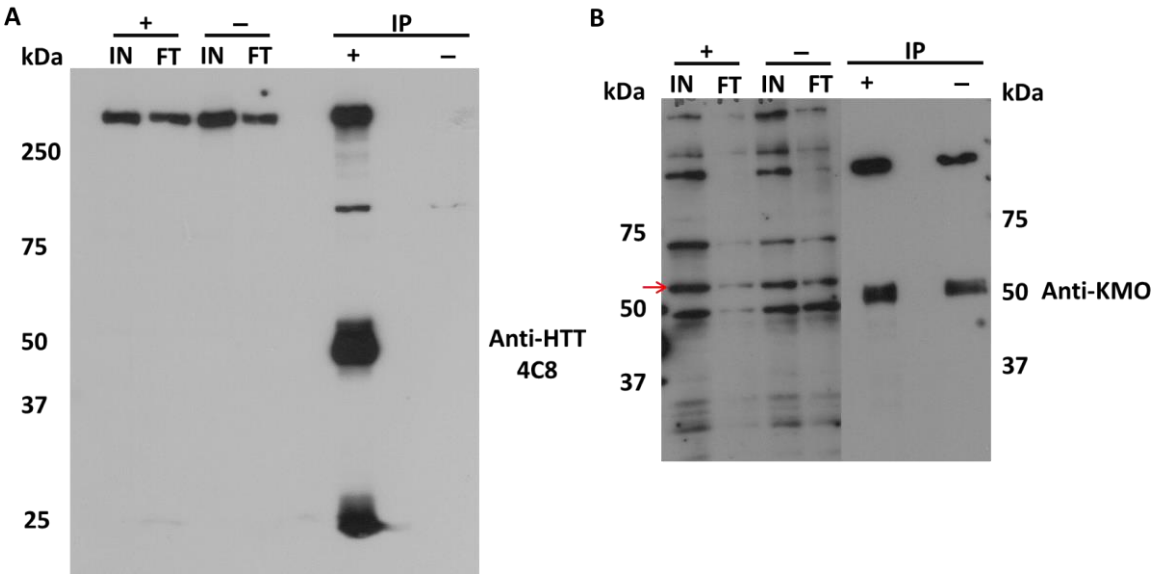

Figure 5-10 Co-IP of HTT-FL on HEK293T cells expressing flKMO.
Co-IP of HTT-FL was performed using anti-HTT, 4C8 antibody (MAB2166) on HEK293T cells lysate. A) Confirmation of HTT-FL co-immunoprecipitation using 4C8 antibody. B) Anti-KMO antibody (10698-1-AP) was used to reveal absence of co-immunoprecipitation. Co-IPs were performed under stringent conditions. Lanes indicated with + or – correspond to the use of antibody-conjugated beads or unconjugated beads, respectively. IN = input and FT = flow-through.

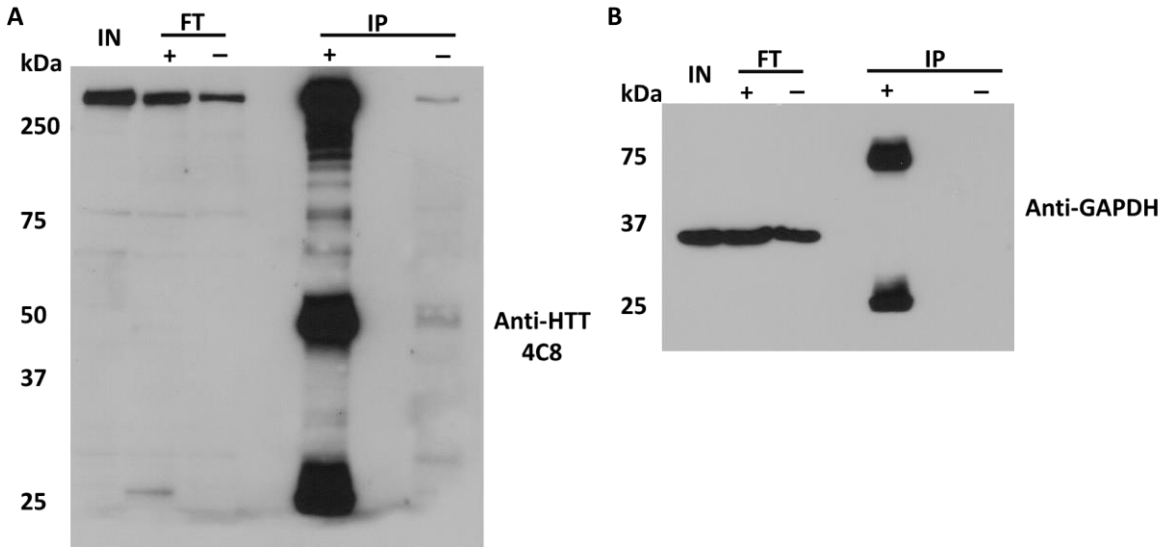

Figure 5-11 Co-IP of HTT-FL on HEK293T cells expressing flKMO, for GAPDH co-immunoprecipitation.
Co-IP of HTT-FL performed using anti-HTT, 4C8 antibody (MAB2166) on HEK293T cells lysate. A) Confirmation of HTT-FL co-immunoprecipitation using 4C8 antibody. B) Lack of co-immunoprecipitation of GAPDH revealed using anti-GAPDH (sc-32233). Co-IPs were performed under normal conditions. Lanes indicated with + or – correspond to the use of antibody-conjugated beads or unconjugated beads, respectively. IN = input and FT = flow-through.

5.3 Discussion

The aim of this chapter was to validate the interaction of endogenous KMO and HTT-FL, thus a cell model that express both was needed. LCL cells were here used based on validation of KMO expression using immunoblotting. To our knowledge, aside from monocyte derived cells (Chiarugi *et al.*, 2001a; Jones *et al.*, 2015), KMO expression and activity in lymphocytes has not been studied prior to the work presented here. Although KMO expression did not seem to be very high in LCL, it was sufficient for my experimental needs.

Several reasons could explain the low level of KMO in LCL. Wilson *et al.* (2014) analysed the expression of human KMO in bacterial cells in both the soluble and insoluble fractions found more KMO in the insoluble pellet (Wilson *et al.*, 2014). This is explained by the tendency of KMO to associate with the mitochondrial membrane. In my experiments, only the supernatant of cell extracts was used for protein analysis by SDS-PAGE and therefore not all endogenous KMO may have been extracted from LCL. On the other hand, a very recent study showed that KMO activity was not induced in human lymphocytes upon INF-γ stimulation (doses ranged from 0-1000 IU/ml) for 24, 48 or 72 hr, using flow cytometry; suggesting the lack of expression of KMO in lymphocytes (Jones *et al.*, 2015). A possible hypothesis to explain this discrepancy could be that LCL cells are immortalised and genetic alteration may have occurred and led to KMO expression, as both monocytes and lymphocytes are derived from the same haematopoietic progenitor stem cells. Moreover, it has been shown that KMO exhibits tumour-promoting effects by regulating proliferation, migration and invasion of hepatocellular carcinoma (Jin *et al.*, 2015), which implies that KMO expression might be needed for proliferation of LCL cells, providing a model to study endogenous proteins in a cell line context.

Endogenous HTT-FL expression in LCL cells, however, was previously established, as it was detected as one band in WT LCL and two bands in HD LCL corresponding to WT HTT and mHTT. The two bands were observable on a 4% SDS-PAGE when the difference in the CAG repeat between WT HTT and mHTT is >40 (Trottier *et al.*, 1995). In this study, 10% SDS-PAGE was used to immunoblot HTT-FL and the difference would not have been detected as the mHTT used here has only 42 CAG. This suggests that if interaction is to be detected between KMO and HTT-FL, the use of cells

homozygous for clearly distinguishable mHTT and WT HTT alleles in the cells/ tissues should be used so that interaction of WT HTT cannot be mistaken with mHTT.

The other issue encountered while characterising KMO localisation in LCL cells was that more than 60% of immunogold labelling was not mitochondrial, indicating other possible cellular localisations for endogenous KMO. It is not feasible to determine the reliability of the KMO antibodies employed when the labelling is widely spread of a mitochondrial protein. One possibility is that the epitope recognised by the antibodies cross-reacts with other proteins. This could be eliminated by using a quenching control, where the antibody is incubated with KMO protein prior to exposing it to the grid. If immunogold labelling of LCL cells persist with the quenched antibody, it means the labelling is unspecific (De Paul *et al.*, 2012). This control was not included in this study due to the requirement for purified KMO which was not practical to achieve. Moreover it seemed unlikely that all four antibodies were unspecific. Therefore, these findings could better be confirmed using sub-cellular fractionation studies.

However, another possible explanation that needs to be addressed here about the unusual KMO localisation is that it might be attributed to the presence of KMO splice isoforms. To date there are no studies suggesting that these isoforms are expressed *in vivo*. Moreover, the 452 aa KMO isoform lacks most of the sequence encoding for the first putative KMO TM domain. Although missing the second putative TM leads to mis-targeting of KMO to the mitochondria (Section 3.2.4.1), as well as lacking both TM domains (Hirai *et al.*, 2010; Wilson *et al.*, 2014), KMO localisation has not been investigated when only the first putative TM domain is deleted. Therefore further studies are needed to fine map KMO localisation. The idea of the presence of other KMO isoforms is also supported by Giorgini *et al.* (2013) , which found slight 3-HK production was still detected in KMO knockout mice.

In my work herein, KMO was not co-immunoprecipitated with HTT-FL in either LCL or in HEK293T cells, although in the second case flKMO was transfected into HEK293T cells which eliminates the lack of sufficient expression being a possible reason. The presence of the ambiguous band (>50 kDa) - when revealing with anti-KMO antibody - did not provide an informative conclusion on the interaction of KMO and HTT-FL, and requires mass spectrometry analysis to reveal its identity. One could also consider the use of a different bead matrix (e.g. sepharose or magnetic) instead of

agarose beads to possibly reduce nonspecific interactions, or the use of either flKMO-RFP or flKMO-CC in HEK293T cells to permit use of anti-tag antibodies. Furthermore, liver tissue from mice might be a better option to confirm any possible interaction between endogenous KMO and HTT-FL, as well as mHTT fragments, as KMO expression in WT mouse liver lysate was strongly confirmed (data not shown). However, as co-IP is based on immunoprecipitation of preformed complexes, weak and transit interactions may not be detected (Herrmann *et al.*, 2001), unlike the BiFC system which can stabilise such interactions (Kerppola, 2008). Therefore application of chemical cross-linking prior to immunoprecipitation might improve the interaction outcome (Herrmann *et al.*, 2001).

Finally, the results presented here on GAPDH and HTT interaction are in agreement with the literature: indeed, GAPDH interaction with HTT fragments was demonstrated to be stronger than HTT-FL, where HTT fragments were clearly detectable after binding to immobilised GAPDH beads, unlike HTT-FL (Burke *et al.*, 1996). This confirms the findings in LCL and HEK293T cells where GAPDH was not co-immunoprecipitated with HTT-FL.

CHAPTER 6 GENERAL DISCUSSION, FUTURE PERSPECTIVES AND CONCLUDING REMARKS

Better understanding of the physiological role of KMO would facilitate drug development targeting KMO not only for HD therapy, but would also provide a fundamental concept for treating other neurodegenerative disorders via pharmacological modulation of KP. In the previous chapters, I studied sub-cellular localisation and interactions of KMO, with the main focus on the novel KMO-HTT interaction which initiated filling the gap in our knowledge of HD mechanisms in relation to KMO. Thus, this chapter will mainly discuss the possible biological relevance of KMO-HTT interactions in the context of the current literature, as well as attempt to address the question posed earlier in the main introduction: 'what are the biological consequences of KMO inhibition and consequent alterations in KP metabolite levels in the CNS and periphery?'. In addition, I will highlight further research that could be carried out to support these findings.

6.1 The KMO-HTT interaction: connecting the dots to HD mechanisms

The hypothesis that KMO interacts with HTT stemmed from the identification of shared interactors between HTT and KMO (Thevandavakkam, 2011) and the idea that KIPs might potentially mediate KMO and HTT interactions. As HTT is known to interact with multiple proteins and has been hypothesised to function as a scaffold for protein complex assembly (Sun *et al.*, 2001), it could be that HTT plays a role in the KMO interaction network, and may associate this mitochondrial protein with proteins in other cellular compartments. As the BiFC system is capable of detecting both direct and indirect interactions (Kerppola, 2008), it cannot be excluded that the detected KMO-HTT interaction could be a part of protein complex, and thus might facilitate other functions of KMO as well as elucidate the underlying mechanisms of mitochondrial dysfunction in HD.

Moreover, as KMO interacts most strongly with WT HTT, as opposed to expanded polyQ mutant forms of this protein, this interaction might play an important role in KMO activity. Evidence of WT HTT expression in glial cells (Li *et al.*, 1993), and elevation in KMO activity coupled with the expression of mHTT in microglia have been demonstrated (Giorgini *et al.*, 2008). Thus it is possible that WT HTT regulates

microglia activation via its interaction with KMO, and presence of mHTT disrupts this regulation. Consequently, the mechanism of KMO-HTT interaction might provide new insights into drug production, for example the use of a molecule that binds to KMO mimicking WT HTT binding instead of inhibiting the active site of KMO. However, one may argue whether the KMO interaction with WT HTT is sustainable in the presence of mHTT. Based on the hypothesis that loss of function of WT HTT contributes to HD pathogenesis (Cattaneo *et al.*, 2001), it can be postulated that the capability of WT HTT to bind to KMO might be hindered by mHTT sequestering WT HTT (Kazantsev *et al.*, 1999), and therefore enzymatic activity is no longer regulated, leading to an increase in activity. Overall, the identification of a potential KMO-HTT interaction has highlighted the possibility that modulation of KMO activity could occur via an interaction with HTT. If so, this work may ultimately enhance our understanding of the mechanisms underlying HD.

To help address the concern of KMO inhibition, especially in pre-symptomatic individuals, one needs to understand the role of the KMO activity and KP metabolites as well as the impact of KMO inhibition on KP homeostasis, as will be discussed in the following two sections.

6.2 The role of the KP bridging the nervous and immune systems

Tryptophan metabolism through the kynurenine route is essential for health as well as disease development. The implication of this enzymatic cascade on the function of the immune system is receiving growing interest due to its role in both brain and immune disorders (Stone *et al.*, 2013). The role of KP and activated microglia in the CNS (in HD context) were discussed earlier in the introductory review Section (1.3), and thus the focus herein will be on the peripheral immune induction hence current KMO inhibitors act peripherally.

The IDO-induced KP mediate immunoregulation by suppression of T cells proliferation and increasing their susceptibility to apoptosis (Mándi and Vécsei, 2012). Increased IDO activity also potentiates L-KYN ligand activation of the aryl hydrocarbon receptor (AHR), which subsequently stimulates regulatory T cell generation contributing further to immunosuppression (Mezrich *et al.*, 2010; Nguyen *et al.*, 2010). The IDO immunoregulatory mechanism is essential for the maintenance of immune tolerance during pregnancy, autoimmunity and transplantation (Mándi and Vécsei, 2012).

However, the capacity of IDO for immunosuppression is a disadvantage when it comes to tumour growth, whereby tumour cells overexpress IDO to induce tolerance to tumour derived antigens (Mellor and Munn, 2004).

Immunoregulation functionality is not restricted to the IDO enzyme; KMO is also up-regulated upon immune induction (Stone *et al.*, 2013) and it has been shown that KMO inhibition, using Ro 61-8048, is protective against neurological symptoms and increased life span in a mouse model of cerebral malaria caused by *Plasmodium berghei* ANKA infection (Clark *et al.*, 2005). Furthermore, KMO is linked to human African trypanosomiasis (sleeping sickness), a serious infectious disease, which in late stages spreads to the CNS, leading to encephalitis. Interestingly, KMO inhibition with Ro 61-8048 in a mouse model of this disease results in significant reduction of neuroinflammation in the late stages of the infection, which indicates that targeting KMO for neuro-infectious disease can serve as a promising therapeutic strategy (Rodgers *et al.,* 2009). Recently, Jin *et al.* (2015) demonstrated that KMO is overexpressed in human hepatocellular carcinoma and exhibited tumour-promoting properties (Jin *et al.*, 2015). While Mole *et al.* (2016) showed that KMO plays a role in multiple organs dysfunction caused by acute pancreatitis (pancreatic inflammatory condition). Both KMO knockout mice and KMO inhibition in rat, using the newly described peripheral KMO inhibitor GSK180, provided protection which was correlated to elevated L-KYN and KYNA and lowered tryptophan and 3-HK in the plasma (Mole *et al.*, 2016).

In addition, the immune tolerance of IDO is possibly attributed to two mechanisms: tryptophan depletion which results in obstructing T cell proliferation due to their vulnerability to tryptophan starvation (Dounay *et al.*, 2015). The second mechanism is the suppression of T helper 1 and natural killer cells due to apoptotic induction mediated by KP metabolites 3-HK, 3-hyroxyanthranilic acid and QUIN (Dounay *et al.*, 2015). The latter mechanism further supports the essential role of KMO and its downstream metabolites in regulating immune responses.

Due to the excitotoxic and agonistic roles of QUIN at NMDA receptors (Stone and Perkins, 1981), it is one of the most studied KP metabolites. Interestingly, under normal conditions, QUIN is found at nanomolar levels in the brain (Martin *et al.*, 1992), whereas in the periphery its presence is more profound (micromolar range) and QUIN

immunoreactivity has been detected in all types of immune cells (Moffett *et al.*, 1994; Moffett and Namboodiri, 2003). Moffett and Namboodiri (2003) reasoned the elevated levels of QUIN in leucocytes may exist so that it can be released controllably to serve as an immune regulator; and possibly be maintained as a substrate for NAD^+ synthesis (Moffett and Namboodiri, 2003). The latter was postulated to be due to the poly (ADP-ribose) polymerization (PARP) reaction that leads to NAD^+ depletion. PARP activity is stimulated upon oxidative stress induced DNA damage during immune response (Moffett and Namboodiri, 2003). As QUIN is also capable of generating ROS (Braidy *et al.*, 2009), it could be a protective mechanism to induce its synthesis in the case of inflammation. Stone (2001) also proposed that the potential of immune cells to produce QUIN might be attributed to its implication in normal immunosurveillance (Stone, 2001). In addition, in the mouse brain QUIN levels are less affected by KMO deletion as compared to the periphery, indicating that it might also be important for the normal function of the brain (Giorgini *et al.*, 2013).

6.3 Further implications of KMO inhibition

As inhibition or genetic deletion of KMO increases KP flux towards the neuroprotective side by reducing 3-HK/KYNA ratio (Campesan *et al.*, 2011; Zwilling *et al.*, 2011), this section examines the possible implication of this modulation on the antagonist of NMDA and α7nACh receptors, KYNA (Wonodi and Schwarcz, 2010). Schizophrenia for instance is a psychiatric disorder that exhibits raised KYNA levels, which has been demonstrated in the prefrontal cortex of post-mortem brains (Schwarcz *et al.*, 2001), and CSF of schizophrenic patients (Erhardt *et al.*, 2001; Linderholm *et al.*, 2012; Nilsson *et al.*, 2005). Additionally, increased cortical KYNA concentrations might be linked to cognitive deficits in rats (Chess *et al.*, 2007). Although KATII activity was normal in the post-mortem schizophrenic cortex, KYNA levels were elevated and coupled with attenuation in KMO activity (Sathyasaikumar *et al.*, 2011), and thus L-KYN might be more readily accessible for KYNA synthesis suggesting the underlying increase in schizophrenia. In fact, several studies suggest association between KMO polymorphisms and schizophrenia. Aoyama *et al.* (2006) was first to assign linkage of a *KMO* single nucleotide polymorphism (SNP) (rs2275163) to schizophrenia in a Japanese population, which however was not reproducible in their second cohort (Aoyama *et al.*, 2006). Nevertheless, further subsequent reports confirmed an association between this *KMO* SNP and schizophrenia (Wonodi and Schwarcz, 2010;

Wonodi *et al.,* 2011; Wonodi *et al.,* 2014). Holtze *et al.* (2012) analysed the association of 15 *KMO* SNPs and identified another SNP (rs1053230) that correlates with the elevated CSF KYNA levels (Holtze *et al.*, 2012).

All things considered, KMO is a vital enzyme in the KP metabolism of the brain and immune system. KMO inhibition provides protection against neuroinflammation as in HD and on the other hand, decline in its activity contributes to cognitive dysfunction as in schizophrenia. Current KMO inhibitors are capable of alleviating symptoms and increasing life span. However, due to the links between impaired KMO activity and schizophrenia, it is important that KMO inhibition as a therapy in HD is closely monitored. The goal in such approaches should be to *normalise* the KP, and not inhibit KMO to the point of pushing the cascade towards psychosis. Nonetheless, it may be that the link between schizophrenia and KMO inhibition is most profound during early development (Forrest *et al.,* 2015), and that inhibition of KMO in the context of adult onset diseases will not have these issues. Further research is required to unravel the mechanisms underlying KMO targeted therapy.

6.4 Future perspectives

In order to complement the KMO-HTT interaction findings, KMO enzymatic activity needs to be monitored *in vitro* and also in the context of cell models. Initially a cell model could be employed (e.g. HEK293T cells) that lacks endogenous KMO such that any changes in KMO activity can be interpreted as a result of HTT expression, as KMO expression would not be regulated by its normal endogenous promoter. KMO enzymatic activity could be determined by measuring the conversion of L-KYN into 3-HK from cell extracts expressing KMO and WT HTT, KMO and mHTT, or KMO alone. In addition, endogenous HTT-FL could be knocked down in HEK293T cells, to test the possibility that it might regulate enzymatic activity of exogenous KMO. If such regulation of KMO activity exists, this could also be extended to *in vitro* kinetics assays using recombinant purified KMO and WT HTT to determine the steady-state kinetic parameters of KMO in the presence and absence of WT HTT.

Furthermore, the hypothesis that expression of mHTT might modulate KMO interactions with WT HTT could be tested using the constructs flKMO-CC and 19Q-VN in tandem with untagged mHTT. Interestingly, the BiFC system could also be employed to establish whether any effects on flKMO-CC and 19Q-VN is due to

sequestration of 19Q-VN into mHTT aggregates by using the multi-colour BiFC approach (Hu and Kerppola, 2003). For example, instead of using untagged mHTT, 97Q-VC (which is available in house) can be used, leading to differential spectra properties. Interaction of flKMO-CC with 19Q-VN is 510 nm, whereas re-constitution of Venus halves would result in 529 nm (Shyu *et al.*, 2006). Herrera *et al.* (2011) showed that 19Q-VN and 97Q-VC interact and aggregates were detectable (Herrera *et al.*, 2011). Although the two BiFC signals would be distinguishable using confocal, interactions intensities cannot be compared to one another due to the presence of mHTT aggregates, and in fact the Scan^R screening station spectra filters will fail to detect the two BiFC signals separately.

To investigate the effect of HTT aggregation on the KMO interaction with mHTT, phosphomimic BiFC HTT constructs can be used. The effect of phosphorylation on aggregation was discussed earlier in (Section 1.2.2). We have in house three phosphomimic substitutions (T3D, S13D and S16D) of our BiFC 19Q-VN and 97Q-VN which modulate HTT aggregation and localisation of HTT, and thus localisation studies could be performed prior to BiFC to study the impact of phosphomimmicking on mitochondrial localisation of these BiFC constructs. In addition, other possible suggested experiments could also be carried out and were highlighted in the relevant Discussion Sections (3.3, 4.3 and 5.3), in previous chapters.

6.5 Concluding remarks

KMO is a critical enzyme in the KP that synthesises 3-HK and ultimately influences generation of the further downstream metabolite QUIN. These neurotoxic metabolites play a major role in HD pathogenesis placing KMO amongst the promising therapeutic targets for HD via its regulation of the KP. This work confirmed exogenous KMO localisation at the outer mitochondrial membrane providing the first human KMO electron micrograph. Moreover, it has shed light on the importance of the C-terminus of KMO in mitochondrial targeting and protein interaction. The major finding was identifying KMO as an interacting protein of HTT. This interaction was supported with co-localisation of KMO and HTT at the mitochondria, further emphasising the importance of mitochondria in the pathology of HD. Interestingly, the KMO-HTT interaction is compromised when HTT is mutated, suggesting a possible regulatory role of WT HTT on KMO activity mediated by their interaction. Further research is needed

to prove this concept and provide better understanding of the role of KMO in HD mechanisms.

APPENDIX CLONING MAPS

Cloning maps of plasmids listed in Section (2.1.5) are presented here. cDNA of proteins of interest were inserted into mammalian expression vectors pcDNA3.1, where cDNA expression was controlled by CMV promoter. pcDNA3.1 features, as indicated on the maps, antibiotic resistance genes: AmpR to allow selections of transformed bacteria using ampicillin, and NeoR/ZeoR that confers resistance against neomycin/zeocin for selections of stably transfected mammalian cells. All plasmid maps were constructed using SnapGene software (Version 3.1).

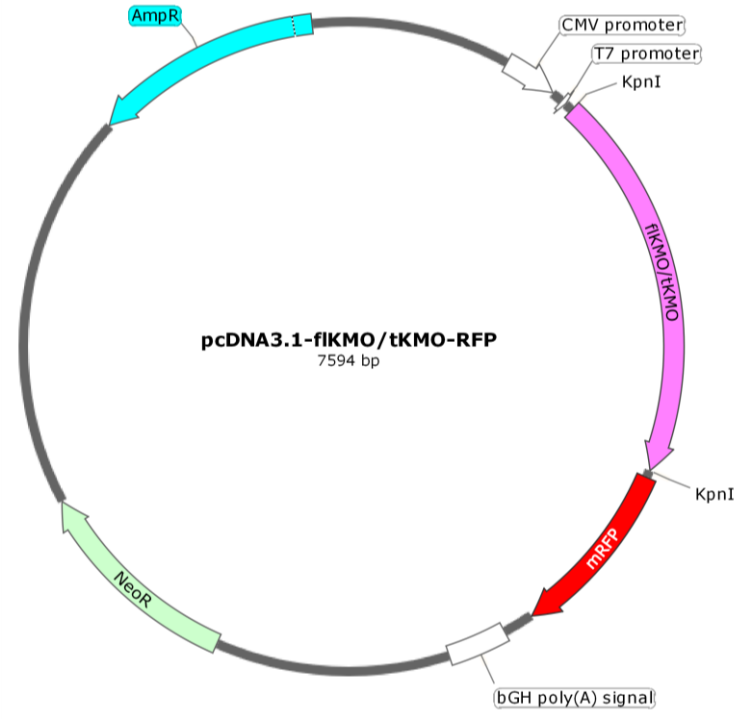

Figure 1 Cloning of KMO-RFP constructs. flKMO/tKMO were PCR amplified to introduce the flanking restriction sites *KpnI*, which was then inserted into the *KpnI* pcDNA3.1-mRFP digested plasmid N-terminally of mRFP.

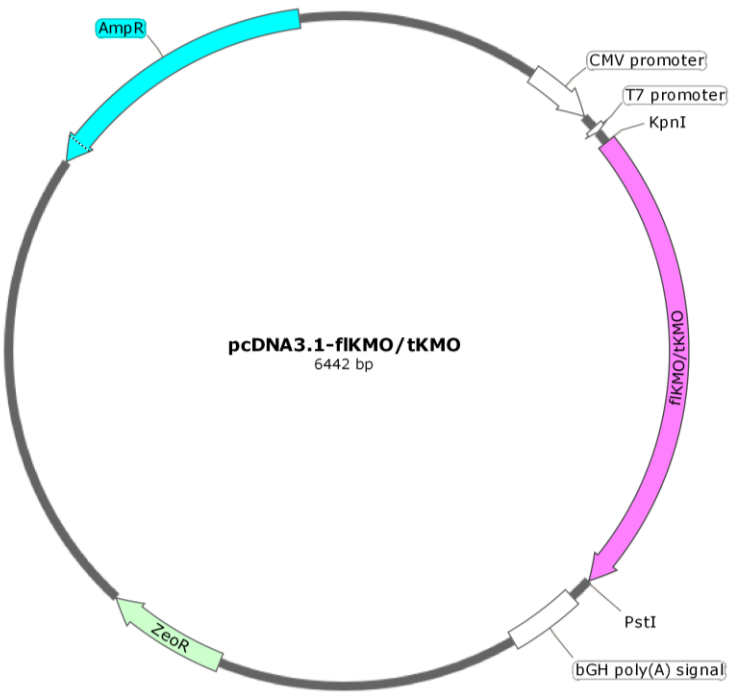

Figure 2 Construction of untagged KMO. flKMO/tKMO were PCR amplified using primers encoded *KpnI-PstI* sites. Amplified KMO inserted into pcDNA3.1 double digested with *KpnI-PstI*.

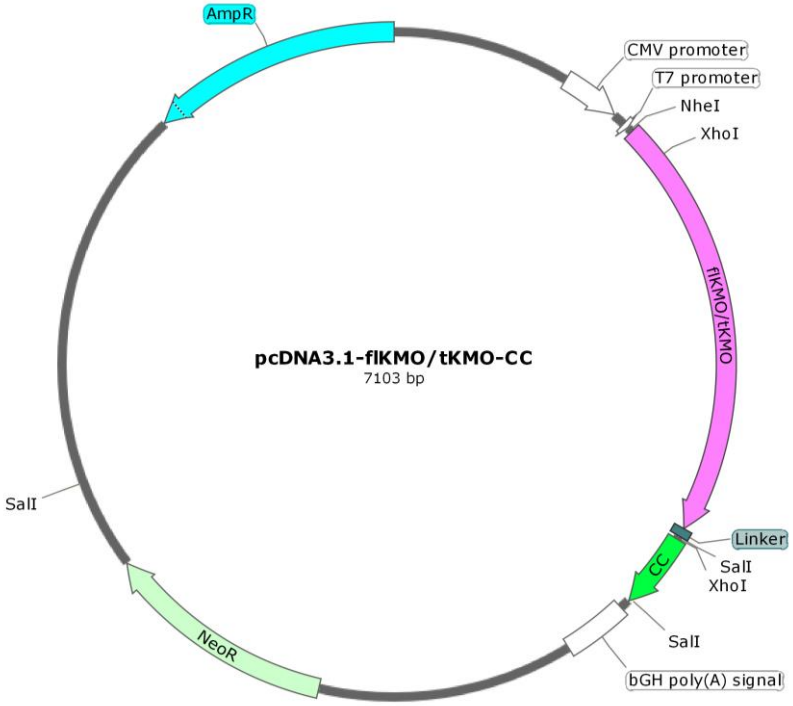

Figure 3 Construction of KMO-CC BiFC plasmids. The parent plasmid was pcDNA3.1-DJ-1-CC (refer to Section 2.1.3), DJ-1 was excised with *NheI* and *XhoI*. flKMO/tKMO were PCR amplified to introduce *NheI* site and $(GGGGS)_2$ linker as well as *SalI* site C-terminally, after sequential digestion flKMO/tKMO was ligated into *NheI-XhoI* sites of the pcDNA3.1-CC plasmid.

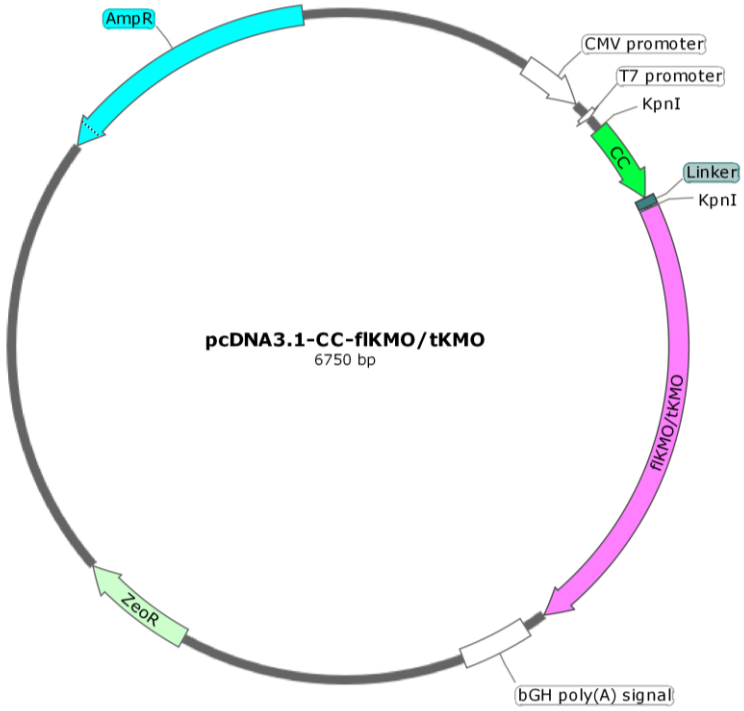

Figure 4 Cloning of CC-KMO BiFC constructs. Untagged KMO plasmids from Figure 2 were used. CC was PCR amplified to introduce *KpnI* sites which was then inserted N-terminally of untagged flKMO/tKMO plasmids digested with *KpnI*.

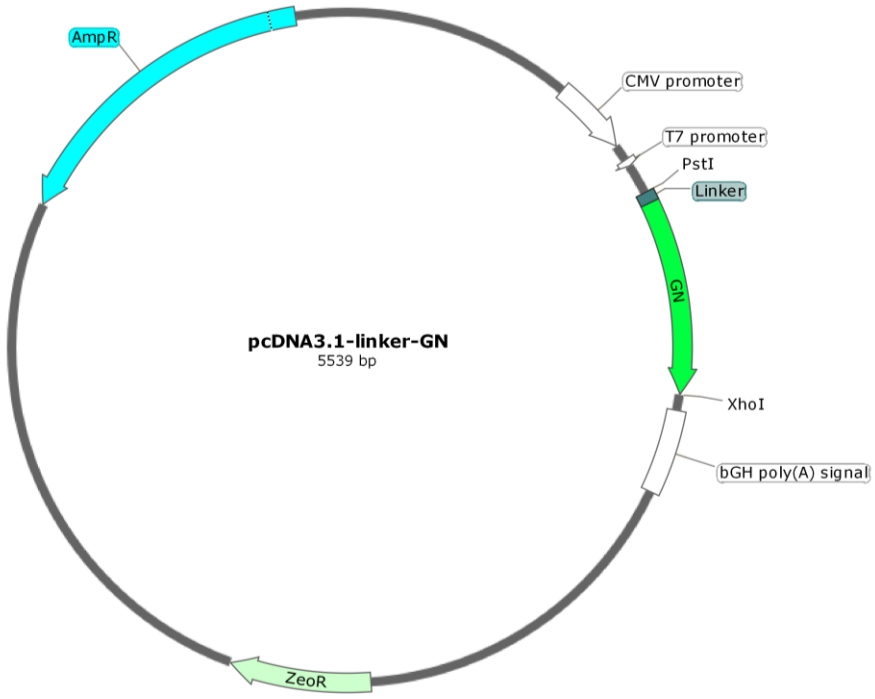

Figure 5 Construction of BiFC linker-GN backbone. GN was amplified using primers that introduced *PstI* site and the $(GGGGS)_2$ linker N-terminally as well as *XhoI* site C-terminally to allow insertion into *PstI-XhoI* sites of pcDNA3.1 empty plasmid.

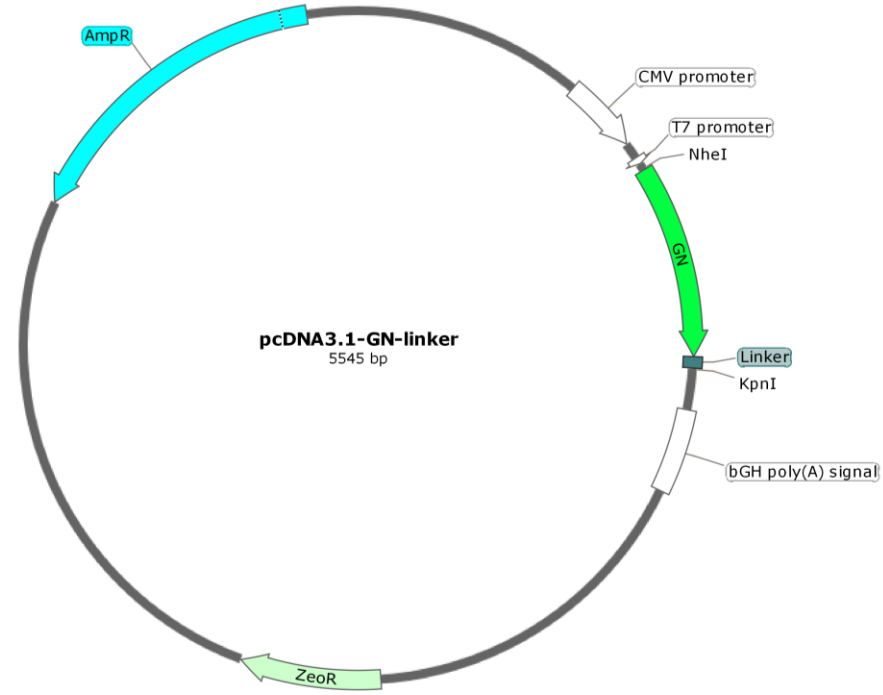

Figure 6 Generation of BiFC GN-linker backbone. GN was amplified suing primers that introduce *NheI* site N-terminally and *KpnI* site as well as $(GGGGS)_2$ linker C-terminally, which was then inserted into *NheI-KpnI* sites of pcDNA3.1 empty plasmid.

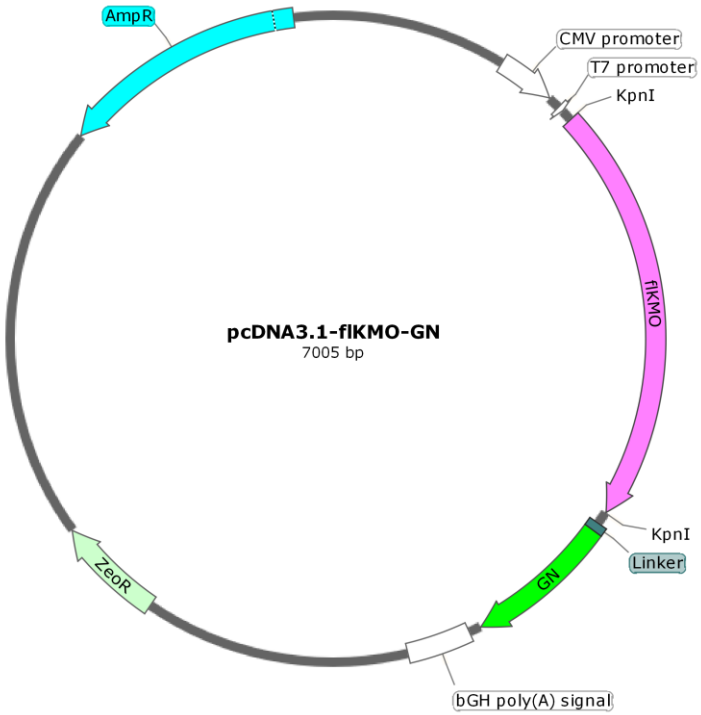

Figure 7 Construction of flKMO-GN BiFC plasmid. flKMO was PCR amplified to introduce *KpnI* flanking sites, then was inserted into *KpnI* site of linker-GN backbone generated in Figure 5.

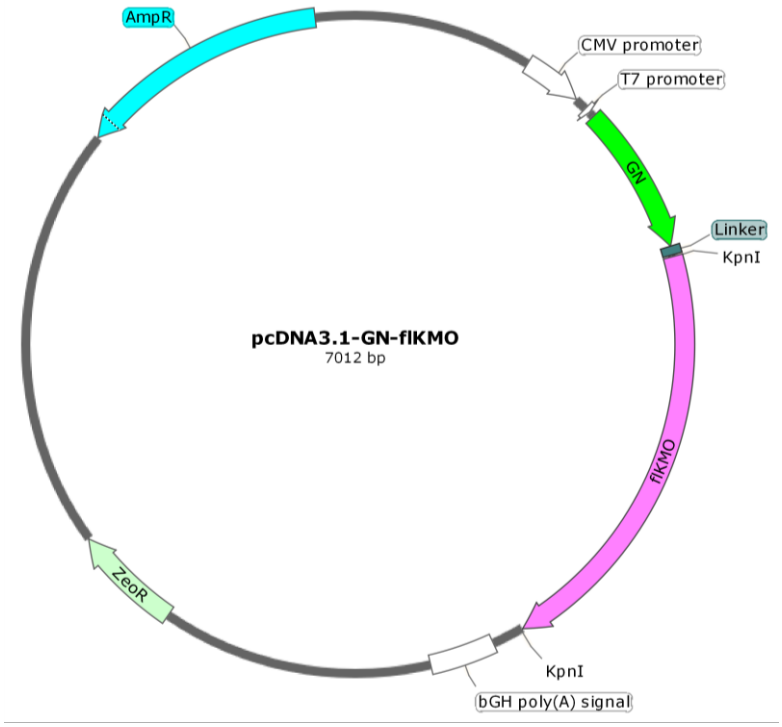

Figure 8 Cloning of GN-flKMO BiFC construct. flKMO was PCR amplified to introduce *KpnI* flanking sites, then was inserted into *KpnI* site of GN-linker backbone generated in Figure 6.

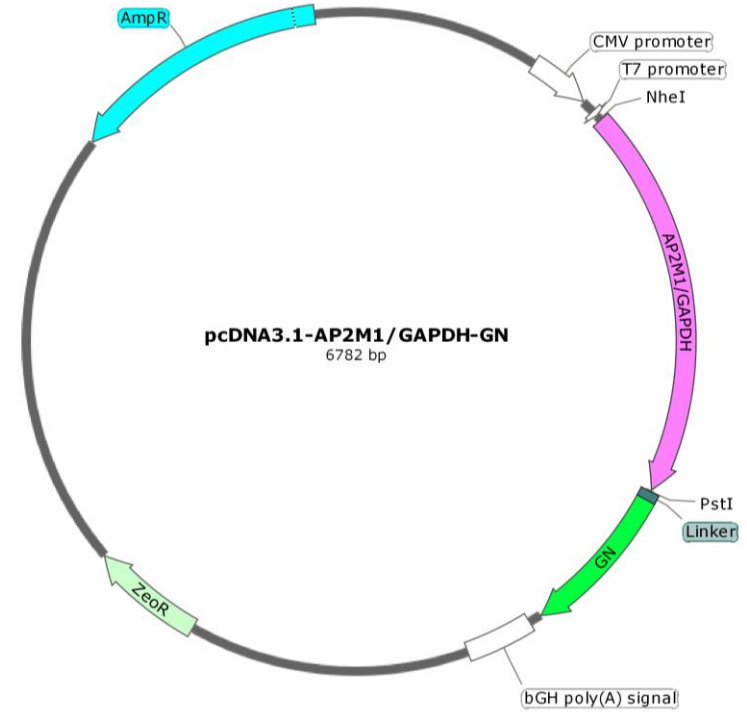

Figure 9 Cloning of AP2M1/GAPDH-GN BiFC constructs. AP2M1/GAPDH were PCR amplified to introduce *NheI* and *PstI* sites, which were then inserted into *NheI-PstI* sites of linker-GN backbone generated in Figure 5.

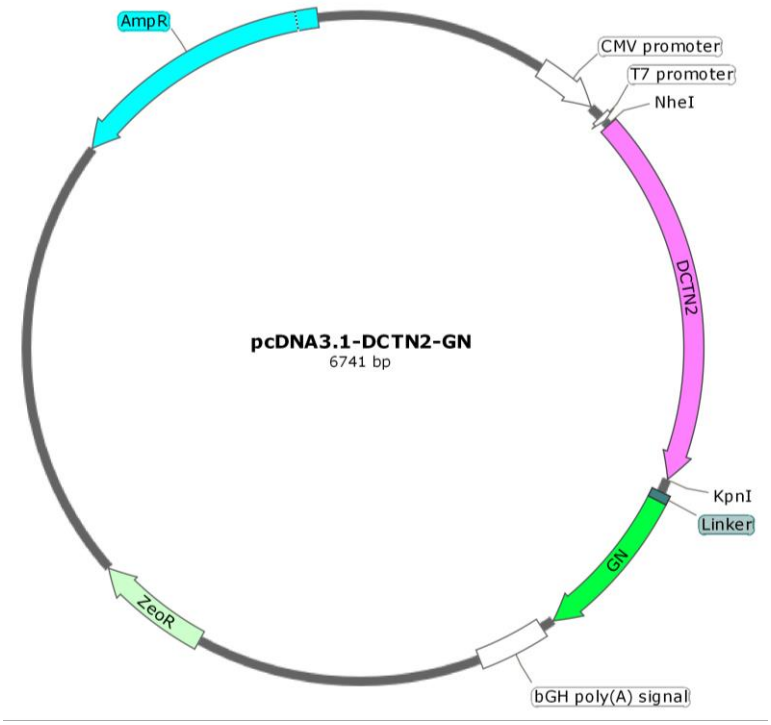

Figure 10 Construction of DCTN2-GN BiFC plasmid. DCTN2 was PCR amplified to introduce *NheI* and *KpnI* sites, which was then inserted into *NheI-KpnI* sites of linker-GN backbone generated in Figure 5.

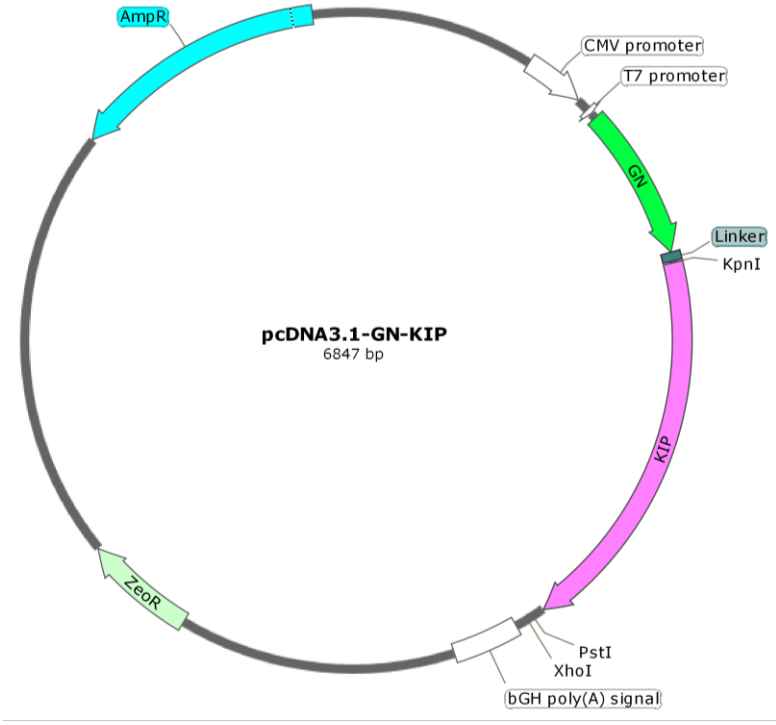

Figure 11 BiFC GN-KIP plasmids construction. KIPs (AP2M1/GAPDH/DACTN2) were PCR amplified to introduce the flanking sites of *KpnI-PstI* for AP2M1 and GAPDH or *KpnI-XhoI* for DCTN2. Digested PCR products were then inserted into GN-linker backbone generated in Figure 6 at *KpnI-PstI* sites or *KpnI-XhoI* sites for AP2M1 and GAPDH or DCTN2, respectively.

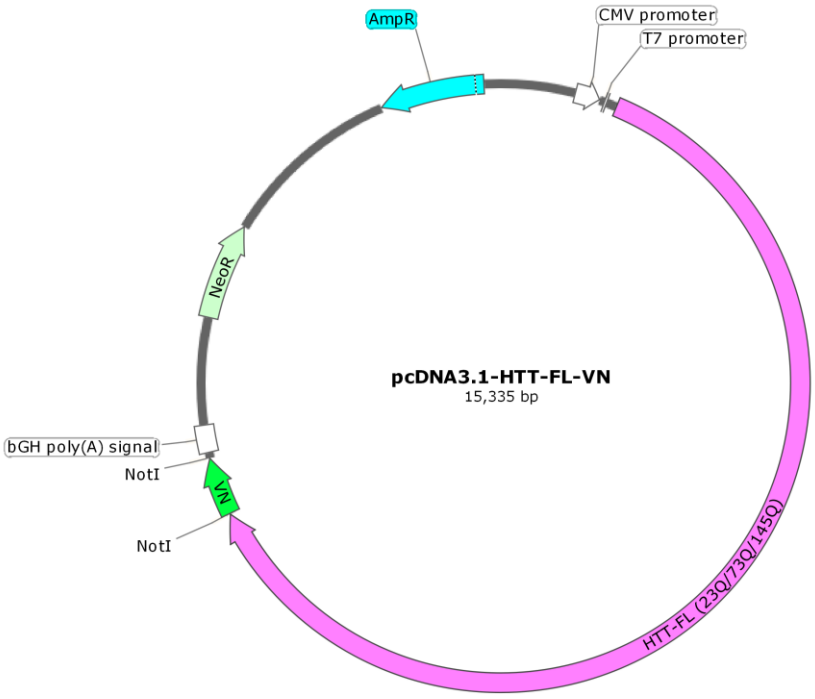

Figure 12 Construction of HTT-FL-VN BiFC plasmids. pcDNA3.1 containing HTT-FL (23Q/73Q/145Q) were digested with *NotI*. VN was PCR amplified to introduce *NotI* flanking sites which was then digested with *NotI* and ligated into pcDNA3.1-HTT-FL.

BIBLIOGRAPHY

Aiken C.T., Steffan J.S., Guerrero C.M., Khashwji H., Lukacsovich T., Simmons D., Purcell J.M., Menhaji K., Zhu Y.-Z. and Green K. (2009) Phosphorylation of Threonine 3 Implications for Huntingtin Aggregation and Neurotoxicity. *Journal of Biological Chemistry.* **284**, 29427-29436.

Alberati-Giani D., Cesura A.M., Broger C., Warren W.D., Röver S. and Malherbe P. (1997) Cloning and Functional Expression of Human Kynurenine 3-Monooxygenase. *FEBS letters.* **410**, 407-412.

Allegri G., Costa C.V.L., Bertazzo A., Biasiolo M. and Ragazzi E. (2003) Enzyme Activities of Tryptophan Metabolism Along the Kynurenine Pathway in Various Species of Animals. *Il Farmaco.* **58**, 829-836.

Amaral M., Levy C., Heyes D.J., Lafite P., Outeiro T.F., Giorgini F., Leys D. and Scrutton N.S. (2013) Structural Basis of Kynurenine 3-Monooxygenase Inhibition. *Nature.* **496**, 382-385.

Ambrose C.M., Duyao M.P., Barnes G., Bates G.P., Lin C.S., Srinidhi J., Baxendale S., Hummerich H., Lehrach H. and Altherr M. (1994) Structure and Expression of the Huntington's Disease Gene: Evidence against Simple Inactivation Due to an Expanded CAG Repeat. *Somatic cell and molecular genetics.* **20**, 27-38.

Amet N., Lee H.-F. and Shen W.-C. (2009) Insertion of the Designed Helical Linker Led to Increased Expression of Tf-Based Fusion Proteins. *Pharmaceutical research.* **26**, 523-528.

Amori L., Guidetti P., Pellicciari R., Kajii Y. and Schwarcz R. (2009) On the Relationship between the Two Branches of the Kynurenine Pathway in the Rat Brain in Vivo. *Journal of neurochemistry.* **109**, 316-325.

Andrade M.A. and Bork P. (1995) HEAT Repeats in the Huntington's Disease Protein. *Nature genetics.* **11**, 115-116.

Andrew S.E., Goldberg Y.P., Kremer B., Telenius H., Theilmann J., Adam S., Starr E., Squitieri F., Lin B. and Kalchman M.A. (1993) The Relationship between Trinucleotide (CAG) Repeat Length and Clinical Features of Huntington's Disease. *Nature genetics.* **4**, 398-403.

Aoyama N., Takahashi N., Saito S., Maeno N., Ishihara R., Ji X., Miura H., Ikeda M., Suzuki T. and Kitajima T. (2006) Association Study between Kynurenine 3-Monooxygenase Gene and Schizophrenia in the Japanese Population. *Genes, Brain and Behavior.* **5**, 364-368.

Arnold I., Pfeiffer K., Neupert W., Stuart R.A. and Schägger H. (1998) Yeast Mitochondrial F1F0-ATP Synthase Exists as a Dimer: Identification of Three Dimer-Specific Subunits. *The EMBO journal.* **17**, 7170-7178.

Atwal R.S., Xia J., Pinchev D., Taylor J., Epand R.M. and Truant R. (2007) Huntingtin Has a Membrane Association Signal That Can Modulate Huntingtin Aggregation, Nuclear Entry and Toxicity. *Human molecular genetics.* **16**, 2600-2615.

Atwal R.S., Desmond C.R., Caron N., Maiuri T., Xia J., Sipione S. and Truant R. (2011) Kinase Inhibitors Modulate Huntingtin Cell Localization and Toxicity. *Nature chemical biology.* **7**, 453-460.

Bae B.-I., Xu H., Igarashi S., Fujimuro M., Agrawal N., Taya Y., Hayward S.D., Moran T.H., Montell C. and Ross C.A. (2005) p53 Mediates Cellular Dysfunction and Behavioral Abnormalities in Huntington's Disease. *Neuron.* **47**, 29-41.

Ball H.J., Sanchez-Perez A., Weiser S., Austin C.J., Astelbauer F., Miu J., McQuillan J.A., Stocker R., Jermiin L.S. and Hunt N.H. (2007) Characterization of an Indoleamine 2, 3-Dioxygenase-Like Protein Found in Humans and Mice. *Gene.* **396**, 203-213.

Beadle G., Mitchell H. and Nyc J. (1947) Kynurenine as an Intermediate in the Formation of Nicotinic Acid from Tryptophane by Neurospora. *Proceedings of the National Academy of Sciences of the United States of America.* **33**, 155-158.

Beal M.F., Kowall N.W., Ellison D.W., Mazurek M.F., Swartz K.J. and Martin J.B. (1986) Replication of the Neurochemical Characteristics of Huntington's Disease by Quinolinic Acid. *Nature.* **321**, 168 - 171.

Beal M.F., Matson W.R., Storey E., Milbury P., Ryan E.A., Ogawa T. and Bird E.D. (1992) Kynurenic Acid Concentrations Are Reduced in Huntington's Disease Cerebral Cortex. *Journal of the neurological sciences.* **108**, 80-87.

Bender D.A. and McCreanor G.M. (1982) The Preferred Route of Kynurenine Metabolism in the Rat. *Biochimica et Biophysica Acta (BBA)-General Subjects.* **717**, 56-60.

Benton R., Sachse S., Michnick S.W. and Vosshall L.B. (2006) Atypical Membrane Topology and Heteromeric Function of *Drosophila* Odorant Receptors in Vivo. *PLoS biology.* **4**, 240-257.

Berlinguer-Palmini R., Masi A., Narducci R., Cavone L., Maratea D., Cozzi A., Sili M., Moroni F. and Mannaioni G. (2013) Gpr35 Activation Reduces Ca^{2+} Transients and Contributes to the Kynurenic Acid-Dependent Reduction of Synaptic Activity at CA3-CA1 Synapses. *PloS one.* **8**, 1-11.

Bertazzo A., Ragazzi E., Biasiolo M., Costa C.V.L. and Allegri G. (2001) Enzyme Activities Involved in Tryptophan Metabolism Along the Kynurenine Pathway in Rabbits. *Biochimica et Biophysica Acta (BBA)-General Subjects.* **1527**, 167-175.

Bertolino M., Vicini S. and Costa E. (1989) Kynurenic Acid Inhibits the Activation of Kainic and N-Methyl-D-Aspartic Acid-Sensitive Ionotropic Receptors by a Different Mechanism. *Neuropharmacology.* **28**, 453-457.

Birch P.J., Grossman C.J. and Hayes A.G. (1988) Kynurenic Acid Antagonises Responses to Nmda Via an Action at the Strychnine-Insensitive Glycine Receptor. *European journal of pharmacology.* **154**, 85-87.

Björkqvist M., Wild E.J., Thiele J., Silvestroni A., Andre R., Lahiri N., Raibon E., Lee R.V., Benn C.L. and Soulet D. (2008) A Novel Pathogenic Pathway of Immune Activation Detectable before Clinical Onset in Huntington's Disease. *The Journal of experimental medicine.* **205**, 1869-1877.

Block-Galarza J., Chase K.O., Sapp E., Vaughn K.T., Vallee R.B., DiFiglia M. and Aronin N. (1997) Fast Transport and Retrograde Movement of Huntingtin and HAP-1 in Axons. *Neuroreport.* **8**, 2247-2250.

Bogdanov M.B., Andreassen O.A., Dedeoglu A., Ferrante R.J. and Beal M.F. (2001) Increased Oxidative Damage to DNA in a Transgenic Mouse Model of Huntington's Disease. *Journal of neurochemistry.* **79**, 1246-1249.

Bolte S. and Cordelieres F. (2006) A Guided Tour into Subcellular Colocalization Analysis in Light Microscopy. *Journal of microscopy.* **224**, 213-232.

Bordelon Y.M., Chesselet M.F., Nelson D., Welsh F. and Erecińska M. (1997) Energetic Dysfunction in Quinolinic Acid-Lesioned Rat Striatum. *Journal of neurochemistry.* **69**, 1629-1639.

Braidy N., Grant R., Adams S., Brew B.J. and Guillemin G.J. (2009) Mechanism for Quinolinic Acid Cytotoxicity in Human Astrocytes and Neurons. *Neurotoxicity research.* **16**, 77-86.

Browne S.E., Ferrante R.J. and Beal M.F. (1999) Oxidative Stress in Huntington's Disease. *Brain pathology.* **9**, 147-163.

Burke J.R., Enghild J.J., Martin M.E., Jou Y.-S., Myers R.M., Roses A.D., Vance J.M. and Strittmatter W.J. (1996) Huntingtin and DRPLA Proteins Selectively Interact with the Enzyme GAPDH. *Nature medicine.* **2**, 347-350.

Burke K.A., Kauffman K.J., Umbaugh C.S., Frey S.L. and Legleiter J. (2013) The Interaction of Polyglutamine Peptides with Lipid Membranes Is Regulated by Flanking Sequences Associated with Huntingtin. *Journal of Biological Chemistry.* **288**, 14993-15005.

Cabantous S., Nguyen H.B., Pedelacq J.-D., Koraïchi F., Chaudhary A., Ganguly K., Lockard M.A., Favre G., Terwilliger T.C. and Waldo G.S. (2013) A New Protein-Protein Interaction Sensor Based on Tripartite Split-GFP Association. *Scientific reports.* **3**, srep02854.

Campesan S., Green E.W., Breda C., Sathyasaikumar K.V., Muchowski P.J., Schwarcz R., Kyriacou C.P. and Giorgini F. (2011) The Kynurenine Pathway Modulates Neurodegeneration in a *Drosophila* Model of Huntington's Disease. *Current Biology.* **21**, 961-966.

Carlin J.M., Borden E.C., Sondel P.M. and Byrne G.I. (1989) Interferon-Induced Indoleamine 2, 3-Dioxygenase Activity in Human Mononuclear Phagocytes. *Journal of leukocyte biology.* **45**, 29-34.

Caron N.S., Desmond C.R., Xia J. and Truant R. (2013) Polyglutamine Domain Flexibility Mediates the Proximity between Flanking Sequences in Huntingtin. *Proceedings of the National Academy of Sciences.* **110**, 14610-14615.

Carpenedo R., Pittaluga A., Cozzi A., Attucci S., Galli A., Raiteri M. and Moroni F. (2001) Presynaptic Kynurenate-Sensitive Receptors Inhibit Glutamate Release. *European Journal of Neuroscience.* **13**, 2141-2147.

Cattaneo E., Rigamonti D., Goffredo D., Zuccato C., Squitieri F. and Sipione S. (2001) Loss of Normal Huntingtin Function: New Developments in Huntington's Disease Research. *Trends in neurosciences.* **24**, 182-188.

Chen X., Zaro J.L. and Shen W.-C. (2013) Fusion Protein Linkers: Property, Design and Functionality. *Advanced drug delivery reviews.* **65**, 1357-1369.

Chen Y. and Guillemin G.J. (2009) Kynurenine Pathway Metabolites in Humans: Disease and Healthy States. *International journal of tryptophan research: IJTR.* **2**, 1-19.

Chess A.C., Simoni M.K., Alling T.E. and Bucci D.J. (2007) Elevations of Endogenous Kynurenic Acid Produce Spatial Working Memory Deficits. *Schizophrenia bulletin.* **33**, 797-804.

Chiarugi A., Calvani M., Meli E., Traggiai E. and Moroni F. (2001a) Synthesis and Release of Neurotoxic Kynurenine Metabolites by Human Monocyte-Derived Macrophages. *Journal of Neuroimmunology.* **120**, 190-198.

Chiarugi A., Meli E. and Moroni F. (2001b) Similarities and Differences in the Neuronal Death Processes Activated by 3-Hydroxykynurenine and Quinolinic Acid. *Journal of neurochemistry.* **77**, 1310-1318.

Choo Y.S., Johnson G.V., MacDonald M., Detloff P.J. and Lesort M. (2004) Mutant Huntingtin Directly Increases Susceptibility of Mitochondria to the Calcium-Induced Permeability Transition and Cytochrome *c* Release. *Human molecular genetics.* **13**, 1407-1420.

Clark C.J., Mackay G.M., Smythe G.A., Bustamante S., Stone T.W. and Phillips R.S. (2005) Prolonged Survival of a Murine Model of Cerebral Malaria by Kynurenine Pathway Inhibition. *Infection and immunity.* **73**, 5249-5251.

Conner J.M., Lauterborn J.C., Yan Q., Gall C.M. and Varon S. (1997) Distribution of Brain-Derived Neurotrophic Factor (BDNF) Protein and mRNA in the Normal Adult Rat CNS: Evidence for Anterograde Axonal Transport. *The Journal of Neuroscience.* **17**, 2295-2313.

Cornett J., Cao F., Wang C.-E., Ross C.A., Bates G.P., Li S.-H. and Li X.-J. (2005) Polyglutamine Expansion of Huntingtin Impairs Its Nuclear Export. *Nature genetics.* **37**, 198-204.

Cull-Candy S., Brickley S. and Farrant M. (2001) NMDA Receptor Subunits: Diversity, Development and Disease. *Current opinion in neurobiology.* **11**, 327-335.

Davies S.W., Mark T., Cozens B.A., Raza A.S., Mahal A., Mangiarini L. and Bates G.P. (1999) From Neuronal Inclusions to Neurodegeneration: Neuropathological Investigation of a Transgenic Mouse Model of Huntington'sdisease. *Philosophical Transactions of the Royal Society B: Biological Sciences.* **354**, 971-979.

De Carvalho L.P., Bochet P. and Rossier J. (1996) The Endogeneous Agonist Quinolinic Acid and the Non Endogenous Homoquinolinic Acid Discriminate between NMDAR2 Receptor Subunits. *Neurochemistry international.* **28**, 445-452.

De Castro F., Price J. and Brown R. (1956) Reduced Triphosphopyridinenucleotide Requirement for the Enzymatic Formation of 3-Hydroxykynurenine from L-Kynurenine. *Journal of the American Chemical Society.* **78**, 2904-2905.

De Paul A.L., Torres A.I., Quintar A.A., Maldonado C.A., Mukdsi J.H., Petiti J.P. and Gutiérrez S. (2012) Immunoelectron Microscopy: A Reliable Tool for the Analysis of Cellular Processes. In: Dehghani H. (ed) *Applications of Immunocytochemistry.* INTECH Open Access Publisher.

DiFiglia M., Sapp E., Chase K., Schwarz C., Meloni A., Young C., Martin E., Vonsattel J.-P., Carraway R. and Reeves S.A. (1995) Huntingtin is a Cytoplasmic Protein Associated with Vesicles in Human and Rat Brain Neurons. *Neuron.* **14**, 1075-1081.

DiFiglia M., Sapp E., Chase K.O., Davies S.W., Bates G.P., Vonsattel J. and Aronin N. (1997) Aggregation of Huntingtin in Neuronal Intranuclear Inclusions and Dystrophic Neurites in Brain. *Science.* **277**, 1990-1993.

Dounay A.B., Tuttle J.B. and Verhoest P.R. (2015) Challenges and Opportunities in the Discovery of New Therapeutics Targeting the Kynurenine Pathway. *Journal of medicinal chemistry.* **58**, 8762-8782.

Duyao M.P., Auerbach A.B., Ryan A., Persichetti F., Barnes G.T., McNeil S.M., Ge P., Vonsattel J.P., Gusella J.F. and Joyner A.L. (1995) Inactivation of the Mouse Huntington's Disease Gene Homolog Hdh. *Science.* **269**, 407-410.

Elmslie K.S. and Yoshikami D. (1985) Effects of Kynurenate on Root Potentials Evoked by Synaptic Activity and Amino Acids in the Frog Spinal Cord. *Brain research.* **330**, 265-272.

Erhardt S., Blennow K., Nordin C., Skogh E., Lindström L.H. and Engberg G. (2001) Kynurenic Acid Levels Are Elevated in the Cerebrospinal Fluid of Patients with Schizophrenia. *Neuroscience letters.* **313**, 96-98.

Erickson J.B., Flanagan E.M., Russo S. and Reinhard J.F. (1992) A Radiometric Assay for Kynurenine 3-Hydroxylase Based on the Release of 3 H 2 O During Hydroxylation of L-[3, 5-3 H] Kynurenine. *Analytical biochemistry.* **205**, 257-262.

Evans S.J., Douglas I., Rawlins M.D., Wexler N.S., Tabrizi S.J. and Smeeth L. (2013) Prevalence of Adult Huntington's Disease in the UK Based on Diagnoses Recorded in General Practice Records. *Journal of Neurology, Neurosurgery & Psychiatry.* **84**, 1156-1160.

Faber P.W., Barnes G.T., Srinidhi J., Chen J., Gusella J.F. and MacDonald M.E. (1998) Huntingtin Interacts with a Family of WW Domain Proteins. *Human molecular genetics.* **7**, 1463-1474.

Fatokun A.A., Hunt N.H. and Ball H.J. (2013) Indoleamine 2, 3-Dioxygenase 2 (IDO2) and the Kynurenine Pathway: Characteristics and Potential Roles in Health and Disease. *Amino Acids.* **45**, 1319-1329.

Fiszer A. and Krzyzosiak W.J. (2013) RNA Toxicity in Polyglutamine Disorders: Concepts, Models, and Progress of Research. *Journal of Molecular Medicine.* **91**, 683-691.

Forrest C., McNair K., Pisar M., Khalil O., Darlington L. and Stone T. (2015) Altered Hippocampal Plasticity by Prenatal Kynurenine Administration, Kynurenine-3-Monoxygenase (KMO) Deletion or Galantamine. *Neuroscience.* **310**, 91-105.

Foster A.C., Miller L.P., Oldendorf W.H. and Schwarcz R. (1984a) Studies on the Disposition of Quinolinic Acid after Intracerebral or Systemic Administration in the Rat. *Experimental neurology.* **84**, 428-440.

Foster A.C., Vezzani A., French E.D. and Schwarcz R. (1984b) Kynurenic Acid Blocks Neurotoxicity and Seizures Induced in Rats by the Related Brain Metabolite Quinolinic Acid. *Neuroscience letters.* **48**, 273-278.

Frid P., Anisimov S.V. and Popovic N. (2007) Congo Red and Protein Aggregation in Neurodegenerative Diseases. *Brain Research Reviews.* **53**, 135-160.

Fukui S., Schwarcz R., Rapoport S.I., Takada Y. and Smith Q.R. (1991) Blood–Brain Barrier Transport of Kynurenines: Implications for Brain Synthesis and Metabolism. *Journal of neurochemistry.* **56**, 2007-2017.

Futter M., Diekmann H., Schoenmakers E., Sadiq O., Chatterjee K. and Rubinsztein D.C. (2009) Wild-Type but Not Mutant Huntingtin Modulates the Transcriptional Activity of Liver X Receptors. *Journal of medical genetics.* **46**, 438-446.

Ghosh I., Hamilton A.D. and Regan L. (2000) Antiparallel Leucine Zipper-Directed Protein Reassembly: Application to the Green Fluorescent Protein. *Journal of the American Chemical Society.* **122**, 5658-5659.

Gil J.M. and Rego A.C. (2008) Mechanisms of Neurodegeneration in Huntington's Disease. *European Journal of Neuroscience.* **27**, 2803-2820.

Giorgini F., Guidetti P., Nguyen Q.V., Bennett S.C. and Muchowski P.J. (2005) A Genomic Screen in Yeast Implicates Kynurenine 3-Monooxygenase as a Therapeutic Target for Huntington's Disease. *Nature genetics.* **37**, 526-531.

Giorgini F., Möller T., Kwan W., Zwilling D., Wacker J.L., Hong S., Tsai L.C.L., Cheah C.S., Schwarcz R. and Guidetti P. (2008) Histone Deacetylase Inhibition Modulates Kynurenine Pathway Activation in Yeast, Microglia, and Mice Expressing a Mutant Huntingtin Fragment. *Journal of Biological Chemistry.* **283**, 7390-7400.

Giorgini F., Huang S.-Y., Sathyasaikumar K.V., Notarangelo F.M., Thomas M.A., Tararina M., Wu H.-Q., Schwarcz R. and Muchowski P.J. (2013) Targeted Deletion of Kynurenine 3-Monooxygenase in Mice a New Tool for Studying Kynurenine Pathway Metabolism in Periphery and Brain. *Journal of Biological Chemistry.* **288**, 36554-36566.

Goda K., Hamane Y., Kishimoto R. and Ogishi Y. (1999) Radical Scavenging Properties of Tryptophan Metabolites. *Adv Exp Med Biol.* **467**, 397-402.

Gookin T.E. and Assmann S.M. (2014) Significant Reduction of BiFC Non-Specific Assembly Facilitates in Planta Assessment of Heterotrimeric G-Protein Interactors. *The Plant Journal.* **80**, 553-567.

Guidetti P., Eastman C.L. and Schwarcz R. (1995) Metabolism of [5-3h] Kynurenine in the Rat Brain in Vivo: Evidence for the Existence of a Functional Kynurenine Pathway. *Journal of neurochemistry.* **65**, 2621-2632.

Guidetti P. and Schwarcz R. (1999) 3-Hydroxykynurenine Potentiates Quinolinate but Not NMDA Toxicity in the Rat Striatum. *European Journal of Neuroscience.* **11**, 3857-3863.

Guidetti P., Luthi-Carter R.E., Augood S.J. and Schwarcz R. (2004) Neostriatal and Cortical Quinolinate Levels Are Increased in Early Grade Huntington's Disease. *Neurobiology of disease.* **17**, 455-461.

Guillemin G.J., Kerr S.J., Smythe G.A., Smith D.G., Kapoor V., Armati P.J., Croitoru J. and Brew B.J. (2001) Kynurenine Pathway Metabolism in Human Astrocytes: A Paradox for Neuronal Protection. *Journal of neurochemistry.* **78**, 842-853.

Guillemin G.J., Smith D.G., Smythe G.A., Armati P.J. and Brew G.J. (2003) Expression of the Kynurenine Pathway Enzymes in Human Microglia and Macrophages. *advance in experimental medicine and biology.* **527**, 105-112.

Guillemin G.J., Smythe G., Takikawa O. and Brew B.J. (2005) Expression of Indoleamine 2, 3-Dioxygenase and Production of Quinolinic Acid by Human Microglia, Astrocytes, and Neurons. *Glia.* **49**, 15-23.

Gutekunst C.-A., Li S.-H., Yi H., Ferrante R.J., Li X.-J. and Hersch S.M. (1998) The Cellular and Subcellular Localization of Huntingtin-Associated Protein 1 (HAP1): Comparison with Huntingtin in Rat and Human. *The Journal of Neuroscience.* **18**, 7674-7686.

Haber R., Bessette D., Hulihan-Giblin B., Durcan M.J. and Goldman D. (1993) Identification of Tryptophan 2, 3-Dioxygenase Rna in Rodent Brain. *Journal of neurochemistry.* **60**, 1159-1162.

Harjes P. and Wanker E.E. (2003) The Hunt for Huntingtin Function: Interaction Partners Tell Many Different Stories. *Trends in biochemical sciences.* **28**, 425-433.

Heiser V., Scherzinger E., Boeddrich A., Nordhoff E., Lurz R., Schugardt N., Lehrach H. and Wanker E.E. (2000) Inhibition of Huntingtin Fibrillogenesis by Specific Antibodies and Small Molecules: Implications for Huntington's Disease Therapy. *Proceedings of the National Academy of Sciences.* **97**, 6739-6744.

Herrera F., Tenreiro S., Miller-Fleming L. and Outeiro T.F. (2011) Visualization of Cell-to-Cell Transmission of Mutant Huntingtin Oligomers. *PLoS Currents.* **3**, RRN1210.

Herrmann J.M., Westermann B. and Neupert W. (2001) Analysis of Protein-Protein Interactions in Mitochondria by Co-immunoprecipitation and Chemical Cross-Linking. *Methods in cell biology.* **65**, 217-230.

Heyes M., Saito K., Crowley J., Davis L., Demitrack M., Der M., Dilling L., Elia J., Kruesi M. and Lackner A. (1992) Quinolinic Acid and Kynurenine Pathway Metabolism in Inflammatory and Non-Inflammatory Neurological Disease. *Brain.* **115**, 1249-1273.

Heyes M., Achim C., Wiley C., Major E., Saito K. and Markey S. (1996) Human Microglia Convert L-Tryptophan into the Neurotoxin Quinolinic Acid. *Biochem. J.* **320**, 595-597.

Hiatt S.M., Shyu Y.J., Duren H.M. and Hu C.-D. (2008) Bimolecular Fluorescence Complementation (BiFC) Analysis of Protein Interactions in Caenorhabditis Elegans. *methods.* **45**, 185-191.

Hilmas C., Pereira E.F., Alkondon M., Rassoulpour A., Schwarcz R. and Albuquerque E.X. (2001) The Brain Metabolite Kynurenic Acid Inhibits A7 Nicotinic Receptor Activity and Increases Non-A7 Nicotinic Receptor Expression: Physiopathological Implications. *The Journal of Neuroscience.* **21**, 7463-7473.

Hirai K., Kuroyanagi H., Tatebayashi Y., Hayashi Y., Hirabayashi-Takahashi K., Saito K., Haga S., Uemura T. and Izumi S. (2010) Dual Role of the Carboxyl-Terminal Region of Pig Liver L-Kynurenine 3-Monooxygenase: Mitochondrial-Targeting Signal and Enzymatic Activity. *Journal of biochemistry.* **148**, 639-650.

Hoffner G., Kahlem P. and Djian P. (2002) Perinuclear Localization of Huntingtin as a Consequence of Its Binding to Microtubules through an Interaction with B-Tubulin: Relevance to Huntington's Disease. *Journal of cell science.* **115**, 941-948.

Holtze M., Saetre P., Engberg G., Schwieler L., Werge T., Andreassen O.A., Hall H., Terenius L., Agartz I., Jönsson E.G., Schalling M. and Erhardt S. (2012) Kynurenine 3-Monooxygenase Polymorphisms: Relevance for Kynurenic Acid Synthesis in Patients with Schizophrenia and Healthy Controls. *Journal of psychiatry & neuroscience.* **37**, 53-57.

Horn U., Ullrich V. and Staudinger H. (1971) Purification and Characterization of L-Kynurenine 3-Hydroxylase (Ec 1.14. 1.2.) from Rat Liver. *Hoppe-Seyler´ s Zeitschrift für physiologische Chemie.* **352**, 837-842.

Hu C.-D. and Kerppola T.K. (2003) Simultaneous Visualization of Multiple Protein Interactions in Living Cells Using Multicolor Fluorescence Complementation Analysis. *Nature biotechnology.* **21**, 539-545.

Huntington G. (1872) On Chorea. *Med Surg Report.* 317- 321.

Hwang Y.T., Pelitire S.M., Henderson M.P.A., Andrews D.W., Dyer J.M. and Mullen R.T. (2004) Novel Targeting Signals Mediate the Sorting of Different Isoforms of the Tail-Anchored Membrane Protein Cytochrome B5 to Either Endoplasmic Reticulum or Mitochondria. *The Plant Cell Online.* **16**, 3002-3019.

Jin H., Zhang Y., You H., Tao X., Wang C., Jin G., Wang N., Ruan H., Gu D. and Huo X. (2015) Prognostic Significance of Kynurenine 3-Monooxygenase and Effects on Proliferation, Migration, and Invasion of Human Hepatocellular Carcinoma. *Scientific reports.* **5**, 1-12.

Johnson J. and Ascher P. (1987) Glycine Potentiates the NMDA Response in Cultured Mouse Brain Neurons. *Nature.* **325**, 529-531.

Jones S.P., Franco N.F., Varney B., Sundaram G., Brown D.A., de Bie J., Lim C.K., Guillemin G.J. and Brew B.J. (2015) Expression of the Kynurenine Pathway in Human Peripheral Blood Mononuclear Cells: Implications for Inflammatory and Neurodegenerative Disease. *PloS one.* **10**, 1-18.

Kaltenbach L.S., Romero E., Becklin R.R., Chettier R., Bell R., Phansalkar A., Strand A., Torcassi C., Savage J. and Hurlburt A. (2007) Huntingtin Interacting Proteins Are Genetic Modifiers of Neurodegeneration. *PLoS Genet.* **3**, e82.

Kazantsev A., Preisinger E., Dranovsky A., Goldgaber D. and Housman D. (1999) Insoluble Detergent-Resistant Aggregates Form between Pathological and Nonpathological Lengths of Polyglutamine in Mammalian Cells. *Proceedings of the National Academy of Sciences.* **96**, 11404-11409.

Kegel K.B., Sapp E., Yoder J., Cuiffo B., Sobin L., Kim Y.J., Qin Z.-H., Hayden M.R., Aronin N. and Scott D.L. (2005) Huntingtin Associates with Acidic Phospholipids at the Plasma Membrane. *Journal of Biological Chemistry.* **280**, 36464-36473.

Kegel K.B., Sapp E., Alexander J., Valencia A., Reeves P., Li X., Masso N., Sobin L., Aronin N. and DiFiglia M. (2009a) Polyglutamine Expansion in Huntingtin Alters Its Interaction with Phospholipids. *Journal of neurochemistry.* **110**, 1585-1597.

Kegel K.B., Schewkunow V., Sapp E., Masso N., Wanker E.E., DiFiglia M. and Goldmann W.H. (2009b) Polyglutamine Expansion in Huntingtin Increases Its Insertion into Lipid Bilayers. *Biochemical and biophysical research communications.* **387**, 472-475.

Kerppola T.K. (2006a) Design and Implementation of Bimolecular Fluorescence Complementation (BiFC) Assays for the Visualization of Protein Interactions in Living Cells. *Nature protocols.* **1**, 1278-1286.

Kerppola T.K. (2006b) Visualization of Molecular Interactions by Fluorescence Complementation. *Nature reviews Molecular cell biology.* **7**, 449-456.

Kerppola T.K. (2008) Bimolecular Fluorescence Complementation (BiFC) Analysis as a Probe of Protein Interactions in Living Cells. *Annual review of biophysics.* **37**, 465-487.

Khurana R., Uversky V.N., Nielsen L. and Fink A.L. (2001) Is Congo Red an Amyloid-Specific Dye? *Journal of Biological Chemistry.* **276**, 22715-22721.

Leavitt B.R., Guttman J.A., Hodgson J.G., Kimel G.H., Singaraja R., Vogl A.W. and Hayden M.R. (2001) Wild-Type Huntingtin Reduces the Cellular Toxicity of Mutant Huntingtin in Vivo. *The American Journal of Human Genetics.* **68**, 313-324.

Lee J.M., Ramos E., Lee J.H., Gillis T., Mysore J., Hayden M., Warby S., Morrison P., Nance M. and Ross C. (2012) CAG Repeat Expansion in Huntington Disease Determines Age at Onset in a Fully Dominant Fashion. *Neurology.* **78**, 690-695.

Li S.-H., Schilling G., Young W., Margolis R., Stine O., Wagster M., Abbott M., Franz M., Ranen N. and Folstein S. (1993) Huntington's Disease Gene (IT15) Is Widely Expressed in Human and Rat Tissues. *Neuron.* **11**, 985-993.

Li W., Serpell L.C., Carter W.J., Rubinsztein D.C. and Huntington J.A. (2006) Expression and Characterization of Full-Length Human Huntingtin, an Elongated HEAT Repeat Protein. *Journal of Biological Chemistry.* **281**, 15916-15922.

Liebig J.v. (1853) Über Kynurensäure. *Justus Liebigs Annalen der Chemie.* **86**, 125-126.

Lihavainen E., Mäkelä J., Spelbrink J.N. and Ribeiro A.S. (2015) Detecting and Tracking the Tips of Fluorescently Labeled Mitochondria in U2OS Cells. *Image Analysis and Processing—ICIAP 2015.* Springer, 363-372.

Lin M.T. and Beal M.F. (2006) Mitochondrial Dysfunction and Oxidative Stress in Neurodegenerative Diseases. *Nature.* **443**, 787-795.

Linderholm K.R., Skogh E., Olsson S.K., Dahl M.-L., Holtze M., Engberg G., Samuelsson M. and Erhardt S. (2012) Increased Levels of Kynurenine and Kynurenic Acid in the CSF of Patients with Schizophrenia. *Schizophrenia bulletin.* **38**, 426-432.

Lowe D.M., Gee M., Haslam C., Leavens B., Christodoulou E., Hissey P., Hardwicke P., Argyrou A., Webster S.P. and Mole D.J. (2013) Lead Discovery for Human Kynurenine 3-Monooxygenase by High-Throughput Rapidfire Mass Spectrometry. *Journal of biomolecular screening.* **19**, 508-515.

Lugo-Huitrón R., Blanco-Ayala T., Ugalde-Muñiz P., Carrillo-Mora P., Pedraza-Chaverrí J., Silva-Adaya D., Maldonado P., Torres I., Pinzón E. and Ortiz-Islas E. (2011) On the Antioxidant Properties of Kynurenic Acid: Free Radical Scavenging Activity and Inhibition of Oxidative Stress. *Neurotoxicology and teratology.* **33**, 538-547.

Lugo-Huitrón R., Ugalde Muñiz P., Pineda B., Pedraza-Chaverrí J., Ríos C. and Pérez-de la Cruz V. (2013) Quinolinic Acid: An Endogenous Neurotoxin with Multiple Targets. *Oxidative medicine and cellular longevity.* **2013**, 1-14.

Ma L., Morton A.J. and Nicholson L.F. (2003) Microglia Density Decreases with Age in a Mouse Model of Huntington's Disease. *Glia.* **43**, 274-280.

MacDermott A.B., Mayer M.L., Westbrook G.L., Smith S.J. and Barker J.L. (1986) NMDA-Receptor Activation Increases Cytoplasmic Calcium Concentration in Cultured Spinal Cord Neurones. *Nature.* **321**, 519-522.

Maeda Y., Ueda H., Kazami J., Kawano G., Suzuki E. and Nagamune T. (1997) Engineering of Functional Chimeric Protein *G–Vargula* luciferase. *Analytical biochemistry.* **249**, 147-152.

Manders E., Verbeek F. and Aten J. (1993) Measurement of Co-Localization of Objects in Dual-Colour Confocal Images. *Journal of microscopy.* **169**, 375-382.

Mándi Y. and Vécsei L. (2012) The Kynurenine System and Immunoregulation. *Journal of Neural Transmission.* **119**, 197-209.

Maragakis N.J. and Rothstein J.D. (2001) Glutamate Transporters in Neurologic Disease. *Archives of neurology.* **58**, 365-370.

Martin A., Heyes M.P., Salazar A.M., Kampen D.L., Williams J., Law W.A., Coats M.E. and Markey S.P. (1992) Progressive Slowing of Reaction Time and Increasing Cerebrospinal Fluid Concentrations of Quinolinic Acid in Hiv-Infected Individuals. *The Journal of neuropsychiatry and clinical neurosciences.* **4**, 270-279.

Martindale D., Hackam A., Wieczorek A., Ellerby L., Wellington C., McCutcheon K., Singaraja R., Kazemi-Esfarjani P., Devon R. and Kim S.U. (1998) Length of Huntingtin and Its Polyglutamine Tract Influences Localization and Frequency of Intracellular Aggregates. *Nature genetics.* **18**, 150-154.

Mellor A.L. and Munn D.H. (2004) Ido Expression by Dendritic Cells: Tolerance and Tryptophan Catabolism. *Nature Reviews Immunology.* **4**, 762-774.

Metz R., DuHadaway J.B., Kamasani U., Laury-Kleintop L., Muller A.J. and Prendergast G.C. (2007) Novel Tryptophan Catabolic Enzyme IDO2 Is the Preferred Biochemical Target of the Antitumor Indoleamine 2, 3-Dioxygenase Inhibitory Compound D-1-Methyl-Tryptophan. *Cancer research.* **67**, 7082-7087.

Mezrich J.D., Fechner J.H., Zhang X., Johnson B.P., Burlingham W.J. and Bradfield C.A. (2010) An Interaction between Kynurenine and the Aryl Hydrocarbon Receptor Can Generate Regulatory T Cells. *The Journal of Immunology.* **185**, 3190-3198.

Miller B.R. and Bezprozvanny I. (2010) Corticostriatal Circuit Dysfunction in Huntington's Disease: Intersection of Glutamate, Dopamine and Calcium. *Future neurology.* **5**, 735-756.

Modregger J., DiProspero N.A., Charles V., Tagle D.A. and Plomann M. (2002) Pacsin 1 Interacts with Huntingtin and Is Absent from Synaptic Varicosities in Presymptomatic Huntington's Disease Brains. *Human molecular genetics.* **11**, 2547-2558.

Moffett J.R., Espey M.G. and Namboodiri M.A. (1994) Antibodies to Quinolinic Acid and the Determination of Its Cellular Distribution within the Rat Immune System. *Cell and tissue research.* **278**, 461-469.

Moffett J.R. and Namboodiri M.A. (2003) Tryptophan and the Immune Response. *Immunology and cell biology.* **81**, 247-265.

Mole D.J., Webster S.P., Uings I., Zheng X., Binnie M., Wilson K., Hutchinson J.P., Mirguet O., Walker A. and Beaufils B. (2016) Kynurenine-3-Monooxygenase Inhibition Prevents Multiple Organ Failure in Rodent Models of Acute Pancreatitis. *Nature medicine.* **22**, 202-209.

Moroni F., Russi P., Lombardi G., Beni M. and Carla V. (1988) Presence of Kynurenic Acid in the Mammalian Brain. *Journal of neurochemistry.* **51**, 177-180.

Moroni F. (1999) Tryptophan Metabolism and Brain Function: Focus on Kynurenine and Other Indole Metabolites. *European journal of pharmacology.* **375**, 87-100.

Moroni F., Cozzi A., Sili M. and Mannaioni G. (2012) Kynurenic Acid: A Metabolite with Multiple Actions and Multiple Targets in Brain and Periphery. *Journal of Neural Transmission.* **119**, 133-139.

Mrzljak L. (2013) Development of Kynurenine Monooxygenase (KMO) Inhibitor CHDI-340246 for the Treatment of Huntington's Disease: A Progress Update. *CHDI Foundation 7th Annual HD Therapeutics Conference.*

Murray M.F. (2007) The Human Indoleamine 2, 3-Dioxygenase Gene and Related Human Genes. *Current drug metabolism.* **8**, 197-200.

Nasir J., Floresco S.B., O'Kusky J.R., Diewert V.M., Richman J.M., Zeisler J., Borowski A., Marth J.D., Phillips A.G. and Hayden M.R. (1995) Targeted Disruption of the Huntington's Disease Gene Results in Embryonic Lethality and Behavioral and Morphological Changes in Heterozygotes. *Cell.* **81**, 811-823.

Neuwald A.F. and Hirano T. (2000) HEAT Repeats Associated with Condensins, Cohesins, and Other Complexes Involved in Chromosome-Related Functions. *Genome research.* **10**, 1445-1452.

Nguyen N.T., Kimura A., Nakahama T., Chinen I., Masuda K., Nohara K., Fujii-Kuriyama Y. and Kishimoto T. (2010) Aryl Hydrocarbon Receptor Negatively Regulates Dendritic Cell Immunogenicity Via a Kynurenine-Dependent Mechanism. *Proceedings of the National Academy of Sciences.* **107**, 19961-19966.

Nijtmans L.G., Henderson N.S. and Holt I.J. (2002) Blue Native Electrophoresis to Study Mitochondrial and Other Protein Complexes. *methods.* **26**, 327-334.

Nilsson L., Linderholm K., Engberg G., Paulson L., Blennow K., Lindström L., Nordin C., Karanti A., Persson P. and Erhardt S. (2005) Elevated Levels of Kynurenic Acid in the Cerebrospinal Fluid of Male Patients with Schizophrenia. *Schizophrenia research.* **80**, 315-322.

Nishimoto Y., Takeuchi F. and Shibata Y. (1975) Isolation of L-Kynurenine 3-Hydroxylase from the Mitochondrial Outer Membrane of Rat Liver. *Journal of biochemistry.* **78**, 573-581.

Nishimoto Y., Takeuchi F. and Shibata Y. (1977) Molecular Properties of L-Kynurenine 3-Hydroxylase from Rat Liver Mitochondria. *Journal of biochemistry*. **81**, 1413-1425.

Nisimoto Y., Takeuchi F. and Shibata Y. (1975) Isolation of L-Kynurenine 3-Hydroxylase from the Mitochondrial Outer Membrane of Rat Liver. *Journal of biochemistry*. **78**, 573-581.

Nisimoto Y., Takeuchi F. and Shibata Y. (1977) Molecular Properties of L-Kynurenine 3-Hydroxylase from Rat Liver Mitochondria. *Journal of biochemistry*. **81**, 1413-1425.

Ohashi K., Kiuchi T., Shoji K., Sampei K. and Mizuno K. (2012) Visualization of Cofilin-Actin and Ras-Raf Interactions by Bimolecular Fluorescence Complementation Assays Using a New Pair of Split Venus Fragments. *Biotechniques*. **52**, 45-50.

Okamoto H., Yamamoto S., Nozaki M. and Hayaishi O. (1967) On the Submitochondrial Localization of L-Kynurenine-3-Hydroxylase. *Biochemical and biophysical research communications*. **26**, 309-314.

Okuda S., Nishiyama N., Saito H. and Katsuki H. (1996) Hydrogen Peroxide-Mediated Neuronal Cell Death Induced by an Endogenous Neurotoxin, 3-Hydroxykynurenine. *Proceedings of the National Academy of Sciences*. **93**, 12553-12558.

Okuda S., Nishiyama N., Saito H. and Katsuki H. (1998) 3-Hydroxykynurenine, an Endogenous Oxidative Stress Generator, Causes Neuronal Cell Death with Apoptotic Features and Region Selectivity. *Journal of neurochemistry*. **70**, 299-307.

Okuno E., Nakamura M. and Schwarcz R. (1991) Two Kynurenine Aminotransferases in Human Brain. *Brain research*. **542**, 307-312.

Orr A.L., Li S., Wang C.-E., Li H., Wang J., Rong J., Xu X., Mastroberardino P.G., Greenamyre J.T. and Li X.-J. (2008) N-Terminal Mutant Huntingtin Associates with Mitochondria and Impairs Mitochondrial Trafficking. *The Journal of Neuroscience*. **28**, 2783-2792.

Orrenius S. (2004) Mitochondrial Regulation of Apoptotic Cell Death. *Toxicology letters*. **149**, 19-23.

Panov A.V., Gutekunst C.-A., Leavitt B.R., Hayden M.R., Burke J.R., Strittmatter W.J. and Greenamyre J.T. (2002) Early Mitochondrial Calcium Defects in Huntington's Disease Are a Direct Effect of Polyglutamines. *Nature neuroscience*. **5**, 731-736.

Pavese N., Gerhard A., Tai Y., Ho A., Turkheimer F., Barker R., Brooks D. and Piccini P. (2006) Microglial Activation Correlates with Severity in Huntington Disease a Clinical and Pet Study. *Neurology*. **66**, 1638-1643.

Pearson S. and Reynolds G. (1992) Increased Brain Concentrations of a Neurotoxin, 3-Hydroxykynurenine, in Huntington's Disease. *Neuroscience letters*. **144**, 199-201.

Perkins M. and Stone T. (1982) An Iontophoretic Investigation of the Actions of Convulsant Kynurenines and Their Interaction with the Endogenous Excitant Quinolinic Acid. *Brain research*. **247**, 184-187.

Perutz M.F., Johnson T., Suzuki M. and Finch J.T. (1994) Glutamine Repeats as Polar Zippers: Their Possible Role in Inherited Neurodegenerative Diseases. *Proceedings of the National Academy of Sciences*. **91**, 5355-5358.

Petrasch-Parwez E., Nguyen H.P., Löbbecke-Schumacher M., Habbes H.W., Wieczorek S., Riess O., Andres K.H., Dermietzel R. and Von Hörsten S. (2007) Cellular and Subcellular Localization of Huntington Aggregates in the Brain of a Rat Transgenic for Huntington Disease. *Journal of Comparative Neurology.* **501**, 716-730.

Pierozan P., Zamoner A., Soska Â.K., Silvestrin R.B., Loureiro S.O., Heimfarth L., e Souza T.M., Wajner M. and Pessoa-Pureur R. (2010) Acute Intrastriatal Administration of Quinolinic Acid Provokes Hyperphosphorylation of Cytoskeletal Intermediate Filament Proteins in Astrocytes and Neurons of Rats. *Experimental neurology.* **224**, 188-196.

Plun-Favreau H., Klupsch K., Moisoi N., Gandhi S., Kjaer S., Frith D., Harvey K., Deas E., Harvey R.J. and McDonald N. (2007) The Mitochondrial Protease Htra2 Is Regulated by Parkinson's Disease-Associated Kinase Pink1. *Nature cell biology.* **9**, 1243-1252.

Polidori M.C., Mecocci P., Browne S.E., Senin U. and Beal M.F. (1999) Oxidative Damage to Mitochondrial DNA in Huntington's Disease Parietal Cortex. *Neuroscience letters.* **272**, 53-56.

Prescott C., Weeks A.M., Staley K.J. and Partin K.M. (2006) Kynurenic Acid Has a Dual Action on AMPA Receptor Responses. *Neuroscience letters.* **402**, 108-112.

Repici M., Straatman K.R., Balduccio N., Enguita F.J., Outeiro T.F. and Giorgini F. (2013) Parkinson's Disease-Associated Mutations in Dj-1 Modulate Its Dimerization in Living Cells. *Journal of Molecular Medicine.* **91**, 599-611.

Ridley R., Frith C., Crow T. and Conneally P. (1988) Anticipation in Huntington's Disease Is Inherited through the Male Line but May Originate in the Female. *Journal of medical genetics.* **25**, 589-595.

Rigamonti D., Bauer J.H., De-Fraja C., Conti L., Sipione S., Sciorati C., Clementi E., Hackam A., Hayden M.R. and Li Y. (2000) Wild-Type Huntingtin Protects from Apoptosis Upstream of Caspase-3. *The Journal of Neuroscience.* **20**, 3705-3713.

Rigamonti D., Sipione S., Goffredo D., Zuccato C., Fossale E. and Cattaneo E. (2001) Huntingtin's Neuroprotective Activity Occurs Via Inhibition of Procaspase-9 Processing. *Journal of Biological Chemistry.* **276**, 14545-14548.

Rockabrand E., Slepko N., Pantalone A., Nukala V.N., Kazantsev A., Marsh J.L., Sullivan P.G., Steffan J.S., Sensi S.L. and Thompson L.M. (2007) The First 17 Amino Acids of Huntingtin Modulate Its Sub-Cellular Localization, Aggregation and Effects on Calcium Homeostasis. *Human molecular genetics.* **16**, 61-77.

Rodgers J., Stone T.W., Barrett M.P., Bradley B. and Kennedy P.G. (2009) Kynurenine Pathway Inhibition Reduces Central Nervous System Inflammation in a Model of Human African Trypanosomiasis. *Brain.* **132**, 1259-1267.

Ross C.A., Aylward E.H., Wild E.J., Langbehn D.R., Long J.D., Warner J.H., Scahill R.I., Leavitt B.R., Stout J.C. and Paulsen J.S. (2014) Huntington Disease: Natural History, Biomarkers and Prospects for Therapeutics. *Nature Reviews Neurology.* **10**, 204-216.

Rossi F., Schwarcz R. and Rizzi M. (2008) Curiosity to Kill the KAT (Kynurenine Aminotransferase): Structural Insights into Brain Kynurenic Acid Synthesis. *Current opinion in structural biology.* **18**, 748-755.

Saka Y., Hagemann A.I., Piepenburg O. and Smith J.C. (2007) Nuclear Accumulation of Smad Complexes Occurs Only after the Midblastula Transition in Xenopus. *Development.* **134**, 4209-4218.

Sánchez A.M.E., Mejía-Toiber J. and Massieu L. (2008) Excitotoxic Neuronal Death and the Pathogenesis of Huntington's Disease. *Archives of medical research.* **39**, 265-276.

Sapp E., Kegel K., Aronin N., Hashikawa T., Uchiyama Y., Tohyama K., Bhide P., Vonsattel J. and DiFiglia M. (2001) Early and Progressive Accumulation of Reactive Microglia in the Huntington Disease Brain. *Journal of Neuropathology & Experimental Neurology.* **60**, 161-172.

Sathasivam K., Neueder A., Gipson T.A., Landles C., Benjamin A.C., Bondulich M.K., Smith D.L., Faull R.L., Roos R.A. and Howland D. (2013) Aberrant Splicing of Htt Generates the Pathogenic Exon 1 Protein in Huntington Disease. *Proceedings of the National Academy of Sciences.* **110**, 2366-2370.

Sathyasaikumar K.V., Stachowski E.K., Wonodi I., Roberts R.C., Rassoulpour A., McMahon R.P. and Schwarcz R. (2011) Impaired Kynurenine Pathway Metabolism in the Prefrontal Cortex of Individuals with Schizophrenia. *Schizophrenia bulletin.* **37**, 1147-1156.

Schwarcz R., Whetsell W.O. and Mangano R.M. (1983) Quinolinic Acid: An Endogenous Metabolite That Produces Axon-Sparing Lesions in Rat Brain. *Science.* **219**, 316-318.

Schwarcz R., Rassoulpour A., Wu H.-Q., Medoff D., Tamminga C.A. and Roberts R.C. (2001) Increased Cortical Kynurenate Content in Schizophrenia. *Biological psychiatry.* **50**, 521-530.

Schwarcz R. and Pellicciari R. (2002) Manipulation of Brain Kynurenines: Glial Targets, Neuronal Effects, and Clinical Opportunities. *Journal of Pharmacology and Experimental Therapeutics.* **303**, 1-10.

Schwarcz R. (2004) The Kynurenine Pathway of Tryptophan Degradation as a Drug Target. *Current opinion in pharmacology.* **4**, 12-17.

Schwarcz R., Bruno J.P., Muchowski P.J. and Wu H.Q. (2012) Kynurenines in the Mammalian Brain: When Physiology Meets Pathology. *Nature Reviews Neuroscience.* **13**, 465-477.

Seong I.S., Ivanova E., Lee J.-M., Choo Y.S., Fossale E., Anderson M., Gusella J.F., Laramie J.M., Myers R.H. and Lesort M. (2005) HD CAG Repeat Implicates a Dominant Property of Huntingtin in Mitochondrial Energy Metabolism. *Human molecular genetics.* **14**, 2871-2880.

Sharp A.H., Loev S.J., Schilling G., Li S.-H., Li X.-J., Bao J., Wagster M.V., Kotzuk J.A., Steiner J.P. and Lo A. (1995) Widespread Expression of Huntington's Disease Gene (IT15) Protein Product. *Neuron.* **14**, 1065-1074.

Shin J.-Y., Fang Z.-H., Yu Z.-X., Wang C.-E., Li S.-H. and Li X.-J. (2005) Expression of Mutant Huntingtin in Glial Cells Contributes to Neuronal Excitotoxicity. *The Journal of cell biology.* **171**, 1001-1012.

Shyu Y.J., Liu H., Deng X. and Hu C. (2006) Identification of New Fluorescent Protein Fragments for Biomolecular Fluorescence Complementation Analysis under Physiological Conditions. *Biotechniques.* **40**, 61-66.

Simmons D.A., Casale M., Alcon B., Pham N., Narayan N. and Lynch G. (2007) Ferritin Accumulation in Dystrophic Microglia Is an Early Event in the Development of Huntington's Disease. *Glia.* **55**, 1074-1084.

Smith R., Brundin P. and Li J.-Y. (2005) Synaptic Dysfunction in Huntington's Disease: A New Perspective. *Cellular and Molecular Life Sciences CMLS.* **62**, 1901-1912.

Steffan J.S., Agrawal N., Pallos J., Rockabrand E., Trotman L.C., Slepko N., Illes K., Lukacsovich T., Zhu Y.-Z. and Cattaneo E. (2004) SUMO Modification of Huntingtin and Huntington's Disease Pathology. *Science.* **304**, 100-104.

Stone T.W. and Perkins M.N. (1981) Quinolinic Acid: A Potent Endogenous Excitant at Amino Acid Receptors in Cns. *European journal of pharmacology.* **72**, 411-412.

Stone T.W. (1993) Neuropharmacology of Quinolinic and Kynurenic Acids. *Pharmacological reviews.* **45**, 309-379.

Stone T.W. (2001) Kynurenines in the Cns: From Endogenous Obscurity to Therapeutic Importance. *Progress in neurobiology.* **64**, 185-218.

Stone T.W., Stoy N. and Darlington L.G. (2013) An Expanding Range of Targets for Kynurenine Metabolites of Tryptophan. *Trends in pharmacological sciences.* **34**, 136-143.

Sugars K.L. and Rubinsztein D.C. (2003) Transcriptional Abnormalities in Huntington Disease. *Trends in Genetics.* **19**, 233-238.

Sugars K.L., Brown R., Cook L.J., Swartz J. and Rubinsztein D.C. (2004) Decreased Camp Response Element-Mediated Transcription an Early Event in Exon 1 and Full-Length Cell Models of Huntington′ S Disease That Contributes to Polyglutamine Pathogenesis. *Journal of Biological Chemistry.* **279**, 4988-4999.

Sun Y., Savanenin A., Reddy P.H. and Liu Y.F. (2001) Polyglutamine-Expanded Huntingtin Promotes Sensitization of N-Methyl-D-Aspartate Receptors Via Post-Synaptic Density 95. *Journal of Biological Chemistry.* **276**, 24713-24718.

Tabrizi S., Cleeter M., Xuereb J., Taanman J.W., Cooper J. and Schapira A. (1999) Biochemical Abnormalities and Excitotoxicity in Huntington's Disease Brain. *Annals of neurology.* **45**, 25-32.

Tai Y.F., Pavese N., Gerhard A., Tabrizi S.J., Barker R.A., Brooks D.J. and Piccini P. (2007) Microglial Activation in Presymptomatic Huntington's Disease Gene Carriers. *Brain.* **130**, 1759-1766.

Takahashi Y., Karbowski M., Yamaguchi H., Kazi A., Wu J., Sebti S.M., Youle R.J. and Wang H.-G. (2005) Loss of Bif-1 Suppresses Bax/Bak Conformational Change and Mitochondrial Apoptosis. *Molecular and cellular biology.* **25**, 9369-9382.

Takikawa O., Kuroiwa T., Yamazaki F. and Kido R. (1988) Mechanism of Interferon-Gamma Action. Characterization of Indoleamine 2, 3-Dioxygenase in Cultured Human Cells Induced by Interferon-Gamma and Evaluation of the Enzyme-Mediated Tryptophan Degradation in Its Anticellular Activity. *Journal of Biological Chemistry.* **263**, 2041-2048.

Takikawa O., Tagawa Y.-i., Iwakura Y., Yoshida R. and Truscott R.J. (1999) Interferon-Gamma-Dependent/Independent Expression of Indoleamine 2, 3-Dioxygenase. *Tryptophan, Serotonin, and Melatonin.* Springer, 553-557.

Tam S., Spiess C., Auyeung W., Joachimiak L., Chen B., Poirier M.A. and Frydman J. (2009) The Chaperonin Tric Blocks a Huntingtin Sequence Element That Promotes the Conformational Switch to Aggregation. *Nature structural & molecular biology.* **16**, 1279-1285.

Tan L., Yu J.-T. and Tan L. (2012) The Kynurenine Pathway in Neurodegenerative Diseases: Mechanistic and Therapeutic Considerations. *Journal of the neurological sciences.* **323**, 1-8.

Tao X., Finkbeiner S., Arnold D.B., Shaywitz A.J. and Greenberg M.E. (1998) Ca 2+ Influx Regulates Bdnf Transcription by a CREB Family Transcription Factor-Dependent Mechanism. *Neuron.* **20**, 709-726.

Tavares R.G., Tasca C.I., Santos C.E., Alves L.c.B., Porciúncula L.O., Emanuelli T. and Souza D.O. (2002) Quinolinic Acid Stimulates Synaptosomal Glutamate Release and Inhibits Glutamate Uptake into Astrocytes. *Neurochemistry international.* **40**, 621-627.

Telenius H., Kremer H., Thellmann J., Andrew S., Almqvist E., Anvret M., Greenberg C., Greenberg J., Lucotte G. and Squltierl F. (1993) Molecular Analysis of Juvenile Huntington Disease: The Major Influence on $(CAG)_n$ Repeat Length Is the Sex of the Affected Parent. *Human molecular genetics.* **2**, 1535-1540.

The Huntington's Disease Collaborative Research Group. (1993) A Novel Gene Containing a Trinucleotide Repeat That Is Expanded and Unstable on Huntington's Disease Chromosomes. *Cell.* **72**, 971-983.

Thevandavakkam M.A. (2011) Deciphering the Kynurenine-3-Monooxygenase Intercome. PhD Thesis. Leicester (UK), The University of Leicester.

Thomas S.R. and Stocker R. (1999) Redox Reactions Related to Indoleamine 2, 3-Dioxygenase and Tryptophan Metabolism Along the Kynurenine Pathway. *Redox Report.* **4**, 199-220.

Thompson L.M., Aiken C.T., Kaltenbach L.S., Agrawal N., Illes K., Khoshnan A., Martinez-Vincente M., Arrasate M., O'Rourke J.G. and Khashwji H. (2009) IKK Phosphorylates Huntingtin and Targets It for Degradation by the Proteasome and Lysosome. *The Journal of cell biology.* **187**, 1083-1099.

Trottier Y., Devys D., Imbertl G., Saudoul F. and Anz I. (1995) Cellular Localization of the Huntington's Disease Protein. *Nature genetics.* **10**, 104-110.

Tymianski M., Charlton M., Carlen P. and Tator C.H. (1993) Source Specificity of Early Calcium Neurotoxicity in Cultured Embryonic Spinal Neurons. *The Journal of Neuroscience.* **13**, 2085-2104.

Uemura T. and Hirai K. (1998) L-Kynurenine 3-Monooxygenase from Mitochondrial Outer Membrane of Pig Liver: Purification, Some Properties, and Monoclonal Antibodies Directed to the Enzyme. *Journal of biochemistry.* **123**, 253-262.

Vonsattel J.-P., Myers R.H., Stevens T.J., Ferrante R.J., Bird E.D. and Richardson Jr E.P. (1985) Neuropathological Classification of Huntington's Disease. *Journal of Neuropathology & Experimental Neurology.* **44**, 559-577.

Walter M., Chaban C., Schütze K., Batistic O., Weckermann K., Näke C., Blazevic D., Grefen C., Schumacher K. and Oecking C. (2004) Visualization of Protein Interactions in Living Plant Cells Using Bimolecular Fluorescence Complementation. *The Plant Journal.* **40**, 428-438.

Wang J., Simonavicius N., Wu X., Swaminath G., Reagan J., Tian H. and Ling L. (2006) Kynurenic Acid as a Ligand for Orphan G Protein-Coupled Receptor Gpr35. *Journal of Biological Chemistry.* **281**, 22021-22028.

Watanabe Y., Yoshida R., Sono M. and Hayaishi O. (1981) Immunohistochemical Localization of Indoleamine 2, 3-Dioxygenase in the Argyrophilic Cells of Rabbit Duodenum and Thyroid Gland. *Journal of Histochemistry & Cytochemistry.* **29**, 623-632.

Wei M.C., Zong W.-X., Cheng E.H.-Y., Lindsten T., Panoutsakopoulou V., Ross A.J., Roth K.A., MacGregor G.R., Thompson C.B. and Korsmeyer S.J. (2001) Proapoptotic Bax and Bak: A Requisite Gateway to Mitochondrial Dysfunction and Death. *Science.* **292**, 727-730.

Westrate L.M., Drocco J.A., Martin K.R., Hlavacek W.S. and MacKeigan J.P. (2014) Mitochondrial Morphological Features Are Associated with Fission and Fusion Events. *PloS one.* **9**, e95265.

Wheeler V.C., Persichetti F., McNeil S.M., Mysore J.S., Mysore S.S., MacDonald M.E., Myers R.H., Gusella J.F. and Wexler N.S. (2007) Factors Associated with HD CAG Repeat Instability in Huntington Disease. *Journal of medical genetics.* **44**, 695-701.

Wilson K., Mole D., Binnie M., Homer N., Zheng X., Yard B., Iredale J., Auer M. and Webster S. (2014) Bacterial Expression of Human Kynurenine 3-Monooxygenase: Solubility, Activity, Purification. *Protein expression and purification.* **95**, 96-103.

Wilson K., Mole D.J., Homer N.Z., Iredale J.P., Auer M. and Webster S.P. (2015) A Magnetic Bead–Based Ligand Binding Assay to Facilitate Human Kynurenine 3-Monooxygenase Drug Discovery. *Journal of biomolecular screening.* **20**, 292-298.

Winkler D., Beconi M., Toledo-Sherman L.M., Prime M., Ebneth A., Dominguez C. and Muñoz-Sanjuan I. (2013) Development of Lc/Ms/Ms, High-Throughput Enzymatic and Cellular Assays for the Characterization of Compounds That Inhibit Kynurenine Monooxygenase (KMO). *Journal of biomolecular screening.* **18**, 879-889.

Wonodi I. and Schwarcz R. (2010) Cortical Kynurenine Pathway Metabolism: A Novel Target for Cognitive Enhancement in Schizophrenia. *Schizophrenia bulletin.* **36**, 211-218.

Wonodi I., Stine O.C., Sathyasaikumar K.V., Roberts R.C., Mitchell B.D., Hong L.E., Kajii Y., Thaker G.K. and Schwarcz R. (2011) Downregulated Kynurenine 3-Monooxygenase Gene Expression and Enzyme Activity in Schizophrenia and Genetic Association with Schizophrenia Endophenotypes. *Archives of general psychiatry.* **68**, 665-674.

Wonodi I., McMahon R.P., Krishna N., Mitchell B.D., Liu J., Glassman M., Hong L.E. and Gold J.M. (2014) Influence of Kynurenine 3-Monooxygenase (KMO) Gene Polymorphism on Cognitive Function in Schizophrenia. *Schizophrenia research.* **160**, 80-87.

Wu C., Scott J. and Shea J.-E. (2012) Binding of Congo Red to Amyloid Protofibrils of the Alzheimer Aβ 9–40 Peptide Probed by Molecular Dynamics Simulations. *Biophysical journal.* **103**, 550-557.

Xia J., Lee D.H., Taylor J., Vandelft M. and Truant R. (2003) Huntingtin Contains a Highly Conserved Nuclear Export Signal. *Human molecular genetics.* **12**, 1393-1403.

Yamazaki F., Kuroiwa T., Takikawa O. and Kido R. (1985) Human Indolylamine 2, 3-Dioxygenase. Its Tissue Distribution, and Characterization of the Placental Enzyme. *Biochem. J.* **230**, 635-638.

Yu P., Li Z., Zhang L., Tagle D.A. and Cai T. (2006) Characterization of Kynurenine Aminotransferase Iii, a Novel Member of a Phylogenetically Conserved Kat Family. *Gene.* **365**, 111-118.

Yu Z.-X., Li S.-H., Evans J., Pillarisetti A., Li H. and Li X.-J. (2003) Mutant Huntingtin Causes Context-Dependent Neurodegeneration in Mice with Huntington's Disease. *The Journal of Neuroscience.* **23**, 2193-2202.

Zeitlin S., Liu J.P., Chapman D.L., Papaioannou V.E. and Efstratiadis A. (1995) Increased Apoptosis and Early Embryonic Lethality in Mice Nullizygous for the Huntington's Disease Gene Homologue. *Nature genetics.* **11**, 155-163.

Zeron M.M., Chen N., Moshaver A., Lee A.T.-C., Wellington C.L., Hayden M.R. and Raymond L.A. (2001) Mutant Huntingtin Enhances Excitotoxic Cell Death. *Molecular and Cellular Neuroscience.* **17**, 41-53.

Zeron M.M., Fernandes H.B., Krebs C., Shehadeh J., Wellington C.L., Leavitt B.R., Baimbridge K.G., Hayden M.R. and Raymond L.A. (2004) Potentiation of Nmda Receptor-Mediated Excitotoxicity Linked with Intrinsic Apoptotic Pathway in YAC Transgenic Mouse Model of Huntington's Disease. *Molecular and Cellular Neuroscience.* **25**, 469-479.

Zheng Z. and Diamond M.I. (2012) Huntington Disease and the Huntingtin Protein. *Progress in molecular biology and translational science.* **107**, 189-214.

Zuccato C., Ciammola A., Rigamonti D., Leavitt B.R., Goffredo D., Conti L., MacDonald M.E., Friedlander R.M., Silani V. and Hayden M.R. (2001) Loss of Huntingtin-Mediated BDNF Gene Transcription in Huntington's Disease. *Science.* **293**, 493-498.

Zuccato C., Valenza M. and Cattaneo E. (2010) Molecular Mechanisms and Potential Therapeutical Targets in Huntington's Disease. *Physiological reviews.* **90**, 905-981.

Zwilling D., Huang S., Sathyasaikumar K., Notarangelo F., Guidetti P., Wu H., Lee J., Truong J., Andrews-Zwilling Y. and Hsieh E. (2011) Kynurenine 3-Monooxygenase Inhibition in Blood Ameliorates Neurodegeneration. *Cell.* **145**, 863-874.